

THE UNIVERSITY OF CALGARY

SYMBIOTIC STARS: THE GEOMETRY OF THE RADIO
EMITTING REGIONS

BY

Harold T. Kenny

A THESIS

SUBMITTED TO THE FACULTY OF GRADUATE STUDIES
IN PARTIAL FULFILLMENT OF THE REQUIREMENTS FOR THE
DEGREE OF DOCTOR OF PHILOSOPHY

DEPARTMENT OF PHYSICS AND ASTRONOMY

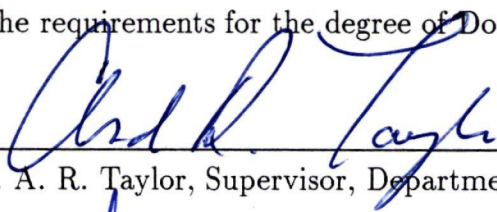
CALGARY, ALBERTA

June, 1995

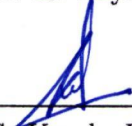
© Harold T. Kenny 1995

THE UNIVERSITY OF CALGARY
FACULTY OF GRADUATE STUDIES

The undersigned certify that they have read, and recommend to the Faculty of Graduate Studies for acceptance, a thesis entitled, "Symbiotic Stars: The Geometry of the Radio Emitting Regions" submitted by Captain Harold T. Kenny in partial fulfillment of the requirements for the degree of Doctor of Philosophy.



Dr. A. R. Taylor, Supervisor, Department of Physics and Astronomy



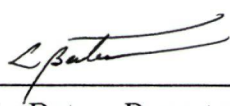
Dr. S. Kwok, Department of Physics and Astronomy




Dr. R. B. Hicks, Department of Physics and Astronomy



Dr. M. R. Williams, Department of Computer Science



Dr. L. Bates, Department of Mathematics and Statistics



Dr. L. A. Willson, Iowa State University

Date 5 June 1995

Abstract

Radio emission from symbiotic stars is examined to determine the density, distribution, and dynamics of material in the circumstellar nebulae. AT observations have been made of four southern systems with declinations $< -55^\circ$ (BI Cru, He 2-106, HD 149427, and RR Tel). Four northern objects have been observed both at the VLA and MERLIN (HM Sge, V1016 Cyg, AG Peg and Z And).

Observations are analysed in terms of the the STB model (Seaquist, Taylor and Button 1984), and various CW (“Colliding Winds”) models. Three configurations of CW models are considered: the “CWc” (concentric) model; the “CWb” (binary) model; and the “CWo” (orbital) model. The CWc and CWb models derive from earlier works (Kwok, Purton and Fitzgerald 1978; Kwok 1987a; Girard and Willson 1987), and various refinements and extensions are introduced here: *e.g.* the treatment of thermal pressure in the unshocked stellar winds, and the derivation of densities and thicknesses for the interaction zones. The CWo model is essentially original.

The radio morphologies and spectra of the observed systems are well explained in terms of the models considered. The southern systems are consistent with the STB model and also with the CWb model. The binary separations indicated for BI Cru and He 2-106 ($\sim 3000D_{\text{kpc}}$ AU) are, however, much larger than appropriate for known processes of accretional heating of the hot component. Z And is consistent with both a simple STB model, and with a modified STB model including a “no-recombination” (NR) shell. AG Peg is well explained by the CWo model, with variable hot component mass loss. HM Sge and V1016 Cyg are interpreted with reference to a combined STB/CW model.

Acknowledgements

In completing this thesis, I have incurred many debts of gratitude. I would like to thank Russ Taylor, my supervisor, an inspired and generous research scientist, and a nice guy. Of the many other individuals to whom I owe special thanks, I would like especially to recognize Richard Davis who assisted with my observations at Jodrell Bank, and Anastasius Tzioumis who guided my efforts at the Australia Telescope. I would also like to thank my regiment, the P.P.C.L.I., which encouraged my academic aspirations and made my study possible. I would further like to acknowledge that my study was ultimately sponsored by the people of this land; may they be well repaid. $\text{Ἔσοι θεμελιό, βα ἡδαιτ ἕομ βυίοσας Ἀ ἐδδαιτ Ἀμ να ναοισῆ, ἱκολῶσι, ἡοιηροισῆ Ἀζυρ βαητο μο ἱηηρεδμ. ἱρ Ἀρ ἰδο Ἀ ἕφυδμ με μο ἡηηροιδιτο; τᾶ ἱύιλ Ἀζαμ ζο ο'έημοιοῦ ἱύηηταρ ζο ἕομ ἰοηαμ Ἀμ Ἀ ἡβηοηηηαηαηρ.$

Contents

Approval Page	ii
Abstract	iii
Διομηκεδστ	iv
Acknowledgements	v
List of Tables	x
List of Figures	xi
Epigram	xiv
1 A BACKGROUND TO THE STUDY OF SYMBIOTIC STARS	1
1.1 The Cool Component	3
1.2 The Hot Component	6
1.3 The Nebular Component	10
1.4 Outbursts	13
1.4.1 Outburst Subclasses	13
1.4.2 Outburst Models	15
1.5 Symbiotic Stars as Interacting Binary Systems	18
1.5.1 Formation and Evolution	19
1.6 Outstanding Questions	22
2 CURRENT MODELS OF RADIO EMISSION	25
2.1 The Seaquist, Taylor and Button (STB) Model	25
2.1.1 The Model	25
2.1.2 Observational Evidence for STB Phenomena	27
2.1.3 New Treatments of Derived Quantities	31
2.2 Colliding Winds (CW) Models	35
2.2.1 Shocks	35
2.2.2 Single Star Wind Models	39
2.2.3 Wind Models in Binary Systems	43
2.2.4 Observational Evidence for CW Phenomena	47

3	EXTENSIONS OF COLLIDING WINDS (CW) MODELS	50
3.1	Binary Colliding Winds (CWb) Model	52
3.1.1	Isothermal Approximation	52
3.1.2	Interaction Boundary Location	64
3.1.3	Shell Thickness and Density	70
3.1.4	Ionization	74
3.1.5	Model Images	75
3.1.6	Model Spectra	78
3.1.7	Comparison with the STB Model	80
3.2	Concentric Colliding Winds (CWc) Model	83
3.2.1	Shell Velocity and Location	85
3.2.2	Shell Thickness and Density	87
3.2.3	Shell Temperature	88
3.2.4	Ionization	94
3.3	Orbital Colliding Winds (CWo) Model	94
3.3.1	Qualitative Development	94
3.3.2	Spiral Wall Velocity	102
3.3.3	Spiral Wall Compression	105
3.3.4	Interaction with the Remnant Cool Wind	107
4	OBSERVATIONS	110
4.1	High Resolution Radio Imaging	110
4.1.1	Previous Results	110
4.1.2	Limitations of Resolution and Sensitivity	112
4.1.3	Instrumental Specifications and Calibration	114
4.1.4	Model Testing	121
4.2	Program Stars	122
4.2.1	Selection	122
4.2.2	Tabular Data	122
4.2.3	Observational Histories	133
4.3	Details of the Observing Program	150
4.3.1	Schedule of Observations	150
4.3.2	Combined Array Imaging: MERLIN/VLA	151
5	SOUTHERN SYMBIOTICS	154
5.1	Observations	154
5.1.1	Flux Density Measurements	154
5.1.2	Visibility Analysis	157
5.1.3	Images	161
5.2	Discussion	164

5.2.1	STB Model	164
5.2.2	CWb Model	168
5.2.3	CWo Model, and Equatorially Enhanced Mass Loss	171
5.2.4	Conclusions	172
6	Z ANDROMEDAE	173
6.1	Observations	173
6.1.1	Flux Density Variations	173
6.1.2	Spectral Index Variations	175
6.1.3	MERLIN/VLA Imaging	179
6.2	Discussion	182
6.2.1	Flux Density and Spectral Index	182
6.2.2	Image Interpretation	187
6.3	Conclusions	191
7	AG PEGASI	193
7.1	Observations	193
7.2	Central Source Variations	197
7.3	The Inner Nebula: Visibility Analysis	200
7.4	Lobe Enhancements of the Inner Nebula	205
7.5	CW Model Images and Spectra	211
7.6	Aspects of the Binary System	216
7.7	Conclusions	218
8	HM SAGITTAE and V1016 CYGNI	220
8.1	Images	220
8.2	Preliminary Discussion	222
8.3	Visibility Analysis	225
8.4	HM Sge: Expansion and Position Angle Rotation	229
8.5	STB/CW Model for HM Sge	233
8.6	Spectra	240
8.7	Binary Separations and Distances	246
8.8	Conclusions	250
9	DISCUSSION OF THE SYMBIOTIC PHENOMENON	252
9.1	The Cool Component	252
9.2	The Hot Component	252
9.3	The Nebular Component	253
9.4	Outbursts	256
9.5	Radio Statistics	259
9.6	New Questions	260

10 CONCLUSIONS	262
10.1 Summary	262
10.2 Further Work	265
Bibliography	267
A CWb Boundary Governing Equations	285
B Model Imaging	287
C Apparent Density: Compressed Nebulae	290
D Alternative Designations of Program Stars	292

List of Tables

4.1	Symbiotic Stars Previously Resolved at Radio Wavelengths .	111
4.2	Positions of Program Stars	123
4.3	Distances to Program Stars	125
4.4	Outburst and Spectral Classifications	126
4.5	Reported Periods	128
4.6	Masses of Stellar Components	129
4.7	Radii of Stellar Components	130
4.8	Temperatures of Stellar and Nebular Components	132
4.9	Nebular Density and Flow Parameters	134
4.10	Schedule of Observations	152
4.11	Data Calibration	153
5.1	Radio Observations of Southern Symbiotics	155
5.2	Southern Sources: Fitted Gaussian Parameters	158
6.1	Z And: Spectral Indices from Monitoring Program	177
7.1	AG Peg: 5 GHz Flux Densities by Component	197
7.2	Nebular Shell Model: Fitted Parameters for AG Pegasi	202
8.1	Fitted Visibility Parameters: HM Sge and V1016 Cyg	228
8.2	Binary Nebular Features of HM Sge at 22.5 GHz	229
8.3	STB Fits to HM Sge and V1016 Cyg	244

List of Figures

1.1	Infrared/Optical/UV Spectrum of AG Pegasi	2
1.2	UV Spectra: CI Cyg and AG Peg	7
2.1	Schematic of the STB Model	26
2.2	Ionization Boundaries in the STB Model	28
2.3	STB Model: Distribution of Orbital Separations	30
2.4	STB Model: Asymptotic Angle of the Ionization Cone	33
2.5	STB Model: Recombination Limit	35
2.6	Change of Flow Variables through a Shock	37
2.7	Isothermal Shock	38
2.8	KPF Model	42
2.9	GW Model	43
2.10	Geometry of the GW Model	44
2.11	Boundary Oriented Coordinates in the GW Model	45
3.1	The θ -Cone: Wind and Shell Flow	54
3.2	Cooling Function, $T > 10^4$ K	60
3.3	Radiative Cooling Timescales	61
3.4	Adiabatic Temperature Profiles	62
3.5	Effect of Thermal Pressure: Constant v_1	67
3.6	Interaction Cone Opening Angles and Stream Velocities	69
3.7	CWb Model Images	77
3.8	Spectral Variations with Viewing Angle	79
3.9	Flux Density Levels: CWb and STB Models	81
3.10	“Concentric” Winds in a Symbiotic System	84
3.11	Concentric Shell in the Shell Frame	86
3.12	Critical Cooling Radii in the CWc Model	93
3.13	Global Morphology of a Rotating Jet Source	95
3.14	Rotating Dual Jet	96
3.15	Evacuation of the Interarm Regions	97
3.16	Finite Angle Interaction Cone in 3 Dimensions	98
3.17	Global Development of Finite Angle Interaction Streams	98
3.18	Three Dimensional Stream Morphology	99
3.19	Features of the CWo Model	101
3.20	Flow Separation in the CWb Model	103
4.1	The MERLIN Array	115
4.2	Radio Telescopes in Australia	117

4.3	AG Pegasi: Outburst Light Curve in Visual Magnitudes . . .	141
4.4	Images of AG Pegasi at three Resolutions	142
4.5	HM Sge Nebula, [N II] $\lambda 6583$	145
4.6	Model Shell Structure of HM Sge	147
4.7	UV Image of HM Sge	148
5.1	Radio Flux Densities of Southern Sources	156
5.2	Southern Symbiotic Sources: Visibility Curves	159
5.3	AT Images of He 2-106 and BI Cru	162
5.4	AT Images of RR Tel and HD 149427	163
5.5	STB Model: Crescent Morphology	165
5.6	STB Model: Unipolar Morphology	166
5.7	CWb Model: Crescent Morphology	169
5.8	CWb Model: Unipolar Morphology	170
6.1	Z And: Radio Light Curve, 1982 - 1987	174
6.2	Z And: Variations with Optical Phase	176
6.3	Z And: Examples of Linear and Non-Linear Spectra	178
6.4	Z And: <i>uv</i> Tracks	179
6.5	Z And: Real Visibility Curve	180
6.6	Z And: Near Simultaneous VLA/MERLIN Observations . .	181
6.7	Flux Density Modulation with Orbital Phase: STB Geometry	183
6.8	Z And: U Magnitude Variations with Optical Phase	186
6.9	Z And: STB Model Images at 5 GHz	190
7.1	AG Peg: VLA Images in Four Epoches, 5 GHz	194
7.2	AG Peg: <i>uv</i> Tracks	195
7.3	AG Peg: Combined Array Images, MERLIN/VLA	196
7.4	AG Pegasi: Central Flux Density Variations, 5 GHz	199
7.5	Spherical Shell Model	201
7.6	Fitted Visibility Curve: AG Pegasi, 01 Mar 1990, 5 GHz . .	202
7.7	AG Pegasi, Expansion of the Inner Nebula	203
7.8	AG Pegasi: Evolution of Real Visibility Curves	204
7.9	AG Pegasi: Mass of the Inner Nebula by Epoch	205
7.10	AG Peg: 5 GHz Images with Central Source Subtracted . . .	207
7.11	A Model of Lobe Enhancements of the Inner Nebula	209
7.12	AG Peg: CW Model Images for the Inner Nebula	213
7.13	AG Peg: Model Spectra of the Central Object	215
7.14	AG Peg: Model Image of the Central Object	216
8.1	HM Sge: 5 GHz Images	221

8.2	V1016 Cygni: 5 GHz Images	223
8.3	Real Visibility Fits: HM Sge and V1016 Cyg	227
8.4	HM Sge: 22.5 GHz VLA Images between 1982 and 1988 . . .	230
8.5	HM Sge: Evolution of Binary Nebular Features	231
8.6	V1016 Cygni: 22.5 GHz VLA Image	232
8.7	STB/CW Model for HM Sge	234
8.8	HM Sge: STB/CW Model Images	237
8.9	STB Spectral Fits: HM Sge and V1016 Cyg	242
8.10	Orbital Solution for HM Sge	247
B.1	Geometry for Optical Depth Determination: $1/r^2$ Density . .	289

My in risible universe youldly haud find
 Sulch oxtreabeeforeness meat soveal behind.
 Your feats end enormous, your volumes immense,
 (May the Graces I hoped for sing your Ondtship song sense!),
 Your genus is worldwide, your spacest sublime!
 But, Holy Saltmartin, why can't you beat time

(James Joyce, *Finnegans Wake*)

Be - dad he re - vives! See how he ris - es; and
 Tim-oth-y ris - ing from the bed says, fling your whis - key
 round like blaz - es, Thundering Jay-sus ye think I'm dead?

(Traditional Song)

Chapter 1

A BACKGROUND TO THE STUDY OF SYMBIOTIC STARS

Stars have traditionally been classified as symbiotic by reference to their spectra. The defining characteristics include:

1. a cool continuum ($T \sim 2500$ K);
2. late-type absorption features (*e.g.* TiO, VO bands);
3. a blue continuum;
4. strong emission lines from ionized species (“nebular lines”: *e.g.* H I, He I, He II, [O III]); and
5. a Balmer jump in emission.

These characteristics are well represented in the spectrum of AG Pegasi shown in Figure 1.1. Allen (1979) proposed that, in order to restrict the symbiotic classification to a more physically homogeneous sample, that the classification be reserved to objects which have exhibited, at some time:

6. emission lines of species with ionization potential ≥ 55 eV (*e.g.* He II).

In recent years, the observational data relating to symbiotic stars has increased dramatically. The opening of new wavelength domains, particularly the radio and the UV, has provided many new insights into the “symbiotic phenomenon”. The picture

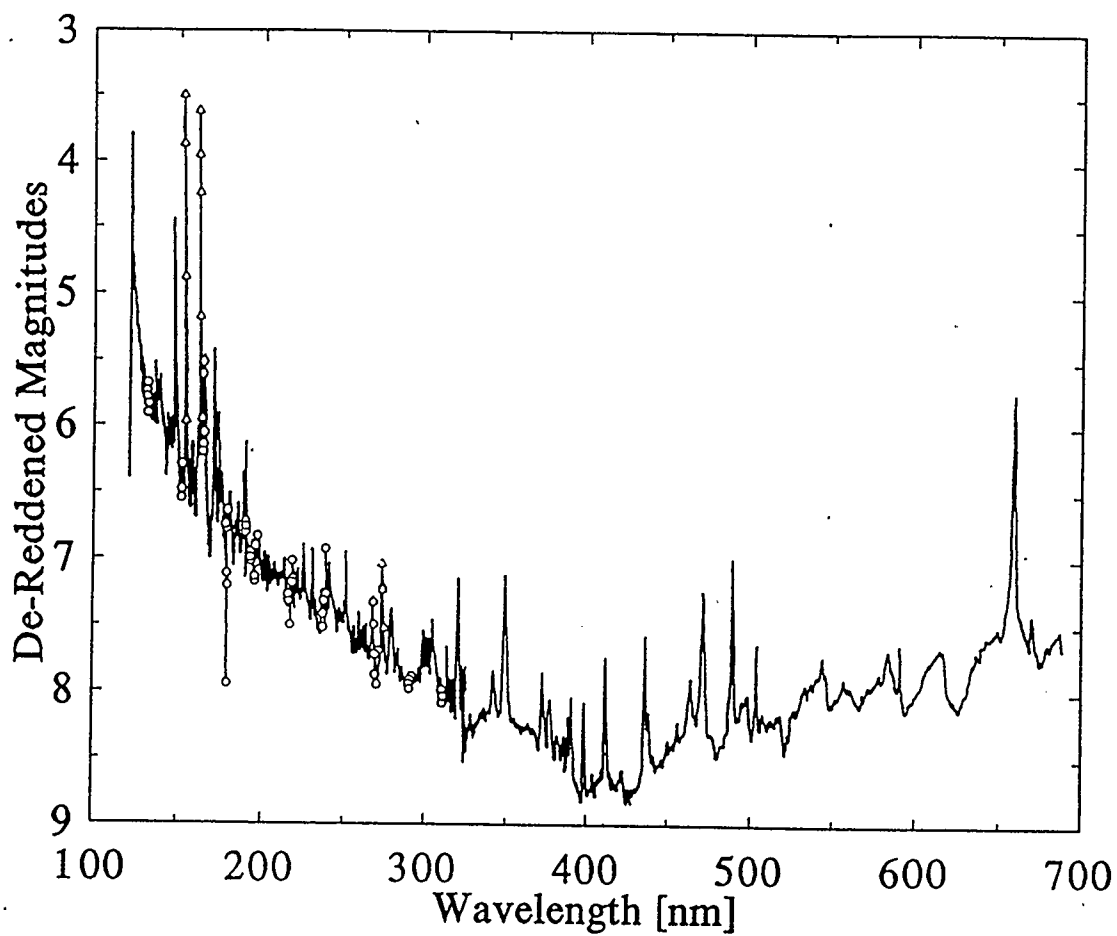


Figure 1.1: Infrared/Optical/UV Spectrum of AG Pegasi
Data from Keyes and Plavec (1980a). Ultraviolet (UV) observations were made with the *International Ultraviolet Explorer* (IUE).

which has emerged is of an interacting binary system in which one of the components is a late-type star, normally a red giant (RG). The aim of this introductory chapter is to present the observational evidence supporting this interpretation.

To facilitate discussion, three distinct physical entities will be assumed: a “cool component”, associated with the red continuum and absorption features; a “hot component”, associated with the blue continuum; and a “nebular component” associated with the Balmer jump and nebular lines.

1.1 The Cool Component

The cool component is apparently a late-type star; that is, a large star ($\gtrsim 50 R_{\odot}$) of low temperature (~ 3000 K) in the late stages of stellar evolution. The existence of a late-type star is most clearly seen in the spectrum below $1\mu\text{m}$; here the characteristics are essentially indistinguishable from those of ordinary late-type stars (Allen 1982). To offer a more detailed demonstration, it is first necessary to distinguish between two symbiotic populations: S (stellar) and D (dusty) type.

The distinction between S and D-type symbiotics is based upon infrared magnitudes (bands: J,H,K and L). In S-type systems, the 1-4 μm continuum appears very much as expected for a cool star. In D-type systems, there exists an additional component of emission with characteristics typically associated with circumstellar dust. The S/D type categorization is correlated with many other observed characteristics, and suggests some fundamental physical difference between the two populations. From the point of view of the cool component, it appears that S-type cool components are normal late-type objects while D-type cool component are Mira variables,

i.e. more evolved stars which have developed extensive circumstellar dust shrouds.

Little doubt has ever been raised that S-type cool components were late-type stars. The temperature associated with the red continuum (~ 3000 K), as well as the nature and intensity of the absorption features, strongly favors this interpretation. In fact, many S-type systems were originally classified as late-type stars with peculiar emission lines.

In D-type systems, the presence of a cool star is less obvious since no strong optical continuum is observed. It is now generally accepted, however, that the weakness of this continuum is a result of strong circumstellar dust extinction. Recent evidence for the presence of a cool star includes the identification of H₂O and CO bands in the spectra near $2 \mu\text{m}$, indicating temperatures ~ 2000 K (*e.g.* Whitelock 1988).

Spectral and luminosity classes are of fundamental importance in understanding the nature and evolutionary status of stellar systems; the cool components in S-type systems have been typically classified as M III. The appropriateness of standard spectral/luminosity classification in symbiotic systems has recently been challenged, however, on the basis that symbiotic cool components appear to lose more mass than single objects of the same class (*e.g.* Kenyon 1988c, $\sim 10^{-6} M_{\odot}\text{yr}^{-1}$ from radio and infrared fluxes). Additional investigations have tended to support the standard classification methods (*e.g.* Kenyon and Fernandez-Castro 1987; Kenyon 1988c; Shulte-Ladbeck 1988; Nussbaumer *et al.* 1988).

The apparent enhancement of mass loss from late-type stars in symbiotic systems may arise in a number of ways. Kenyon and Gallagher (1983), following a similar proposal by Arons (1973) and Modisette and Kondo (1980), suggested that heating of the outer atmosphere of the cool component by its companion could induce mass

transfer. Alternatively, Kenyon and Gallagher (1983) suggested that the presence of a companion might sufficiently reduce the gravity in the extended atmosphere of the cool component to account for the observed enhancement. In Section 3.3.3, a further mechanism will be discussed: the apparent enhancement of mass loss due to the compression of circumstellar material in colliding winds (CW) geometry.

As noted above, D-type cool components are commonly considered to be Mira variables. They resemble Miras not only in supporting extensive dusty envelopes, but also in exhibiting periodic (90 - 700 d), large amplitude ($2 < \Delta m < \sim 6$; $m \equiv$ visual magnitude) infrared variations. These variations are consistently explained in terms of stellar pulsations (*e.g.* Willson 1987; Whitelock, Pottasch and Feast 1987; Bowen and Beach 1987), and the pulsations in turn encourage both mass loss enhancement and the formation of dust grains. Relatively well defined period/luminosity and period/mass-loss-rate relations have been determined for Miras (*e.g.* Glass *et al.* 1987; Schild 1989). It follows that observed periods may be used to infer such fundamental parameters as luminosity, mass loss rate, and distance (see Whitelock 1988).

Before leaving the discussion of cool components it is useful to point out the existence of a subclass of D-type systems, *viz* D'. HD 149427, one of the program stars for this thesis, is of this type (*e.g.* Allen 1984b). In D' systems there is little or no indication of dust emission at $2.2 \mu\text{m}$; however a large color index, indicative of dust, is seen between 2.2 to $3.8 \mu\text{m}$. Further, the infrared spectra of these systems do not exhibit the silicate features normally associated with Mira systems (Roche, Allen and Aitken 1983), nor do they exhibit molecular bands of TiO, CO or H₂O. It is inferred that the cool component is of type F or G ("yellow symbiotics", Glass

and Webster 1973) rather than M or K. The dust emission in D' systems suggests a temperature of ~ 500 K, which is considerably cooler than that associated with normal D-type systems (~ 800 K; Kenyon, Fernández-Castro, and Stencel 1988).

1.2 The Hot Component

Historically, it was recognized at an early stage that a high temperature regime was required in symbiotic systems in order to explain the levels of ionization and excitation observed in the nebular emission lines. In fact, the term "symbiotic" refers to the surprising compatibility of this high temperature domain with the lower temperature domain of the cool component. The association of the hot component with a discrete stellar object was not convincingly demonstrated, however, until UV spectra became available (IUE satellite, launched 1978). Even today the nature of the hot component is ill-understood.

Two types of UV continua were observed with the IUE. Most resembled that of AG Peg (Figure 1.1 and 1.2), and may be understood as the Rayleigh-Jeans tail of a hot black body, plus free-bound emission from an ionized nebula. Others, however, resembled that of CI Cyg (Figure 1.2), being fairly flat and reminiscent of an A or B type star. In neither case was the blue continuum a natural extension of the infrared and optical continua; two distinct physical entities were clearly present.

IUE observations have also been used to determine temperatures for the nebular component (*e.g.* Nussbaumer 1988), and the resulting values ($1 - 2 \times 10^4$ K) have important implications for the hot component. The temperatures are those expected for diffuse material in the presence of a strong ionizing source, and are an order of

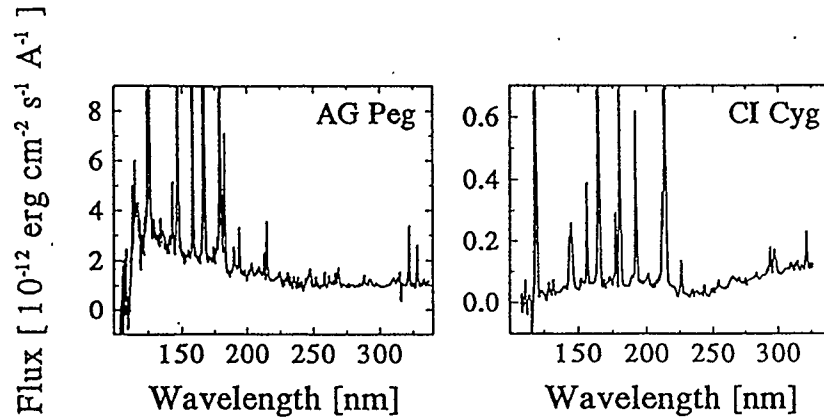


Figure 1.2: UV Spectra: CI Cyg and AG Peg
(Data from Kenyon, 1988a.)

magnitude lower than would be expected if the emitting material was predominantly collisionally ionized. It appears therefore that the hot component must act primarily as the source of ionizing photons. Using the “Zanstra method”, a hot component temperature of $\sim 10^5$ K may be inferred (*e.g.* Boyarchuk 1975). A temperature of this order is consistent with the failure to detect X-rays from most symbiotic systems (upper limit $\sim 10^6$ K, Allen 1981a).

Temperatures of $\sim 10^5$ K provide further confirmation that the hot and cool components cannot be explained as different manifestations of a single physical object. Molecular species such as TiO or VO, observed in the cool spectrum, could not exist in direct contact with a strong 10^5 K source. It is natural therefore to interpret the hot and cool components as companion stars in a binary system.

The hot component cannot be a normal star. Although it has been noted that the blue continua in some systems resemble those of A or B-type stars (*e.g.* CI Cyg, Figure 1.2), such stars do not provide enough high energy photons to act as ionizing

sources for the nebular component. Further, the low total luminosity of the hot component indicates that the emitting region must be much smaller than that associated with an A or B-type star. The resemblance of hot components to the central stars of planetary nebulae ($T \gtrsim 10^5$ K) has led to suggestions that symbiotic stars might represent early stages of planetary nebula formation. Statistically, however, more symbiotic stars are observed than could be consistently explained as proto-planetary nebulae in late-type binary systems.

In terms of our overall understanding of symbiotic systems, the most likely candidates for hot components are compact stars energized by mass accretion from the cool component wind. If the compact object is a white dwarf (WD), the gravitational potential well is sufficiently deep that the requisite luminosity may be achieved from wind accretion at large separations. If the compact object is a main sequence (MS) star, much higher accretion rates are required because of the more shallow potential well. To achieve the required accretion rates for an MS accretor, the stars must be relatively close together. Roche lobe overflow (see below) and accretion disk formation (Shapiro and Teukolsky 1983) are therefore expected.

Kenyon and Webbink (1984) modelled IUE continuum colors from 21 symbiotic systems. They found that the hot components of 10 objects were well modelled as hot WDs ($T \sim 10^5$ K), 6 objects were best interpreted as MS stars with accretion disks, and the remaining 5 objects could not be fitted by either model. Their analysis also considered the possibility that some objects might include both an “excited” WD with an accretion disk, however none of the objects studied were well explained in this way.

As noted above, accretion onto the hot component may occur via Roche lobe

overflow or directly from a stellar wind. In a binary system, each component is surrounded by a “Roche lobe”, the largest gravitational equipotential surface which contains only the one star. The Roche lobes of the two components meet at a single point between the stars which is known as the inner Lagrangian point. If the cool component expands to fill its Roche lobe, matter will flow through the Lagrangian point onto the hot component. By virtue of the orbital motion of the system, the exchanged mass will have a net angular momentum about the hot component, and an accretion disk may therefore form. If accretion takes place directly from the cool component wind, both the accretion rate and the angular momentum per unit accreted mass will be significantly reduced (*e.g.* Livio 1988, Shapiro and Teukolsky 1983). The reduction of angular momentum per unit mass will make accretion disk formation less likely.

Mass loss is observed in some systems at high velocities, *i.e.* several hundreds to several thousands of km s^{-1} . This mass loss is normally attributed to the hot component rather than the cool component for several reasons: *i.e.* no evidence exists for high velocity outflows from single late-type stars; symbiotic cool components have been found to emerge essentially unchanged following the cessation of the high velocity mass loss; and the velocities observed greatly exceed the the escape velocities of late-type stars. High velocity outflows are normally associated with outbursts (*e.g.* AG Peg, V1329 Cyg, RR Tel, HM Sge, V1016 Cyg, T CrB, RS Oph, R Aqr).

1.3 The Nebular Component

The presence of a nebular component was first discerned from optical emission lines of highly ionized species such as [O III], *i.e.* “nebular lines”. These lines can only arise at very low densities and would be collisionally de-excited in a stellar photosphere. Similarly, the observed existence of Balmer jumps in emission require that the emitting region be optically thin to Balmer continuum photons, *i.e.* a diffuse nebula. The origin of the nebular component has recently been given considerable attention, and the discussion below will tend to indicate that it consists predominantly of stellar wind material from the cool component.

Radio continuum emission provides one of the primary diagnostics of the nebular component. Seaquist and Taylor (1990) make the following generalizations from a detailed radio survey of symbiotic stars:

- About 25% of observed symbiotics have been detected at 5 GHz at a level of > 0.5 mJy. All symbiotic systems which are either close, or intrinsically bright (outbursting systems), have been detected. These details are consistent with the hypothesis that all symbiotic systems are radio emitters.
- Most radio detected symbiotic stars do not vary in flux density by more than 30% over a period of several years.
- Radio spectra are consistent with thermal bremsstrahlung emission: $-0.1 < \alpha < 2$, where the spectral index, α , is defined by a power law relationship between flux density and frequency, $S_\nu \propto \nu^\alpha$. Statistically, the peak of the spectral index distribution occurs at ~ 1.0 .

- Symbiotic spectra tend to turn over to optical thinness near 30 GHz. Statistically, D-type systems tend to turn over at slightly lower frequencies than do S-type systems.
- Radio luminosity is positively correlated with the spectral type (a “numerical” quantity) of the cool component.
- Radio luminosity is positively correlated with infrared luminosity.
- D-type systems tend to be more radio luminous than S-type systems.

Many of the radio characteristics point to the cool component as the primary source of nebular material. The fact that most detected systems are relatively constant in flux density suggests that the observed systems are generally in quiescence, *i.e.* not experiencing a major outburst. In quiescence, the cool component should be the primary source of nebular material since late-type stars, as a class, are expected to support substantial stellar winds. The hot component may be expected to lose mass only in outburst. Radio emission correlates with the numerical spectral type of the cool component, and since mass loss rate is also known to correlate with spectral type (*e.g.* Dupree 1986), it follows that radio emission correlates with the cool component mass loss rate. It may be inferred that a substantial proportion of the radio emitting material is supplied by the cool component. The same conclusion follows from the fact that D-type systems are generally more radio luminous than S-type systems: D-type cool components are high mass loss objects (Mira variables). The correlation between radio and infrared luminosities also points to the cool component as the source of radio emission; infrared emission correlates with the quantity of

circumstellar dust, and this dust is almost certainly associated with cool component mass loss.

The abundances observed in the nebular component also point back to the cool component. Nussbaumer *et al.* (1988) have used UV emission lines to determine the relative abundances of C, N and O in the nebulae of novae and symbiotic stars. Novae exhibit abundance enhancements characteristic of the CNO cycle, presumably related to ejection of material during a thermonuclear runaway on the surface of a compact star. Since symbiotic abundances do not exhibit similar enhancement, it would appear that their nebulae are not primarily composed of WD outburst ejecta. Instead the observed abundances resemble those of normal RGs, suggesting an origin for nebular material on the cool component.

The mass of the nebular component may be estimated in a number of ways. The mass in ionized material is best determined from radio continuum emission (*e.g.* Wright and Barlow, 1975), and values on the order of $10^{-4} M_{\odot}$ appear to be typical (Kenyon, Fernández-Castro, and Stencel 1988). Neutral masses are obtained from infrared emission and tend to be approximately two orders of magnitude lower than ionized masses (Kenyon, Fernández-Castro, and Stencel 1988), suggesting that the winds are highly ionized. Further techniques of mass estimation make use of CO rotational transitions and maser emission (OH, H₂O, Si), however these emission processes are seldom observed among the symbiotic population. Their absence may be accounted for either by the dissociation of the necessary molecular species by the hot component, and/or absorption of the characteristic radiation in passing through ionized thermal gas.

The nebular component may be used to investigate the physical distinction be-

tween S and D-type systems. In the discussion of radio properties, it was pointed out that D-type nebular components tend to be more optically thin than S-type systems of comparable flux density. It may be inferred that the nebulae in D-type systems are of lower average density. The same conclusion arises from analysis of the optical spectra. Allen (1979) showed that, while no demonstrable correlation existed between infrared type and the ionization potential of the strongest emission lines, the D-type systems exhibited higher levels of [OIII] emission. He concluded that D-type nebula must experience less collisional de-excitation, implying that their average densities must be lower.

The diversity of velocities and densities represented within the nebular components of some systems is very curious. In AG Peg, for instance, velocities of ~ 72 , ~ 125 , ~ 180 , ~ 230 , ~ 300 , and ~ 382 km s⁻¹ have been simultaneously detected (*e.g.* Kenyon 1986). In other systems, such as RR Tel, V1016 Cyg, and RX Pup, correlations have been found between expansion velocities and ionization potentials, suggesting that strong density gradients are also present (*e.g.* Kenyon 1986). Colliding winds (CW) phenomena, as will be discussed in Section 3.3.1 provide one possible explanation for the diverse velocity and density domains internal to the nebular components of some systems.

1.4 Outbursts

1.4.1 Outburst Subclasses

Symbiotic stars are generally classified according to their outburst characteristics as: symbiotic novae; recurrent novae; or classical symbiotic stars. The classical

symbiotic stars constitute the main body of the population (~ 130 systems), while the recurrent and symbiotic novae are very much in a minority (~ 10).

Allen (1980b) defines symbiotic novae as a class of objects whose spectra show a simultaneous presence of nebular and cool star characteristics, and that have had a large visual outburst in the recent past. Viotti (1988) places only 8 systems in this subclass, including four of the systems observed in this work: AG Peg, HM Sge, V1016 Cyg and RR Tel.

Symbiotic nova outbursts strongly resemble those of classical novae both photometrically and spectroscopically. Light curves show a sharp rise to peak luminosity, followed by a much more gradual decay. The typical evolutionary time scale for eruptions of symbiotic novae is much longer than for classical novae, *i.e.* decades or centuries rather than months. For this reason, symbiotic novae have sometimes been designated “slow novae”. The amplitudes of symbiotic nova outbursts fall in the range $2.5 < \Delta m < 11$, with the average being ~ 5.6 . The fact that the amplitudes are considerably lower than observed for classical novae (6 - 16 mag) is normally attributed to the high quiescent luminosity of the cool component.

Recurrent novae are symbiotic systems which have exhibited two or more distinct outbursts, reaching absolute magnitudes at maximum comparable to those of classical novae, and in which the ejection of a discrete shell in outburst, at velocities $\gtrsim 200 \text{ km s}^{-1}$, has been observed (Webbink *et al.* 1987). In addition to having been observed in more than one major outburst, recurrent novae differ from symbiotic novae in their decay time scales: months for recurrent novae *vs* decades for symbiotic novae. The recurrence time scales for recurrent novae are on the order of years to decades, and formidable theoretical difficulties exist in explain how sufficient matter

could so quickly reaccumulate following shell ejection. Livio (1988) suggests that only four systems (T Pyx, T CrB, U Sco, and RS Oph) are legitimate members of this subclass.

Classical symbiotic stars may be defined as those symbiotic systems which undergo frequent visual outbursts of a few magnitudes on the time scale of a few months (Allen 1984b). Typically, the spectrum during outburst resembles that of an F-type supergiant with bright H I and He I lines. Recurrence time scales vary from years to decades. Unlike recurrent novae, there is normally little similarity between consecutive outbursts of the same system.

1.4.2 Outburst Models

Historically, various attempts have been made to explain symbiotic outbursts in terms of single star models. Most single star models (*e.g.* coronal models, star spot models) are *ad hoc*, and do not suggest an initiating mechanism. One single star model, which was initially fairly successful, described symbiotic nova systems as young planetary nebulae: *e.g.* Barratta, Cassatella, and Viotti (1974); Ahern *et al.* (1977); Kwok (1977); Flower, Nussbaumer and Schild (1979); Nussbaumer and Schild (1981); Kindl, Marxer, and Nussbaumer (1982). This interpretation is now strongly denied, however, by evidence for the continuing presence of a cool component in systems following outburst: *e.g.* Harvey (1974); Taranova and Yudin (1983); Puetter *et al.* (1978).

Binary models suggest a wide variety of outburst possibilities, as indeed is necessary to account for the wealth of observed characteristics. Outbursts associated with binary interaction may be classified as: thermonuclear outbursts; accretion powered

outbursts; or ionization outbursts. Each of these types will now be discussed.

Thermonuclear outbursts are normally associated with accretion onto a WD (white dwarf). An accreting WD has three possible configurations, depending upon the accretion rate. The configuration of steady shell burning will exist for accretion rates between 1×10^{-7} and $4 \times 10^{-7} M_{\odot}\text{yr}^{-1}$, for a $1 M_{\odot}$ accretor (Mikolajewska and Kenyon 1992, Paczyński and Zytkow 1978, Fujimoto 1982). For higher accretion rates, matter will accumulate above the burning shell and will expand to supergiant dimensions on a thermal time scale (*i.e.* the time scale associated with the thermal velocity of the accreted matter; Mikolajewska and Kenyon 1992, Paczyński and Rudak 1980, Iben 1982). Below this range, burning can not be sustained continuously but will occur in flashes, igniting only when shell pressures reach the critical value. The degeneracy at the surface of a WD implies a decoupling of temperature and pressure, and therefore the outburst will be highly explosive (Mikolajewska and Kenyon 1992, Fujimoto 1982; Iben 1982). As accretion rates decrease below $1 \times 10^{-7} M_{\odot}\text{yr}^{-1}$, the time between successive outbursts increases.

By the term “accretion powered outburst” it is meant that the release of gravitational potential energy from the accreted material accounts for the observed increase in luminosity. It will be noted that although thermonuclear outbursts require accretion, they are not “accretion powered”. Conversely, accretion powered events do not involve thermonuclear fusion.

Accretion powered outbursts can only match the observed luminosity increases for very high accretion rates ($10^{-5} - 10^{-3} M_{\odot}\text{yr}^{-1}$). Such rates may only be achieved *via* Roche lobe overflow and in this geometry an accretion disk is almost certain to form (Shapiro and Teukolsky 1983). Accretion powered outbursts need not always

involve shell ejection. Sufficient increase of emission may be provided by the excitation of the accretion disk during an episode of enhanced accretion. Bulk ejection is not forbidden, however, and may occur if the accretion luminosity exceeds the Eddington limit ("supercritical accretion"). Observationally, a supercritical accretion event is difficult to distinguish from a thermonuclear runaway (*e.g.* Bath 1977).

In order to support an accretion powered outburst, an episode of increased mass transfer is required. Mechanisms commonly invoked to explain such episodes include: orbital eccentricity, resulting in increased mass transfer at periastron passage (*e.g.* Taylor and Gregory 1984); enhanced mass loss from the cool component (*e.g.* instabilities in the cool component atmosphere - Bath 1977; or a helium shell flash within the cool component itself - Mikolajewska and Kenyon 1992); and accretion disk instabilities (Kenyon 1986; Cannizzo and Kaitchuck 1992).

Ionization outbursts are defined to occur when the observed increase in luminosity is associated with the rapid ionization of nebular material. One model of this type (Nussbaumer and Vogel, 1987) involves an episode of enhanced mass loss from the cool component; the outburst occurs as the newly ejected gas is ionized by the hot component on short time scales. A different type of ionization outburst, proposed by Bryan and Kwok (1991), involves an increase in ionizing photon luminosity from the hot component, and a resulting increase in ionization of the pre-existing circumstellar envelope. In this case, no sudden ejection of material from either of the stellar components is required. The importance of ionization outbursts at visual wavelengths has not been widely acknowledged (*e.g.* Mikolajewska and Kenyon 1992).

These various models appear capable of explaining the many diverse types of ob-

served outburst. Symbiotic novae are consistently explained as thermonuclear shell flashes on WDs (*e.g.* Mikolajewska and Kenyon, 1992). Recurrent nova systems appear to support both thermonuclear and accretion events (*e.g.* Livio 1988). Outbursts of classical symbiotic stars may be caused by a variety of mechanisms from weak shell flashes (AG Dra: Friedjung 1988), to thermal expansion from steady shell burning (Z And, BF Cyg: Mikolajewska and Kenyon 1992), to accretion powered outbursts (CI Cyg, AX Per: Mikolajewska and Kenyon 1992), to ionization outbursts (RX Pup, R Aqr: Mikolajewska and Kenyon 1992). A further category of classical symbiotic stars has been termed “*pre-symbiotic novae*” by Kenyon and Fernández-Castro (1987). These systems contain a luminous hot component and are thought to be advancing toward a thermonuclear outburst.

1.5 Symbiotic Stars as Interacting Binary Systems

Although conclusive evidence of binarity does not exist for every individual symbiotic system, a strong general case may be made for binarity within the class. Unequivocal evidence exists for the seven systems which have been shown to be eclipsing: CI Cyg (Belyakina 1970); BF Cyg (Mikolajewska, Kenyon, and Mikolajewski 1989); SY Mus (Kenyon *et al.* 1985); AR Pav (Mayall 1937); R Aqr (Willson, Garnavich and Mattei 1981) and AX Per (Mikolajewska 1988). An additional number of systems (~ 14 : Kenyon 1986; Garcia and Kenyon 1988) exhibit their binary nature in the periodic shifts of photospheric absorption lines, indicative of binary motion. The orbital periods obtained for these systems are typically several years. It is significant that no spectroscopic periods have been determined for D-type systems. It is widely believed

this deficiency arises because of the wider binary separations of these systems, which imply radial velocity shifts below current limits of sensitivity.

Binarity has also been argued for additional systems (~ 33) in which periodic photometric variations have been detected (Kenyon 1986). These variations are normally explained as a “reflection effect”: at orbital conjunction of the hot component, the cool component reflects additional hot component radiation toward the Earth. Photometric periods are generally in very close agreement with spectroscopic periods, confirming their correspondence to orbital motion.

Where orbital periods have been determined, it is also possible to make estimates of both binary separation and Roche lobe radii (for reasonable estimates of system mass). It is thereby possible to determine whether Roche lobe overflow is occurring. Binary separations are typically a few AU, and Roche lobe overflow appears to exist in approximately half of the systems. These values arise exclusively from S-type systems.

1.5.1 Formation and Evolution

Since the weight of evidence strongly suggests that symbiotic stars are interacting binary systems, it is worthwhile to investigate the evolutionary implications of this hypothesis. A binary system consisting originally of two MS=“main sequence” stars (both $\sim 1M_{\odot}$; “primary” originally more massive than the “secondary”) and will evolve through the following sequence of configurations:

(I) MS primary + MS secondary;

(II) RG=“red giant” primary + MS secondary;

- (III) WD primary + MS secondary;
- (IV) WD primary + RG secondary; and
- (V) WD primary + WD secondary;

The symbiotic phenomenon may exist in stage II and/or IV, since a RG is present in both cases. A given system may exhibit symbiotic behavior in both stages II and IV, or in one stage and not the other. Symbiotic systems in stage II will be referred to as “MS accretors” while systems in stage IV will be referred to as “WD accretors”.

For MS accretors, Roche lobe overflow is necessary to produce a sufficient supply of ionizing photons to power the nebular component. Roche lobe overflow increases the ionizing luminosity both by increasing the accretion rate, and by encouraging the formation of an accretion disk which will more efficiently radiate away the excess kinetic energy of the accreted matter. When a cool component “overflows” its Roche Lobe, the natural limits of the stellar atmosphere become that of the Roche lobe; further expansion as a Mira variable in the late stages of stellar evolution is therefore inhibited. Further, the material which would normally be available in forming a Mira envelope is likely to be removed from the late-type star through mass transfer in Roche geometry (Bowen and Willson 1991). It may be inferred that D-type systems, which are known to contain Mira variables, are much less likely to be MS accretors.

Between stages II and III, the primary component evolves as a planetary nebula. An interesting circumstance might occur if the secondary has entered the RG stage by this point. Observationally the system would appear symbiotic, possessing all of the elements of symbiosis: cool component, hot component, nebular component. The hot component (“central star of the planetary nebula”) would be capable of ionizing

the nebular component without the need for mass transfer from the cool component. This configuration is termed a “natural symbiotic star” by Kenyon (1986), and is expected to be relatively rare because of the low probability of both components evolving simultaneously off of the MS.

In stage IV, accretion onto the compact object (WD) may take place either from a stellar wind or *via* Roche lobe overflow. If Roche lobe overflow occurs, however, the high associated accretion rates will encourage sustained surface burning and may result in the thermal expansion of the accreted envelope to supergiant dimensions (Section 1.4). Such objects might not be detected as symbiotic stars (Kenyon 1985), and therefore most observed symbiotic WD accretors are likely to accrete *via* a stellar wind. Stellar wind accretion onto WDs may result in either D or S-type systems, depending upon the evolutionary stage of the cool component.

The theoretical considerations above would suggest that MS accretors (Roche lobe overflow) will not generally be observed as D-type systems, and WD accretors will not normally be observed in Roche lobe overflow. Most D-type systems are therefore expected to involve wind accreting WDs, while S-type systems may include Roche lobe accreting MS stars as well as wind accreting WDs.

The observational distinctions between S and D-type systems appear to be related to the physical distinctions between MS and WD accretors. It is therefore worthwhile to list the correspondences which have been identified in this chapter.

- D-type nebulae tend to be large and diffuse as expected for WD accretors, while S-type nebulae tend to be small and compact as expected for MS accretors (*e.g.* Allen 1979, “collisional de-excitation” of [OIII] in S-type systems).

- The low wind-accretion rates expected for WD accretors suggest that eruptions should occur predominantly as thermonuclear flashes; D-type systems are over-represented in the class of symbiotic novae, whose eruptions are interpreted as shell flashes.
- The failure to detect orbital motion in D-type systems suggests that their binary separations are larger than those of S-type systems; binary separations for WD accretors are expected to exceed those for MS accretors.

1.6 Outstanding Questions

The aim of this chapter was to present evidence in support of the interacting binary interpretation of symbiotic stars. As a conclusion, a list of specific questions arising from the general discussion will now be offered. Those questions to be addressed in the present study are indicated by asterisks.

The Cool Component

- How does the presence of the hot component alter the late stages of stellar evolution? Can material which has been processed in nuclear fusion be transferred to the accreting star (*e.g.* U Scorpius)?
- * Why do late-type stars in symbiotic systems, even in wide configurations, appear to systematically lose mass at higher rates than their single counterparts?
- Cool components in Roche lobe overflowing systems can not expand naturally as asymptotic giant branch (AGB) objects. Which observed systems represent these more evolved objects?

The Hot Component

- What are the physical properties of the hot component?
- How do the properties of the hot component correlate to other characteristics of symbiotic systems and how does this correlation fit into evolutionary scenarios?
- How widespread are hot component winds among classical symbiotic stars, *e.g.* RX Pup ($v > 800 \text{ km s}^{-1}$, Allen and Wright 1988)?

The Nebular Component

- Where is the nebular dust located? Where and when is it formed?
- * Is asymmetry a normal characteristic of all symbiotic nebulae?
- * Is cool component mass loss equatorially enhanced? If so, does this enhancement arise from binary influences or normal mass loss processes?
- * How do gradients in nebular density and velocity develop and propagate? What is the role of wind interactions in shaping and exciting the nebular matter?

Outbursts

- How frequently occurring are accretion disks, especially among wind accreting objects? How do they form and evolve? What effects do disks have upon the initiation and evolution of outbursts? How are they affected by outbursts? What types of structure are supported within the disks?
- What role do magnetic fields play in accretion and outburst? What magnetic properties are associated with accretion disks?

- What are the prerequisites for the formation of symbiotic jets (CH Cyg, R Aqr)? How are bipolar outflows confined?
- * What are the physical requirements for quiescent behavior? How is the quiescent environment affected by outburst? How does the environment evolve following outburst?

Binary Models

- Is the evolutionary scenario highlighted in Section 1.5 correct?
- Do single stars exist among the population currently classified as symbiotic?
- How can Roche lobe overflowing WD accretors be identified?
- Do symbiotic novae represent transient phases of “normal” symbiotic stars, or an essentially different population?
- Are D' systems protoplanetary nebulae?
- Why is a smooth transition not observed between the properties (*e.g.* orbital periods, outburst recurrence timescales) of symbiotic stars and cataclysmic variables?

Radio imaging at high resolution can potentially detect the geometry of symbiotic nebulae, and in this thesis radio observations have been used to address a number of the outstanding questions listed above. These questions include matters of the status and evolution of the nebular component, as well as matters of the stellar components in their role of supplying and exciting the nebular matter. The next two chapters discuss theoretical considerations which affect the geometry of the nebulae.

Chapter 2

CURRENT MODELS OF RADIO EMISSION

2.1 The Seaquist, Taylor and Button (STB) Model

2.1.1 The Model

The STB model (Seaquist, Taylor and Button 1984; Taylor and Seaquist 1984) is a model of quiescent radio emission from symbiotic stars. It assumes a system whose main components are those suggested by the multi-frequency discussion of Chapter 1 (Figure 2.1), *i.e.* :

- a cool component: late-type mass-losing star;
- a hot component: source of ionization; and
- a nebular component: ionized gas consisting of mass lost by the cool component.

The model parameters which determine the radio properties include: the binary separation, a ; the mass loss rate and velocity from the cool star, \dot{M} and v respectively; and the luminosity in ionizing photons, L_{ph} .

The ionization boundary is defined by the locus of points at which ionizing photons are completely consumed along paths outward from the ionizing star. The boundary is described in polar coordinates (r, θ) , by the equation:

$$f(r, \theta) = X_{\text{stb}}, \quad (2.1)$$

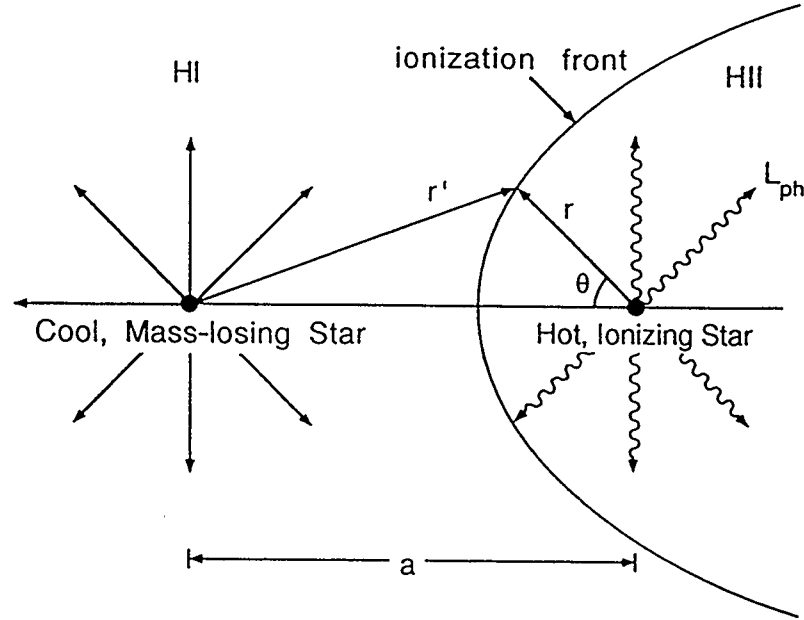


Figure 2.1: Schematic of the STB Model
(After Taylor and Seaquist, 1984.)

H I \equiv neutral hydrogen. H II \equiv ionized hydrogen.

where the function $f(r, \theta)$ is given by Taylor and Seaquist (1984). The parameter X_{stb} is defined in terms of physical parameters in the model;

$$X_{\text{stb}} \equiv \frac{aL_{\text{ph}}}{4\pi\alpha^{(2)}A}, \quad (2.2)$$

$$\text{where } A \equiv \frac{\dot{M}}{4\pi\mu_m m_H v}, \quad (2.3)$$

$\alpha^{(2)}$ is the recombination coefficient to all but the ground state of hydrogen, μ_m is the mean molecular weight of ions, and m_H is the mass of a hydrogen atom. Three distinct geometries are permitted, corresponding to particular domains of X_{stb} as shown in Figure 2.2. Similar geometries emerge for CW (colliding winds) models, and therefore it is useful to define model independent terminology at this point.

Nebular geometries in which the ionized region is completely enclosed by neutral material will be referred to as “closed” (upper panel of Figure 2.2). Geometries in which the cone of ionized material sweeps over the hot component will be referred to as “H-facing” (central panel of Figure 2.2), and geometries in which the cone of ionized material sweeps over the cool component will be referred to as “C-facing” (lower panel of Figure 2.2).

2.1.2 Observational Evidence for STB Phenomena

As noted above, the assumptions of the STB model in terms of the nature of the physical components are strongly supported by observational evidence (Chapter 1). Perhaps the strongest assumption is the association of the nebular component with mass lost by the cool component, and the arguments for this association were summarized in Section 1.3.

In order to make the STB model analytically tractable, a $1/r^2$ density law is assumed for the nebular component. This assumption is fairly restrictive. It excludes, for instance, the entire class of Roche lobe overflowing systems. Further, symbiotic systems typically experience outbursts and it is not clear to what extent the nebular structure is disrupted by such events. Although an outburst might contribute little to the nebula in terms of mass, its contribution in terms of momentum might be significant.

For the above reasons, many symbiotic systems may not be described in detail by the STB model. The model may, however, provide reasonable approximations of nebular structure for a large fraction of the symbiotic population. The statistical suitability of the model is supported by the fact that radio emitting symbiotic stars

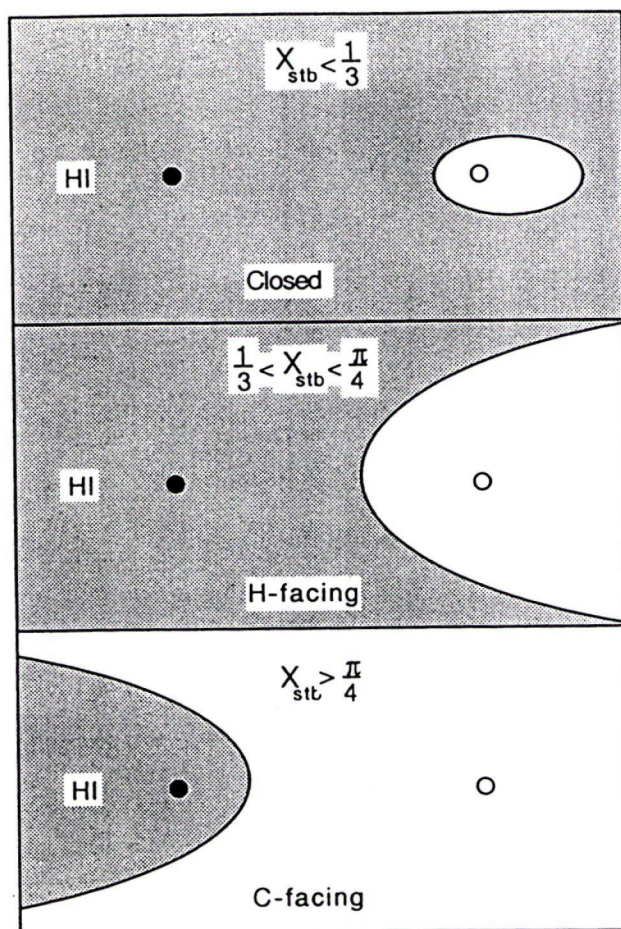


Figure 2.2: Ionization Boundaries in the STB Model

(After Taylor and Seaquist, 1984.)

In this figure, the black dot corresponds to the cool component (late-type, mass-losing star) and the open circle corresponds to the hot component (ionizing star). The characteristic shape of the ionization boundary is shown for three ranges of the parameter X_{stb} .

seldom vary in flux density by more than 30% over periods of years, indicating that the circumstellar material remains stable on time scales of interest (Seaquist and Taylor 1990). Further, a considerable fraction of the population (D type, $\sim 25\%$) are known to possess extensive circumstellar envelopes indicative of long preceding periods of quiescence and nebular stability.

An additional criticism of the assumed $1/r^2$ density law concerns the possibility that mass loss from late-type stars is equatorially enhanced (*e.g.* Johnson and Jones 1991). The shape of the ionization boundary will clearly be effected by such departures from spherical symmetry and numerical values of mass loss rate and binary separation derived from the STB model could, in such cases, be systematically in error. The qualitative predictions of the STB model however (*e.g.* spectral index distribution, relative binary separations of subclasses) might still be correct.

The STB model has been very successful in explaining the radio properties of symbiotic stars for very reasonable values of a , L_{ph} and \dot{M} . One important example is the consistent prediction of observed spectral indices. The survey work of Seaquist and Taylor (1990) has indicated an average radio spectral index of ~ 1.0 , and a tendency to turn over to optical thinness near ~ 30 GHz. Both of these spectral properties are understood naturally in terms of the STB model (Seaquist and Taylor 1990).

Another success of the STB model has been the derivation of binary separations for various objects. The discussions of Chapter 1 indicated that D-type systems are likely to have larger binary separations than S-type systems. Seaquist and Taylor (1990) have used the STB model to compute binary separations for a large number of systems, and the results are plotted in Figure 2.3. D and S-type systems are clearly

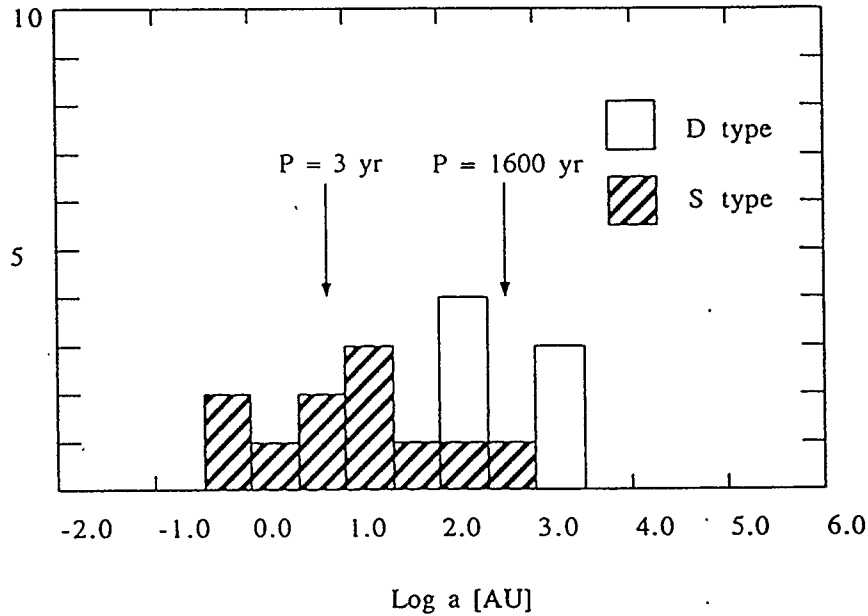


Figure 2.3: STB Model: Distribution of Orbital Separations
(Data from Seaquist and Taylor, 1990.)

The distribution of orbital separations for radio-emitting symbiotic stars is shown, as derived from the STB model. A value of unity has been assumed for X_{stb} . Values of optically thin turnover frequencies required for calculations have been estimated from the ratio of 5 GHz and $H\beta$ flux densities. A total system mass of $3 M_{\odot}$ has been used to calculate periods.

separated on the basis of binary separation as expected. Further, the average period of ~ 3 yr for S-type systems (Figure 2.3) is in close agreement with the average value of 2.4 yr inferred in the review of observed periods by Kenyon (1986, 21 systems). The average period of 1600 yr suggested by Seaquist and Taylor for D-type systems is consistent with the present non-detection of radial velocity shifts for any of these systems ($\gtrsim 20$ yr required, Kenyon 1986).

A final observational support of the STB model has been offered by Munari (1989). Munari uses the orbital modulation of UV emission lines in bright S-type

symbiotics to demonstrate that UV emission originates in the side of the atmosphere of the late-type component illuminated by radiation of the compact companion. This configuration is that predicted by the STB model.

2.1.3 New Treatments of Derived Quantities

Binary Separation

In the previous section, results were presented in which binary separations were obtained using the STB model. For Figure 2.3, Seaquist and Taylor (1990) assumed a value of $X_{\text{stb}} = 1$ and computed binary separations from derived values of flux density at the optically thin turnover frequency.

A more rigorous determination of the binary separation, a , may be performed if the nebular geometry (X_{stb}) is known. Taylor and Seaquist (1984) have shown that the optically thin turnover frequency in the STB model is given by:

$$\nu_t^{2.1} = 8 \times 10^{66} T_e^{-1.35} (q_o a)^{-3} \left(\frac{\dot{M}}{v} \right)^2 \quad [\text{GHz}] \quad (2.4)$$

where T_e is the electron temperature, a is the binary separation in [cm], and \dot{M}/v is the ratio of the cool component mass loss rate and velocity in $[M_{\odot} \text{yr}^{-1}][\text{km s}^{-1}]^{-1}$. The quantity q_o is the distance from the cool component to the ionization boundary along the line joining the two stars, in units of binary separation. An expression for this quantity may be derived from the relationship $X_{\text{stb}} = f(r, \theta)$ (Taylor and Seaquist 1984), at $\theta = 0$, *i.e.*

$$q_o = \frac{1}{1 + \sqrt[3]{3X_{\text{stb}}}}. \quad (2.5)$$

Substituting Equation 2.5 into Equation 2.4 and solving for the binary separation,

$$a = 2 \times 10^{22} T_e^{-0.45} \left(\frac{M_2}{v_2} \right)^{2/3} \nu_t^{-0.7} (1 + \sqrt[3]{3X_{\text{stb}}}). \quad (2.6)$$

From this expression it may be seen that the binary separation is not extremely sensitive to X_{stb} , as noted by Seaquist and Taylor (1990).

Asymptotic Cone Angles

The parameter X_{stb} plays a central role in the STB model and it may be estimated readily from radio images. Since only the ionized portion of the circumstellar envelope emits radio waves, the opening angle of the ionization cone will strongly influence the observed radio morphology. The observed morphology may therefore be used to estimate the opening angle, and this angle may in turn be used to compute X_{stb} ,

$$2X_{\text{stb}} \sin^3 \theta - \sin \theta \cos \theta + \theta - \pi = 0, \quad X_{\text{stb}} > \frac{1}{3}. \quad (2.7)$$

This equation is derived from $X_{\text{stb}} = f(r, \theta)$ by letting r in the expression for $f(r, \theta)$ go to ∞ . The asymptotic opening angle of the ionized cone is the supplementary angle of θ . Values of opening angle are plotted in Figure 2.4 for $1/3 < X_{\text{stb}} < 10$. Below $X_{\text{stb}} = 1/3$, the nebulae are closed and therefore the cone angle is undefined.

No-Recombination (NR) Radius: Effects of Orbital Motion

When orbital motion is considered, the emitting region expands beyond the boundaries suggested by a naïve application of the STB model. As the hot component sweeps along its orbital path it will tend to drag the ionization boundaries with it and fluid elements within the circumstellar envelope will therefore be alternately

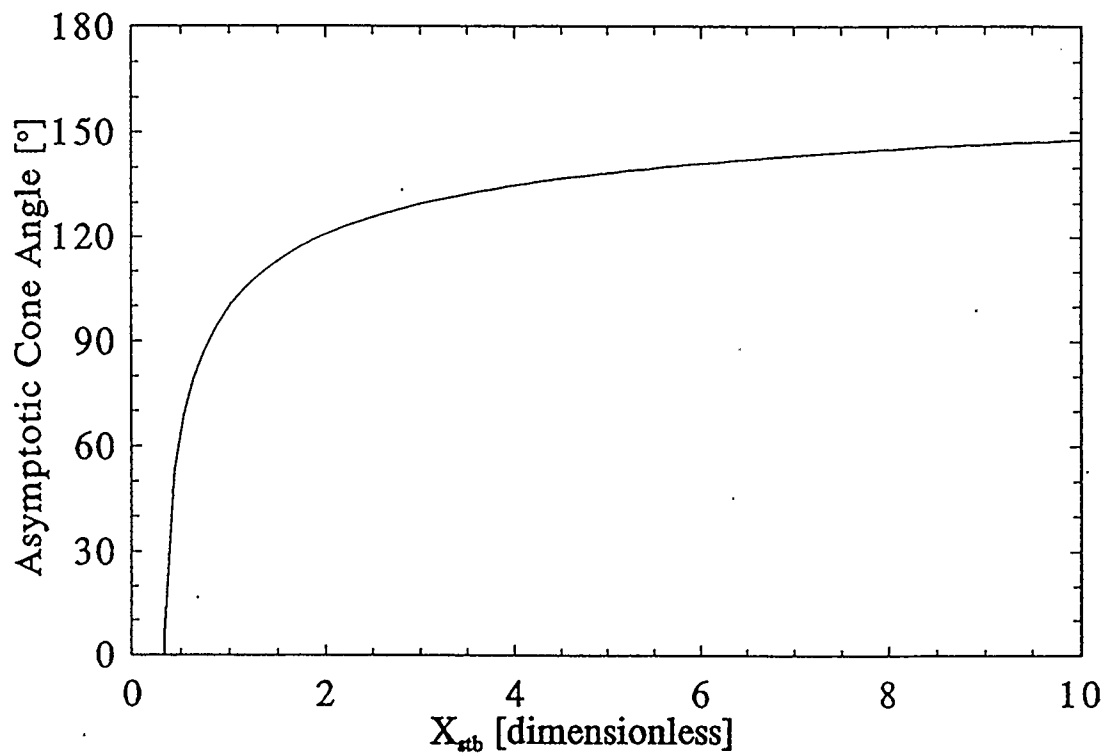


Figure 2.4: STB Model: Asymptotic Angle of the Ionization Cone

illuminated and unilluminated. Unilluminated matter will begin to recombine, and since the recombination time varies inversely with density, the recombination time will increase outward from the system centre. At some critical radius, the recombination time will be equal to the orbital period and beyond this point the nebula will remain ionized throughout the entire orbital cycle. The critical radius will be referred to as the “no-recombination” (NR) radius, R_{nr} . The value of the R_{nr} is given by (Seaquist, Taylor and Button 1984):

$$R_{\text{nr}} \simeq \left(\frac{\alpha \dot{M} P}{4\pi \mu_m m_H v} \right)^{1/2}, \quad (2.8)$$

where α is the recombination coefficient for hydrogen to all levels including the ground state, \dot{M} and v are the mass loss rate and velocity from the cool component respectively, μ_m is the mean atomic weight of ions, and P is the period between successive illuminations of a particular element of solid angle. The value of P will be shorter than the orbital period by a factor θ_a/π , where θ_a is the asymptotic opening angle of the ionization cone. It is implicitly assumed that the distance scales of interest are much larger than a . For $r > R_{\text{nr}}$ the nebula will form a steady-state ring or “doughnut” (“NR shell”), flaring outward at the asymptotic cone angle.

For the purposes of model imaging, an additional component of emission must be considered. The above discussion would suggest two components: the STB ionization cone, and the “NR” shell. However, material lying within the “hole” of the “NR” doughnut, but outside of the ionization cone will not recombine immediately; an “ionization trail” will be left behind (Figure 2.5). When a particular element of solid angle passes from the ionization cone due to orbital motion, recombination will begin in the inner regions where density is highest and spread outward. The extent

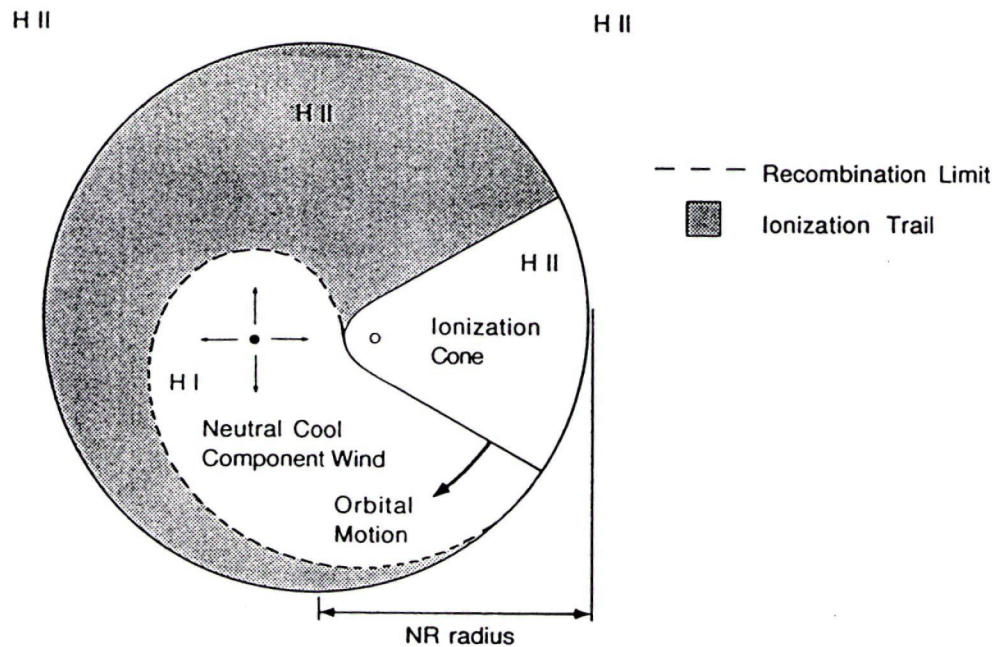


Figure 2.5: STB Model: Recombination Limit

The hot component is denoted by an open circle (○) and the cool component is denoted by a filled circle (●). Due to orbital motion, regions will pass in and out of the “ionization cone”. As regions pass out of the cone, recombination will begin in the denser regions near the system center and spread outward. At a given instant in time, the global recombination limit will be as shown by the dotted line. The RN (“no recombination”) radius, beyond which recombination will not occur at any time during an orbital period, is also shown.

to which recombination will have progressed at any given time will depend upon how long the region has been unilluminated (Figure 2.5).

2.2 Colliding Winds (CW) Models

2.2.1 Shocks

When stellar winds collide with densities and velocities such that they do not stream through each other, a zone of interaction is established between them (*e.g.* Dyson

and Williams 1980). If the pressures (momentum fluxes) associated with the flows are the same, then the physical location of the interaction shell will remain fixed. If the pressures are not balanced, the shell will move in the direction determined by the vector sum of the momentum fluxes, until balance is achieved.

Consider the case in which a steady state has been established in arbitrary geometry, and the interaction shell is stationary. Within the shell, the kinetic energy of the inflowing material (from either side) is converted to either thermal energy, or PdV work consumed in the compression of the gases. A region of high density and temperature develops between the opposing flows and presents a barrier to further material approaching it from either side.

As further gas now approaches the region of interaction, information of the existence of a barrier is communicated backward at the speed of sound. If the approaching gas is moving subsonically it will gradually pass to conditions of lower velocity, higher density and higher temperature. Stellar winds are normally supersonic, however, and in this case information is communicated backward too slowly to permit a gradual transition from ambient to disturbed conditions. The incoming gas therefore receives no prior warning of the impending transition. The discontinuous change in velocity, density, pressure and temperature is referred to as a shock (Figure 2.6).

Although shock transitions are discontinuous, they occur so as to conserve mass, momentum and energy. The conserved quantities (ϕ , ζ , ξ) are expressed by the Rankine-Hugiot "jump" conditions:

$$\phi \equiv \rho v \qquad \text{(mass flux)} \qquad (2.9)$$

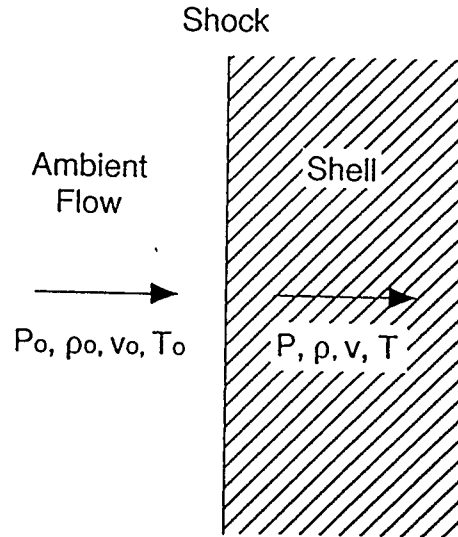


Figure 2.6: Change of Flow Variables through a Shock

Gas passes through the shock conserving mass, momentum and energy (Rankine-Hugonot conditions). There is a discontinuous change in pressure, density, velocity and temperature. Ambient quantities are given the subscript “o”, while shocked quantities are unsubscripted.

$$\zeta \equiv P + \rho v^2 \quad (\text{momentum flux})$$

$$\xi \equiv \frac{1}{2}v^2 + \frac{5}{2} \frac{P}{\rho} \quad (\text{specific total energy})$$

where ρ is density, v is velocity, and P is pressure.

Shocks are normally treated in two approximations: adiabatic and isothermal. The adiabatic approximation assumes that all of the energy deposited within the interaction shell is retained within it. The isothermal approximation assumes that energy is transmitted out of the disturbed region so efficiently that the temperature of the shocked gas returns almost immediately to the preshock value (Figure 2.7). In practice, the adiabatic approximation is made when radiative losses are small compared to the total rate of energy transfer through the shock. The isothermal approximation is used when the radiative losses approach the total rate of energy transfer.

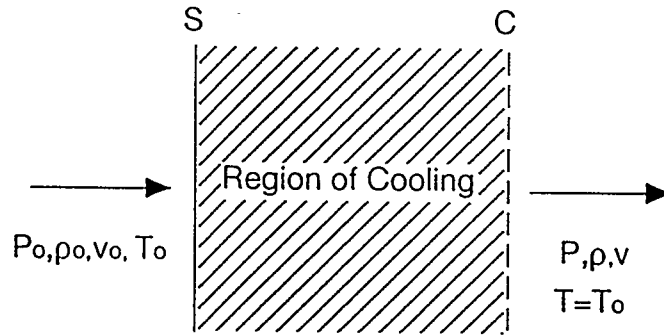


Figure 2.7: Isothermal Shock

Gas passes through shock S conserving mass, momentum and energy (Rankine-Hugonot conditions). The gas then experiences rapid cooling so that by the time it reaches surface C, it has reassumed its preshock temperature. In the isothermal approximation, S and C are so close, relative to other dimensions of interest, that they are considered a single surface. Ambient quantities are given the subscript “o”, while shocked quantities are unsubscripted.

Across an adiabatic shock, the velocity decreases according to the following expression:

$$v = \left(\frac{M_o^2 + 3}{4M_o^2} \right) v_o, \quad (2.10)$$

where v_o and v are the ambient and shocked velocities (relative to the shock) respectively, and M_o is the ambient Mach number (*i.e.* $M \equiv v_o/a_o$ where a_o is the speed of sound in the ambient flow). The general expression for the adiabatic sound speed in an ideal monatomic gas is,

$$a = \sqrt{\frac{5}{3} \frac{kT}{\mu_m m_H}}, \quad (2.11)$$

where k is Boltzmann’s constant, T is temperature, μ_m is the mean molecular weight of massive particles, and m_H is the mass of a hydrogen atom. Note that in Equation 2.10, the velocity across the shock decreases by a factor of 4 for strong shocks

($M_o \gg 1$).

Across an isothermal shock, the velocity decreases according to the expression:

$$v = \frac{c_o^2}{v_o}, \quad (2.12)$$

where v is the shocked velocity, v_o is the ambient velocity, and c_o is the ambient isothermal sound speed in a monatomic ideal gas,

$$c_o = \sqrt{\frac{kT_o}{\mu_m m_H}}. \quad (2.13)$$

The density across an isothermal shock increases by a factor of M_o^2 .

Note that it is possible for the shocked velocity to remain supersonic. If this is the case, further shocks might then occur interior to the disturbed region.

2.2.2 Single Star Wind Models

The pioneering work in the study of colliding stellar winds was that of Kwok, Purton and Fitzgerald (1978), and the model proposed in that work will be referred to as the ‘‘KPF’’ model. In this model a star has lost mass in a slow, late-type wind during an earlier epoch, but is now ejecting a much faster, more diffuse wind. The fast wind quickly overtakes the material ejected in the earlier epoch and the two flows interact:

The mean free path within the late-type wind, in a frame comoving with it, is given by:

$$\begin{aligned} l &= (n\sigma)^{-1} \\ &= \left(\frac{4\pi\mu_m m_H v}{\sigma M} \right) r^2 \end{aligned}$$

$$\simeq \left(\frac{r_{[\text{cm}]}}{5 \times 10^{10}} \right)^2 \text{ cm} \quad (2.14)$$

where n is the number density of hydrogen atoms, σ is the collisional cross section of a neutral hydrogen atom (10^{-16} cm^2), m_H is the mass of a hydrogen atom, μ_m is the mean molecular weight of nebular material, v and \dot{M} are the velocity and mass loss rate associated with the late-type wind respectively, and r is the distance from the center of mass loss. The standard density expression within a stellar wind (Equation 2.17) has been substituted in the second line, and typical values of \dot{M} and v have been used to obtain the third line. Kwok, Purton and Fitzgerald (1978) have argued that since the mean free path through the late-type wind is small compared to other dimensions of interest, that mixing is inefficient at the point of contact of the opposing winds. At 1 AU the mean free path in the late-type wind is $\sim 1 \text{ km}$, while at 1 pc it is $\sim 2 \text{ AU}$. The shocked flows from both sides are therefore conceived to be separated by an impenetrable contact discontinuity.

Material is added to the shell from the central, fast wind and from the remnant late-type wind as it is overtaken by the shell and swept up. For most configurations of interest, the contribution from the late-type wind strongly dominates. Using the equations for conservation of mass and momentum, Kwok, Purton and Fitzgerald (1978) demonstrate that the shell velocity with respect to the system centre will quickly reach a constant value, typically $\sim 20\text{-}50 \text{ km s}^{-1}$. A shell thickness may also be derived by requiring a balance between the thermal pressure within the shell and the incident ram pressures on both sides. For a shell temperature of 10^4 K , Kwok, Purton and Fitzgerald (1978) derive a shell thickness of $\sim 0.2r$, where r is the distance to the shell from the central source of mass loss.

Later analyses of the concentric interacting winds problem (*e.g.* Kahn 1983) have drawn a sharp distinction between matter entering the shell from the central fast wind, and that being swept up from the remnant late-type wind. The “contact discontinuity”, it was argued, would be impermeable. The suggested configuration is that shown in Figure 2.8. An “inner shock” separates the unshocked hot component wind at the system centre from the shocked hot component wind. This feature is followed by the contact discontinuity separating shocked fast wind from shocked late-type wind. Further from the system center, an “outer shock” is encountered beyond which the late-type wind continues to flow freely. Finally, an “ionization front” is shown within the shocked late-type wind, indicating that material in this region may remain unionized, or cool and recombine, unless adequate high energy photons are supplied.

The shocked fast wind in this model will acquire very high temperatures; $\sim 10^6 - 10^7$ K, assuming no radiative losses. High shell temperatures imply low densities and consequently the “hot shell” becomes physically thick. Kwok (1988) suggests that as much as 96% of the volume between the central object and the “contact discontinuity” is filled by shocked fast wind.

The impermeable “contact discontinuity” assumed in this model is an idealization which may be a reasonable approximation if flow conditions are suitably uniform and steady. In Chapter 3 of this work, an alternative approach will be offered in which complete mixing of the two flows is assumed.

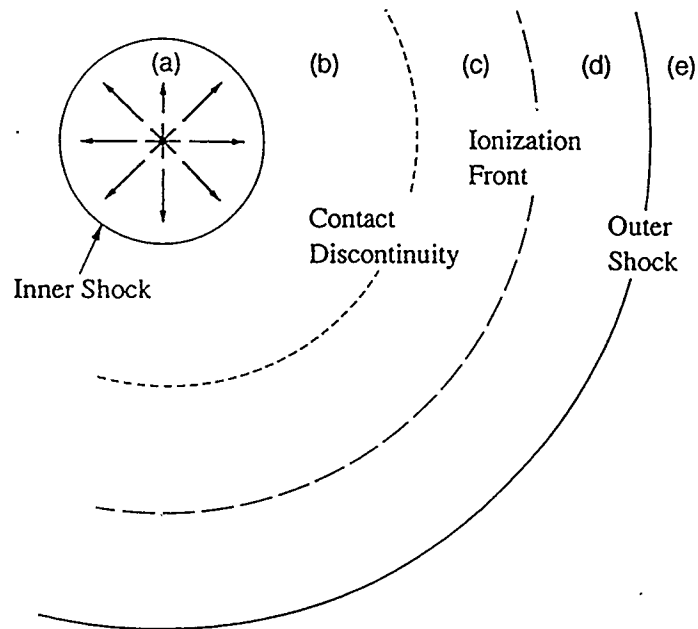


Figure 2.8: KPF Model
(After Kwok, 1987a.)

- (a) Ambient fast wind.
- (b) Shocked fast wind.
- (c) Ionized component of swept up late-type wind.
- (d) Neutral component of swept up late-type wind.
- (e) Ambient late-type wind.

According to the analysis of various authors (*e.g.* Kahn 1983, Kwok 1983a, Kwok 1988) the contact discontinuity and the outer shock are so close as to constitute a single outer boundary layer. The “bubble”, region b, is hot and diffuse and fills $\sim 96\%$ of the space enclosed by the outer boundary.

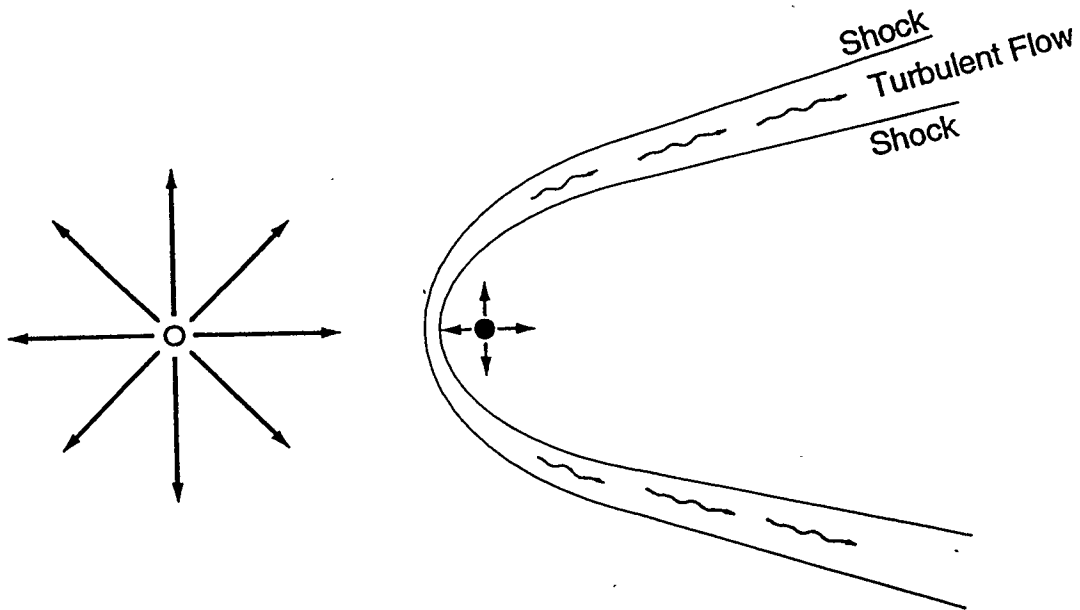


Figure 2.9: GW Model

After Girard and Willson, 1987. When two supersonic winds collide, shocks form on both sides of the interaction, and shocked material streams out between the shocks.

2.2.3 Wind Models in Binary Systems

Girard and Willson (1987) present a colliding winds (CW) model in which the winds do not originate from a single central star at different times, but instead originate from two different stars at the same time. The model which they derive will be hereafter referred to as the “GW model”. A schematic diagram of the configuration is shown in Figure 2.9. The situation is more complex than that of concentric flows because shocked material does not accumulate in a simple concentric shell but rather retains distinct dynamical qualities of its own.

To simplify the analysis, Girard and Willson (1987) consider an infinitesimally thin shell (“boundary”) and ignore the binary motion of the system. They also assume that both stars have spherically symmetric winds of constant rate and velocity.

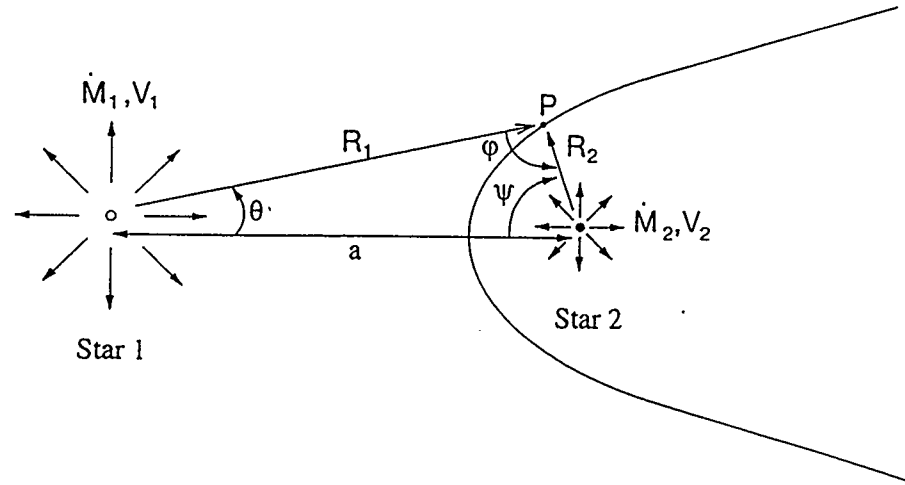


Figure 2.10: Geometry of the GW Model
(After Girard and Willson, 1987.)

Two stars (designated 1 and 2) are separated by distance a , and are characterized by winds of constant mass loss rate and velocity: \dot{M}_1 , \dot{M}_2 , and v_1 , v_2 respectively. Various vectors and angles are also defined, as discussed in the text.

It is useful at this point to consider the GW model in considerable detail since it provides the framework for the derivation of binary CW models with finite shell thickness in Chapter 3 (CWb model).

Figure 2.10 serves to define all quantities. Two stars, designated 1 and 2 are separated by a distance a . Mass loss rates and velocities are given by \dot{M}_1 , and v_1 for star 1 and \dot{M}_2 and v_2 for star 2. The vector \mathbf{R}_1 is used to locate arbitrary points, P , along the interaction boundary with respect to the position of star 1. The vector \mathbf{R}_2 locates P with respect to star 2. The angle from the line joining the two stars to \mathbf{R}_1 is designated θ , and the angle from this same line to \mathbf{R}_2 is designated ψ . A further angle, ϕ , is defined between \mathbf{R}_1 to \mathbf{R}_2 .

Figure 2.11 defines a second coordinate system which is specific to a given position, P , along the shell. The coordinate system is oriented so that one component

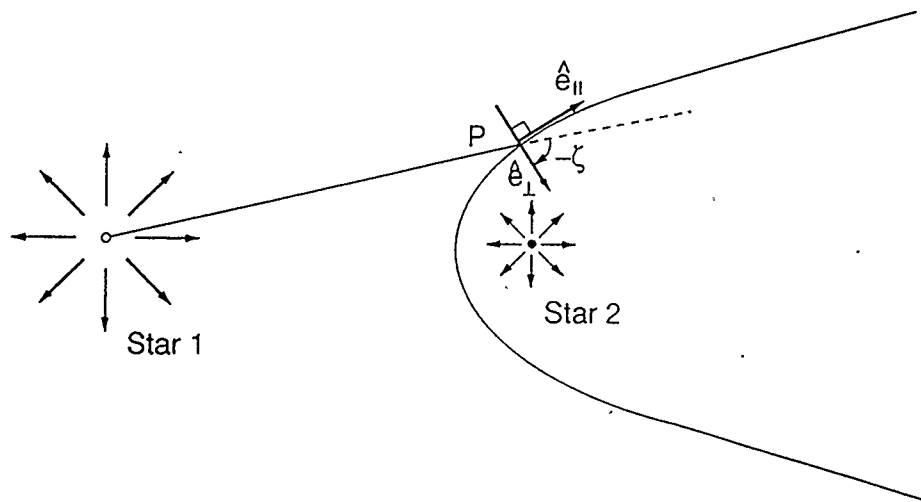


Figure 2.11: **Boundary Oriented Coordinates in the GW Model**

Coordinate are defined along the shell such that at each point P , a unit vector \hat{e}_{\parallel} lies tangent to the boundary, and a second unit vector \hat{e}_{\perp} lies perpendicular (pointing toward the star 2 side). The angle $-\zeta$ relates the $(\hat{e}_{\parallel}, \hat{e}_{\perp})$ coordinate system to the (R_1, θ) polar coordinate system.

points along the shell (subscript \parallel), and the other points in a direction normal to the shell (subscript \perp). The angle $-\zeta$ is the angle from $R_1(P)$ to $\hat{e}_{\perp}(P)$. Hence the angle ζ relates the two coordinate systems:

$$\tan \zeta = -\frac{1}{R_1} \frac{dR_1}{d\theta}. \quad (2.15)$$

In terms of the (\parallel, \perp) coordinates, the components of fluid velocity inside the thin boundary are designated $(v_{\parallel}, v_{\perp})$. The components of wind velocity from stars 1 and 2, immediately outside the boundary, are $(v_{\parallel,1}, v_{\perp,1})$ and $(v_{\parallel,2}, v_{\perp,2})$ respectively. These components are related to the mass loss velocities from the two stars as follows:

$$v_{\parallel,1} = -v_1 \sin \zeta, \quad v_{\perp,1} = v_1 \cos \zeta$$

$$v_{\parallel,2} = -v_2 \sin(\phi - \zeta), \quad v_{\perp,2} = v_2 \cos(\phi - \zeta) \quad (2.16)$$

The density within the undisturbed winds from stars 1 and 2 follow immediately from the equation of mass continuity, *i.e.*

$$\begin{aligned} \rho_1 &= \frac{\dot{M}_1}{4\pi R_1^2 v_1}, \quad \text{and} \\ \rho_2 &= \frac{\dot{M}_2}{4\pi R_2^2 v_2}. \end{aligned} \quad (2.17)$$

Since the interaction region is assumed to be infinitesimally thin, a surface density, σ , is used in the place of a density within the shell.

The equations governing the position of, and flow along, the boundary follow from the conservation of momentum,

$$0 = -\rho_2 v_{\perp,2} (v_{\parallel,2} - v_{\parallel}) + \rho_1 v_{\perp,1} (v_{\parallel,1} - v_{\parallel}) - \sigma v_{\parallel} \frac{\cos \zeta}{R_1} \frac{dv_{\parallel}}{d\theta}, \quad (2.18)$$

$$0 = -\rho_2 v_{\perp,2}^2 + \rho_1 v_{\perp,1}^2 + \sigma v_{\parallel}^2 \frac{\cos \zeta}{R_1} \left(1 + \frac{d\zeta}{d\theta} \right). \quad (2.19)$$

The first two terms in Equation 2.18 represent the parallel momentum flux contributed by the two winds at a given point along the shell, and the third term represents the momentum flux associated with the parallel flow already within the shell. In Equation 2.19, the first two terms represent the perpendicular momentum fluxes contributed by the two winds at a given point along the shell (the opposing ram pressures), and the third term arises from the centripetal acceleration of the flow along the curved shell. The conservation of mass entering the shell yields a further relationship,

$$\dot{M}_1(1 - \cos\theta) + \dot{M}_o(1 + \cos(\phi + \theta)) = 4\pi R_1 \sin\theta \sigma v_{\parallel}. \quad (2.20)$$

The system of equations 2.15 to 2.20 may be integrated to yield $R(\theta)$, $v(\theta)$, $\sigma(\theta)$, and $\zeta(\theta)$ at each angle θ along the boundary. Girard and Willson (1987) have shown that the shape of the boundary is completely determined by a single parameter mw , where m is the ratio of mass loss rates, and w is the ratio of the mass loss velocities:

$$\begin{aligned} m &\equiv \dot{M}_1/\dot{M}_2, \\ w &\equiv v_1/v_2. \end{aligned} \quad (2.21)$$

The parallel flow velocity is found to increase in a roughly linear fashion outward along the shell and reaches a constant value as the interaction cone opening angle approaches its asymptotic limit.

2.2.4 Observational Evidence for CW Phenomena

Interest in colliding winds began with the study the symbiotic novae V1016 Cyg and HM Sge which went into outburst in 1964 and 1975 respectively. These systems were known to possess late-type stars previous to their outbursts and hence it was reasonable to assume that their quiescent environments had been filled with late-type mass loss. With the initiation of outburst, high velocity winds were detected (“Wolf-Rayet” type, $\sim 1000 - 2000 \text{ km s}^{-1}$; *e.g.* Fitzgerald and Houk 1970, Belyakina, Gershberg and Shakhovskaya 1978): an interaction of winds appeared inevitable. The colliding winds hypothesis proved successful in explaining many of the outburst characteristics of these systems, including the profiles of optical emission lines and

the presence of X-ray emission (*e.g.* Wallerstein *et al.* 1984; Willson *et al.* 1984). Further support of the hypothesis was found in radio images (*e.g.* Kwok, Bignell and Purton 1984; Taylor 1988; Kenny, Taylor and Seaquist 1991) which provided evidence for the restructuring of the circumstellar environments.

Late-type winds should exist in symbiotic systems as a class (Section 1.3), and therefore CW phenomena are expected whenever high velocity outflows develop. High velocity outflows have been observed among symbiotic and recurrent novae, and in a number of peculiar symbiotic systems. The symbiotic nova AG Peg, for instance, exhibits very broad emission lines with P Cygni profiles suggesting velocities of $\sim 900 \text{ km s}^{-1}$ (Penston and Allen, 1985), and the observed radio morphology is readily interpreted in terms of colliding winds (Kenny 1989). Other systems exhibiting Wolf-Rayet features include the symbiotic novae V1329 Cyg (Crampton *et al.* 1970), and RR Tel (Penston *et al.* 1983; Ponz, Cassatella, and Viotti 1982). Among the recurrent novae, extremely high velocities have been measured at maximum, *e.g.* $\sim 5000 \text{ km s}^{-1}$ for T CrB, and $\sim 3500 \text{ km s}^{-1}$ for RS Oph (Livio 1988). RS Oph was also observed with the European VLBI Network (EVN) during its most recent outburst and was shown to possess a jet with velocity $> 2000 \text{ km s}^{-1}$ (Taylor *et al.* 1988c; Taylor *et al.* 1989a). The radio jet of CH Cyg was measured to have an outflow velocity of $> 1050 \text{ km s}^{-1}$ in a recent outburst (Taylor, Seaquist and Mattei 1986), while observations of the C IV I($\lambda 1548$)/I($\lambda 1550$) doublet of R Aqr can be explained in terms of an optically thick wind ($700 \lesssim v_{\text{wind}} \lesssim 1000 \text{ km s}^{-1}$, Michalitsianos *et al.* 1988). Colliding winds must necessarily be considered in all of these systems.

It is not clear how widespread CW phenomena may be among the general population of symbiotic stars. High velocity outflows appear to be confined to outbursts,

and no evidence exists for such outflow in quiescence. In as much as all symbiotic stars experience outbursts of some nature, however, transient CW phenomena may be common.

Chapter 3

EXTENSIONS OF COLLIDING WINDS (CW) MODELS

The KPF model (Section 2.2.2) and the GW model (Section 2.2.3) may be applied directly to certain classes of problems (*e.g.* Kwok 1987a; Wallerstein *et al.* 1984; Willson *et al.* 1984). If model imaging is to be performed however, a consistent treatment of shell thickness is necessary. One of the original contributions of this thesis is to perform such a treatment. Models will be derived in three configurations:

- The Binary Colliding Winds (CWb) Model, considers a configuration which is parallel to that of the GW model (Section 2.2.3). In addition to considering a finite thickness interaction shell, thermal pressures are included in locating the interaction boundaries.
- The Concentric Colliding Winds (CWc) Model, considers a configuration which is parallel to that of the KPF model (Section 2.2.2). The derivation of the model in Section 3.2 begins with an alternative formulation of the original KPF model which is consistent with the approach taken for the CWb model.
- The Orbital Colliding Winds (CWo) Model, considers the effects of orbital motion upon the CWb model. In this model, the large scale nebular structure consists of walls of compressed nebular material wrapped spirally about the system center. When further interaction takes place with surrounding cool

component mass loss, additional interaction feature may develop in accordance with the CWc model: *i.e.* an “equatorial interaction belt” and “polar interaction caps”.

The models to be derived will assume that shocked matter from both winds is well mixed. This assumption, although obviously an idealization, is not without a physical basis.

In the binary CW problem, the formative configuration consists of two independent streams of matter, of widely differing velocities, densities and temperatures, separated by a contact discontinuity. Perturbations initiated along the discontinuity may grow and encourage a mixing of the two streams. Once mixing is established in one location, it will be difficult to maintain a stratified structure through the rest of the shell. Stevens, Blondin and Pollock (1992) perform numerical simulations of early-type colliding winds and discover that various dynamical instabilities (*e.g.* thermal instabilities, Kelvin Helmholtz instabilities, thin-shell instabilities) disrupt the configuration on short time scales. It appears likely that this same conclusion may be extended to symbiotic colliding winds (Stevens 1993).

In the concentric CW problem, the disturbed nebular material does not flow along the interaction boundaries and therefore streaming instabilities are less important. Other instabilities may continue to play an important role. As an example, numerical simulations of the concentric CW problem in SN 1987A have been performed by Arnett, Fryxell and Muller (1989; see also Shu 1992). Rayleigh-Taylor instabilities followed by Kelvin-Helmholtz instabilities result in complete disruption of the idealized configuration on the time scale of hours. In addition to the role played by

instabilities, mixing may be encouraged by irregularities in the winds themselves. If the wind flows vary, or are characterized by the ejection of “blobs” and/or “bullets” (*e.g.* Robert, Drissen and Moffat 1989), the opposing streams are very likely to penetrate one another.

3.1 Binary Colliding Winds (CWb) Model

The derivation of the CWb model will begin with a detailed justification for the use of the isothermal approximation. The governing equations for the location of the interaction boundary will then be derived using the same formalisms and notation as Girard and Willson (1987, Section 2.2.3). The procedure for assigning finite thicknesses to points along the interaction boundary will then be described, and the consistency of the assumption of ionization within the unshocked winds will be discussed. Finally, the general characteristics of model images and spectra will be examined, and comparisons made to the STB model.

3.1.1 Isothermal Approximation

The GW model (Section 2.2.3) treats the binary CW problem in the approximation that the interaction shell is infinitesimally thin. In order to generalize this model to shells of non-zero thickness it is necessary that temperatures be assigned to points along the interaction boundary. In this section an expression for temperature will be derived under the assumption that radiative energy losses are negligible (adiabatic approximation). It will be shown that cooling times derived from this “adiabatic temperature” are short compared to other time scales of interest, and therefore that

the isothermal approximation is to be favored. In the isothermal approximation shocked material will quickly equilibrate to the temperature associated with stellar material in the presence of a strong ionizing source ($\sim 10^4$ K, Spitzer 1978). The approach taken to the derivation here is similar to that outlined by Dyson and Williams (1980, pp.119-126) for shocks in general.

Derivation of an Adiabatic Temperature

In Figure 3.1, the components of the binary CW problem are illustrated, and global flow characteristics are defined. The angle θ from star 1 is used to locate arbitrary points along the interaction boundary, and the angle from star 2, ψ , is considered to be a function of θ . A “ θ -cone” as the region containing all points on the interaction boundary with angles to star 1 of less than θ .

The mass fluxes into the θ -cone from stars 1 and 2, assuming isotropic mass loss, are given respectively by:

$$\dot{M}_{\theta 1} = \frac{\dot{M}_1}{2}(1 - \cos\theta), \text{ and.} \quad (3.1)$$

$$\dot{M}_{\theta 2} = \frac{\dot{M}_2}{2}(1 - \cos\psi). \quad (3.2)$$

The total mass flux into the θ -cone is therefore:

$$\dot{M}_{\theta} = \frac{\dot{M}_1}{2}(1 - \cos\theta) + \frac{\dot{M}_2}{2}(1 - \cos\psi). \quad (3.3)$$

The particle flux into the θ -cone is given by $\dot{N}_{\theta} = \dot{M}_{\theta} / \mu_a m_H$ where m_H is the mass of a hydrogen atom, and μ_a is the mean molecular weight of all particles including

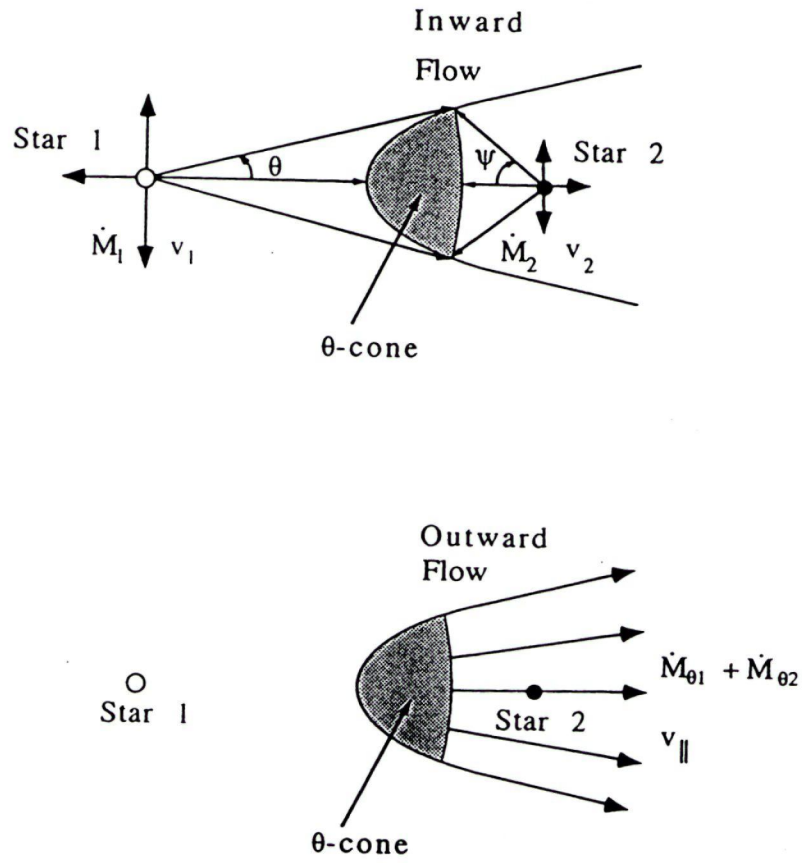


Figure 3.1: The θ -Cone: Wind and Shell Flow

TOP: The cone angle θ defines a region of surface on the shell boundary, the " θ -cone". Star 1 loses mass at velocity v_1 and rate \dot{M}_1 , some fraction of which enters the θ -cone, $\dot{M}_{1,\theta}$. Star 2 loses mass at velocity v_2 and rate \dot{M}_2 , some fraction of which also enters the θ -cone, $\dot{M}_{2,\theta}$. BOTTOM: Material flows out of the θ -cone along the interaction shell at a velocity of v_{\parallel} and a rate of $\dot{M}_{1,\theta} + \dot{M}_{2,\theta}$.

electrons. Under the assumption that the nebular material is of solar composition, and that H and He are completely ionized, $\mu_a \sim 0.6$. The same value of μ_a is assumed for both winds. The assumption of complete ionization will be discussed in Section 3.1.4. Using Equations 3.1 and 3.2, the combined particle flux may be written:

$$\dot{N}_\theta = \frac{\dot{M}_1}{2\mu_a m_H}(1 - \cos\theta) + \frac{\dot{M}_2}{2\mu_a m_H}(1 - \cos\psi). \quad (3.4)$$

Consider now the energy contributed by star 1 to the θ -cone. Its kinetic energy flux, assuming that the wind is at the terminal velocity, is given by

$$\dot{K}_{\theta 1} = \frac{1}{2} \left[\frac{\dot{M}_1}{2}(1 - \cos\theta) \right] v_1^2. \quad (3.5)$$

Its thermal energy flux follows from its particle flux, and the fact that the thermal energy per particle in an ideal gas at thermal equilibrium is given by $U = \frac{3}{2}kT_w$, where T_w is the wind temperature, and k is Boltzmann's constant.

$$\dot{U}_{\theta 1} = \frac{3}{4} \frac{kT_w}{\mu_a m_H} \dot{M}_1(1 - \cos\theta). \quad (3.6)$$

The total energy flux from star 1 into the θ -cone may therefore be written:

$$\dot{E}_{\theta 1} = \frac{1}{2} \left[\frac{\dot{M}_1}{2}(1 - \cos\theta) \right] v_1^2 + \frac{3}{4} \frac{kT_w}{\mu_a m_H} \dot{M}_1(1 - \cos\theta). \quad (3.7)$$

Similarly for star 2:

$$\dot{E}_{\theta 2} = \frac{1}{2} \left[\frac{\dot{M}_2}{2}(1 - \cos\psi) \right] v_2^2 + \frac{3}{4} \frac{kT_w}{\mu_a m_H} \dot{M}_2(1 - \cos\psi). \quad (3.8)$$

Note that a common wind temperature has been assumed for both winds. It will be assumed that $T_w \sim 10^4$ K, consistent with the presence of an ionizing source of sufficient luminosity that both winds are completely ionized before passing into the zone of interaction (Section 3.1.4). The total flux of energy into the θ -cone is simply $\dot{E}_{\theta,\text{in}} = \dot{E}_{\theta 1} + \dot{E}_{\theta 2}$.

The flux of energy out of the θ -cone also includes a kinetic and a thermal component, and may be written:

$$\begin{aligned} \dot{E}_{\theta,\text{out}} = & \frac{1}{2} \left[\frac{\dot{M}_1}{2}(1 - \cos\theta) + \frac{\dot{M}_2}{2}(1 - \cos\psi) \right] v_{\parallel}^2 \\ & + \frac{3}{2} \frac{kT}{\mu_a m_H} \left[\frac{\dot{M}_1}{2}(1 - \cos\theta) + \frac{\dot{M}_2}{2}(1 - \cos\psi) \right], \end{aligned} \quad (3.9)$$

where v_{\parallel} is the flow velocity outward along the shell, and T is the temperature of the outflowing material at position θ along the boundary. Mass conservation, and Equations 3.3 and 3.4 have been used to derive this expression.

Combining Equations 3.7 through 3.9:

$$\begin{aligned} \dot{E}_{\theta,\text{in}} - \dot{E}_{\theta,\text{out}} = & \frac{1}{4} [\dot{M}_1(1 - \cos\theta)(v_1^2 - v_{\parallel}^2) + \dot{M}_2(1 - \cos\theta)(v_2^2 - v_{\parallel}^2)] \\ & + \frac{3}{2} \frac{k\dot{M}_{\theta}}{\mu_a m_H} (T_w - T). \end{aligned} \quad (3.10)$$

It is expected that $\dot{E}_{\theta,\text{in}}$ will differ from $\dot{E}_{\theta,\text{out}}$ by an amount equal to the PdV work done in compressing the inflowing wind volumes (V_1 and V_2) to the volume of the outflowing material, V . That is:

$$\dot{E}_{\theta,\text{in}} - \dot{E}_{\theta,\text{out}} = P \frac{dV}{dt} - \left(P_1 \frac{dV_1}{dt} + P_2 \frac{dV_2}{dt} \right), \quad (3.11)$$

where P_1 and P_2 are pressures associated with the two winds as they contact the interaction boundary.

The quantities dV_1/dt and dV_2/dt represent the volumes of gas from each star entering the shocked region per second, while dV/dt represents the volume of gas exiting the θ -cone along the boundary. Note that dV_1/dt , dV_2/dt , P_1 and P_2 all vary along the interaction boundary so that Equation 3.11, as written, is non-trivial. To simplify the problem, the volume fluxes may be expressed as densities:

$$\begin{aligned}\frac{dV_i}{dt} &= \frac{dV_i}{dM_i} \frac{dM_i}{dt} \\ &= \frac{1}{\rho_i} \dot{M}_i,\end{aligned}\tag{3.12}$$

where the index i may designate star 1, star 2 or the boundary flow. Using this identity, Equation 3.11 may be rewritten,

$$\dot{E}_{\theta,\text{in}} - \dot{E}_{\theta,\text{out}} = \frac{P}{\rho} \dot{M}_{\theta} - \frac{P_1}{\rho_1} \dot{M}_{\theta 1} - \frac{P_2}{\rho_2} \dot{M}_{\theta 2}.\tag{3.13}$$

Using the ideal gas law, $P/\rho = kT/(\mu_a m_H)$, this expression becomes:

$$\dot{E}_{\theta,\text{in}} - \dot{E}_{\theta,\text{out}} = \frac{kT}{\mu_a m_H} \dot{M}_{\theta} - \frac{kT_w}{\mu_a m_H} \dot{M}_{\theta 1} - \frac{kT_w}{\mu_a m_H} \dot{M}_{\theta 2},\tag{3.14}$$

Rearranging terms and using Equations 3.1 through 3.3:

$$\dot{E}_{\theta,\text{in}} - \dot{E}_{\theta,\text{out}} = \frac{k\dot{M}_{\theta}}{\mu_a m_H} (T - T_w).\tag{3.15}$$

Under the adiabatic approximation, the value of $\dot{E}_{\theta,\text{in}} - \dot{E}_{\theta,\text{out}}$ given in Equation 3.15 may be equated to that given in Equation 3.10. Proceeding in this way the adiabatic temperature is given by:

$$\begin{aligned}
T_{\text{adia}}(\theta) &= T_w + \frac{1}{10} \frac{\mu_a m_H}{k \dot{M}_\theta} \left[\dot{M}_1 (1 - \cos\theta) (v_1^2 - v_{\parallel}^2) + \dot{M}_2 (1 - \cos\psi(\theta)) (v_2^2 - v_{\parallel}^2) \right] \\
&= T_w + \frac{\mu_a m_H v_2^2}{5k} \left[\frac{m(1 - \cos\theta)(w^2 - v^2) + (1 - \cos\psi)(w^2 - v^2)}{m(1 - \cos\theta) + (1 - \cos\psi)} \right], \quad (3.16)
\end{aligned}$$

where as previously $m \equiv \dot{M}_1/\dot{M}_2$, $w \equiv v_1/v_2$, and $v \equiv v_{\parallel}/v_2$. The temperature expressed in this equation is the value, after mixing, for all particles which have entered the disturbed stream at boundary points interior to θ and have subsequently flowed to θ .

An important limiting case of Equation 3.16 exists at $\theta = 0$. This is the “static point”, the central point of contact of the opposing winds. Although \dot{M}_θ is zero at this point, and therefore Equation 3.16 is indeterminate, a solution may be obtained by taking the limit as $\theta \rightarrow 0$. Two successive applications of l’Hopital’s rule are required. The expression obtained using the CWb governing equations (Section 3.1.2) is:

$$\begin{aligned}
T_o &= T_w + \frac{1}{5} \frac{\mu_a m_H}{k} \left[\frac{w^2(w+1) + b(w^3+1)}{w(w+1) + b(w+1)} \right] v_2^2 \\
&= T_w + 14.5 \left[\frac{w^2(w+1) + b(w^3+1)}{w(w+1) + b(w+1)} \right] v_{2[\text{km s}^{-1}]}^2, \quad (3.17)
\end{aligned}$$

where b is the “thermal factor” to be formally introduced in Section 3.1.2 and is defined $b \equiv kT_w/\mu_a m_H v_2^2$. When thermal pressure within the winds is not important, $b \rightarrow 0$ and the expression simplifies to:

$$T_o = T_w + 14.5 v_{1[\text{km s}^{-1}]} v_{2[\text{km s}^{-1}]} \quad (3.18)$$

It is of interest that the adiabatic temperature at the static point is independent of the mass loss rate from either of the stars, and depends only upon the wind velocities

and temperatures. For symbiotic stars, thermal pressures are important in the cool component wind. For typical flow velocities of $v_1 = 1000 \text{ km s}^{-1}$ (hot component) and $v_2 = 10 \text{ km s}^{-1}$ (cool component), and a wind temperature of 10^4 K , Equation 3.17 produces a result which is a factor of 2 higher than that of Equation 3.18.

Radiative Cooling

In the presence of a strong ionizing source, nebular material of solar composition will equilibrate to a temperature of $\sim 10^4 \text{ K}$, as previously noted. The time required to achieve equilibrium for material whose temperature is near 10^4 K is given by Spitzer (1978, p.139) as

$$t_c = \frac{2.0 \times 10^4}{n_H} \text{ [yr]}, \quad (3.19)$$

$$(3.20)$$

where n_H is the proton number density.

If the temperature greatly exceeds 10^4 K , then the cooling time is given by

$$t_c = 3k\mu_m m_H \left(\frac{1}{\Lambda/n_H^2} \right) \left(\frac{T}{\rho} \right), \quad (3.21)$$

where Λ is the cooling function [$\text{erg cm}^{-3} \text{ s}^{-1}$], and μ_m is the mean atomic weight of ions (~ 1.2). The quantity Λ/n_H^2 is a function of T alone and values are plotted in Figure 3.2. It will be noted that Λ/n_H^2 increases rapidly with temperatures for $T \gtrsim 10^4$ and this explains why equilibrium is rapidly achieved in the vicinity of 10^4 . Beyond $\sim 10^6 \text{ K}$, however Λ/n_H^2 decreases sharply and cooling times are correspondingly increased (Equation 3.21).

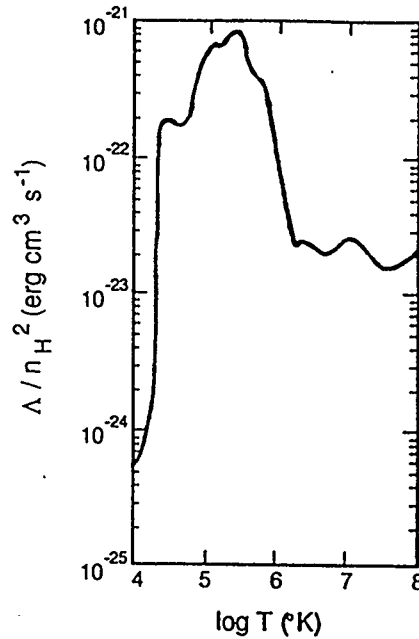


Figure 3.2: Cooling Function, $T > 10^4$ K
(After Spitzer 1978, p. 62)

Adiabatic temperatures given by Equation 3.17 for the static point in the binary CW problem are of the order of a few times 10^5 K for typical wind parameters (e.g. $v_1 = 1000$ km s $^{-1}$, $v_2 = 10$ km s $^{-1}$, $T_w = 10^4$ K). At these temperatures, the cooling function takes relatively high values (Figure 3.2) and hence cooling is generally effective.

To provide a measure of the effectiveness of radiative cooling, consider a point lying one binary separation outward along the interaction boundary. A residence time, t_r , may be defined as the time required for matter at this point to travel one binary separation at the velocity $v_{||}$. Cooling may be considered effective whenever the residence time exceeds the cooling time, i.e. $t_c/t_r < 1$. In Figure 3.3 the ratio t_c/t_r is plotted against $m \equiv \dot{M}_1/\dot{M}_2$. Typical values of other mass loss parameters have been used as shown. The plot indicates that t_r greatly exceeds t_c over the range

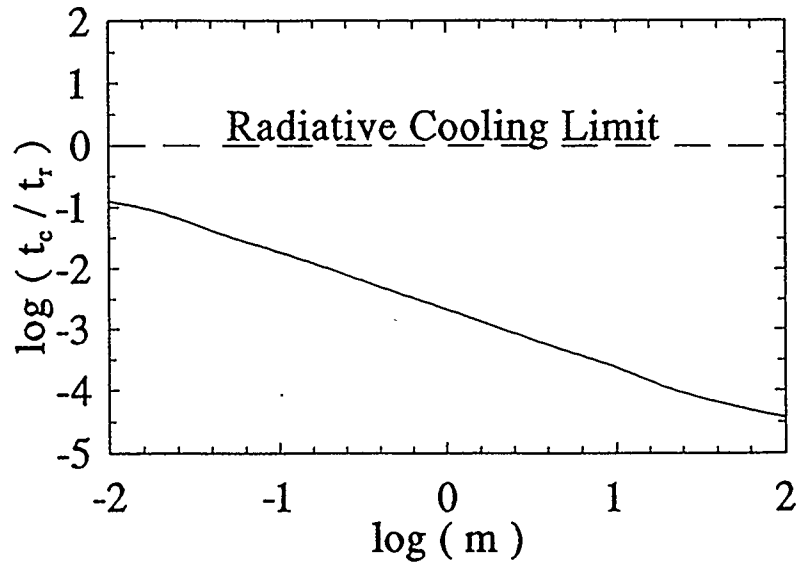


Figure 3.3: Radiative Cooling Timescales

Plotted parameters are: t_c (cooling time, Equation 3.19); t_r (residence time $\equiv a/v_{||}$); and $m \equiv \dot{M}_1/\dot{M}_2$. Radiative cooling is effective below the horizontal dashed line. Model parameters are: $v_1 = 1000 \text{ km s}^{-1}$, $v_2 = 10 \text{ km s}^{-1}$, $\dot{M}_2 = 1 \times 10^{-7} M_{\odot}\text{yr}^{-1}$, and $a = 10 \text{ AU}$. The ratio t_c/t_r increases linearly with a and more slowly with \dot{M}_2 .

of plotted values ($1 \times 10^{-9} < \dot{M}_1 < 1 \times 10^{-5} M_{\odot}\text{yr}^{-1}$). In this way, the adiabatic approximation has proven inconsistent, and the isothermal approximation (10^4 K) will be generally adopted for the applications which follow.

Before leaving the adiabatic approximation, it is of interest to examine the behavior of the temperature outward from the interaction apex, as plotted in Figure 3.4. Intuitively one might expect temperatures to decrease outward along the boundary, however “inverted” temperature profiles are also shown to occur.

Inverted profiles develop because of the differences in velocity, and associated energy, of particles entering the interaction shell from the two winds. Star 1 has been considered the “hot component”, and accordingly a high velocity, $v_1 = 1000 \text{ km s}^{-1}$, has been assumed for its wind. A velocity of $v_2 = 10 \text{ km s}^{-1}$ had been assumed

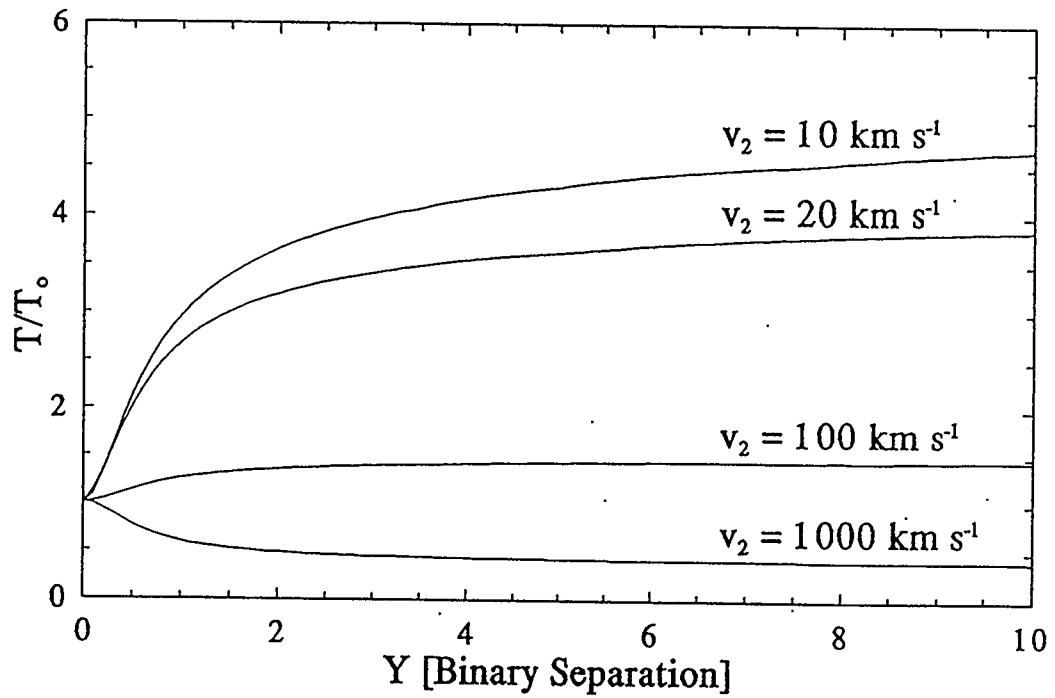


Figure 3.4: Adiabatic Temperature Profiles

Adiabatic temperature profiles are shown for nebular models with $\dot{M}_1 = 10^{-7}$, $\dot{M}_2 = 10^{-7}$, $v_1 = 1000 \text{ km s}^{-1}$, and $T_w = 10^4 \text{ K}$. Temperatures have been normalized to the temperature at the static point, T_0 . Values are plotted against Y , the distance perpendicular to the line passing through the two stars.

for the “cool component” (Star 2) wind. The adiabatic temperature derived in Equation 3.16 scales with the difference between the kinetic energy of the inflowing winds and that of the outflowing stream along the interaction boundary, *i.e.*

$$T_{\text{adia}}(\theta) \approx \frac{1}{5} \frac{\mu_a m_H}{k \dot{M}_\theta} \left(\frac{1}{2} \dot{M}_{\theta 1} v_1^2 + \frac{1}{2} \dot{M}_{\theta 2} v_2^2 - \frac{1}{2} \dot{M}_\theta v_{\parallel}^2 \right), \quad (3.22)$$

where it has been assumed that $T_w \ll T_{\text{adia}}$. Defining $f_{\theta 1}$ and $f_{\theta 2}$ as the fractional mass flux contributions of each wind (*i.e.* $f_{\theta 1} \equiv \dot{M}_{\theta 1} / \dot{M}_\theta$ and $f_{\theta 2} \equiv \dot{M}_{\theta 2} / \dot{M}_\theta$), it follows from Equation 3.22 that

$$\begin{aligned} T_{\text{adia}} &\propto f_{\theta 1} v_1^2 + f_{\theta 2} v_2^2 - v_{\parallel}^2 \\ &\propto f_{\theta 1} w^2 + f_{\theta 2} - v^2. \end{aligned} \quad (3.23)$$

where $w \equiv v_1/v_2$ and $v \equiv v_{\parallel}/v_2$. The condition for an inverted temperature profile may be therefore be expressed,

$$w^2 \Delta f_{\theta 1} > \Delta(v^2) - \Delta f_{\theta 2}, \quad (3.24)$$

where Δ indicates changes in the indicated quantities for some positive change of θ . All of the model nebulae represented in Figure 3.4 are C-facing, *i.e.* the interaction boundary sweeps over the cool component. It may be shown for this geometry that $\Delta f_{\theta 1}$ and $\Delta(v^2)$ will always be positive and $\Delta f_{\theta 2}$ will always be negative. The factor w^2 amplifies the effect of changes in $f_{\theta 1}$ in Equation 3.24, and ensures that the condition for an inverted profile may be satisfied for reasonable system parameters (even though $\Delta f_{\theta 1} + \Delta f_{\theta 2} = 1$).

3.1.2 Interaction Boundary Location

For the purposes of numerical simulation, an infinitely thin interaction shell is assumed in locating the interaction boundary. Once the boundary has been located, a density and thickness is assigned to each point along it. The error introduced by initially assuming an infinitely thin shell should be small so long as the thickness of the shell at the locations of interest is much smaller than the displacement from the system center at the same location (*e.g.* Kallrath 1991).

The system of equations to be derived represents an improvement over the governing equations of the GW model since the thermal pressures in the unshocked winds of the two stars will be included. The conservation of mass requires that density varies inversely with wind velocity (Equation 2.17) and therefore, by the ideal gas law, the thermal pressure also varies inversely with wind velocity. Thermal pressure will become significant for low velocity winds such as those associated with symbiotic cool components. The ratio of ram pressure to thermal pressure is given by $\rho v^2/P$, where ρ is the density within the wind, v is the wind velocity, and P is the thermal pressure. Substitution for P/ρ using the ideal gas law yields a ratio of $\mu_a m_H v^2/kT$, where μ_a is the mean atomic weight of all particles including electrons. For a temperature of $T = 10^4$ K a ratio of 1 is obtained at a velocity of ~ 12 km s⁻¹, which is typical for late-type winds. It follows that the total pressure from the cool component wind will include approximately equal contributions from ram and thermal pressures.

The first governing equation of the CWb model is identical to that of the GW model (Equation 2.18). With the inclusion of thermal pressures, the second governing

equation Equation 2.19 becomes:

$$0 = -\rho_2 v_{1,2}^2 - P_2 + \rho_1 v_{1,1}^2 + P_1 + \sigma v_{\parallel}^2 \frac{\cos \zeta}{R_1} (1 + \zeta'). \quad (3.25)$$

where P_1 and P_2 are the thermal pressures for winds 1 and 2 respectively and the prime (') denotes a derivative with respect to θ . This equation may be rewritten in dimensionless form by defining the quantities:

$$\begin{aligned} r_1 &\equiv \frac{R_1}{a}; & r_2 &\equiv \frac{R_2}{a}; \\ m &\equiv \frac{M_1}{M_2}; & w &\equiv \frac{v_1}{v_2}; \\ v &\equiv \frac{v_{\parallel}}{v_2}; & q &\equiv \frac{\sigma v_2 a}{M_2}; \\ b &\equiv \frac{kT_w}{\mu_a m_H v_2^2}; \text{ and} & \eta &\equiv \sqrt{\frac{w(1+b)}{m(w^2+b)}}. \end{aligned} \quad (3.26)$$

Quantities are defined consistent with the GW model (Section 2.2.3), *i.e.* : a is the binary separation, R_1 and R_2 are distances from stars 1 and 2 respectively, v_{\parallel} is the velocity along the shell, and σ is the surface density. Both winds have been assumed to have the same temperature, T_w , and mean atomic weight, μ_a . Substitution of the definitions at 3.26 into Equation 3.25 yields:

$$\zeta' = \frac{r_1}{4\pi q v^2 \cos \zeta} \left[\frac{(\cos^2(\phi - \zeta) + b)}{r_2^2} - \frac{m}{w r_1^2} (w^2 \cos^2 \zeta + b) \right] - 1. \quad (3.27)$$

The boundary conditions of the CWb governing equations, unlike those of the GW model, are coupled to one another. The following conditions are therefore altered from those given by Girard and Willson (1987).

$$r_1|_{\theta=0} = [\eta + 1]^{-1},$$

$$v'|_{\theta=0} = \frac{2}{3} \left(\frac{1}{\eta^{-2} + m} \right) \left[\frac{\eta + 1}{\eta^3} + \zeta'|_{\theta=0}(\eta^{-2} - mw) \right], \text{ and}$$

$$(\zeta'|_{\theta=0})^2 4(1 - mw\eta^2) + \zeta'|_{\theta=0}[11 + 3b - mw\eta^2 + (10 + 3b)\eta^{-1}]$$

$$+ (1 + \eta^{-1})[4 + (6 + 3b)\eta^{-1}] = 0. \quad (3.28)$$

Physical considerations require ζ to increase negatively with θ , and hence the positive discriminant is taken in the expression for ζ' above. The full set of differential governing equations for the CWb boundary location is given in Appendix A.

The importance of the inclusion of thermal terms in locating the interaction boundary is illustrated in Figure 3.5. Boundaries are plotted for various combinations of flow parameters, all of which have the same value of mw (ratio of intrinsic ram pressures). In the GW model the interaction boundary is completely determined by mw , however Figure 3.5 indicates that CWb models, sharing the same value of mw , may have significantly different boundaries depending upon their values of v_2 . As v_2 decreases, the density within the cool component wind increases, and the accompanying increase in thermal pressure pushes the interaction boundary toward the hot component. Altering v_1 with mw fixed has little effect since the pressure in the hot component wind is constituted almost entirely by the ram pressure.

The opening angle of the interaction cone is of interest as a potentially observable quantity in radio imaging (Section 2.1.3). In the GW model the angle approaches an asymptotic limit, however in the CWb model the opening angle continues to evolve

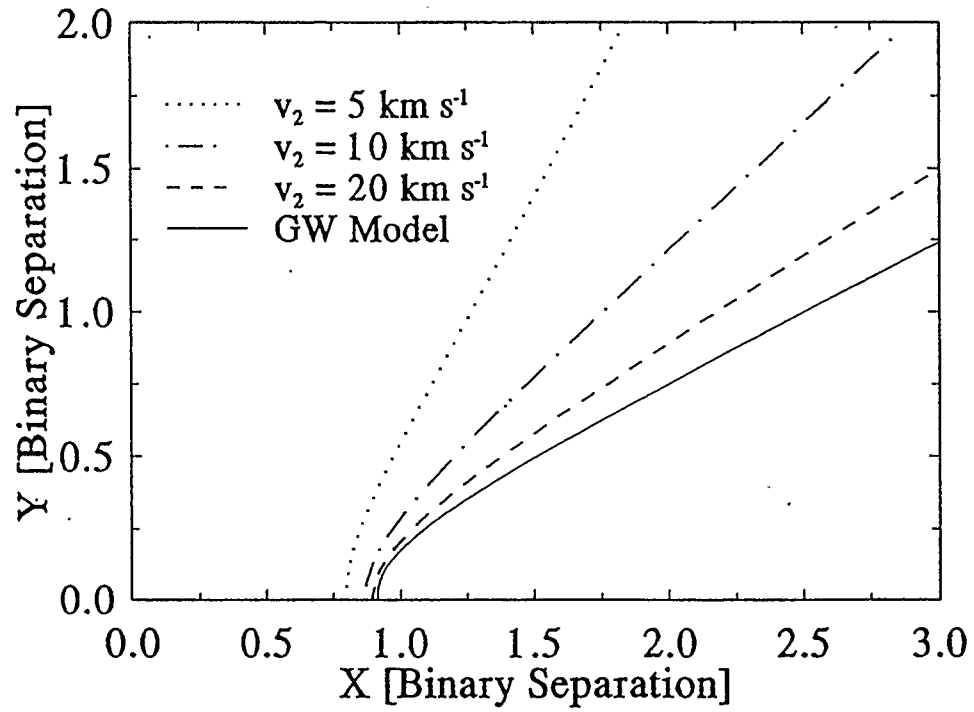


Figure 3.5: Effect of Thermal Pressure: Constant v_1

Model CWb interaction boundaries have been drawn for various velocities of the cool component wind, v_2 . The velocity of the hot component wind has been held constant at $v_1 = 1000 \text{ km s}^{-1}$. Values of m have been adjusted to maintain mw at a constant value of 100. The hot component is located at coordinates (0,0) and the cool component is located at (1,0).

even at large separations due to the domination of thermal pressure from the cool component wind (“thermal curvature”). Thermal pressure comes to dominate since it decreases only with $1/r^2$, while ram pressure decreases both with $1/r^2$ and with the angle between the wind flow and the interaction boundary. The distance at which this thermal curvature becomes important is normally $\gtrsim 100$ binary separations for typical parameters, and hence it remains reasonable to state a characteristic opening angle for a given combination of model parameters (Figure 3.6). For very low values of m , thermal curvature may lead to closed CWb nebulae on scales of interest.

Another quantity of considerable importance is the terminal velocity in the interaction stream. This quantity is again somewhat ill-defined within the context of the CWb model. Since the interaction stream continues to be accelerated by thermal pressure from the cool component wind even at large distances, the stream velocity does not reach an asymptotic limit. Within distance scales of interest, however, values of $v \equiv v_{\parallel}/v_2$ are reasonably constant (Figure 3.6).

It is useful to define a geometry factor, X_{cwb} , to distinguish between classes of model geometries:

$$X_{\text{cwb}} \equiv \frac{1}{\eta^2} \approx \frac{mw}{1+b}. \quad (3.29)$$

This parameter will play a role within the CWb model similar to that played by X_{stb} and mw in the STB and GW models respectively. It may be interpreted physically as the ratio between the “intrinsic flow pressures” of the component winds. The term “intrinsic flow pressure” refers to the outward pressure associated with a given wind, in isolation, at some fiducial radius.

For $X_{\text{cwb}} < 1$, the static point will lie nearer the hot component than the cool

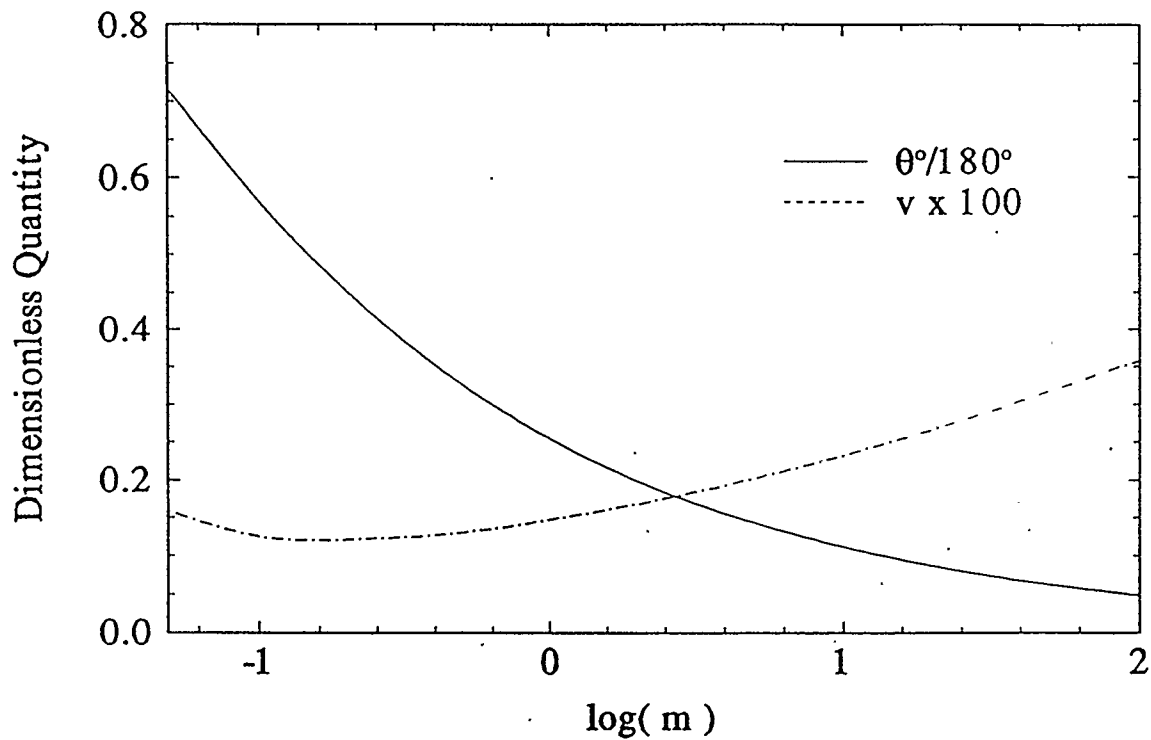


Figure 3.6: Interaction Cone Opening Angles and Stream Velocities
 Flow parameters, $\dot{M}_2 = 3 \times 10^{-7} M_\odot \text{yr}^{-1}$, $v_1 = 1000 \text{ km s}^{-1}$, and $v_2 = 10 \text{ km s}^{-1}$, are held fixed while $m \equiv \dot{M}_1/\dot{M}_2$ is varied. Curves are plotted for the opening angle of the interaction cone (θ), and the “terminal” interaction stream velocity (v) at a distance of $r_1 = 100$ from the hot component.

component and the interaction cone will be H-facing. For $X_{\text{cwb}} > 1$ the static point will lie closer to the cool component, and the interaction cone will be C-facing in the vicinity of the apex; at larger separations, however, the cone may become H-facing due to the effects of thermal curvature.

3.1.3 Shell Thickness and Density

Conditions at the Interaction Apex

Analytic solutions exist for the interaction shell thickness and density at the central point of contact between the two winds (“static point”). Conditions at this point are of particular interest since they are closely related to observable characteristics including the optically thick turnover of the radio spectrum (Section 3.1.6).

The location of the static point may be determined by the condition of balance between the total pressures of the two winds. The total pressure from wind 1, including both the thermal pressure and the ram pressure, is given by

$$P_{T1} = \rho_1 v_1^2 + \frac{\rho_1 k T_w}{\mu_a m_H} = \frac{\dot{M}_1}{4\pi R_1^2 v_1} v_2^2 (w^2 + b), \quad (3.30)$$

where ρ_1 is the density in wind 1, R_1 is the distance from star 1, b is the “thermal factor” ($b \equiv kT_w / \mu_a m_H v_2^2$) and all remaining symbols have been previously defined. Equation 2.17 for density in a stellar wind has been used to obtain the final expression. A similar equation may be written for wind 2, *i.e.*

$$P_{T2} = \rho_2 v_2^2 + \frac{\rho_2 k T_w}{\mu_a m_H} = \frac{\dot{M}_2}{4\pi R_2^2 v_2} v_2^2 (1 + b). \quad (3.31)$$

Values of R_1 and R_2 for the static point are obtained by equating P_{T1} and P_{T2}

($r_1|_{\theta=0} = [\eta + 1]^{-1}$, Equation 3.28). Note that the sum of these values is the binary separation, *i.e.* $R_1 + R_2 = a$.

Since the interaction shell will have a finite thickness, the values of R_1 and R_2 at the shell boundaries will differ from those at the static point. Let Δ_1 be the distance from the static point to the shell boundary in the star 1 direction, and let Δ_2 be defined similarly in the star 2 direction. The total thickness of the shell is therefore given by $\Delta_1 + \Delta_2$.

If σ is the surface density of the shell at the static point, then the shell density is given by $\sigma/(\Delta_1 + \Delta_2)$. The surface density is known at all points along the boundary once the governing equations (Equation A.1) have been integrated outward. An expression for the shell pressure may now be written in terms of the shell thickness and surface density, using the ideal gas law, *i.e.*

$$P_s = \left(\frac{\sigma}{\Delta_1 + \Delta_2} \right) \frac{kT_s}{\mu_a m_H}. \quad (3.32)$$

It will be assumed that the temperature within the shell, T_s , is equal to the temperature of the winds, T_w , in accordance with the isothermal approximation as discussed in Section 3.1.1.

Equating the shell pressure (Equation 3.32) to the inward pressures at the interaction boundaries (Equations 3.30 and 3.31), expressions for the two components of shell thickness may be written:

$$\begin{aligned} \frac{\sigma}{\Delta_1 + \Delta_2} &= \frac{\dot{M}_1}{4\pi(R_1 - \Delta_1)^2 v_1} \left(\frac{w^2}{b} + 1 \right); \text{ and} \\ \frac{\sigma}{\Delta_1 + \Delta_2} &= \frac{\dot{M}_2}{4\pi(R_2 - \Delta_2)^2 v_2} \left(\frac{1}{b} + 1 \right). \end{aligned}$$

(3.33)

This pair of equations may be solved to obtain the shell thicknesses in dimensionless form:

$$\begin{aligned} \delta_1 &= \delta_2/\eta; \text{ and} \\ \delta_2 &= r_2 - \frac{1}{8\pi q} \left(\frac{1+b}{b} \right) (1+1/\eta) \left\{ \sqrt{16\pi q \left(\frac{b}{1+b} \right) \left(\frac{\eta}{1+\eta} \right)^2 + 1} - 1 \right\}, \end{aligned} \quad (3.34)$$

where: δ_1 and δ_2 are defined as Δ_1/a and Δ_2/a respectively; q , η , and r_2 are dimensionless quantities defined in Equation 3.26; and a is the binary separation.

The value of q at $\theta = 0$ follows from the governing equations (A.1) in the limit that $\theta \rightarrow 0$,

$$q|_{\theta=0} = \frac{(\eta^{-2} + m)(1 + \eta)}{8\pi v'|_{\theta=0}}, \quad (3.35)$$

where $v'|_{\theta=0}$ is given in Equation 3.28. Using the definition of q and the relationship $\rho = \sigma/(\Delta_1 + \Delta_2)$, the density may be expressed:

$$\rho|_{\theta=0} = \frac{q|_{\theta=0} \dot{M}_2}{a^2 v_2 (\delta_1 + \delta_2)}. \quad (3.36)$$

The density at the static point is expected to represent the high extreme within the interaction shell. Wallerstein *et al.* (1991) have used Bowen fluorescence emission (UV) to estimate densities on the order of $10^{11} - 10^{12} \text{ cm}^{-3}$ for a number of systems (*e.g.* AG Dra, HM Sge, V1016 Cyg, V1329 Cyg and Z And). Such values may be obtained from Equation 3.36 for very reasonable flow parameters.

The CWb model is a general formulation of the binary CW problem and is not restricted to symbiotic stars. In some applications, the adiabatic approximation may be appropriate, and in such case small changes are required in Equations 3.33 and 3.35. Specifically, the quantity σ is replaced by $\sigma^* \equiv \sigma T_s/T_w$, and the quantity q is replaced by $q^* \equiv q T_s/T_w$, where T_s is the adiabatic shell temperature from Equation 3.16. Equations 3.35 and 3.36 are unchanged. Adiabatic shells, because of their higher temperatures, will be less dense and more physically thick than their isothermal counterparts.

Conditions along the Interaction Shell

The principles applied to the derivation of a thickness at the static point may also be applied further outward along the interaction boundary, however additional complications are encountered. The most serious complication concerns the assumption of an infinitely thin shell in locating the interaction boundary. For a finite thickness interaction cone, the inward pressures at the inner and outer boundaries are somewhat different than would exist at the single interface of an infinitely thin shell. To overcome this systematic effect, it was necessary to begin at the static point and solve outward along the boundary for shell thicknesses in finite steps.

Shell densities were found to decrease outward in close agreement with a $1/r^2$ law, and shell thicknesses were found to increase linearly with r . Decreases in density and increases in thickness occurred more slowly in the vicinity of the interaction cone apex where the effects of shell curvature were strongly felt.

3.1.4 Ionization

The CWb model as derived, in the previous sections, assumes complete ionization of the interaction stream and the incoming winds. The consistency of this assumption will now be examined.

The requirement for ionizing photons to penetrate through the interaction shell and into the cool component wind is greatest at the static point. Consider the ionizing photon luminosity required to ionize through a static homogeneous shell of thickness Δ and proton number density n_H , at a distance R_1 from the ionizing source (hot component).

$$L_{\text{ph}} = 4\pi n_H^2 \alpha^{(2)} R_1^2 \Delta, \quad (3.37)$$

where $\alpha^{(2)}$ is the recombination coefficient to all levels of hydrogen except the ground state, and μ_m is the mean atomic weight of massive particles. When the hot component also supports a wind of rate \dot{M}_1 and velocity v_1 , an additional term, $\dot{M}_1 / \alpha^{(2)} 4\pi \mu_m m_H R_1 v_1$, must be included on the right hand side of this equation, however, this term is much smaller than $4\pi n_H^2 \alpha^{(2)} R_1^2 \Delta$ for parameters of interest. From the functional dependencies in Equation 3.37, it follows that the requirement for ionizing photon luminosity decreases outward along the interaction shell, *i.e.* $n_H \propto R_1^{-2}$, $\Delta \propto R_1$, and therefore $L_{\text{ph}} \propto R_1^{-1}$. Consequently, complete ionization is a reasonable assumption if the luminosity requirement is satisfied at the static point.

As an example, consider a system with $\dot{M}_1 = 1 \times 10^{-8} M_{\odot} \text{yr}^{-1}$, $\dot{M}_2 = 1 \times 10^{-7} M_{\odot} \text{yr}^{-1}$, $v_1 = 1000 \text{ km s}^{-1}$, $v_2 = 10 \text{ km s}^{-1}$, and a binary separation of 10 AU. The conditions at the static point, which occurs at a distance of $R_1 = 6.7 \text{ AU}$

from the hot component, are: $\Delta = 0.5$ AU, and $n_H = 2 \times 10^8 \text{ cm}^{-3}$. The required ionizing photon luminosity from Equation 3.37, is $1.3 \times 10^{46} \text{ s}^{-1}$. Such a value, is not unreasonable for an excited WD ($T \sim 200,000$ K). In fact, the analysis of UV data by Mürset *et al.* (1991) has suggested that symbiotic hot components may have much higher luminosities, *e.g.* HM Sge: $L_{\text{ph}} \sim 2 \times 10^{48} \text{ s}^{-1}$.

The requirement for ionizing photons increases with increasing values of \dot{M}_2 and decreasing values of a . Since $n_H \propto a^{-2}$ (Equation 3.36), $\Delta \propto a$, and $R_1 \propto a$, it follows that $L_{\text{ph}} \propto 1/a$. For fixed m , L_{ph} increases with \dot{M}_2^2 since n_H increases linearly with \dot{M}_2 (Equation 3.36).

3.1.5 Model Images

Radio observations of unresolved CW sources yield only flux density measurements. When emission is resolved, additional quantitative information may be obtained including the total angular size of the emitting region, the angular size of the optically thick surface, and the interaction cone opening angle (Section 2.1.3). Physical models such as the STB and CW models permit the determination of densities and thicknesses of emitting regions for given sets of input parameters, and hence the associated intensity distribution may also be inferred (see Appendix B - “model imaging”). By matching observed images with model images, it is possible to place constraints on physical parameters including the mass loss rates, velocities, and the binary separation.

The distance from Earth of a given system may not be determined through model imaging in the context of the CWb model. When wind parameters are appropriately scaled, equivalent images may be produced at different distances. The mass loss

rates, \dot{M}_1 and \dot{M}_2 , scale with distance to the 3/2 power while the binary separation scales linearly with distance.

In Figure 3.7 a sequence of radio images is presented showing the morphologies expected in the context of the CWb model (thermal bremsstrahlung emission assumed). All of the system parameters have been held fixed, except for m , whose value is shown independently with each image. The fixed parameters are: $\dot{M}_2 = 3 \times 10^{-7} D_{\text{kpc}}^{3/2} M_{\odot} \text{yr}^{-1}$; $v_1 = 1000 \text{ km s}^{-1}$; $v_2 = 10 \text{ km s}^{-1}$; $a = 10 D_{\text{kpc}} \text{ AU}$; viewing angle = 90° . The viewing angle is defined as the angle between the line of sight and the line joining the two stars. Locations of hot and cool components are indicated in each image.

For large values of m in Figure 3.7 (*e.g.* upper left), the interaction cones sweeps strongly over the cool component (C-facing) giving an elongated, unipolar appearance. As m decreases, however, the interaction cone opens more widely giving rise to a crescent shaped morphology (upper right). For values of m which are smaller yet (*e.g.* lower left), the pressures from both winds become roughly equal and the distribution takes on a more linear, “bipolar” appearance. Further decreases in m result again in crescent shaped morphologies, with the sense of the curvature now inverted (lower right, H-facing). Flux densities in Figure 3.7 are found to be relatively insensitive to large changes in m .

The morphologies shown in Figure 3.7 will only be observed if the orbital period is sufficiently long. As an example, consider the model represented by the image in the lower left of Figure 3.7 ($m = 0.25$), assuming a distance of 1 kpc. The terminal interaction stream velocity is $\sim 130 \text{ km s}^{-1}$, implying that $\sim 30 \text{ yr}$ will be required for material to stream to the limits of observed emission, $\sim 0.''2$. Unless the orbital

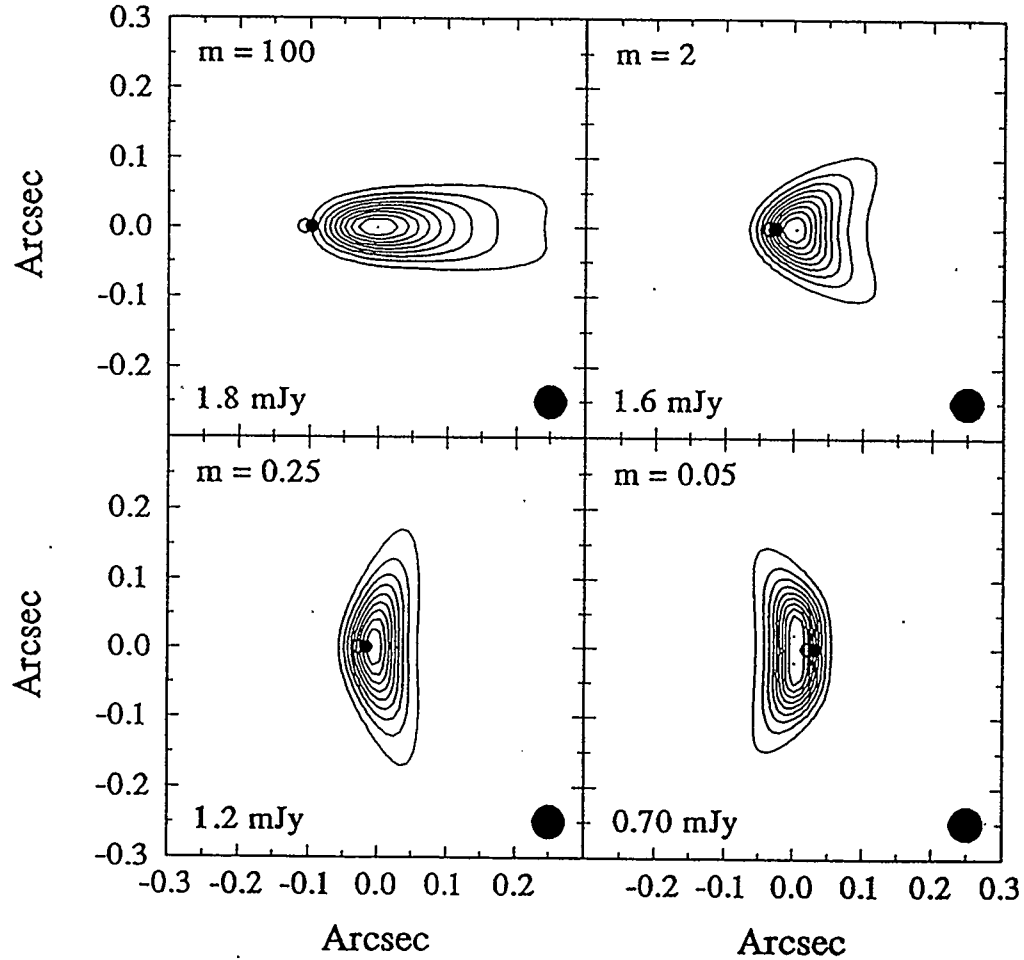


Figure 3.7: CWb Model Images

The sequence of model images above show the development of the radio structure at 5 GHz with decreasing m . Other parameters are fixed: $\dot{M}_2 = 3 \times 10^{-7} D_{\text{kpc}}^{3/2} [M_{\odot} \text{yr}^{-1}]$, $v_1 = 1000 [\text{km s}^{-1}]$, $v_2 = 10 [\text{km s}^{-1}]$, $a = 10 D_{\text{kpc}} [\text{AU}]$, viewing angle = 90° . The contour interval is 10% of the peak intensity. Images have been convolved with a $0.''05$ beam. The geometry factor, X_{cwb} , takes values of 4200, 84, 11, and 2.1 from left to right, top to bottom. Locations of hot (o) and cool (•) components are indicated.

period greatly exceeds 30 yr (D-type system), the predicted CWb morphology will be significantly altered by the orbital motion. The Orbital Colliding Winds (CWo) model, to be derived in Section 3.3, describes the morphologies which arise when orbital periods are much smaller than the evolutionary time scales of interest.

3.1.6 Model Spectra

Spectral information may assist greatly in constraining CWb model parameters of symbiotic systems. In fact, since most symbiotic systems are unresolved, spectral techniques are more generally applicable than those of model imaging.

Model CWb spectra are shown in Figure 3.8 for a model system which fits into the sequence of Figure 3.7 with $m = 0.2$. The spectral features characteristic of the model are well displayed in the spectrum for a viewing angle 0° . At low frequencies, the nebula is completely optically thick to its outer limit (100 binary separations), and therefore the spectral index has a value of 2. The low frequency turndown would not occur if the outer radius of the nebula were infinite. At intermediate frequencies, the outer regions are optically thin and the majority of emission arises from a central optically thick core whose size is frequency dependent; the spectral index has a value near 0.6 as expected for a $1/r^2$ density distribution (Wright and Barlow, 1975). At high frequencies, the spectral index takes a value of -0.1 as expected for an optically thin thermal bremsstrahlung source.

A comparison of the curves for viewing angles of 0° and 90° reveals significant differences, particularly at low frequencies. Not until complete optical thinness has been reached do the curves coincide. The viewing angle is a function of orbital phase, and therefore the CWb model would predict that variations in flux density should

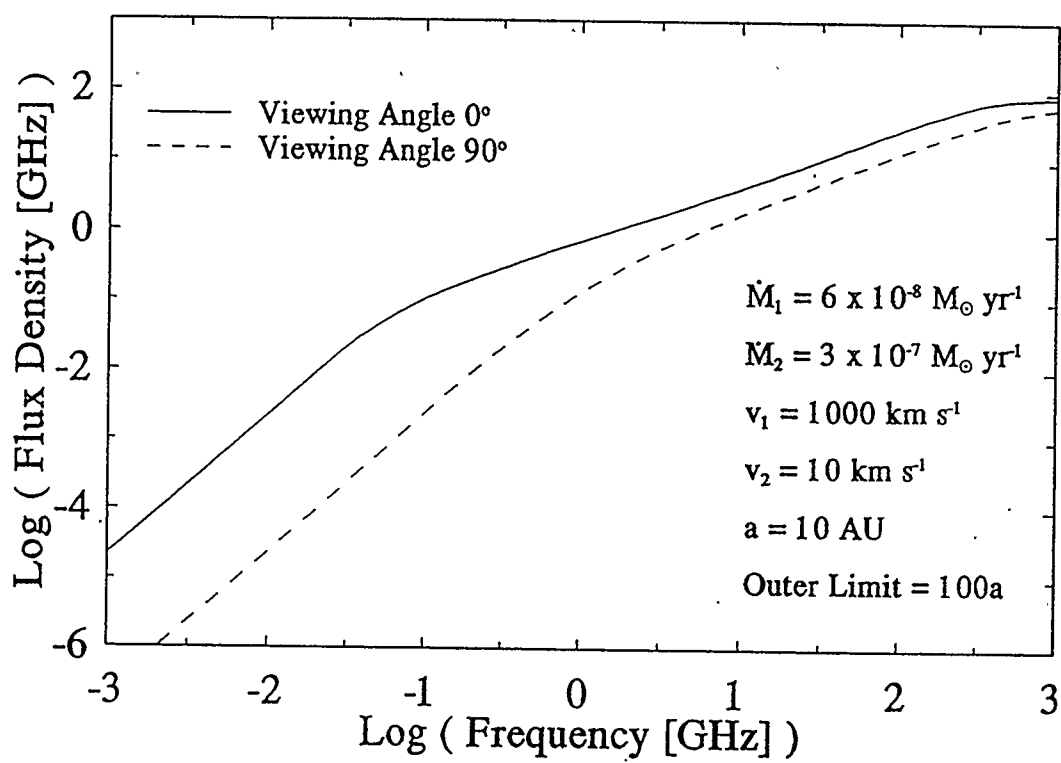


Figure 3.8: Spectral Variations with Viewing Angle

Model spectra for viewing angles of 0° and 90° are plotted, both corresponding to the system parameters indicated.

be observed over the orbital cycle even under steady state conditions. Further, since the spectral shape is also a function of viewing angle, variations in spectral index with orbital phase should also be observed.

The frequency of the optically thin turnover (*i.e.* high frequency turnover) is a strong indicator of system parameters. For the purpose of analysis, this turnover may be defined to occur at the point where the optical depth has a value of unity through the interaction cone apex for a viewing angle of 0° . This definition is equivalent to that previously applied to the STB model (Equation 2.4). The CWb turnover frequency is given by:

$$\nu_t = \left\{ \frac{0.21T^{-1.35}}{\mu_m m_H} \frac{1}{a(\delta_1 + \delta_2)} \left(\frac{q|_{\theta=0} \dot{M}_2}{av_2} \right)^2 \right\}^{1/2.1}, \quad (3.38)$$

where: T is the electron temperature; μ_m is the mean atomic weight of ions; m_H is the mass of a hydrogen atom; a is the binary separation; δ_1 and δ_2 are the dimensionless thickness parameters (Equation 3.35); $q|_{\theta=0}$ is the dimensionless surface density parameter at the static point (Equation 3.35); and \dot{M}_2 and v_2 are the mass loss rate and velocity from the cool component respectively.

3.1.7 Comparison with the STB Model

Before leaving the general discussion of the CWb model, a number of comparisons may be made with the STB model. In Figure 3.9, model STB and CWb flux densities have been plotted for systems with common values of \dot{M}_2 , and v_2 . Flux densities for the CWb model include only the emission from interaction regions and do not include the ionized component of the free flowing cool component wind. Hence the model STB and CWb curves do not converge in the limit of low m . The plotted

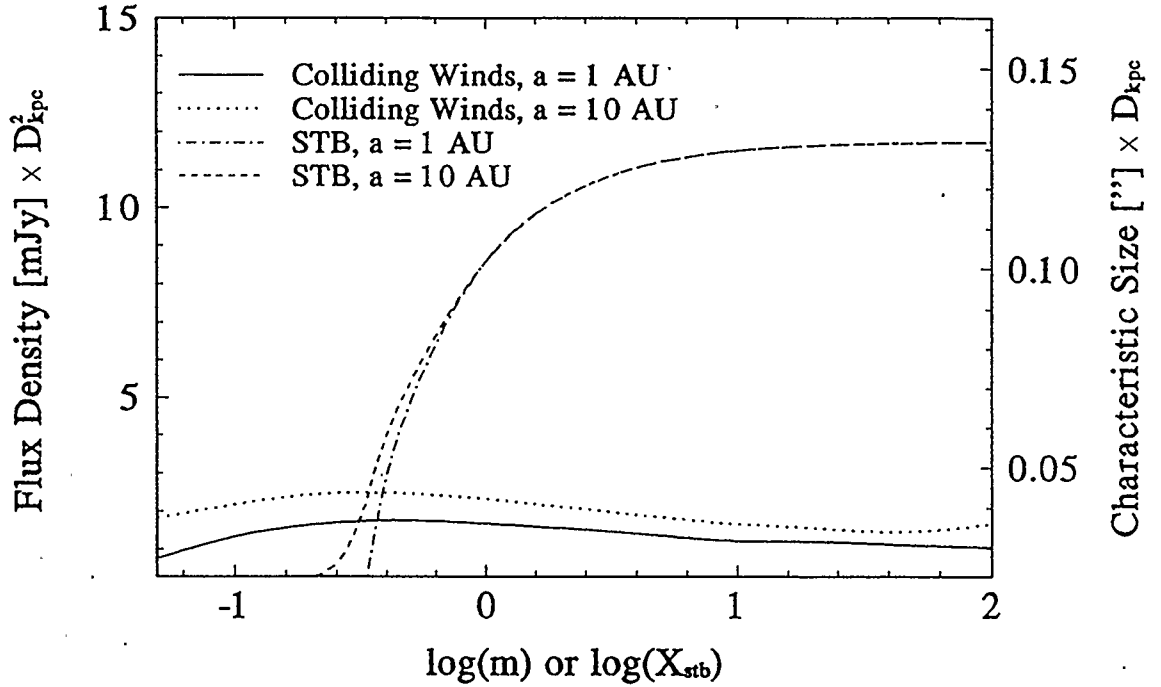


Figure 3.9: Flux Density Levels: CWb and STB Models

Model flux densities at 5 GHz are plotted against X_{stb} (STB model) and m (CWb model). The cool component in both models is assumed to have a mass loss rate of $3 \times 10^{-7} M_{\odot} \text{yr}^{-1}$ and a mass loss velocity of 10 km s^{-1} . The mass loss velocity for the hot component in the CWb model is assumed to be 1000 km s^{-1} . The right hand vertical axis gives an estimate of angular size assuming optically thick emission. A viewing angle of 0° has been assumed for both models.

values of flux density indicate that emission of the “STB type” strongly dominates that of the “CWb type” for reasonable values of the geometry factors, *i.e.* $X_{\text{stb}} \gtrsim 1$ and $m \lesssim 1$. The general inference is that STB sources are more likely to be detected than their CWb counterparts, and near STB sources are more likely to be resolved.

Curves are plotted for two different binary separations in Figure 3.9, *i.e.* 1 and 10 AU. In the range $1 < a < 10$, CWb flux densities increase significantly with increasing binary separation since the interaction apex becomes increasingly optically thin. This effect diminishes rapidly however for further increases in a , *e.g.* $a = 100$

AU gives $4/D_{\text{kpc}}^2$ mJy for $m = 1$.

The presence of a hot component wind in a symbiotic system should normally lead to the development of a CWb nebula, however this does not exclude the possibility of a coexisting STB nebula. In fact, the “turning on” of the hot component in outburst will be likely to increase the ionizing photon luminosity, thereby giving rise to a more extensive STB nebula. When CWb and STb phenomena coexist, the CW characteristics may dominate if the CWb nebula is strongly C-facing; the majority of the cool component wind would then be collected into the interaction stream. However, the hot component wind would have to persist over a long period of time in order to disrupt the large scale quiescent environment from which most of the STB flux density emerges at low radio frequencies.

The optically thin turnover in the symbiotic spectra offers a further means of comparing the STB and CWb models. Equations 2.4 and 3.38 indicate that the turnover frequency scales with $a^{-1/0.7}$ for both models. This inverse dependence is supported by observational statistics (Seaquist and Taylor 1990) which suggest that D-type systems (large binary separation, see Chapter 1) turn over to optical thinness at lower frequencies than their S-type counterparts.

Both models are able to reproduce the observed turnover for D-type systems at ~ 30 GHz, however the associated flux densities in the CWb model are relatively small. Consider a cool component with a mass loss rate of $1 \times 10^{-7} M_{\odot}\text{yr}^{-1}$ and a velocity of 10 km s^{-1} . For a binary separation 20 AU, which might be considered reasonable for D-type systems (Kenyon 1986), a value of $X_{\text{stb}} \sim 1$ would yield a turnover near 30 GHz. The associated ionizing photon luminosity would be $8 \times 10^{44} \text{ s}^{-1}$, which is of the order expected for a WD ($R_{\text{wd}} \sim 0.01R_{\odot}$) at a temperature of

$\sim 10^5$ K. The flux density provided by the STB model at this frequency is relatively high (Figure 3.9). To examine the predictions of the CWb model, a hot component mass loss velocity of ~ 1000 km s $^{-1}$ is assumed. A mass loss rate of $\dot{M}_1 \sim 3 \times 10^{-9}$, or equivalently $m = 0.03$, would be required to produce $\nu_t \sim 30$ GHz. At this value of m , flux densities in the CWb model are very low (Figure 3.9), and sources might therefore be difficult to detect.

3.2 Concentric Colliding Winds (CWc) Model

The interaction between the opposing hot and cool component winds will give rise to a CWb interaction as described in Section 3.1. As the hot component wind expands in a direction away from the cool component, a second interaction may occur as it overtakes the external cool component wind. For large nebular radii the two centers of mass loss may be considered essentially coincident, and hence the model which will be derived to describe this second interaction will be referred to as the “concentric colliding winds” (CWc) model.

The main characteristics of the CWc model, including nebular thicknesses and densities, have been previously discussed by Kwok, Purton and Fitzgerald (1978, KPF model). The aim of the next two subsections will be to reformulate the KPF equations in a manner consistent with that used for the CWb model. This reformulation will facilitate a combining of the CWb and CWc models in Section 3.3. Further, the formulation to be offered here will include a treatment of thermal pressures in the unshocked winds not considered by Kwok, Purton and Fitzgerald (1978). Conditions within the interaction shell will be described by average parameters, consistent with

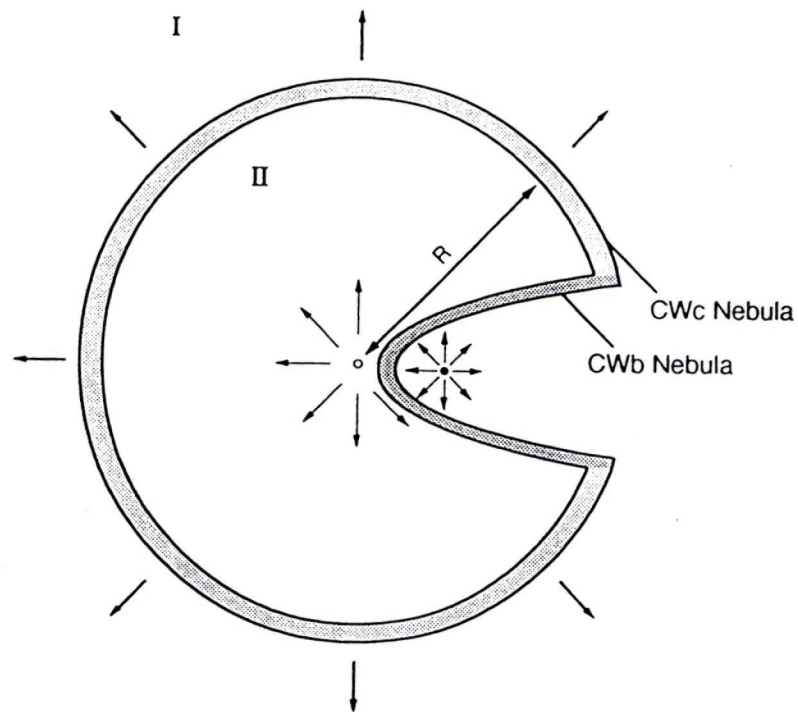


Figure 3.10: “Concentric” Winds in a Symbiotic System

The filled circle (●) in this schematic diagram represents the cool component, the source of a late-type wind, while the open circle (o) represents the hot component. The circumstellar environment (I) is constituted by mass lost by the cool component previous to the initiation of the hot component wind (II). A CWb nebula forms as the opposing winds meet. A CWc nebula forms as the fast wind overtakes the external cool wind.

the assumption of mixing of shocked material from both winds.

3.2.1 Shell Velocity and Location

In the CWc problem, the interaction shell quickly establishes itself at a constant outward velocity (Kwok, Fitzgerald and Purton 1978). The establishment of this equilibrium shell velocity is facilitated by the fact that the ram pressures governing the shell velocity are themselves functions of the shell velocity. The feedback mechanism is not fundamentally altered by the inclusion of thermal pressures in the component winds, and equilibrium shell velocities are still achieved.

Figure 3.11 illustrates the essential features of the model. Mass loss rates and velocities from the hot and cool components respectively are given by \dot{M}_1 and v_1 , and \dot{M}_2 , and v_2 . Expressions are given in the figure for the densities within the winds, ρ_1 and ρ_2 , at some arbitrary radius R . Between the winds, an interaction zone develops and is characterized by pressure, P , density, ρ , and temperature, T . The velocity of material entering the shell from the inside is $v_1 - v_s$, while that of material entering from the outside is $v_s - v_2$, where v_s is the shell velocity.

The rate at which mass enters the shell follows from the conservation of mass,

$$\begin{aligned} \dot{M}_s &= 4\pi R^2(v_1 - v_s)\rho_1 + 4\pi R^2(v_s - v_2)\rho_2 \\ &= \dot{M}_1 \left(1 - \frac{v_s}{v_1}\right) + \dot{M}_2 \left(\frac{v_s}{v_2} - 1\right), \end{aligned} \quad (3.39)$$

where the shell thickness has been assumed to be small compared to R .

The shell velocity, v_s , may be determined by requiring a balance of pressures from both sides of the shell in the comoving frame. The ram and thermal pressures of the

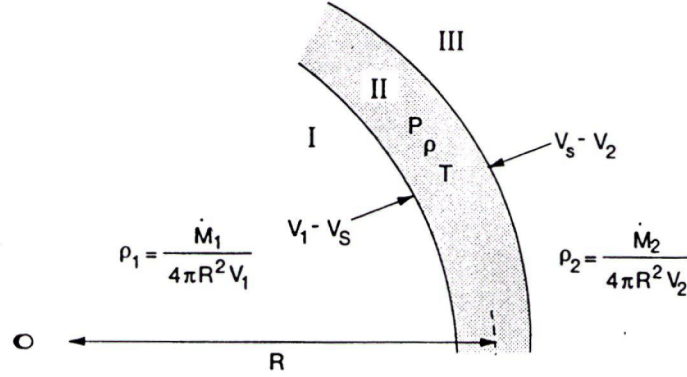


Figure 3.11: Concentric Shell in the Shell Frame

The frame of reference for this figure is at rest with respect to the interaction shell, *i.e.* moving outward at velocity v_s . Region I is filled by the hot component wind (v_1), and region III is filled with the remnant cool component wind (v_2). Region II is the interaction shell describable by average parameters P , ρ , and T (pressure, density and temperature). The velocity of material entering the shell from the inside is $v_1 - v_s$, and the velocity from the outside is $v_s - v_2$.

opposing winds are balance when:

$$\rho_1(v_1 - v_s)^2 + \rho_1 \left(\frac{kT_w}{\mu_a m_H} \right) = \rho_2(v_s - v_2)^2 + \rho_2 \left(\frac{kT_w}{\mu_a m_H} \right), \quad (3.40)$$

where μ_a is the mean atomic weight for all particles including electrons, m_H is the mass of a hydrogen ion, and T_w is the wind temperature. Solving for v_s in terms of the dimensionless variables m , w and b previously defined (Equation 3.26):

$$v_s = \frac{w}{w - m} \left(1 - m + \sqrt{\frac{m}{w}(w - 1)^2 - b \left(\frac{m}{w} - 1 \right)^2} \right) v_2, \quad (3.41)$$

which may be shown to agree with Equation (4) of Kwok, Purton and Fitzgerald (1978) when the thermal factor, b , is set to zero. Equation 3.41 fails when the thermal pressure from wind 2 exceeds the ram pressure from wind 1, *i.e.* the quantity in the square root becomes negative. This pathology occurs only when the hot component wind is diminished to negligible proportions. The direction of motion of

the interaction boundary is reversed under such a reduction, and the problem must be reformulated.

Using Equation 3.41 for v_s , the shell position is given by

$$R = v_s(t - t_o), \quad (3.42)$$

where t is time, and t_o is the hypothetical time at which $R = 0$, given the constant velocity v_s . Similarly, the mass of the shell is given by $M_s = \dot{M}_s(t - t_o)$ where \dot{M}_s is the total rate of mass accumulation within the shell (Equation 3.39). This latter equation assumes that R is much larger than the radius at which interaction was first initiated. Substituting for $t - t_o$ from Equation 3.42, the shell mass may be written as a function of shell position, *i.e.*

$$M_s = \frac{\dot{M}_s R}{v_s}. \quad (3.43)$$

Since both \dot{M}_s and v_s are constant for given flow parameters (Equations 3.39 and 3.41), it follows that the shell mass increases linearly with R .

3.2.2 Shell Thickness and Density

The density within the interaction shell may be determined from the requirement that thermal pressure support the shell from collapse. Equating the shell pressure to the inward pressure on the wind 2 side of the shell,

$$\frac{\rho k T_s}{\mu_a m_H} = \rho_2 (v_s - v_2)^2 + \frac{\rho_2 k T_w}{\mu_a m_H}, \quad (3.44)$$

where T_s is the shell temperature, T_w is the wind temperature and the ideal gas law has been assumed. Solving for the shell density in terms of dimensionless variables,

$$\rho = \left(\frac{(v-1)^2 + b}{b} \right) \left(\frac{\dot{M}_2}{4\pi v_2} \right) \left(\frac{T_w}{T_s} \right) \left(\frac{1}{R^2} \right). \quad (3.45)$$

Assuming a thin shell, this expression for density may be used along with the expression for the total shell mass (Equation 3.43) to derive a shell thickness, *i.e.*

$$\begin{aligned} \Delta &= \frac{\dot{M}}{4\pi R v_s \rho} \\ &= \frac{\dot{M}}{4\pi R v_s} \frac{k T_s}{\mu_a m_H \rho_2 (v_s - v_2)^2} \\ &= \frac{(mw - mv + vw - w)b}{vw[(v-1)^2 + b]} \left(\frac{T_s}{T_w} \right) R, \end{aligned} \quad (3.46)$$

where $v \equiv v_s/v_2$.

3.2.3 Shell Temperature

An adiabatic temperature may be derived for CWc geometry using the same approach as previously taken for the CWb case (Section 3.1.1). Once the adiabatic temperature has been derived, radiative cooling times will be examined in order to identify the domains of adiabatic and isothermal behavior.

Derivation of an Adiabatic Temperature

Consider a quasi-steady-state corresponding to some shell position R , in a frame of reference at rest with respect to the shell. The energy flux into the shell is given by the flux of kinetic and thermal energy contributed from each wind:

$$\begin{aligned}\dot{E}_{R,\text{in}} &= \frac{1}{2} \left[\dot{M}_1 \left(1 - \frac{v_s}{v_1} \right) \right] (v_1 - v_s)^2 + \frac{1}{2} \left[\dot{M}_2 \left(1 - \frac{v_s}{v_2} \right) \right] (v_s - v_2)^2 \\ &+ \frac{3}{2} k T_w \frac{\left[\dot{M}_1 \left(1 - \frac{v_s}{v_1} \right) \right]}{\mu_a m_H} + \frac{3}{2} k T_w \frac{\left[\dot{M}_2 \left(1 - \frac{v_s}{v_2} \right) \right]}{\mu_a m_H}.\end{aligned}\quad (3.47)$$

Within the shell, the energy is entirely thermal, and therefore the energy flux to the shell from the winds is given by

$$\dot{E}_{R,\text{out}} = \frac{3}{2} k T_{\text{adia}} \frac{\dot{M}_s}{\mu_a m_H}, \quad (3.48)$$

where the total shell accumulation rate, \dot{M}_s , is defined in Equation 3.39. The difference between the energy flux deposited by the winds, and the energy flux added to the shell may therefore be expressed,

$$\begin{aligned}\dot{E}_{R,\text{in}} - \dot{E}_{R,\text{out}} &= \frac{1}{2} \left[\dot{M}_1 \left(1 - \frac{v_s}{v_1} \right) \right] (v_1 - v_s)^2 \\ &+ \frac{1}{2} \left[\dot{M}_2 \left(1 - \frac{v_s}{v_2} \right) \right] (v_s - v_2)^2 \\ &+ \frac{3k\dot{M}}{2\mu_a m_H} (T_w - T_{\text{adia}}).\end{aligned}\quad (3.49)$$

Under the adiabatic approximation, the excess energy flux must be accounted for in the PdV work performed in compressing the shell. Proceeding as previously for the CWb model,

$$\begin{aligned}\dot{E}_{R,\text{in}} - \dot{E}_{R,\text{out}} &= P \frac{dV}{dt} - P_1 \frac{dV_1}{dt} - P_2 \frac{dV_2}{dt} \\ &= \frac{P}{\rho} \dot{M} - \frac{P_1}{\rho_1} \dot{M}_1 \left(1 - \frac{v_s}{v_1} \right) - \frac{P_2}{\rho_2} \dot{M}_2 \left(\frac{v_s}{v_2} - 1 \right), \\ &= \frac{k\dot{M}_s}{\mu_a m_H} [T_{\text{adia}} - T_w],\end{aligned}\quad (3.50)$$

where V is the volume of the shell, and V_1 and V_2 are the volumes contributed by the two winds before compression. Equating the two expressions for $\dot{E}_{R,in} - \dot{E}_{R,out}$ (Equations 3.49 and 3.50), the adiabatic temperature may be written:

$$\begin{aligned} T_{\text{adia}} &= T_w + \frac{2\mu_a m_H}{kM} \left\{ \frac{1}{2} \left[\dot{M}_1 \left(1 - \frac{v_s}{v_1} \right) \right] (v_1 - v_s)^2 + \frac{1}{2} \left[\dot{M}_2 \left(\frac{v_s}{v_2} - 1 \right) \right] (v_s - v_2)^2 \right\}, \\ &= T_w + 14.5 \left[\frac{m(w-v)^3 + w(v-1)^3}{m(w-v) + w(v-1)} \right] v_{2[\text{km s}^{-1}]}^2, \end{aligned} \quad (3.51)$$

where v is defined in the same way as in Equation 3.46. For $v_1 = 1000 \text{ km s}^{-1}$ and $v_2 = 10 \text{ km s}^{-1}$, adiabatic temperatures will exceed $\sim 10^6 \text{ K}$ for $m \gtrsim 1$. A precipitous drop in the cooling function occurs for temperatures exceeding 10^6 K (Figure 3.2), and therefore shells within this high temperature domain may not experience efficient radiative cooling.

Radiative Cooling

The characteristic thermal energy per particle under the adiabatic approximation is $(3/2)kT_{\text{adia}}$. If an element of shocked fluid is added to the interaction shell at time $t = 0$, the time by which it has cooled, t_c , may be determined from the expression,

$$\int_0^{t_c} \left(\frac{dE}{dt} \right) dt = \frac{3}{2} kT_{\text{adia}}. \quad (3.52)$$

The rate of energy loss per particle is given by $dE/dt = \Lambda/n_a$, where Λ is the cooling function [$\text{erg cm}^{-3} \text{ s}^{-1}$], and n_a is the number density of all particles within the shell (electrons and ions). Substituting for density (Equation 3.45) and shell radius (Equation 3.42),

$$\frac{dE}{dt} = \frac{\chi}{kT_s(t-t_o)^2}, \quad \text{where}$$

$$\chi \equiv \left(\frac{\Lambda/n_H^2}{16\pi} \right) \left(\frac{\dot{M}_2}{v_2} \right) \left(\frac{(v-1)^2 + b}{v^2} \right), \quad (3.53)$$

where Λ/n_H^2 is given in Figure 3.2, and T_s is the shell temperature. Equation 3.52 may be integrated using Equation 3.53 to give the cooling time for an element of mass added to the shell at radius R ,

$$t_c = \frac{3k^2 T_{\text{adia}} T_s R^2}{2\chi v_s^2 - 3k^2 T_{\text{adia}} T_s R v_s}. \quad (3.54)$$

“Effective” cooling of the shell will be defined to occur if the cooling time at R is smaller than the time required for the shell to accumulate an additional mass which is equal its mass at R . The condition for effective cooling may therefore be written as $R_c < 2R$, where $R_c \equiv v_s(t_c - t_o)$. Using this criterion and Equation 3.54, a critical radius, R^* , may be computed separating the domains of isothermal and adiabatic behavior:

$$\begin{aligned} R < R^*, & \quad \text{isothermal,} \\ R > R^*, & \quad \text{adiabatic,} \end{aligned}$$

$$\text{where } R^* = \frac{\chi v_s}{3k^2 T_{\text{adia}} T_s}. \quad (3.55)$$

This equation indicates that the shell behaves isothermally at very small radii, and becomes adiabatic only at larger radii where the density is too low to support effective cooling. In some cases, however, it will be shown that the initial isothermal

stage does not occur since the CWc interaction begins at $R \sim a$, where a is the binary separation.

In order to demonstrate the sensitivity of Equation 3.55 to the initial stages of interaction, suppose that a significant period of isothermal behavior has had the opportunity to occur. The material accumulated during this period will have cooled to the equilibrium temperature, and therefore the shell temperature, T_s in Equation 3.55, will be $\sim 10^4$ K. The cooling function (Figure 3.2) has a very high value ($\sim 2 \times 10^{-22}$ erg cm³ s⁻¹) at temperatures only slightly higher than 10^4 K, and hence it is possible to maintain effective cooling out to large radii (~ 2000 AU, dashed line in Figure 3.12).

Alternatively, suppose that new material entering the shell is not absorbed into an environment which has previously cooled. Cooling is then governed by the adiabatic temperature, *i.e.* $T_s = T_{\text{adia}}$ in Equation 3.55. When the value of T_{adia} exceeds 10^6 K, the cooling function is \sim two orders of magnitude less than in the neighborhood of 10^4 K (Figure 3.2). The transition to adiabatic behavior will then occur at greatly reduced radii, *i.e.* ~ 10 AU (solid line for $\log(m) > 0$, Figure 3.12). For D-type systems, whose binary separations may exceed 10 AU, the initial isothermal stage may therefore be bypassed.

Another class of CWc problems arises in Section 3.3 (CW_o model). In this case, the central “wind”, which interacts with the external cool component wind, is a mixture of contributions from both the hot and the cool components. The lower velocities associated with this central flow produce much lower adiabatic temperatures. Cooling is therefore normally efficient, and the isothermal approximation is generally appropriate.

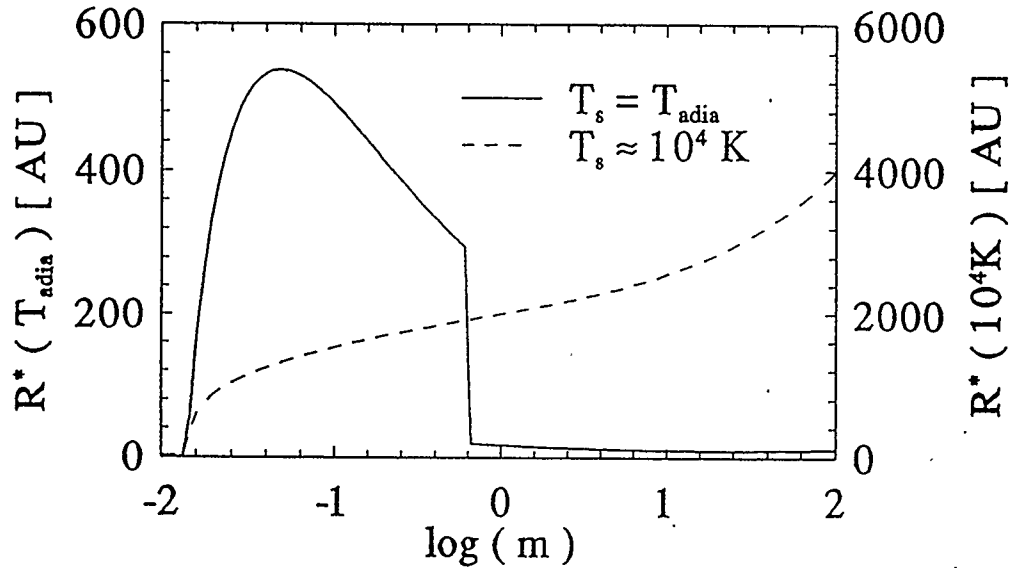


Figure 3.12: Critical Cooling Radii in the CWc Model

Model parameters are: $v_1 = 1000 \text{ km s}^{-1}$, $v_2 = 10 \text{ km s}^{-1}$, $\dot{M}_2 = 1 \times 10^{-7} M_{\odot} \text{ yr}^{-1}$. The parameter m is the ratio of hot component to cool component mass loss rates, *i.e.* $m \equiv \dot{M}_1/\dot{M}_2$. Results are plotted from Equation 3.55 for two values of T_s , as discussed in the text: T_{adia} - solid line, left axis; and 10^4 K - dashed line, right axis. For values of R exceeding the plotted values of R^* , the CWc shell will behave adiabatically. For values of R which are less than the plotted values of R^* , the CWc shell will behave isothermally.

3.2.4 Ionization

The requirements for ionization in the CWc model are expressed in Equation 3.37, previously applied to the CWb model. Unlike the CWb model however, the CWc shell properties do not represent a steady state, but rather change with time as the shell radius increases. For small values of shell radius, relatively large values of L_{ph} are indicated because of the high shell densities. Shock heating may, however, contribute to maintaining ionization at this stage.

For $\dot{M}_1 = 10^{-8} M_{\odot}\text{yr}^{-1}$, $\dot{M}_2 = 10^{-7} M_{\odot}\text{yr}^{-1}$, $v_1 = 1000 \text{ km s}^{-1}$, $v_2 = 10 \text{ km s}^{-1}$ and $R = 1 \text{ AU}$, the required value of L_{ph} is $1.8 \times 10^{45} \text{ s}^{-1}$. WDs with surface temperatures of $\sim 10^5$ will produce ionizing photon luminosities of this order.

3.3 Orbital Colliding Winds (CWo) Model

In this section, the implications of orbital motion upon the geometry of CW nebulae will be considered. The essential characteristics of orbital phenomena will be initially introduced in a qualitative discussion (Section 3.3.1). Expressions for physical quantities, including velocities, densities and linear dimensions, will then be derived (Sections 3.3.2, 3.3.3, and 3.3.4). Girard and Willson (1987) briefly discuss orbital phenomena in terms of particle trajectories, however, the development here is essentially original.

3.3.1 Qualitative Development

The complexity of orbital CW phenomena make it worthwhile to begin discussion from a qualitative point of view. The following discussion will begin by considering

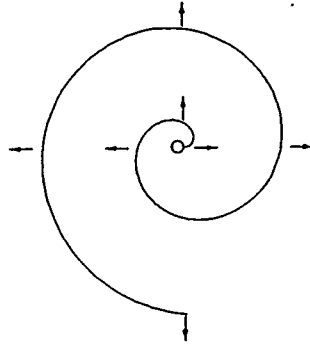


Figure 3.13: Global Morphology of a Rotating Jet Source

A binary system is depicted in which an infinitely thin stream is directed outward from the system center through one of the binary components. Because of the orbital motion, the global structure which develops on the orbital plane is that of an Archimedean spiral.

highly idealized configurations and will proceed to more physically realistic cases. In order to simplify the presentation, while including all of the essential features, C-facing nebulae will be assumed (*i.e.* the interaction cone will be assumed to sweep in the direction of the cool component).

Consider a CW system in which the interaction cone is so narrow as to constitute a unidirectional jet. If the ejecta were able to stream freely, the changing jet orientation with orbital phase would lead to an Archimedean spiral structure. (Figure 3.13). This structure is merely a global density pattern, each element within the stream is moving outward in an essentially radial direction. The tightness of the spiral, *i.e.* the spacing between arms, is determined by the outflow velocity and the orbital period.

It may also be useful at this point to consider, for later reference, the pattern which would develop if the rotating source includes two jets, separated by some angle, ϕ . The global density pattern would be that shown in Figure 3.14, *i.e.* a double spiral

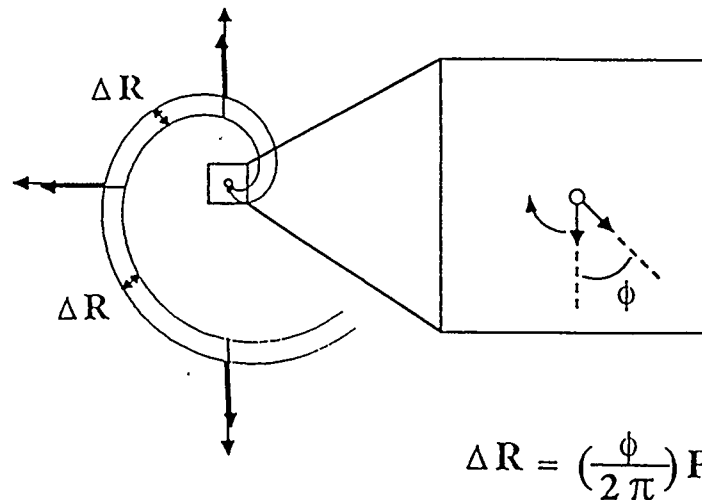


Figure 3.14: Rotating Dual Jet

A rotating dual jet source has axes of ejection separated by an angle ϕ . The resultant global pattern is that of a dual Archimedean spiral, as illustrated. Fluid elements within the spiral pattern move radially. The spacing between spiral arms is given by $\Delta R = (\phi/2\pi)Pv_s$, where P is the rotational period and v_s is the outflow velocity.

with constant spacing. The spacing between spiral arms of the two patterns is given by $(\phi/2\pi)Pv_s$, where P is the rotational period and v_s is the outflow velocity from the two jets.

Consider again the case of a single jet (Figure 3.13). The jet represents an infinitely narrow interaction cone, and so the interarm regions are filled with hot component wind, which is also moving in an essentially radial direction. The hot component wind will have a velocity in excess of that of the interaction stream, and hence the interarm regions will eventually become evacuated (Figure 3.15). The hot component wind from the interarm regions will accumulate in the spiral arms and the arms will be accelerated outward.

Consider now, an interaction cone of finite width. The three dimensional configuration in the neighborhood of the binary system is that shown in Figure 3.16.

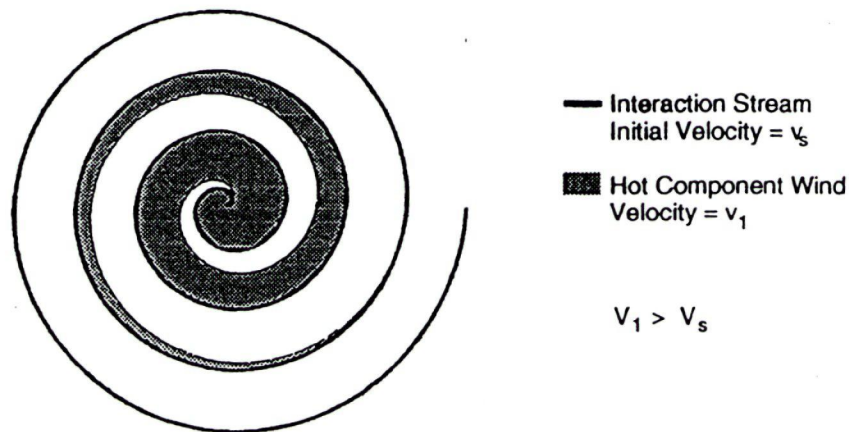


Figure 3.15: Evacuation of the Interarm Regions

The geometry in Figure 3.13 is reproduced here showing that the interarm regions are initially filled with hot component wind. As this wind overtakes the spiral arms, the interarm regions will become evacuated.

There exist three separate streams of material: the hot component wind; the cool component wind; and the interaction stream. In a cross sectional view on the orbital plane, the geometry shown in Figure 3.17 will exist. As shown, the hot component wind will act upon the inside edge of the interaction cone, causing it to collapse into a single wall. The cool component wind, originally enclosed within the cone, will also be merged into the wall. Therefore, at large separations, the structure shown in Figure 3.15 will be recovered. The “collapse” time of the interaction cone will be considered in Section 3.3.2.

In Figure 3.18, an idealized configuration is illustrated to assist in visualizing the global structure which develops off of the orbital plane. A rotating sphere is depicted in which mass is being ejected from a region of solid angle on the equatorial plane whose boundaries are lines of latitude and longitude. The effects of the hot component wind may be ignored for the time being, and instead it may be assumed

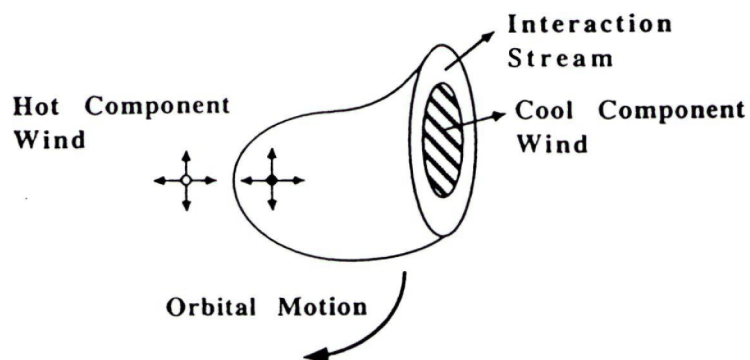


Figure 3.16: Finite Angle Interaction Cone in 3 Dimensions

The hot component is represented by an open circle (o) and the cool component is represented by a filled circle (•).

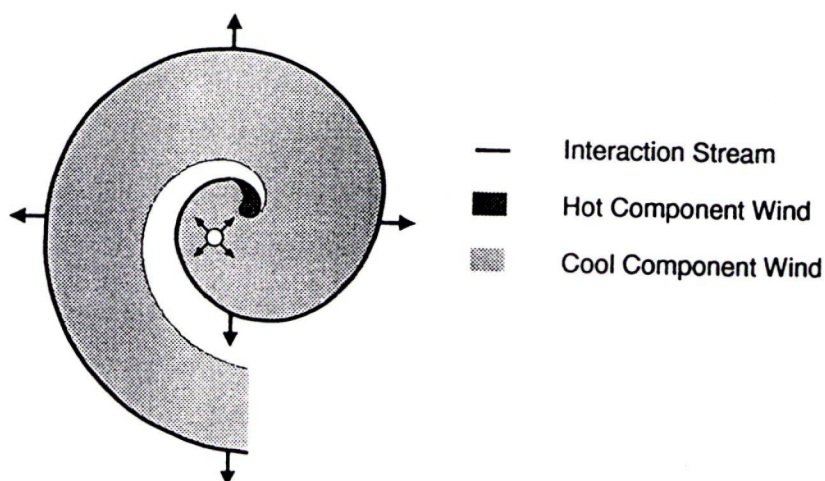


Figure 3.17: Global Development of Finite Angle Interaction Streams

If the interaction stream in Figure 3.15 is of finite opening angle, the interaction cone will enclose a component of free flowing cool component wind. The pressure from the free flowing hot component wind, however, will cause the cone to collapse to a thin wall containing all of the cool component mass loss.

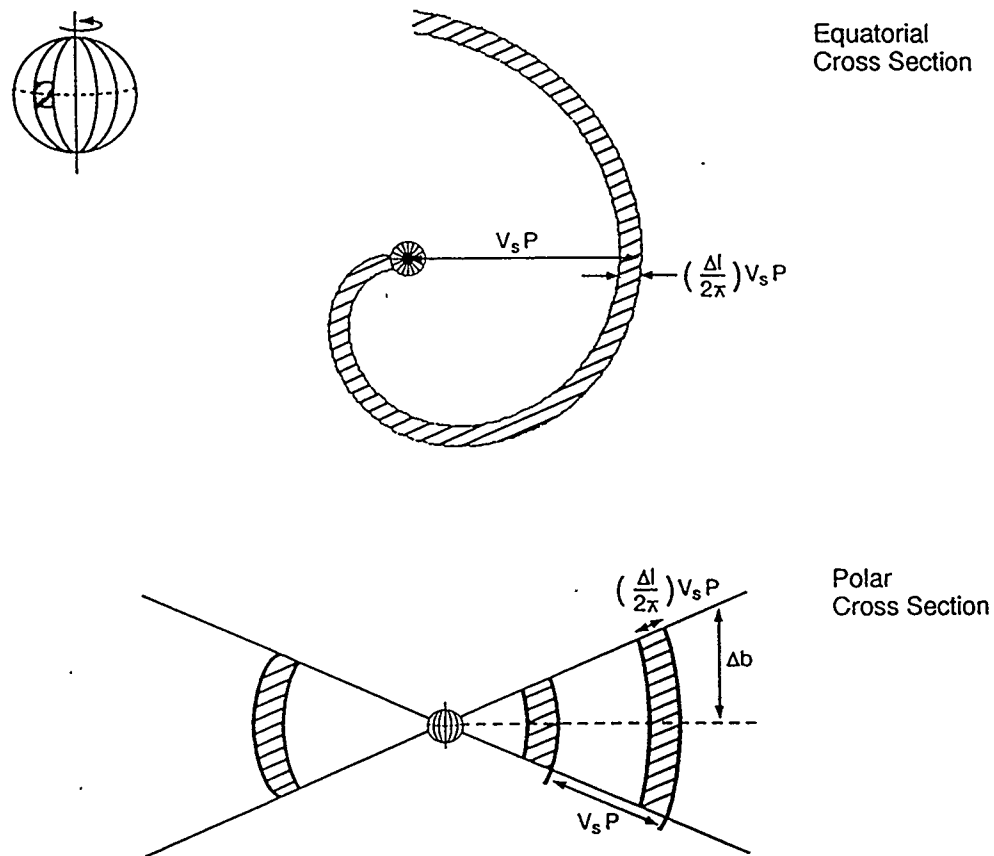


Figure 3.18: Three Dimensional Stream Morphology

A rotating sphere ejects mass at velocity v , from an element of solid angle, centered on the equator, with a width of Δl in longitude and Δb in latitude. Cross sections of the resulting mass loss pattern on the equatorial plane and in the polar direction are shown.

that all mass loss is confined within the limits of Δl in longitude and Δb in latitude (shaded region of the sphere illustrated in Figure 3.18). On the equatorial plane, an Archimedean spiral will develop as previously discussed. Expressions for the width and spacing of the spiral walls are shown in Figure 3.18 in terms of the stream velocity, v_s , the rotational period, P , and the element of longitude Δl .

Because the edges of the emitting solid angle are lines of longitude, the duration

of a “pulse of ejection” in a given direction will be the same at all latitudes. The spacing and width of the spiral walls will therefore be independent of latitude as shown in the polar cross section of Figure 3.18. The idealized shape of the emitting solid angle is also responsible for the “crisp” edges in Figure 3.18.

The idealized three dimensional configuration assumed in Figure 3.18 may now be generalized to more closely resemble a CW system. In CW geometry, the interaction stream will emerge from the edges of the mass emitting solid angle, and free flowing cool component wind will emerge from the interior of the solid angle. The remainder of the sphere will be the source of hot component wind. As in the two dimensional case, the hot component wind overtakes the spiral walls. As the interwall regions are evacuated, the walls are compressed, and the degree of compression depends strongly on the ratio of mass loss rates, $m \equiv \dot{M}_1/\dot{M}_2$. The interwall regions will eventually be refilled by thermal processes, as will be described in the next section. The density pattern consisting of spirally wrapped walls of compressed material will be referred to as a “CWo nebula”.

Further CW features may develop as the outflows come into contact with the external cool component wind, as shown in Figure 3.19. An “equatorial interaction belt” will form where the external wind is contacted by the CWo nebula, and polar interaction caps will form where the external wind is met by the free flowing hot component wind. A long standing problem in symbiotic star research concerns the observed existence of a large number of diverse regions of density and velocity in symbiotic nebulae. The present model offers a unified explanation for this diversity.

It will be recalled that discussion has been restricted to C-facing nebulae (*i.e.* the interaction cone is assumed to sweep in the direction of the cool component). For

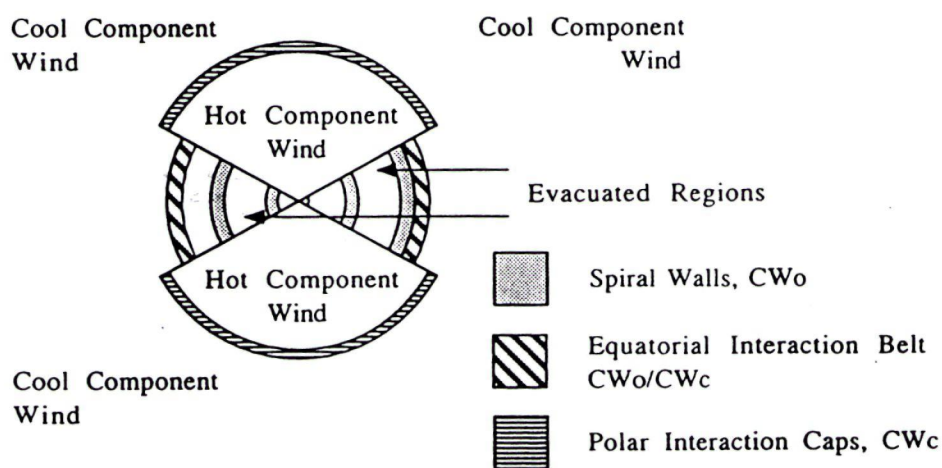


Figure 3.19: Features of the CWo Model

A polar cross section of the complete three dimensional stream morphology of a binary interacting winds system is shown. A simplified shape has been assumed for the interaction "cone" cross section (Figure 3.18).

H-facing nebulae, the structure which develops is somewhat simplified. The hot component wind will be confined to the equatorial regions and the polar directions will be filled with cool component wind. Therefore continuous cool component mass loss will occur in the polar directions without the interruption of wind interaction, *i.e.* no polar interaction caps will develop. The reduced importance of the hot component wind will also result in reduced compression of the spiral walls, a lower spiral stream velocity, and weaker interaction at the equatorial belt.

3.3.2 Spiral Wall Velocity

The radial velocity of the spiral walls in the CWo model may be determined from the conservation of momentum. The presence of orbital motion does not change the total radial momentum flux associated with the various flow components, and therefore the sum of momentum fluxes in the CWo model must equal the sum of momentum fluxes in the CWb model.

In the CWb model, three separate streams may be identified as shown in Figure 3.20: the free flowing hot component wind; the free flowing cool component wind; and the interaction flow. The interaction flow reaches an asymptotic cone angle, θ_a , so that all of the mass lost by star 1 into the solid angle defined by this cone becomes part of the interaction stream. Similarly, material lost from star 2 into the cone of angle $\pi - \theta_a$ is received into the same stream. The mass loss rates associated with the three flows, (hot, cool and interaction stream respectively), are given by:

$$\dot{M}_h = \frac{\dot{M}_1}{2}(1 + \cos\theta_a),$$

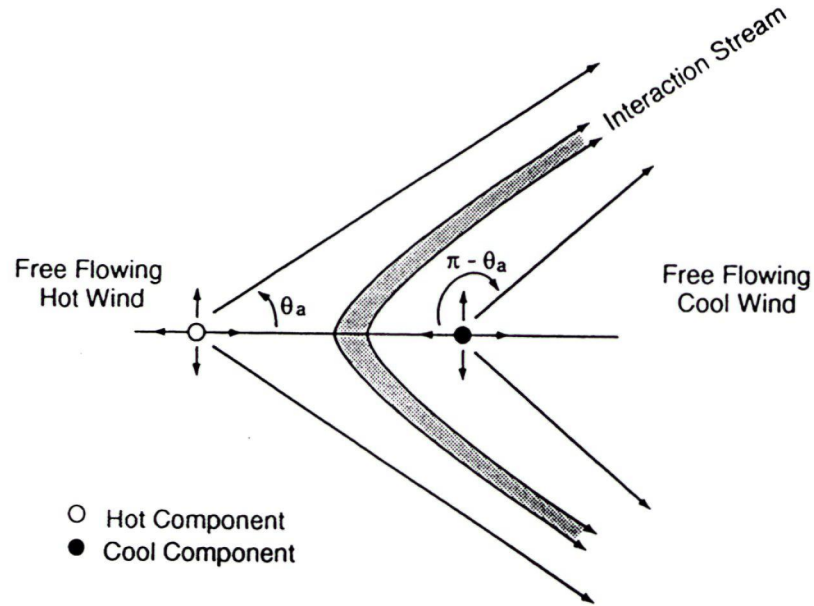


Figure 3.20: **Flow Separation in the CWb Model**

The flow from the inner system in the CWb model is separated into three components: free flowing hot component wind; free flowing cool component wind; and the interaction flow.

$$\begin{aligned}\dot{M}_c &= \frac{\dot{M}_2}{2}(1 - \cos\theta_a), \text{ and} \\ \dot{M}_s &= \frac{\dot{M}_1}{2}(1 - \cos\theta_a) + \frac{\dot{M}_2}{2}(1 + \cos\theta_a),\end{aligned}\quad (3.56)$$

where \dot{M}_1 and \dot{M}_2 are the total mass loss rates from the hot and cool components respectively.

In the CWo model, the C-facing ($\theta_a < 90^\circ$) and H-facing ($\theta_a > 90^\circ$) cases must be considered separately. In both cases, however, a quantity f may be defined as the fraction of the total solid angle subtended by the spiral stream,

$$f = \sin\theta_a. \quad (3.57)$$

Equating momentum fluxes from the CWb and CWo models,

$$\begin{aligned}
(1-f)\dot{M}_1 v_1 + (f\dot{M}_1 + \dot{M}_2)v_{\text{sp}} &= \dot{M}_h v_1 + \dot{M}_c v_2 + \dot{M}_s v_s, & \theta_a < 90^\circ, \text{C - facing,} \\
(1-f)\dot{M}_2 v_2 + (\dot{M}_1 + f\dot{M}_2)v_{\text{sp}} &= \dot{M}_h v_1 + \dot{M}_c v_2 + \dot{M}_s v_s, & \theta_a > 90^\circ, \text{H - facing}
\end{aligned}
\tag{3.58}$$

where v_{sp} is the steady state velocity of the spiral walls after absorbing all of the material in the interarm regions. Solving for v_{sp} ,

$$\begin{aligned}
v_{\text{sp}} &= \frac{\dot{M}_h v_1 + \dot{M}_c v_2 + \dot{M}_s v_s - (1-f)\dot{M}_1 v_1}{f\dot{M}_1 + \dot{M}_2}, & \theta_a < 90^\circ, \text{C - facing,} \\
&= \frac{\dot{M}_h v_1 + \dot{M}_c v_2 + \dot{M}_s v_s - (1-f)\dot{M}_2 v_2}{\dot{M}_1 + f\dot{M}_2}, & \theta_a > 90^\circ, \text{H - facing.}
\end{aligned}
\tag{3.59}$$

For H-facing geometries, $v_{\text{sp}} < v_s$. This implies that the near wall of the spirally wrapped interaction cone can never in fact reach the far wall in the way described in the previous section. Instead, the near wall will eventually be itself overtaken by the far wall of the next wrapping.

Nebular imaging of a CW nebula may reveal either CWb or CWo morphology, depending upon the object observed and the observing instrument employed. CWb morphology will be observed if less than one spiral wrapping occurs on the scale of detected emission. A critical period may therefore be defined, separating the domains in which CWb and CWo geometries will be observed, *i.e.*

$$P_{[\text{yr}]} \gg 4.75 \frac{\theta'' D_{\text{pc}}}{v_{\text{sp}}[\text{km/s}]}, \quad \text{CWb observed,}$$

$$P_{[\text{yr}]} \ll 4.75 \frac{\theta'' D_{\text{pc}}}{v_{\text{sp}}[\text{km/s}]}, \quad \text{CWo observed,} \quad (3.60)$$

where: P is the orbital period in years; θ'' is maximum angular radius, in arcsec, for which emission has been detected; D_{pc} is the distance to the system in parsecs; and v_{sp} is the terminal spiral velocity in km s^{-1} . For a system at .1 kpc, with a characteristic velocity of $v_{\text{sp}} = 200 \text{ km s}^{-1}$, CWo morphology will be observed at $1''$ for periods less than 24 yr. If angular scales are reduced to $0.''1$, CWo morphology will be observed for periods less than 2.4 yr. It follows that D-type systems may be observed with CWb or CWo morphology, while S-type are likely to be only observed with CWo morphology.

3.3.3 Spiral Wall Compression

The “steady state” configuration of a CWo nebula consists of a spirally wrapped series of compressed walls moving outward at a constant velocity. The degree of compression will vary as the walls move outward. If m is large, a highly compressed configuration may arise relatively rapidly and persist to relatively large separations. In all cases, the evacuated interarm regions will eventually be refilled due to thermal processes.

Consider a system with $\dot{M}_1 = 1 \times 10^{-7} M_{\odot} \text{yr}^{-1}$, $m = 1$, $v_1 = 1000 \text{ km s}^{-1}$, and $v_2 = 10 \text{ km s}^{-1}$. Derived parameters include: $\theta_a \sim 40^\circ$, $v_s \sim 130 \text{ km s}^{-1}$, and $v_{\text{sp}} \sim 400 \text{ km s}^{-1}$. For an orbital period of P , the interwall regions are evacuated of hot component wind on a time scale of $\sim 0.10P$, *i.e.* $(1 - \theta_a/\pi)Pv_s/(v_1 - v_s)$, and wall compression takes place on a time scale of $\sim 0.12P$, *i.e.* $(\theta_a/\pi)Pv_s/(v_{\text{sp}} - v_s)$.

The interarm regions are thermally refilled on a longer time scale of $\sim 30P$, *i.e.* $(1 - \theta_a/\pi)Pv_{sp}/v_{th}$, where v_{th} is the thermal velocity ($\sim 10 \text{ km s}^{-1}$ for hydrogen ions at 10^4 K).

If m is small, such that the CWb interaction is H-facing, relationships are altered: compressional processes occur more slowly; the competing effect of thermal refilling becomes more important; and $v_{sp} < v_s$ so that spiral walls from successive wrapping approach each other. If a value of 0.1 is used for m in the above example, spiral wall compression occurs on the time scale of $\sim 0.8P$, *i.e.* $(\theta_a/\pi)Pv_s/(v_{sp} - v_2)$, while the interwall regions are refilled on the time scale of $4P$. Note that v_2 has been used in place of v_s in the computation of compression time since the nebula is H-facing.

The effects of nebular compression upon the observed radio emission will now be considered. Once the steady state velocity has been achieved, the average density within a CWo nebula decreases outward with $1/r^2$ by the conservations of mass. The flow of mass in the spiral stream may be expressed as a “spiral mass loss rate”,

$$\begin{aligned} \dot{M}_{sp} &= f\dot{M}_1 + \dot{M}_2, & \theta_a < 90^\circ, & \text{ C - facing,} \\ \dot{M}_{sp} &= \dot{M}_1 + f\dot{M}_2, & \theta_a > 90^\circ, & \text{ H - facing.} \end{aligned} \quad (3.61)$$

It is useful to express the spiral mass loss rate by a density constant, A_{sp} . In defining this quantity it is assumed that the mass is consistently distributed throughout the region of the spiral walls according to a wind-like density law, *i.e.* $n_e = A_{sp}/r^2$, with

$$A_{sp} = \frac{\dot{M}_{sp}}{4\pi f v_{sp}}. \quad (3.62)$$

From a fluid mechanical point of view, A_{sp} is a useful average quantity, however, it may not be used immediately to compute optical depths since emission is enhanced by compression. The amount of enhancement may be expressed in terms of a “compression factor”, ϵ , which gives the ratio of the volume occupied within the spiral wall structure (after compression), to the total volume subtended by spiral wall structure. If an “apparent” density constant, A_a , is now be defined from the observed intensity distribution, it will be related to A_{sp} by the expression

$$A_a = \frac{1}{\sqrt{\epsilon}} A_{sp}, \quad (3.63)$$

as shown in Appendix C.

Suppose that observations are made in which images and spectral information suggests a $1/r^2$ density distribution. It is standard practice to express the inferred density constant in terms of a mass loss rate, $\dot{M}_a \propto A_a$. Equation 3.63, implies that the reported mass loss rate will exceed the actual value by a factor of $1/\sqrt{\epsilon}$. Various authors (*e.g.* Kenyon 1988c) have commented upon the fact that cool components in symbiotic systems appear to lose more mass than normal late-type stars. This discrepancy might be due in part to compressional processes as discussed here.

3.3.4 Interaction with the Remnant Cool Wind

Interaction of the spiral stream with the remnant cool wind results in an equatorial interaction belt (Section 3.3.1). In the C-facing case ($\theta_a < 90^\circ$), polar interaction caps are also produced. Both the polar and equatorial features are describable in terms of the CWc model. For the polar caps, the CWc model may be applied directly, and the resultant velocity, v_p , is given by Equation 3.41. For the equatorial

belt, the role of the hot component wind is assumed by the spiral stream, and the dimensionless parameters m and w must therefore be redefined:

$$\begin{aligned} m &\equiv \frac{\dot{M}_1}{\dot{M}_2} + \frac{1}{f}, & w &\equiv \frac{v_{\text{sp}}}{v_2}, & \theta_a &< 90^\circ, \text{ C - facing,} \\ m &\equiv \frac{\dot{M}_1}{f\dot{M}_2} + 1, & w &\equiv \frac{v_{\text{sp}}}{v_2}, & \theta_a &> 90^\circ, \text{ H - facing.} \end{aligned} \quad (3.64)$$

Using these identities, the velocity of the equatorial belt, v_o , may be computed from Equation 3.41.

The ion number densities of the polar and equatorial features, n_p and n_o respectively, may also be computed in accordance with the CWc model, *i.e.*

$$n_o = \frac{\rho_2(R_o)}{\mu_m m_H} \left(1 + \frac{(v_o - v_2)^2}{bv_2^2} \right), \quad \text{and} \quad (3.65)$$

$$n_p = \frac{\rho_2(R_p)}{\mu_m m_H} \left(1 + \frac{(v_p - v_2)^2}{bv_2^2} \right), \quad (3.66)$$

where $\rho_2(R_o)$ and $\rho_2(R_p)$ are densities within the cool component wind at distances R_o and R_p respectively, μ_m is the mean molecular weight of ions, and b is the thermal factor (Equation 3.26).

The mass accumulation rates for the equatorial belt and the polar caps, \dot{M}_o and \dot{M}_p respectively, may be determined from the flow rates and densities at the points of contact, *i.e.*

$$\dot{M}_o = f \left[\dot{M}_1 \left(1 - \frac{v_o}{v_{\text{sp}}} \right) + \dot{M}_2 \left(\frac{1}{f} - 1 + \frac{v_o}{v_2} - \frac{v_o}{fv_{\text{sp}}} \right) \right], \quad \theta_a < 90^\circ, \text{ C - facing,}$$

$$\begin{aligned}
&= f\left[\frac{\dot{M}_1}{f}\left(1 - \frac{v_o}{v_{sp}}\right) + \dot{M}_2\left(\frac{v_o}{v_2} - \frac{v_o}{v_{sp}}\right)\right], & \theta_a > 90^\circ, \text{ H-facing, and} \\
\dot{M}_p &= (1 - f)\left[\dot{M}_1\left(1 - \frac{v_p}{v_1}\right) + \dot{M}_2\left(\frac{v_p}{v_2} - 1\right)\right]. & (3.67)
\end{aligned}$$

The mass within the equatorial belt at a specified radius, R_o , is simply $M_o = \dot{M}_o R_o / v_o$, and similarly $M_p = \dot{M}_p R_p / v_p$. Thicknesses for polar and equatorial features, Δ_o and Δ_p , respectively, follow immediately from the derived masses and densities (Equation 3.65),

$$\begin{aligned}
\Delta_o &= \frac{M_o}{4\pi\mu_m m_H R_o^2 f n_o}, & \text{and} & (3.68) \\
\Delta_p &= \frac{M_p}{4\pi\mu_m m_H R_p^2 (1 - f) n_p}.
\end{aligned}$$

Chapter 4

OBSERVATIONS

4.1 High Resolution Radio Imaging

4.1.1 Previous Results

The modern study of radio stars began in the 1970s with the development of multi-antenna, phase stable, tracking interferometers (*e.g.* the NRAO 3 element array in Green Bank, West Virginia; the Westerbork interferometer in Holland). Previous to this time, instruments were generally in a developmental stage, and subsequent observations have not confirmed some of the results reported for radio stars (*e.g.* Hjellming 1988). During the 1980s, the NRAO VLA was able to provide much greater sensitivity and instrumental flexibility than had been previously possible. In the 1990s, a new generation of instruments has been built which will address new problems in stellar radio astronomy (*e.g.* MERLIN, AT). Access to these new instruments has motivated the present work.

Symbiotic stars are among the strongest and most frequently detected radio stars. Radio surveys of the class have been conducted by Gregory and Seaquist (1974), Bath and Wallerstein (1976), Wright and Allen (1978), and Feldman and Kwok (1979). Most recently Seaquist, Taylor and Button (1984) and Seaquist and Taylor (1990) have presented the results of comprehensive surveys at the VLA to a lower limit of flux density of ~ 0.5 mJy. The statistical properties of radio symbiotics as determined by these latter studies were discussed in Section 1.3.

Name	Angular Size (")	Type	Radio Variable?	Comment
V1016 Cyg	0.5	ejecta + wind	Y	symbiotic nova
AG Peg	1.5	ejecta?	Y	symbiotic nova
R Aqr	6.4	ejecta?	N	jet?
HM Sge	0.5	ejecta+wind	Y	symbiotic nova
CH Cyg	1.5	ejecta	Y	jet
RX Pup	0.25*	wind	Y	
RS Oph	0.2	ejecta	Y	recurrent nova
H1-36	5.0	complex+wind	N	
SS 96	0.17*	wind	N	
Hen 1383	4.0	ejecta?	Y	jet?

Table 4.1: Symbiotic Stars Previously Resolved at Radio Wavelengths
(From Taylor 1988 and references therein.)

Angular sizes have been measured at 6 cm except when marked with a “*”, which indicates 2 cm observations.

Observations of symbiotic stars have, in general, consisted of flux density measurements of unresolved objects. In table 4.1 published results for the few systems exhibiting resolved structure have been tabulated. Distinction is made in this table between emission apparently arising from stellar winds and from outburst ejecta. Wind-type systems present a smooth, featureless appearance and are characterized by an angular size which decreases with frequency as expected for a $1/r^2$ density distribution (Wright and Barlow 1975). Emission categorized as “ejecta” exhibits more complexity, and Taylor (1988) notes a strong tendency toward non-spherically symmetric structures with bilateral symmetry.

Modern radio interferometers are able to achieve higher angular resolution than

most current astronomical instruments, and hence radio images provide important constraints for models of symbiotic systems. They indicate the geometries and densities associated with radio emitting regions and are therefore strong indicators of the processes of nebular formation and evolution. Further, images facilitate the separation of emission into components arising from different processes. Images of AG Peg (*e.g.* Kenny 1989), for instance, have revealed features apparently corresponding to: 1) outburst ejecta; 2) a slow wind from the cool component; 3) a fast wind from the hot component; and 4) an interaction shell between the hot and cool component winds.

Radio imaging is also useful in interpreting the statistical properties of the general symbiotic population. The morphologies observed in resolved systems provide important clues to the morphologies which may exist in those systems which are beyond our present imaging capabilities. However, the extrapolation of observed properties to the general population must be undertaken with caution. Among the symbiotic stars resolved in radio emission (table 4.1), the outbursting systems (symbiotic and recurrent novae, and jet-like sources) are greatly over-represented. This is a selection effect due to the high intrinsic radio luminosities of outbursting systems, and the high velocities at which compact outburst ejecta is carried to large distances from the binary system.

4.1.2 Limitations of Resolution and Sensitivity

The limitations in sensitivity and resolution of radio imaging arrays may be understood in terms of the Rayleigh-Jeans Law. An optically thick, thermal source with a temperature of 10^4K (the approximate equilibrium temperature of a photoionized

gas) will have an angular size of:

$$\theta'' = \sqrt{\frac{S_\nu}{5.7 \nu^2}}, \quad (4.1)$$

where θ'' is the angular diameter of the source in arcsec, and S_ν is the flux density in mJy, observed at a frequency ν [GHz].

The resolution of a radio aperture-synthesis instrument is given by $\theta \sim \lambda/D$, where λ is the wavelength of observation and D is the diameter of the array. The maximum diameter of the VLA is 36 km, implying that the highest resolution achievable at 22.5 GHz is $\sim 0.''08$, or $\sim 0.''3$ at 5 GHz. Very few systems (~ 6) have been detected at 22.5 GHz, and of those detected at 5 GHz, most have flux densities < 1 mJy (Seaquist and Taylor 1990). Equation 4.1 indicates that optically thick sources of 1 mJy at 5 GHz will have an angular size of $\sim 0.''08$, a factor of 4 too small to be resolved at the VLA.

Current instrumental limitations are a matter not only of resolution but also of sensitivity. Sensitivity may be defined as the minimum flux density detectable within the FWHM of the array power pattern ("synthesized beam"). For a beam diameter of θ_b'' , the sensitivity required to detect an optically thick source, which is resolved and has an associated electron temperature of 10^4 K, is given by inverting Equation 4.1:

$$S_\nu = 5.7 \nu^2 \theta_b''^2. \quad (4.2)$$

As an example, consider a symbiotic system located at a distance of 1 kpc, whose radio emitting nebula has a characteristic diameter of ~ 10 AU. Imaging of such

systems would require a resolution of $\lesssim 0.''01$, and Equation 4.2 indicates that a sensitivity limit of $10 \mu\text{Jy}/\text{beam}$ would be required for detection if the source is optically thick. A signal to noise ratio of at least 10 is normally required for effective imaging and this implies that the required sensitivity must be $\lesssim 1 \mu\text{Jy}/\text{beam}$. Sensitivity of this order is only now being approached by the world's best instruments. Greater sensitivity still is required for optically thin sources since flux densities are decreased by a factor of τ (optical depth).

4.1.3 Instrumental Specifications and Calibration

The instruments used to obtain observations for this thesis included: the Very Large Array (VLA) in New Mexico; the Multi-Element Radio-Linked INterferometer (MERLIN) in the UK; and the Australia Telescope (AT). The specifications of the VLA were discussed by Kenny (1989, Section 2.4, pp. 68-71). The MERLIN and AT arrays will be briefly discussed here. This section will include a consideration of calibration techniques.

Multi-Element Radio-Linked Interferometer (MERLIN)

The MERLIN array has been in service since 1980 and is operated by the Nuffield Radio Astronomy Laboratories at Jodrell Bank. Over the last several years, the performance of the array has been greatly enhanced by improvements to its sensitivity (increase in bandwidth, cooled receiver systems, multi-bit correlation) and resolution (construction of a new 32 m telescope at Cambridge).

The observations reported here were made using six telescopes of the array: Deford, Cambridge, Knockin, Darnall, Tabley, and the Mark II telescope at Jodrell

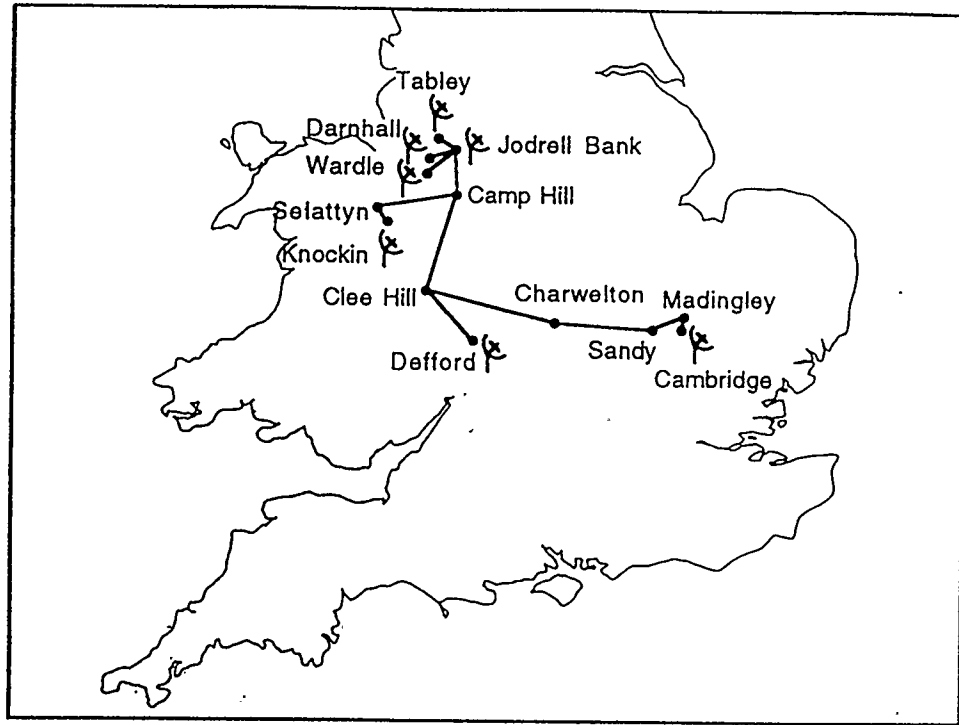


Figure 4.1: The MERLIN Array

Radio telescopes and repeater stations of the MERLIN array are shown along with their microwave links to Jodrell Bank.

Bank. Their geographical locations in Britain are shown in Figure 4.1. The effective aperture of the array is over 230 kilometers, providing a maximum resolution at 5 GHz of $0.''05$. At a given frequency, the resolution of MERLIN exceeds that of the VLA by almost an order of magnitude. The relatively small number of elements in the MERLIN array however requires that observations be made over a 12-24 hour period in order to obtain sufficient uv coverage for imaging. The rms sensitivity for such an observation is 30 - 40 $\mu\text{Jy}/\text{beam}$. The observations reported in this thesis could not have been undertaken with any instrument in the world previous to the recent MERLIN upgrades.

The telescopes of the array are of differing construction. The 25-metre dishes at Darnhall, Knockin and Tabley are made to the same design as the elements of the VLA. The Defford 26-metre telescope is an older instrument with a mesh surface. The Mark II telescope at Jodrell Bank has been in use since the mid 1960s and has a distinctively shaped elliptical bowl measuring 25×38 m. The parabolic surface profile, however, is the same in all directions so that a single focus is achieved. It was resurfaced in 1986 to permit operation at wavelengths as short as one cm.

The 32-metre telescope at Cambridge was designed specifically for the MERLIN array, and was completed in autumn 1990. The surface panels have been set into position to an accuracy of $\sim 300 \mu\text{m}$ rms, and further adjustment using holographic techniques may achieve $\sim 200 \mu\text{m}$ rms over a limited range of elevations. The pointing accuracy at night and in low wind conditions is better than $5''$. The Cambridge telescope is positioned at an extreme limit of the array, and its large collecting area therefore ensures that high sensitivity is achieved on the longest baselines.

The telescopes of the array are controlled centrally from Jodrell Bank. All receivers in the array are cooled to a temperature of 14 K to reduce noise and thereby increase sensitivity. The bandwidth employed at 5 GHz is 15 MHz. When radio astronomy signals are received at the various dishes they are in turn relayed to Jodrell Bank as microwave beams (whence "Radio-Linked"). At Jodrell Bank the signals are correlated by baseline to produce the raw visibility data.

The Australia Telescope (AT)

The recently commissioned AT has opened the southern hemisphere to synthesis imaging. This hemisphere possesses a superior view of the central galactic plane

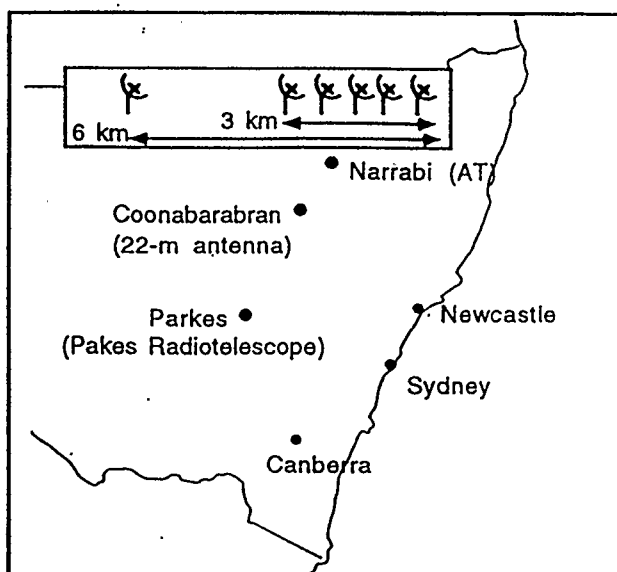


Figure 4.2: Radio Telescopes in Australia

The Australia Telescope (AT) is located just outside of Narrabri as shown.

where most symbiotic stars reside, and hence this instrument is particularly important for symbiotic research. In this thesis, the first radio images of four southern symbiotic systems are presented.

The AT is a six element E-W array located on the Australian continent approximately 500 km NW of Sydney as shown in Figure 4.2. The latitude and longitude of the array are -30° and 150° respectively. Five antennas are located on a 3 km rail track, and a sixth antenna is set in a fixed location 3 km further west. With a maximum baseline of 6 km, a resolution of $1''$ is obtainable at a wavelength of 3 cm. A sensitivity of $40 \mu\text{Jy}/\text{beam}$ may be obtained on a 12 hour observing track at 3 cm.

The array elements of the AT are 22 m in diameter and have a corresponding primary beam size of $5'$ at 3 cm. For continuum observations, a wide band of 128 MHz is used in bandwidth synthesis mode to improve both sensitivity and uv coverage.

Data is obtained on 32 channels across the band, and is concatenated during the calibration process.

Self Calibration/Phase-Referencing

For connected element, radio aperture synthesis arrays, observations of target sources are interspersed with observations of point source calibrators. For a point source, the true visibility amplitude on a baseline between antennas i and k , *i.e.* V_{ik} , is equal to the flux density of the source. The true visibility phase, ψ_{ik} , is zero. The amplitude and phase observed for the point source, Γ_{ik} and ϕ_{ik} respectively, may be used to assign gains in amplitude (g_i) and phase (θ_i) to each antenna,

$$\begin{aligned} V_{ik} &= g_i g_k \Gamma_{ik}, \text{ and} \\ \phi_{ik} &= \psi_{ik} + \theta_i - \theta_k. \end{aligned} \tag{4.3}$$

It has been implicitly assumed that all errors are antenna-based, and this is normally a reasonable approximation.

For a given baseline, the “coherence time” is defined as the time over which the antenna-based gains remain relatively constant. It should be noted that these gains include the effects of the Earth’s atmosphere between the source and the antenna, and therefore the coherence time generally decreases with increasing antenna separation. The coherence time at 5 GHz on the longest baselines at the VLA in “A” configuration is ~ 20 minutes, and that on the longest baselines of MERLIN ~ 5 minutes. The time between successive observations of calibrating point sources is chosen so as not to exceed the coherence time.

The difficulties in calibrating very long baselines have been commonly addressed by a processes referred to as “hybrid mapping” or “self calibration”. This technique makes use of the fact that the sum of observed visibility phases for baselines between any set of three antennas, *i.e.* the “closure phase”, $\Psi_{ijk} \equiv \phi_{ij} + \phi_{jk} + \phi_{ki}$, is independent of antenna-based phase gains. The closure phases may therefore be used as a means to determine the true visibility phases (or equivalently the antenna-based phase gains) and hence the target source may act as its own phase calibrator.

There do not exist enough closure phase relationships to close the system of equations for the antenna-based gains. It is therefore necessary to introduce additional constraints through the use of an initial “model”. If the input model is a reasonable representation of the true intensity distribution, the applied constraints of the closure phases will result in an image which is closer still to the true intensity distribution. The new map may then be used as the input model for a further iteration of self calibration, and the process normally converges rapidly to produce a final image. A parallel procedure for the determination of antenna based amplitude gains may also be employed. In this case, “closure amplitudes” are defined between every set of four antennas.

The weakness of stellar radio sources presents difficulties for the hybrid mapping (self calibration) technique. For the technique to work, it is necessary that the source have enough flux for a strong detection to be made on each baseline within a coherence time, and it is implicitly assumed that all departures from the model arise from antenna based errors. For ill-constrained observations, the technique will tend to collect randomly dispersed flux density into the source regions identified by the model (Wilkinson and Woodall 1991). Wilkinson (1989) demonstrates that this

effect is most pronounced when the number of array elements is low. For an array of 27 elements, the closure phases hold 93 % of the phase information, but for an array of 4 antennas, only 50 % of the phase information is held. For strong sources, where the signal to noise ratio is very high, the constraints imposed by the closure phases are strong, and the problem of collecting random flux density into model features is not serious. For weaker sources, such as symbiotic stars, significant errors may result.

Many of the difficulties associated with hybrid mapping of weak sources may be avoided by employing an alternative approach known as “phase referencing”. Here a strong source is selected in the vicinity of the target source to act as a calibrator. This source is to be self-calibrated, and therefore it is not necessary that it be a point source. However, it must be compact enough to produce a strong signal on all baselines. The process of hybrid mapping the calibrator results in the determination of amplitude and phase gains for the antennas, and this information may then be applied to the observations of the weaker target source.

At the VLA and the AT, phase referencing using point sources is a standard feature of calibration. Phase referencing has also become standard at MERLIN, however, the procedure here is generalized so that calibrators may be slightly resolved. In addition to the standard calibration, all VLA maps presented in this work have further been self-calibrated using the target source. Some AT maps have also been self-calibrated, however, because of the small number of antennas in the array (6), this technique could not be used reliably in every case.

4.1.4 Model Testing

A primary aim in imaging the circumstellar nebulae of symbiotic stars is to test models of radio emission. The simplest approach to this problem is to produce model images corresponding to various combinations of model parameters, and to compare these images to those observed. This will be the approach followed in testing the two physical models considered in this work: the STB model (Seaquist, Taylor and Button 1984); and the CW model (Chapter 3). A brief discussion of model imaging is given in Appx B.

An alternative approach which will also be applied to specific program stars is that of “visibility modelling”. In this case, model images are again produced, however they are then Fourier transformed to the visibility domain for comparison with the observed visibilities. The advantage of transferring the model intensities to the visibility domain, rather than transferring the observed visibilities to the intensity domain, is that the model intensities are mathematically defined and therefore do not suffer from the problem of finite sampling. Finite sampling of observed visibilities leads to a convolution of observed intensities by the “synthesized beam”, which confuses comparison to model intensities. Visibility modelling is best when models possess a large degree of symmetry, especially circular symmetry. The technique is also very useful when sources are only marginally larger than the synthesized beam.

4.2 Program Stars

4.2.1 Selection

Program stars were selected with a view to imaging previously unresolved circumstellar nebulae (Section 4.1.2). Equation 4.1 was used to establish the flux densities required for optically thick sources to be resolved for a given beam size. The requirements to resolve optically thin sources are slightly less restrictive. Optically thin sources will be larger than optically thick sources of the same flux density by a factor of $1/\sqrt{\tau}$, where τ is the optical depth.

The northern symbiotic stars selected for observation by MERLIN were: Z And, AG Peg, HM Sge, and V 1016 Cyg. Of these systems, only Z And had been previously unresolved. The remaining systems, although previously resolved at the VLA, possessed unresolved central components of emission which satisfied the selection criteria. The southern symbiotics selected for observation by the AT were: RR Tel, He 2-106, HD 149427 and BI Cru. None of these sources had been previously resolved.

4.2.2 Tabular Data

In order to facilitate a comparison between the program stars, published determinations of various system parameters are tabulated in this section. As a guide to the literature, Appendix D lists the alternative designations of each system.

The data appearing in the tables which follow is drawn primarily from results published between 1980 and 1992. Earlier and later published results have also been included when they were readily assessable. A format used in many of the tables is to quote parameters in terms of the minimum, maximum and average values appearing

Name		Right Ascension [1950]	Declination [1950]	b [°]
HM Sge	Optical	19 39 41.41 ±0.01	+16 37 33.0 ±0.2	-03.15
	This Work	19 39 41.41 ±0.007	+16 37 33.1 ±0.1	
V1016 Cyg	Optical	19 55 19.824 ±0.006	+39 41 29.38 ±0.07	+ 5.68
	This Work	19 55 19.821 ±0.009	+39 41 29.6 ±0.1	
AG Peg	Optical	21 48 36.19 ±0.07	+12 23 27.35 ±0.17	-30.89
	This Work	21 48 36.175 ±0.004	+12 23 27.29 ±0.06	
Z And	Optical	23 31 15.32 ±0.1	+48 32 31.6 ±0.17	-12.09
	This Work	23 31 15.294 ±0.004	+48 32 31.21 ±0.04	
BI Cru	Optical	12 20 40.3 ±0.1	-62 21 39 ±1	+00.06
	This Work	12 20 40.01 ±0.16	-62 21 38.2 ±1.1	
He 2-106	Optical	14 10 22.7 ±0.1	-63 11 45 ±1	-02.03
	This Work	14 10 23.06 ±0.16	-63 11 46.3 ±1.1	
HD 149427	Optical	16 33 37.68 ±0.03	-55 36 25.5 ±0.3	-05.77
	This Work	16 33 37.77 ±0.13	-55 36 25.4 ±1.1	
RR Tel	Optical	20 00 20.08 ±0.03	-55 52 02.9 ±0.2	-32.24
	This Work	20 00 20.22 ±0.13	-55 52 03.4 ±1.1	

Table 4.2: Positions of Program Stars

References for optical positions are as follows: HM Sge - Costa and Loyola, 1991; V1016 - Clements and Argyle, 1984; AG Peg and Z And - SAO Catalogue; BI Cru and He 2-106 - Kenyon, 1986; RR Tel and HD 149427 - Costa and Loyola, 1991. No corrections for proper motions have been applied.

in the literature consulted. In this way, the reader is provided with an estimate of the actual parameter values, as well as a sense of the accuracy with which such an estimate may be made (or the range of variability of the source). In computing averages, extremely high and low values have been ignored when they would of themselves have seriously altered the overall average.

Table 4.2 lists the optical positions associated with the program stars, as well as the radio positions measured in this work. The optical and radio positions agree to better than two standard deviations in all cases.

Table 4.3 lists published distances to the program stars. Because of the central importance of distances, estimates from all consulted references are listed individually. Although not all estimates are equally reliable, no effort has been made to discriminate between them on the basis of their quality. Distances to symbiotic stars are not in general well determined (Chapter 1), and table 4.3 shows that discrepancies by factors of two and three are common. The distances derived using Mira periods are generally in agreement other determinations. Note that discrepancies of factors of ten exist for HM Sge and V1016 Cyg.

As discussed in Chapter 1, a fundamental distinction appears to exist among symbiotic stars in their outburst classes (classical symbiotic stars, symbiotic novae, and recurrent novae) and infrared types (S, D and D'). The classifications of the program stars are listed in table 4.4. The program stars include a nonrepresentative predominance of symbiotic novae and D-type systems. Systems of these types are intrinsically bright in radio emission and were therefore more likely to meet the selection criteria described in the previous section. The system HD 149427 is unique in being a D' system or "yellow" symbiotic (Section 1.1).

Symbiotic stars of D-type have generally been found to contain Mira variables. This pattern is upheld among the program stars where, as shown in table 4.5, Miras have been detected for all D-type systems and for no S-type systems. Where Miras have been detected, their pulsational periods have been listed in table 4.5. Periods of single Mira stars range from ~ 50 to 750 days with the distribution peaking at ~ 200 days (Hoffmeister, Richter and Wenzel 1985, p.56). The distribution of symbiotic Mira periods peaks at a higher value of ~ 400 days (Whitelock 1988) and this fact is reflected in the values given in table 4.5. Whitelock (1988) points out that the

Name	Recent Distance Determinations [kpc]				Average [kpc]
HM Sge	0.4	1.0	1.8*	2.0*	
	0.5 - 2*	< 2*	2.1 [†]	1	
	0.5 - 3*	2*	2.3 [†]	1*	
	1.3*	2*	4*		1.7 ± 0.8
V1016 Cyg	0.6*	2.3*	3.4*	4.6*	
	2.3*	4.2 ± 1	6*	2.1*	
	3*	4.5	7	2.2*	
	3.3 [†]	10*			3.5 ± 1.6
AG Peg	0.5*	0.5*	0.6*	1.24*	
	0.5*	0.5 - 2.3*	0.6	1.3*	
	0.5	0.6*	0.8*	2.19*	0.89 ± 0.5
Z And	1*	1.12*	2.19*	0.6*	
	1*	1.23*			1.2 ± 0.5
BI Cru	2.0 [†]	2.0 ± 0.2*	4.4*	2.1*	
	3.8*	4.4 ± 0.8*			3.1 ± 1.1
He 2-106	2.3*	2.8 [†]	<7.76*	2.63*	
	< 3.5	> 4.1			3.0 ± 0.7
HD 149427	3.09	6.2	6.75		5.4 ± 1.6
RR Tel	1.65*	2.5 [†]	2.6	4.3*	
	2.4 [†]	> 2.5*	3.6*		2.8 ± 0.8

Table 4.3: Distances to Program Stars

From published values since ~1980. Methods of distance determination are indicated by superscripts: † - methods based on Mira variability; * - other methods requiring absorption estimates. References below are listed in the order given in the table above (left to right, top to bottom):

HM Sge: [267], [205], [149], [235], [37], [269], [311], [162], [293], [112], [222], [269], [129], [172], [182]

V1016 Cyg: [129], [28], [242], [242], [112], [4], [182], [149], [111], [160], [266] [217], [311], [3]

AG Peg: [232], [156], [129], [157], [157], [93], [97], [93], [47], [43], [8], [150]

Z And: [279], [81], [150], [129], [21], [245]

BI Cru: [311], [241], [189], [149], [241], [314]

He 2-106: [149], [311], [307], [105], [186], [203]

HD 149427: [106], [186], [203]

RR Tel: [149], [311], [229], [292], [72], [110], [45]

Name	Outburst Class	Outburst Year	IR Type	Spectral Class
HM Sge	Symb Nova	1975	D	M4-M9
V1016 Cyg	Symb Nova	1965	D	M3-M7
AG Peg	Symb Nova	1855	S	M1.7-M4
Z And	Classical	1910,1915,1939 1959,1969,1984	S	M0-M6.5
BI Cru	-	-	D	M
He 2-106	-	-	D	M
HD 149427	Classical	-	D'	M + (A-F)
RR Tel	Symb Nova	1944	D	M0-M5

Table 4.4: Outburst and Spectral Classifications

References for spectral classes:

HM Sge: [7], [12], [22], [108], [141], [147] [182], [248],

V1016 Cyg: [7], [12], [141], [147], [150] [182], [242], [248],

AG Peg: [7], [8], [12], [22], [38], [43], [44], [46], [47], [55], [61], [141], [147], [150] [157], [264], [248], [326]

Z And: [7], [12], [20], [21], [23], [43], [46], [54], [66], [81], [96], [122], [141], [147], [150], [245], [279], [325]

BI Cru: [7], [12], [141], [149], [248]

He 2-106: [7], [12], [105], [141], [248]

HD 149427: [12]

RR Tel: [7], [8], [12], [141], [248], [312],

higher average value arises due to the absence of short-period symbiotic Miras; she offers two possible explanations. Since pulsational periods are correlated with age (Feast and Whitelock, 1987) she suggests that binary systems may have been rare among older stars. Alternatively, she suggests that the short-period Miras, since they lose mass more slowly than their long-period counterparts (Schild 1989), may be less likely to be observed as symbiotic (lower accretion luminosity).

The final column in table 4.5 indicates further periodicities, either photometric or spectroscopic, which have been reported for the program stars. For AG Peg and Z And these periods are widely regarded as orbital periods.

The masses and radii of the stellar components are of central importance in understanding the status and evolution of symbiotic systems. Published values of these parameters for the program stars are listed in tables 4.6 and 4.7 respectively. Unfortunately, these quantities tend to be poorly determined, especially for the hot component. Quoted values of mass and radius for the cool component tend to be derived from spectral classifications. Quoted values of hot component radius tend to be derived from estimates of luminosity and temperature, both of which may be strongly affected by circumstellar reddening and extinction. Estimates of hot component mass may be derived from either orbital analysis, in the case of S-type systems, or from the mass-luminosity relationship for WD cooling curves, in the case of D-type systems (*e.g.* Mikolajewska and Kenyon 1992).

In table 4:8 temperature determinations are listed for the hot, cool and nebular components. For the stellar components, temperatures are important indicators of evolutionary status. Values quoted tend to be based upon spectral classification for the cool component, and are consistent with those expected for late-type stars. For

Name	IR Type	Mira?	Mira Period [d]	Other Periods Reported [d]
HM Sge	D	yes	540	-
V1016 Cyg	D	yes	460	2000, >7000
AG Peg	S	no	-	820
Z And	S	no	-	756
BI Cru	D	yes	280	-
He 2-106	D	yes	450	-
HD 149427	D'	?	-	-
RR Tel	D	yes	380	500, >4000

Table 4.5: Reported Periods

References for periods:

HM Sge: [14], [182], [208], [304], [311],

V1016 Cyg: [14], [24], [111], [182], [206], [218], [280], [302], [304], [303], [311],

AG Peg: [14], [34], [46], [55], [61], [83], [89], [96], [125], [124], [183], [184], [265]

Z And: [46], [81], [96], [153], [262], [279],

BI Cru: [14], [311], [314]

He 2-106: [14], [72], [149], [311], [312]

RR Tel: [14], [36], [72], [94], [114], [145], [311], [312]

Name	Hot Component Mass [M_{\odot}]	Cool Component Mass [M_{\odot}]
HM Sge	~ 1	1 - 4
V1016 Cyg	~ 1.1	~ 1.5
AG Peg	0.5 - 2	2 - 4
Z And	0.5 - 0.8	1 - 3

Table 4.6: Masses of Stellar Components

Values shown have been derived from results published since ~ 1980 . For the southern systems, the only mass estimates found were a value of $\sim 0.8 M_{\odot}$ for the cool component of BI Cru (Whitelock 1988), and a value of $\sim 0.7 M_{\odot}$ for the hot component of RR Tel (Calabretta 1982). References:

HM Sge: [105], [205], [267], [311],

V1016 Cyg: [52], [217], [218]

AG Peg: [52], [61], [93], [124], [158], [250]

Z And: [22], [52], [81], [325]

Name	Hot Component			Cool Component		
	Radius [R_{\odot}]			Radius [R_{\odot}]		
	min	max	ave	min	max	ave
HM Sge	0.04	2.0	0.4	140	290	220
V1016 Cyg	0.06	1.5	0.6	290	500	400
AG Peg	0.072	1.0	0.6	40	260	120
Z And	0.014	0.3	0.2	75	150	130
BI Cru	-	-	>0.4	-	-	31
He 2-106	-	-	-	-	-	-
HD 149427	-	-	-	-	-	-
RR Tel	0.070	0.17	0.1	-	-	410

Table 4.7: Radii of Stellar Components

Values shown have been derived from results published since ~1980.

HM Sge: [24], [50], [52], [64], [205], [209], [222]

V1016 Cyg: [4], [50], [52], [160], [217], [218] [209],

AG Peg: [43], [52], [61], [93], [96], [150], [156], [157], [158], [124], [209]

Z And: [21], [46], [52], [54], [81], [96], [150], [209], [279], [325]

BI Cru: [189], [241]

RR Tel: [50] [52], [113], [209],

the hot component, temperature estimates vary widely, but tend to exceed those expected for normal WDs or MS stars. Some heating process (*e.g.* nuclear shell burning, accretion) is therefore necessary (Section 1.4). Values of hot component temperature tend to be derived from the Zanstra method or variations of that technique.

Temperature estimates for the nebular component tend to be derived from spectral line ratios, and the values listed in table 4.8 indicate widely ranging results within any given system. The spread of values reflects the simultaneous existence of physically distinct nebular phases. Temperatures on the order of $\sim 10^4$ K are those expected for circumstellar gas at equilibrium in the presence of a hot ionizing source; this domain appears to be well represented among the program stars. Temperatures in excess of 10^6 K provide strong evidence for more energetic processes, *e.g.* eruption and/or wind interaction; not all systems exhibit evidence of this regime. Finally, a dust phase is observed in the nebulae of many systems, and is almost certainly associated with a shielded portion of the mass loss from the cool component. The dust phase is not substantial in the S-type systems, AG Peg and Z And, or in the D' system, HD 149427.

The nebular component is the focus of attention in the present work, and table 4.9 indicates previous determinations of nebular quantities. The estimates of nebular density are widely spread, again because of the existence of distinct nebular regimes. Low values, $\sim 10^4$ cm⁻³, are generally derived from radio emission, and correspond to ionized gas at large distances from the binary system. Very high values, $\gtrsim 10^{10}$ cm⁻³, are derived from UV and/or X-ray observations, and are likely to correspond to the dense region between the stellar components. In the STB model the high density regime would correspond to the ionization apex. In the CWb model, it

Name	Hot Component Temperature [K]			Cool Component Temperature [K]			Nebular Component Temperature [K]		
	Min	Max	Ave	Min	Max	Ave	Gas Min	Gas Max	Dust Ave
HM Sge	4.5×10^4	2.0×10^5	1.3×10^5	2000	2500	2250	8.0×10^3	1.7×10^7	840
V1016 Cyg	1.0×10^4	1.0×10^7	1.1×10^5	1000	3100	2260	8.0×10^3	1.2×10^7	540
AG Peg	1.2×10^4	1.2×10^5	5.2×10^4	2800	3730	3430	4.0×10^3	2.0×10^4	-
Z And	9.0×10^3	1.3×10^5	1.0×10^5	3200	5100	3550	7.8×10^3	2.6×10^4	-
BI Cru	-	-	$> 2.7 \times 10^4$	2250	3000	2530	-	-	750
He 2-106	-	-	3.6×10^4	-	-	2140	8.0×10^3	2.3×10^4	280
HD 149427	2.6×10^4	1.0×10^5	6.5×10^4	-	-	-	8.0×10^3	3.1×10^4	<500
RR Tel	1.4×10^5	2.0×10^5	1.6×10^5	2300	3000	2700	8.0×10^3	4.6×10^6	490

Table 4.8: Temperatures of Stellar and Nebular Components
Values shown have been derived from results published since ~1980.

HM Sge: [24], [37], [64], [88], [128], [149], [172], [173], [209], [222], [223], [205], [235], [269], [280], [293]

V1016 Cyg: [3], [4], [28], [149], [159], [160], [173], [175], [182], [206], [209], [213], [217], [223], [230], [242], [243], [250], [257], [280], [324]

AG Peg: [25], [43], [44], [47], [48], [51], [55], [93], [102], [103], [105], [133], [149], [150], [156], [157], [158], [209], [243], [250], [291]

Z And: [21], [46], [54], [81], [149], [150], [209], [243], [291] [298], [250], [325],

BI Cru: [149] [189], [241], [250], [314],

He 2-106: [149] [223], [231], [250],

HD 149427: [2], [106], [203], [231], [234], [296]

RR Tel: [19], [43] [72], [100], [113], [149], [173], [189], [209], [215], [229], [223], [250],

would correspond to the apex of the interaction cone.

Quoted values of mass loss rate in table 4.9 are derived predominantly from radio and infrared flux densities, and tend to range from $\sim 10^{-7} - 10^{-5} M_{\odot}\text{yr}^{-1}$. Mass loss determinations are complicated by the fact that both stellar components may be losing mass. Further, radio flux densities measure only the ionized component of mass loss, while infrared flux densities measure only the emission from small solid particles in regions where they are shielded from destruction. The lower mass loss estimates in table 4.9 are typical of late-type stars, while the higher estimates are reasonable for Mira variables. The S-type systems, which do not contain Mira variables, appear to have lower associated mass loss rates, as expected (Chapter 1).

Velocity domains are also listed in table 4.9. It is noteworthy that both high and low velocity domains have been identified for most of the program stars. High velocity estimates derive largely from P Cygni profiles of UV emission lines. Low velocity estimates arise more commonly from optical emission line profiles (*e.g.* $H\alpha$, [O III], [OI], [NII], [Ne III], [S III], Al II, Fe II). The existence of both high and low velocity domains for most of the program stars is not surprising from the point of view that selection has tended to favor outbursting systems. The low velocity domain is almost certainly associated with cool component mass loss, while the high velocity domain is likely to correspond to mass ejected by the hot component.

4.2.3 Observational Histories

Brief observational histories will now be given for the program stars. The treatment of each star will be commensurate with the extent of its published literature and the level of analysis undertaken in the present study.

Name	n_e		\dot{M} [$M_{\odot}\text{yr}^{-1}$]		v [km s^{-1}]	
	min	max	min	max	min	max
HM Sge	6.5×10^5	9.5×10^{11}	2×10^{-7}	1×10^{-5}	12	2 000
V1016 Cyg	3.2×10^6	1.3×10^{10}	3.1×10^{-7}	4×10^{-5}	15	1 400
AG Peg	1.3×10^4	4.7×10^{10}	9×10^{-8}	2×10^{-6}	15	2 000
Z And	1.3×10^7	1×10^{12}	3×10^{-8}	5×10^{-7}	26	300
BI Cru	-	-	2×10^{-5}	6×10^{-5}	300	460
He 2-106	-	1×10^{10}	-	$\sim 3 \times 10^{-6}$	-	-
HD 149427	8×10^9	9×10^{14}	-	-	-	-
RR Tel	1.6×10^5	3.2×10^{11}	6×10^{-6}	8×10^{-6}	100	865

Table 4.9: Nebular Density and Flow Parameters

Values shown have been derived from results published since ~ 1980 .

- HM Sge: [3], [7], [17], [24], [37], [50], [57], [64], [77], [88], [129], [149], [162] [172], [173], [205], [222], [223], [256], [247], [235], [267], [269], [300], [304], [306], [308],
- V1016 Cyg: [4], [7], [17], [22], [28], [50], [87], [88], [129], [141], [149], [159], [160], [210], [213], [217], [218], [223], [224], [236], [242], [247], [257], [266], [269], [304], [306], [308]
- AG Peg: [7], [43], [44], [55], [56], [91], [93], [103], [119], [125], [124], [129], [137], [149], [157], [158], [194], [195], [202], [209], [225], [228], [256], [257], [308], [326]
- Z And: [7], [21], [22], [46], [54], [81], [82], [129], [132], [209], [256], [279], [298], [308], [325]
- BI Cru: [149], [189], [241]
- He 2-106: [7], [149], [223], [256]
- HD 149427: [106], [296]
- RR Tel: [7], [110] [113], [149], [223], [229], [233], [256], [297],

RR Telescopii

The symbiotic nova RR Tel went into outburst in 1944. In less than a year, the photographic magnitude brightened from 14 to 7, and for the next five years the optical flux remained relatively constant. After this time, the system entered decline, and the initial increase of 2 magnitudes proceeded over a period of ~ 3 years. The subsequent decrease by another 2 magnitudes was even slower, requiring a further time of ~ 7 years. The system continues to decrease at the present time, and has not yet returned to its preoutburst brightness.

Feast *et al.* (1983b) note that the Mira component in RR Tel was quite unaffected by the outburst. Mira-type variations, with a period of 387 d, were observed previous to the outburst (Gaposchkin 1945), and have been rediscovered since the outburst in optical and infrared emission (Allen 1980a; Feast *et al.* 1983b). The stability of the Mira component provides convincing evidence that the eruption was associated with the hot component.

HD 149427

HD 149427 is not a well-studied object, and is not universally considered to be a symbiotic star. Webster (1966) and Glass and Webster (1973) included it among the "yellow symbiotics" since it was observed to exhibit an F-K spectral type in addition to nebular emission lines. Allen (1979) rejected the system from the symbiotic classification on the basis of its low excitation, but this did not prevent him from including it in a later list of symbiotic stars detected in infrared emission (Allen 1982). Allen 1984b classified the system as type D' (see Section 1.1) on the basis of dust emission below $3 \mu\text{m}$. The system is also included among symbiotic stars by

Hjellming (1981).

Recent work, especially that of Gutiérrez-Moreno, Moreno, and Cortés (1987), has emphasized the similarities of HD 149427 with planetary nebulae. Tylenda *et al.* (1989), however, reaffirm the symbiotic classification by the detection of weak absorption bands of TiO, suggesting the presence of an M-type star. If an M-type star is present, the G-type spectrum may originate in a disk or a wind surrounding the hot companion.

BI Crucis

BI Cru is a relatively well-studied system. It is variable in both the optical and the infrared, and exhibits a significant infrared excess at $10\ \mu\text{m}$. Infrared variations occur with a period of 280 d, justifying the classification of the cool component as a Mira variable (Allen 1974b; Whitelock *et al.* 1983). Emission lines in H I and Fe II are strong on all published spectra (Kenyon 1986), as expected for D-type systems. The emission line spectrum may also be variable: the strong He I and He II emission features reported by Henize and Carlson (1980), Stephenson and Sanduleak (1971) and Henize (1976) are not present in the spectra of Allen (1974b). The fact that the M star remains visible in periods of both high and low excitation suggests that the varying component is the hot star. P Cygni profiles were detected on a few lines by Henize and Carlson (1980) giving velocities of $\sim 450\ \text{km s}^{-1}$. Whitelock *et al.* (1983) also report P Cygni profiles, although corresponding velocities are much lower ($\sim 200\ \text{km s}^{-1}$).

BI Cru is peculiar in a number of respects. For instance, it exhibits various optical absorption features not normally observed among D-type systems (*e.g.* Na I,

Ca II, TiO; Allen 1974b). Further, the absorption bands in H₂O, normally present in Mira variables, are not observed; this absence may be related to the relatively short period of the Mira component (*e.g.* Roche, Allen and Aitken 1983). More unusually, BI Cru is distinguished as one of the very few systems for which maser emission has been detected: OH maser emission is reported by Norris *et al.* (1984), and the possible detection of SiO maser emission is reported by Hall *et al.* (1987). Finally, BI Cru is the only symbiotic system in which CO (2.3 μm) emission is observed (*e.g.* Whitelock *et al.* 1983).

He 2-106

He 2-106 was one of the first systems in which the existence of a Mira variable was firmly established through the periodicity of optical and infrared variations. Feast *et al.* (1983a) derive a period of about 400 d, but Whitelock (1987) refine this estimate to 450 d. The optical spectrum of Allen (1980a) shows very strong emission lines, typical of D-type systems, and the system was also detected by the IRAS satellite (Stenholm and Acker, 1987). Schulte-Ladbeck *et al.* (1990) have observed that the system has a large intrinsic optical polarization $\sim 2\text{--}2.5\%$ with a peculiar wavelength dependence. Broad “unidentified” emission bands, perhaps associated with a disk, are observed at 6830 Å (*e.g.* Allen 1983).

Z Andromedae

Z And has served as the archetype of the class of symbiotic stars since the spectroscopic analysis by Hogg (1932) initiated the study of “stars with combination spectra”. The predominant features in its optical spectrum are those typical of classical, S-type symbiotics, *i.e.* : the continuum of a cool star; bright hydrogen emission

lines; TiO absorption bands at 4762, 5167, 5448, 5862, 6249, 5550, and 7125 Å; and a Balmer discontinuity of ~ 1 mag in emission. The optical emission line spectrum suggests two distinct sources: a stellar component (Mg II, Fe II, Ti II); and a nebular component (He II, N III, [O III]). The UV spectrum is rich in emission lines, with excitation ranging from O I and Mg II up to N V, O V and Mg V. The UV continuum is strong, and rises toward shorter wavelengths. The IR continuum is like that of a normal M giant with some evidence of excesses at 10 and 20 μm . The very strong CO absorption band at 2.3 μm may suggest that the late-type star is of luminosity class II rather than III.

Z And's optical light curve is dominated by 2-3 mag outbursts, five of which have been recorded since 1888. Each outburst was observed to persist for ~ 7 years, and to develop according to the same general pattern. This pattern begins with a slow increase in brightness from $V \sim 10.5 - 11.0$ to $V \sim 9.5$, is followed by a more rapid rise to visual maximum ($V \rightarrow 9$ or 8 mag), and concludes with a slow decline. The B-V and U-B colors increase with increases in V.

Oscillations in the light curve with a period of 757 d are observed both in outburst (0.5 - 1.0 mag) and in quiescence (0.2 - 0.3 mag). Many authors interpret these oscillations in terms of orbital motion (*e.g.* Kenyon 1986, Wallerstein *et al.* 1991, Mürset *et al.* 1991). It has also been noted that large variations in emission line strengths and in the Balmer continuum occur during periods when the red continuum and TiO bands are essentially constant. This fact has led some authors to suggest that the system may be eclipsing (*e.g.* Kenyon 1986).

It is possible that Roche lobe overflow occurs in the Z And system. If the cool component is of luminosity class II (*e.g.* Kenyon 1986, Garcia and Kenyon 1988,

Taranova and Yudin 1986, Seal 1990), it would typically have a radius of $\sim 150 R_{\odot}$. For an orbital period of 757 d (Garcia and Kenyon, 1988), the cool component would then overflow its Roche lobe for reasonable hot component masses (*i.e.* 0.5 - 1 M_{\odot}). The hypothesis of Roche lobe overflow is consistent with the UV observations of Wallerstein *et al.* (1991), which suggest the presence of an accretion disk, and the absence of wind interactions.

The temperature of the hot component in Z And has not been well determined. Altamore *et al.* (1981) fitted the UV continuum between 1200 and 2200 Å with a 43,000 K blackbody of radius 0.26 R_{\odot} . Kenyon and Webbink (1984), however, find it impossible to reconcile such a low temperature with the Balmer continuum at wavelengths exceeding 2200 Å. They therefore favor a hot component temperature of $\sim 100,000$ K (see also Viotti *et al.* 1982, Boyarchuk 1975).

The most recent outburst of Z And is described by Fernández-Castro *et al.* (1995). The outburst began in March 1984 and was characterized by a brightening in the visual range by about one magnitude over typical quiescent values (Mattei and Bortle, 1984). IUE observations during the outburst are interpreted by Fernández-Castro *et al.* (1995) in terms of two separate ejection events (April 1984 and December 1985) with velocities of 250 - 300 km s⁻¹.

AG Pegasi

Kenny (1989) provides a detailed review of AG Pegasi, as well as an analysis of recent radio observations. The review offered here will therefore be brief, and the interested reader is referred to the earlier work.

AG Pegasi is one of the few symbiotic systems for which binarity has been firmly

established through the detection of both periodic radial velocity variations, and a strong UV continuum. The orbital period associated with the system is ~ 820 d (Hutchings *et al.* 1975; Garcia and Kenyon 1988). The stellar components consist of an M3III giant ($M \sim 3 M_{\odot}$, $R \sim 75 R_{\odot}$: Hutchings *et al.* 1975, Schulte-Ladbeck 1988) and a hot component of mass $\sim 1 M_{\odot}$ (Hutchings *et al.* 1975). The cool component is unlikely to fill its Roche lobe (*e.g.* Keyes and Plavec, 1980a; Garcia and Kenyon, 1988).

AG Pegasi is a symbiotic nova system and is currently in decline from an eruption which began ~ 1850 . The outburst resembled a nova eruption both spectroscopically and photometrically (Kenyon 1986), however the system has evolved on the time scale of hundreds of years rather than hundreds of days. The present visual magnitude of the system ($V \sim 8.6$ mag) is only slightly enhanced over the pre-outburst level ($V \sim 9$ mag).

In addition to the major outburst beginning in ~ 1850 , a secondary outburst was initiated ~ 1940 as shown in Figure 4.3. The 1940 flare-up of ~ 1.0 mag was accompanied by changes in the spectrum as well. The spectroscopic temperature decreased to a minimum of ~ 6000 K by visual maximum in 1946, increased thereafter to $\sim 10^4$ K by 1952, and by ~ 1959 had resumed its slow decline (Archipova and Dokachaeva 1962). Merrill (1951a,b) noted rapid variations in the displaced absorption-line components of He I during the 1940 flare-up, and suggested that they might be associated with eruptive prominences.

Kenny, Taylor and Seaquist (1991) identify four components of nebular radio emission as shown in Figure 4.4: an unresolved central source of diameter $< 0.''1$; an inner nebula with diameter of $2''$ and mass $\sim 3 \times 10^{-5} M_{\odot}$; an intermediate

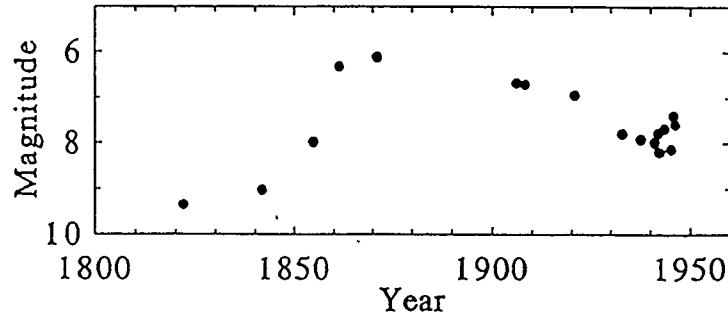


Figure 4.3: AG Pegasi: Outburst Light Curve in Visual Magnitudes
(Data from Merrill, 1959a.)

nebula with a diameter of $\sim 15''$ and mass of $10^{-4} - 10^{-3} M_{\odot}$; and an outer bipolar nebula with an extent of $\sim 1'$ and a mass of $10^{-5} - 10^{-4} M_{\odot}$. The outer nebula is interpreted as the remnant of the 1850 ejection, with the intermediate nebula representing the pre-outburst mass loss from the cool component. Since the system is known to possess a high-velocity wind in the present epoch (Penston and Allen 1985), the unresolved feature is thought to be associated with this wind in some way (*e.g.* Seaquist and Taylor 1992). The properties of the inner nebula are consistent with those expected for an interaction shell between the hot component wind and the remnant cool component wind (Kenny 1989).

HM Sagittae

HM Sge is of particular importance to the class of symbiotic stars. As the most recently erupted symbiotic nova, it is one of few systems whose nova-like behavior has been monitored with modern instruments. HM Sge brightened by ~ 5 mag ($m_v \simeq 16$ to 11) over a period of 5 months between September and April in 1975 (Dokuchaeva

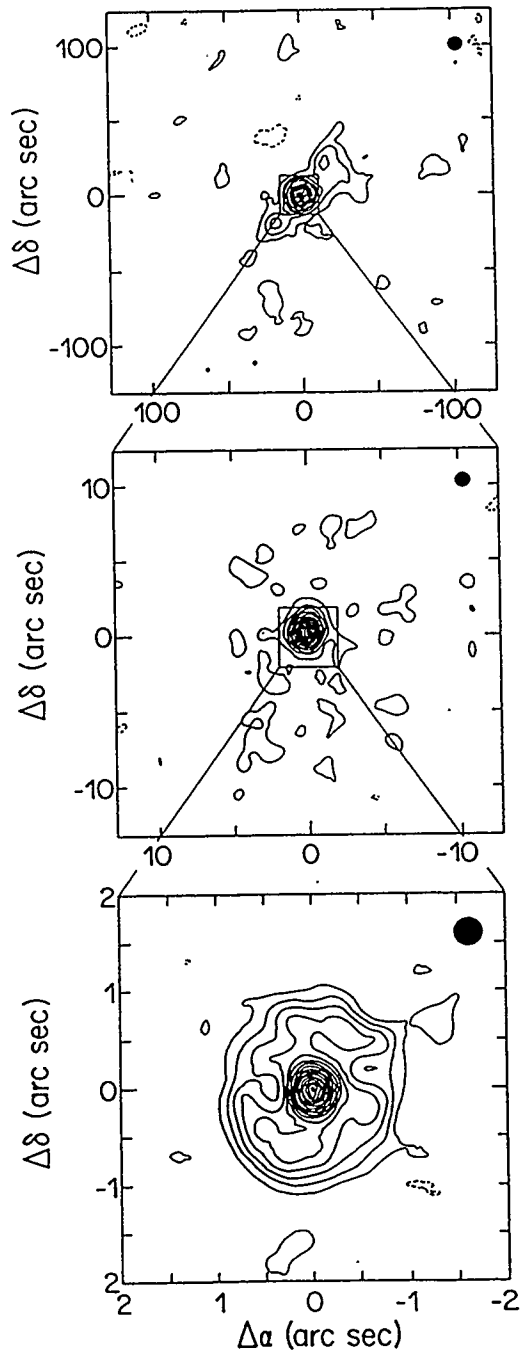


Figure 4.4: Images of AG Pegasi at three Resolutions

The dominant features presented are (*top*) outer nebula (1.5 GHz, natural weighting); (*center*) intermediate nebula (1.5 GHz, uniform weighting); (*bottom*) inner nebula and central unresolved object (5 GHz, uniform weighting). Data from Kenny (1989).

1976). Early radio observations by Feldman (1977), Feldman *et al.* (1978), Kwok and Purton (1978) and Purton *et al.* (1982) showed a secular increase in flux density, widely interpreted as a very slow nova-like expansion of an optically thick shell. Ionization of the circumstellar material lost by the cool component in quiescence can also account for a large portion of the increase in flux density, particularly at low frequencies. Radio images revealing extended radio structure were first presented by Kwok (1981b) and Kwok, Bignell and Purton (1984). Velocities of $\sim 100 \text{ km s}^{-1}$ were reported from these images by Kwok (1982b), and variations on the time scale of days were noted by Purton *et al.* (1982).

In the optical regime, emission lines of increasing excitation and ionization soon appeared (Stover and Siverton 1977; Ciatti, Mammano and Vittone 1978, 1979; Davidson, Humphreys and Merrill 1978), as is normal also for classical novae. The trend toward increasing excitation and ionization levels continued for 6 years after the outburst (Blair *et al.* 1981) but still no optical nebulosity had been resolved.

Wolf-Rayet features with velocities up to 2000 km s^{-1} were observed (Belyakina, Gershberg and Shakhovskaya 1978, 1979; Brown *et al.* 1978; Ciatti, Mammano and Vittone 1978; Wallerstein 1978; Allen 1980b; Andrillat, Ciatti and Swings 1982). These features gradually declined and disappeared altogether by 1979, while the He II $\lambda 1640$ lines became progressively stronger (Blair *et al.* 1981; Feibelman 1982; Stauffer 1984) and UV fluxes for C IV, N IV, N V increased (Mueller and Nussbaumer 1985). The effective temperature increased from $\sim 5 \times 10^4$ to 1.6×10^5 K between 1980 and 1983 (Stauffer 1984, Kwok 1988), and was accompanied by an increase in the observed state of excitation. These evolutionary details are consistent with various outburst models (*e.g.* Kwok 1988, Bath 1977).

Analyses of the UV spectrum are presented by Ciatti, Mammano and Vittone (1978), Brown *et al.* (1978), Boggess, Feibelman and McCracken (1981), and Feibelman (1982). The spectrum is flat over the IUE range and is probably due to two-photon emission plus hydrogen and helium bound-free and free-free processes. High excitation emission lines, typical of central stars of planetary nebulae are also present. X-ray emission was detected by the Einstein satellite (Allen 1982; Kwok and Leahy 1984).

Infrared emission is variable with an amplitude of ~ 1 mag at K, and a period of ~ 500 d (Slovak 1978; Bopp 1981; Taranova and Yudin 1980, 1983; Ipatov, Taranova and Yudin 1985; Lorenzetti, Saraceno and Strafella 1985). The period is long compared to the periods of single Miras, but is comparable to periods of other symbiotic Miras like those of V1016 Cyg and RX Pup.

A large discrepancy exists in the determination of the extinction associated with the system. Thronson and Harvey (1981) obtain a value of $A_V \sim 12$ mag from the IR Brackett decrement, but Davidson *et al.* (1978) and Blair (1981) obtain $A_V \sim 2.5$ and 1.2 respectively using Balmer line ratios. Large amounts of circumstellar extinction are indicated. It appears that the cool component is selectively extinguished, and some authors (*e.g.* Allen 1983; Kenyon, Fernández-Castro and Stencel 1986) infer from this that the hot component must lie partially outside of the dust shroud of the cool component. Due to the inability to obtain reliable values of extinction, distance determinations for HM Sge are also very poor.

Solf (1984) reports high spectral and spatial resolution observations of HM Sge in [N II] and [O III]. Spectroscopic data is obtained for various entrance slit orientations to facilitate image reconstruction. Figure 4.5 shows a map of the relative positions

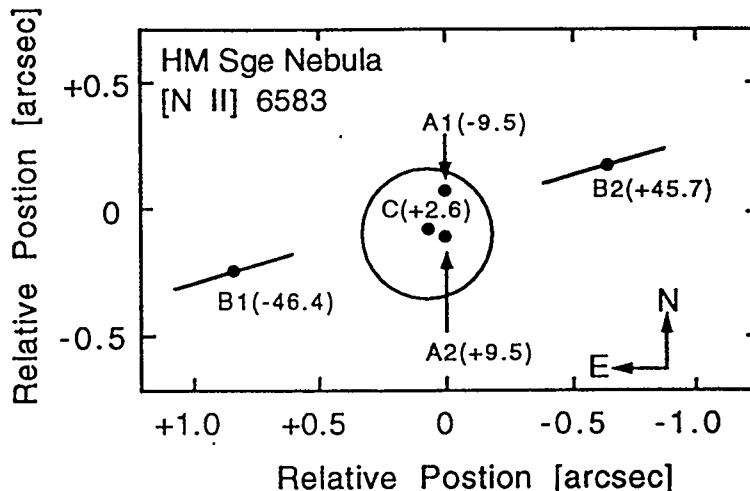


Figure 4.5: HM Sge Nebula, [N II] $\lambda 6583$
(Data from Solf, 1984.)

Locations of nebular features are indicated by filled circles and are labelled A1, A2, B1, B2 and C. The extent of the shell feature, C, is indicated by the large open circle, and the extent of B1 and B2, along the direction of their separation, is given by the ruled lines. The features A1 and A2 are unresolved. Radial velocities relative to the centroid velocity of A1 and A2 are given in parenthesis in units of km s^{-1} . The value associated with C is a shell expansion velocity.

of the five spatially resolved components deduced from the [N II] line spectra. The positional accuracy is better than $0''.1$. The locations of features are indicated by filled circles and are designated: A1, A2, B1, B2, and C. The angular extent of the C feature is given by the large open circle, and the extent of B1 and B2, along the direction of their separation, is given by the lines through their locating dots. The A1 and A2 features are point sources. Radial velocities, relative to the centroid velocity of A1 and A2, are given in parenthesis. The C feature is a shell, and the velocity shown for it is an expansion velocity. The velocity centroid of B1 and B2 appears to coincide with that of A1 and A2, while the centroid of the C component is somewhat offset.

In order to explain his observations, Solf suggested the model shown schemat-

ically in Figure 4.6. The model consists of a highly inclined system in which cool component mass loss has been strongly equatorially enhanced in the epoch preceding the initiation of the hot component wind. Because of this enhancement, the interaction front between colliding winds progresses much more rapidly in the polar directions, giving rise to an “hour-glass” morphology. Solf associates the observed C feature with interaction at the poles, and the observed A features with the knots of strongest emission at the equator. In addition to interaction phenomena, he postulates an impulsive bipolar ejection giving rise to the B features. The proposed model (Figure 4.6) is very successful in explaining Solf’s observations and is also strongly supported by the new observations and analysis to be presented in this chapter.

More recently, Hack and Paresce (1993) have presented a 1980 Å image of HM Sge taken with the Hubble Space Telescope (Figure 4.7). In the central region there exists a compact object which is elongated toward the south. On larger scales of several tenths of arcsec, a more symmetric distribution is apparent with elongation both to north and south and an S-shaped curvature. The UV emission at 1980 Å is expected to come primarily from the CIII] λ 1909 and Si III] λ 1892 lines, and should therefore trace the low-density, high-ionization regions of the system, *i.e.* the hot component wind.

V1016 Cygni

V1016 Cyg is similar to HM Sge in almost every respect. Formerly considered a long period variable star (Nassau and Cameron 1954), it brightened by at least 4 mag between 1963 and 1965 (Fitzgerald *et al.* 1966) to become a principal representative of the symbiotic nova class. Since the outburst, an emission line spectrum has

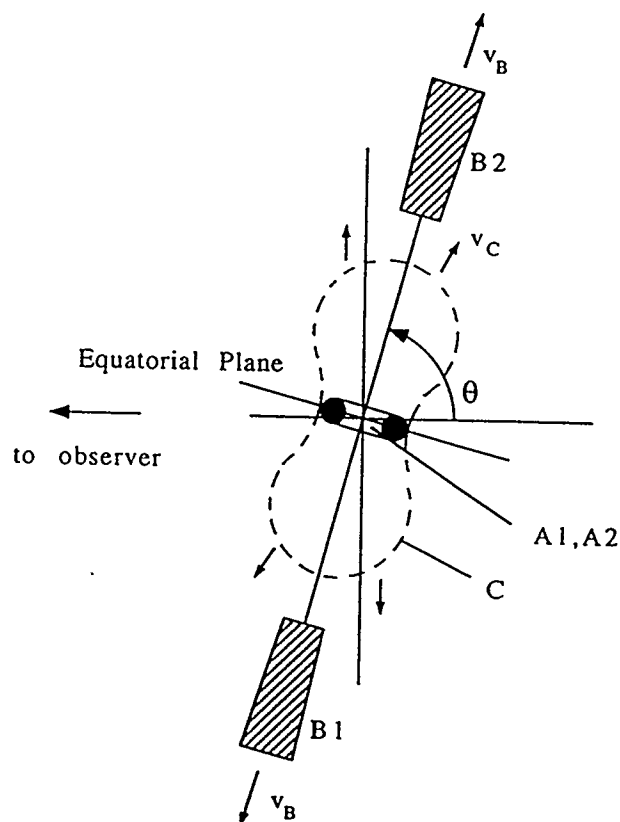


Figure 4.6: Model Shell Structure of HM Sge
(After Solf, 1984.)

Observed features from Figure 4.5, are interpreted as interaction features between the remnant cool component wind and a newly initiated hot component wind. Cool component mass loss from the previous epoch of quiescence is equatorially enhanced. The equatorial interaction features give rise to knots of emission at A1 and A2 while the broader emission feature, C, arises from the polar interactions. An additional phenomenon, an impulsive bipolar ejection, results in features B1 and B2.

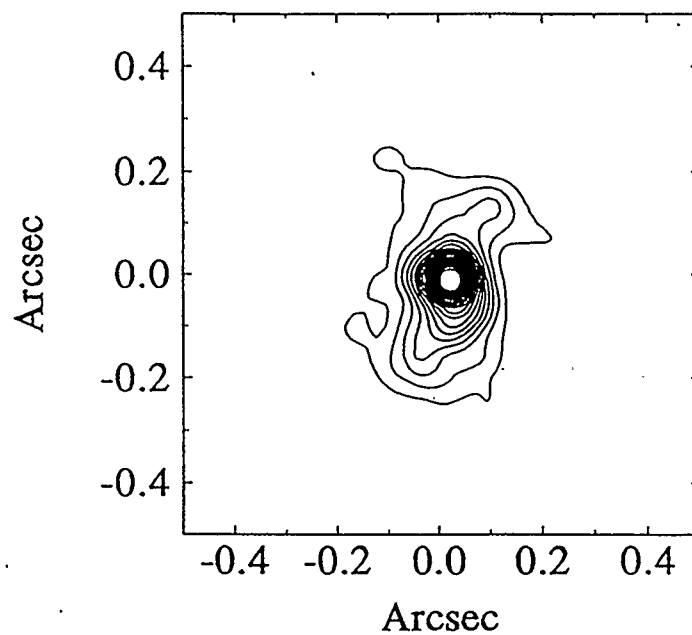


Figure 4.7: UV Image of HM Sge
(Data from Hack and Paresce, 1993.)

This contour plot is made from the central 50×50 pixel² region of the deconvolved 1980 \AA image taken with the Hubble Space Telescope Faint Object Camera. Each contour represents a 5% drop in intensity from the peak contour.

developed and has subsequently increased slowly in excitation (Fitzgerald and Houk, 1970; Mammano and Ciatti, 1975). Infrared observations since the outburst have indicated the continued presence of a long period Mira-type variable (Harvey 1974), with a period of ~ 450 d.

The optical emission lines of V1016 Cyg are basically the same as those for HM Sge, although relative intensities are somewhat different. The excitation of these emission lines is also similar, but somewhat higher than for HM Sge; [O III] λ 4363 emission from is slightly weaker. Various molecular bands have been identified in the optical spectrum of V1016 Cyg despite the weakness of the optical continuum (*e.g.* Mammano and Ciatti, 1975).

Baratta, Cassatella and Viotti (1974) suggest that the optical nebula is $\sim 10^{16}$ cm in extent, with a density of $n_e \approx 5 \times 10^6$ cm $^{-3}$. Densities of this order are also suggested by the absence of [O II] λ 3727 and [S II] λ λ 6717, 6731 (collisional de-excitation). Feibelman (1983) obtains similar densities from C III], N IV] and Ne IV], however the values which he obtains from the N III] quintet are much higher, *i.e.* $\sim 10^9$ cm $^{-3}$. The higher values from N III] apparently correspond to a different region, which is closer to the hot component. The nature of the ionization stages represented in the optical spectrum suggests that the density distribution in the emitting region may be clumpy.

Solf (1983) reports high spectral and spatial resolution observations in [N II] and [O III] for V1016 Cyg, similar to those discussed above for HM Sge (Solf 1984). The results are also similar, although no attempt is made in this earlier work to reconstruct an image from the position angle information. The major nebular features are found to be separated by 0."40 in space and 51 km s $^{-1}$ in radial velocity. Minor

features are also identified, and are postulated to correspond to an equatorial ring, expanding at a rate which is slower than that of the major features. Using a model similar to that suggested for HM Sge (Figure 4.6), Solf (1983) concludes that the binary orbit must be of high inclination ($\sim 78^\circ$).

The IUE spectrum of V1016 Cyg is discussed by Nussbaumer and Schild (1981) and Feibelman (1982a, 1982b). The highest excitation lines are found to be variable, but generally increasing in strength. Wolf-Rayet features were observed briefly (Fitzgerald and Houk 1970) in the early stages of outburst, but faded below detection limits before the launch of the IUE. Feibelman (1982b) notes a splitting of the CIV $\lambda 1550$ and He II $\lambda 1640$ emission lines, which he interprets in terms of the formation of a UV shell.

Purton *et al.* (1982) present multifrequency radio observations of V1016 Cyg indicating a spectral index of 0.82 ± 0.9 , and an optically thin turnover at approximately 50 GHz. They also note a secular increase in the 10.6 GHz flux density at ~ 2.1 mJy (2%) per year between 1973 and 1980. Seaquist and Taylor (1992) report further on the radio spectrum, and present new observations from the JCMT at 264 GHz. They note that no variations exceeding 10% occurred at 5 GHz between 1981 and 1991, suggesting that the present spectrum may represent a quasi-steady state.

4.3 Details of the Observing Program

4.3.1 Schedule of Observations

The observations associated with this thesis are listed in Table 4.10. The details of calibration are provided in table 4.11. The MERLIN observations for AG Peg,

HM Sge and V1016 Cyg were made as part of a collaborative program. It is with the permission of Stewart Eyres, Dr. Richard Davis, and Dr. Phillip Pavelin of the Nuffield Radio Astronomy Laboratories at Jodrell Bank, U.K., and Dr. Michael Bode and Dr. Michael Bang of Liverpool John-Moores University, U.K. that MERLIN results are presented for these objects.

4.3.2 Combined Array Imaging: MERLIN/VLA

One of the original contributions of this work is the combining of data from the VLA and MERLIN to obtain high-resolution, high-sensitivity images of the northern symbiotic nebulae. In the combined data sets, the “short” baselines of the VLA are able to constrain the larger scale source structure, while the finer detail is provided by the longer MERLIN baselines. Before combining data sets, it was necessary to align phase centers to within a fraction of a MERLIN beam.

Name	Date	Julian Date	Loc	Freq [GHz]	Duration [hh:mm]	HPBW ["]
HM Sge	20 Aug 91	8488	VLA	4.9	01:20	0.35
V1016 Cyg	20 Aug 91	8848	VLA	4.9	01:20	0.40
AG Peg	22 Nov 84	6026	VLA	4.9	01:20	0.33
	27 Jul 87	7003	VLA	4.9	01:20	0.35
	01 Mar 90	7951	VLA	4.9	02:10	0.34
	20 Aug 91	8488	VLA	4.9	01:20	0.33
Z And	26 Dec 92	8988	MERLIN	5.0	13:50	0.03
	20 Aug 91	8488	VLA	4.9	01:20	0.33
	25 Jul 92	8828	MERLIN	5.0	18:40	0.03
BI Cru	29 Oct 91	8558	AT	8.6	13:40	1.1
He 2-106	30 Oct 91	8559	AT	8.6	12:30	1.1
	01 Nov 91	8561	AT	8.6	01:00	1.1
HD 149427	31 Oct 91	8560	AT	8.6	12:40	1.1
RR Tel	01 Nov 91	8561	AT	8.6	11:00	1.1

Table 4.10: Schedule of Observations

Julian dates are reported from the base date of 244000. Observing locations are listed as: AT (*Australia Telescope*); VLA (*Very Large Array Telescope*); and MERLIN (*Multi-Element Radio-Linked Interferometer*). All VLA observations were made in A configuration. Resolution is reported as the "Half Power Beam Width" (HPBW) of the synthesized beam obtained using uniform weighting of the visibility data.

Name Name	Julian Date	Freq [GHz]	Primary	Flux Density [Jy]	Secondary	Flux Density [Jy]
HM Sge	8488	4.9	3C 386	7.41	1923+210	1.525 ± 0.002
V1016 Cyg	8488	4.9	3C 386	7.41	2005+403	3.06 ± 0.01
AG Peg	6026	4.9	3C 286	7.41	2136+141	-
	7003	4.9	3C 286	7.41	2136+141	-
	7951	4.9	3C 286	7.41	2136+141	1.27 ± 0.01
	8488	4.9	3C 386	7.41	2136+141	1.460 ± 0.005
	8988	5.0	0Q 208	2.49	2136+141	1.750 ± 0.003
Z And	8488	4.9	3C 386	7.41	2352+495	1.329 ± 0.006
	8828	5.0	0Q 208	2.52	2320+506	1.400 ± 0.005
BI Cru	8558	8.6	1934-638	2.59	1236-684	0.44 ± 0.01
He 2-106	8559	8.6	1934-638	2.59	1320-446	0.53 ± 0.02
	8561	8.6	1934-638	2.59	1320-446	"
HD 149427	8560	8.6	1934-638	2.59	1718-684	3.26 ± 0.04
RR Tel	8561	8.6	1934-638	2.59	1934-638	2.59 ± 0.01

Table 4.11: Data Calibration

Calibrator names are presented in the B1950 format. Julian dates are given from the base date of 244000.

Chapter 5

SOUTHERN SYMBIOTICS

5.1 Observations

5.1.1 Flux Density Measurements

The southern symbiotic sources, RR Tel, HD 149427, He 2-106 and BI Cru were observed using the AT 6 km array between 28 October and 02 November 1991. The flux densities, as determined from integrated image intensities, are listed in table 5.1 along with previously published values. The results are plotted in Figure 5.1.

The present observations for RR Tel and HD 149427 yield flux densities in reasonable agreement with previously published flux densities, although there is some suggestion that the flux density of RR Tel may be decreasing. Assuming that the spectra have remained fixed, spectral indices have been fitted for RR Tel and HD 149427: 0.62 ± 0.14 , and 0.99 ± 0.25 respectively. It may be concluded that both sources are partially optically thick. In the case of RR Tel, the index is very close to that expected for wind-like density distributions (*i.e.* 0.6; Wright and Barlow 1975).

For BI Cru and He 2-106 the present measurements are considerably lower than expected from earlier observations. For BI Cru, the discrepancy may not be significant since the errors associated with the earlier observations are very large. For He 2-106, the earlier observation at 14.5 GHz has a relatively small associated error, and the spectral index between this data point and the new 8.6 GHz point is 3.94. Since spectral indices from symbiotic stars are not normally expected to exceed 2

Name	Frequency [GHz]	Flux Density [mJy]	Telescope	Epoch	Reference
BI Cru	8.6	4.5 ± 0.4	AT	11/1991	this work
	8.9	40 ± 20	Parkes	01/1975	2
	14.5	25 ± 10	Parkes	1977-1978	2
He2-106	5.0	20 ± 10	Parkes	1974-78	1
	8.6	5.1 ± 0.1	AT	11/1991	this work
	14.5	40 ± 4	Parkes	1977-78	1
HD 149427	5.0	11 ± 3	Parkes	1974-78	1
	8.6	20 ± 4	AT	11/1991	this work
	14.5	32 ± 5	Parkes	1977-78	1
RR Tel	5.0	30 ± 4	Parkes	1974-78	1
	5.0	28 ± 5	Parkes	1974-78	2
	6.3	< 30	Parkes	02/1975	2
	8.6	24 ± 4	AT	11/1991	this work
	8.9	32 ± 15	Parkes	01/1975	1
	14.5	54 ± 5	Parkes	1977-78	1

Table 5.1: Radio Observations of Southern Symbiotics

References: 1) Wright and Allen, 1978; and 2) Purton *et al.* 1982. Newly reported flux densities have been measured by integrating image intensities. Alternative estimates of flux density, determined through visibility analysis, are given in table 5.2.

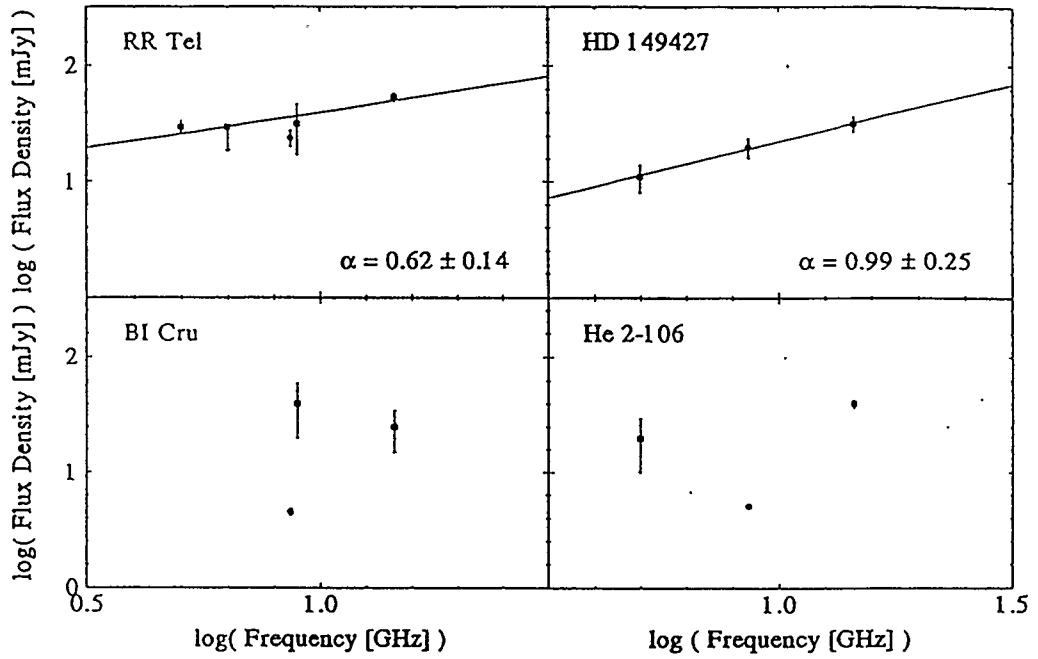


Figure 5.1: Radio Flux Densities of Southern Sources

Flux density measurements listed in table 5.1 are plotted. Linear fits have been performed for RR Tel and HD 149427 yielding spectral indices, α , as shown. Filled circles correspond to new measurements made in this work and filled squares and upper limits correspond to previously published results.

(optically thick thermal emission), it may be suggested that the flux density of the source is decreasing. It is possible, however, that the earlier single-dish observations were confused by a stronger source (200 mJy at 8.6 GHz) which was found to lie approximately $150''$ to the SE of He 2-106. Further, optically thin emission may have been “resolved-out” by the smaller AT beam in the present observations.

5.1.2 Visibility Analysis

Images of the southern symbiotic sources will be presented in the next section, and the observed morphologies will be subsequently discussed in terms of the STB and CWb models. The characteristic angular sizes of the sources are on the order of that of the synthesized beam (“point spread function”), and it is the purpose of this section to discuss whether structure has been detected in the sources at all. In cases of marginal resolution it is often worthwhile to examine data in the visibility domain (Section 4.1.4), and that is the approach which will be taken here.

Visibility analysis has the added benefit of naturally extrapolating the observed visibilities to zero baseline and thereby providing an indication of the total flux density. This technique of flux density determination may represent a substantial improvement over that of integrating image intensities. With the image intensity technique, the selection of the area for intensity integration is sometimes ambiguous, particularly if an extended plateau of emission exists near the noise level (*e.g.* BI Cru - Figure 5.2, table 5.2).

Real visibility curves are shown in Figure 5.2, along with fitted Gaussian functions. Three fitted parameters have been used: a DC-offset (“unresolved flux density”), a Gaussian amplitude (“resolved flux density”), and a Gaussian FWHM. Ob-

Name	Gaussian FWHM ["]	Unresolved Flux Density [mJy]	Resolved Flux Density [mJy]	Total Flux Density [mJy]
BI Cru	8.02 ± 1.40	3.847 ± 0.066	1.87 ± 0.21	5.72 ± 0.20
He2-106	1.28 ± 0.13	2.25 ± 0.26	3.18 ± 0.25	5.43 ± 0.13
HD149427	9.90 ± 0.38	14.09 ± 0.11	13.19 ± 0.28	27.28 ± 0.26
RR Tel	0.946 ± 0.064	14.63 ± 0.96	12.27 ± 0.92	26.90 ± 0.13

Table 5.2: Southern Sources: Fitted Gaussian Parameters

Parameters corresponding to the fitted Gaussian curves in Figure.5.2 are given. The fitted curves are characterized by their angular size (FWHM), amplitude (resolved flux density), and DC-offset (unresolved flux density). The “total flux density” is the sum of the resolved and unresolved contributions.

served visibility data has been shifted so that sources coincide with the array phase center. As a general principle, resolved sources exhibit a systematic increase in flux density toward short baselines in the visibility domain. Such increases are present in all of the plotted curves, although for BI Cru and HD 149427 it is only at very short baselines that flux densities begin to rise significantly. The fitted Gaussians are not expected to reproduce the observed curves in detail, but rather to trace global patterns and thereby provide an estimate of the angular extent of emission. Non-spherical geometry will produce large variations around a simple fit to the visibilities as clearly seen for HD 149427. The fitted curves correspond to the parameters given in table 5.2.

A relatively strong case for resolution may be made for RR Tel. The flux density is observed to increase by 59% from long to short baselines. A simple Gaussian fit (table 5.2) suggests an angular size of ~ 1 " which is approximately of the same

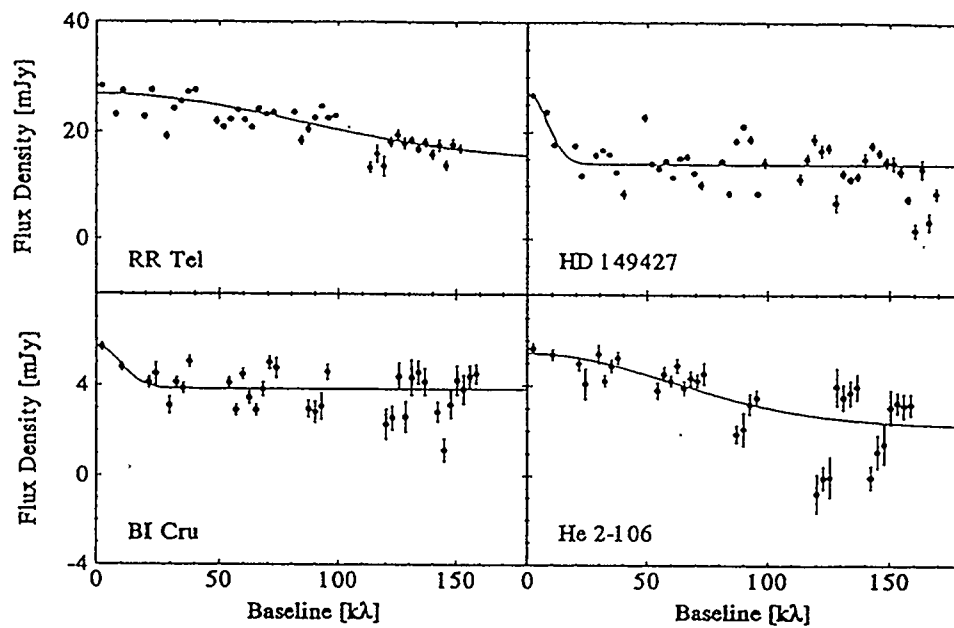


Figure 5.2: Southern Symbiotic Sources: Visibility Curves
Real visibilities are plotted for sources as indicated. Fitted Gaussian curves are also plotted corresponding to the parameters given in table 5.2.

size as the AT beam. In the intensity domain, a two dimensional Gaussian has been fitted with major and minor axes of $0.''65 \pm 0.''10$ and $0.''27 \pm 0.''02$ respectively.

HD 149427 is very poorly fitted by the Gaussian function in Figure 5.2, which is not surprising since its observed intensity distribution (Figure 5.4) departs significantly from circular symmetry. Gaussian fitting in the intensity domain is even less successful. The source is quite clearly resolved in the intensity domain, however (Figure 5.4), with an angular extent of 2-3'' (convolved) along its major axis.

He 2-106 shows a 130% increase in flux density from long to short baselines over the observed range (Figure 5.2), providing convincing evidence of resolution. The fitted Gaussian function has a FWHM of $1.''28 \pm 0.''13$ which exceeds the 1'' FWHM of the synthesized beam. In the visibility domain, a simple two dimensional Gaussian fit yields major and minor axes of $1.''49 \pm 0.''09$ and $0.''19 \pm 0.''19$ respectively, indicating non-circular symmetry.

BI Cru is very marginally resolved, if resolved at all. Only the two visibility points at shortest baseline (Figure 5.2) provide evidence for extended emission. The Gaussian fit in Figure 5.2 suggests that the emission consists of an extended component ($\sim 8''$) with a flux density of ~ 2 mJy, plus an unresolved component with a flux density of ~ 4 mJy. The surface brightness of this diffuse component of emission would fall well below the rms noise level per beam in the intensity domain. In the actual maps, no evidence of the extended component is apparent, and only 4.5 mJy, of the total 5.7 mJy suggested by the Gaussian fit, is measured (table 5.1).

If an extended component of emission exists in BI Cru, it should become apparent at lower resolutions, and may have been detected in earlier observations at Parkes (~ 40 mJy, table 5.1). Earlier observations also suggest that the source may be

optically thin, which would lead to a “resolving-out” of flux density by the AT. The flux density in the intensity domain increases to ~ 5.8 mJy if visibilities are tapered to produce beams of $\approx 15''$, however no new morphological information is recovered.

5.1.3 Images

Observed images of the program stars are shown in Figures 5.3 and 5.4. The morphologies exhibited by He 2-106 and BI Cru (Figure 5.3) are crescent shaped, while those of RR Tel and HD 149427 are unipolar (Figure 5.4). All images are plotted on the same scale. Contour lines are evenly spaced in intensity for HD 149427, He 2-106 and BI Cru. For RR Tel, intensity changes by a factor of two between each contour line. The intensity distribution for RR Tel is therefore much more sharply peaked than that for HD 149427.

In producing these images, various calibration techniques were employed. Calibration at the AT is normally accomplished using point source calibrators, and this procedure was initially applied for all observations. In the case of He 2-106, an additional, stronger source was present in the field and was used as a hybrid mapping source to improve the calibration. RR Tel was self calibrated. Attempts were made to self calibrate HD 149427 and BI Cru, but the results were not considered reliable (see Section 4.1.3).

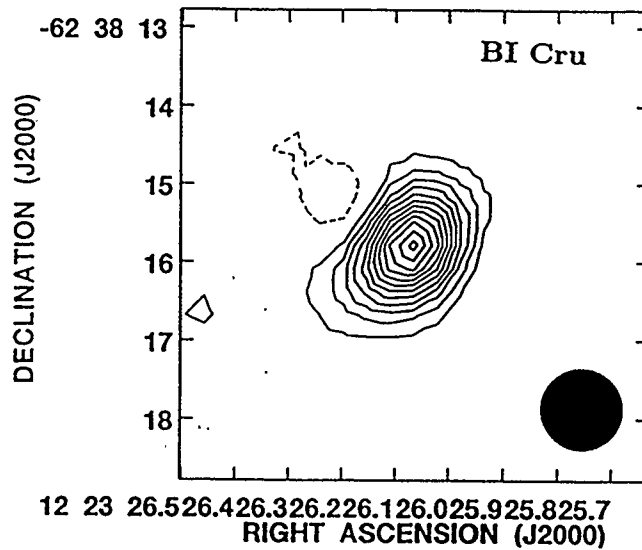
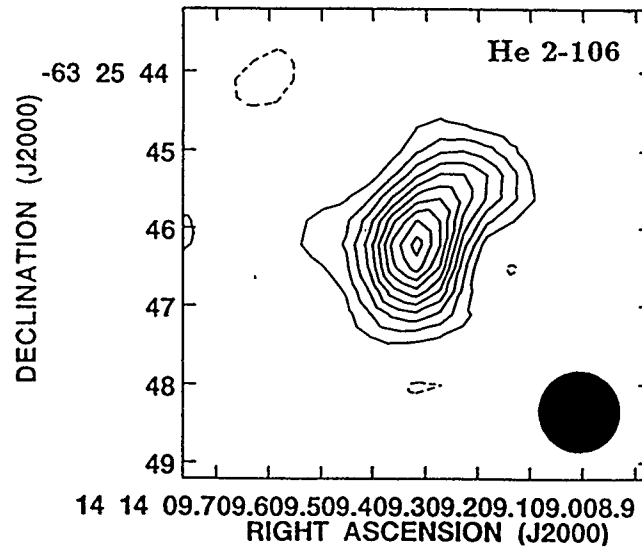


Figure 5.3: AT Images of He 2-106 and BI Cru

Images have been produced with uniform weighting, and contour lines are evenly spaced in intensity. Both images have been restored with a $1''$ beam. The peak intensities are 3.14 and 3.98 mJy/beam for He 2-106 and BI Cru respectively.

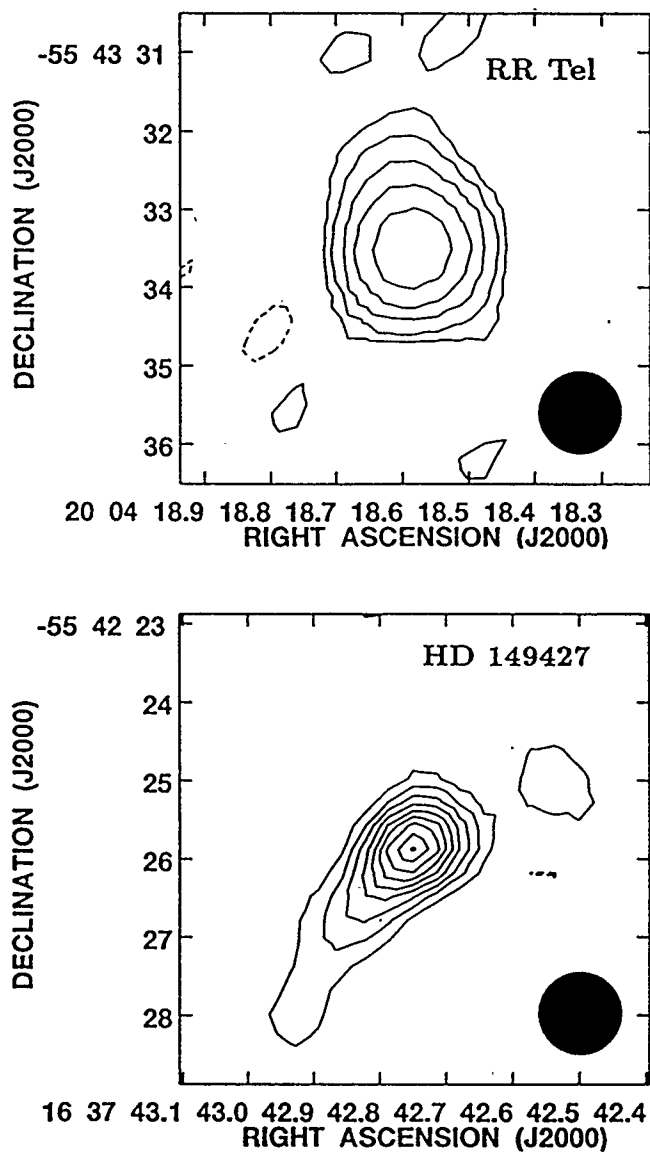


Figure 5.4: AT Images of RR Tel and HD 149427

Images have been produced with uniform weighting. Contour lines are evenly spaced in intensity for HD 149427, while intensity changes by a factor of two between contour lines for RR Tel. Both images have been restored with a $1''$ beam. The peak intensities are 21.5 and 13.8 mJy/beam for RR Tel and HD 149427 respectively.

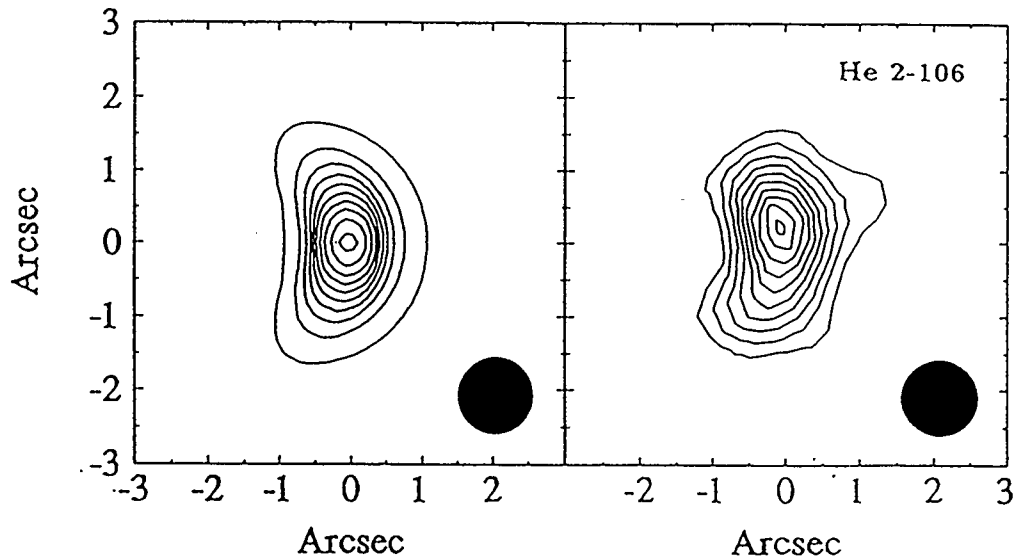
5.2 Discussion

5.2.1 STB Model

The crescent shaped and unipolar morphologies represented in observations of southern symbiotics are similar to those arising from the STB model. Model images reproducing these morphologies are shown in Figures 5.5 and 5.6, along with observed images for comparison.

The aim in producing model images is to derive physical parameters (\dot{M}/v , a , and X_{stb}) from the observed parameters (flux density, angular size and morphology). The predominant effect of X_{stb} is in establishing the image morphology. Similarly, a and \dot{M}/v are primarily responsible for setting the angular size and flux density of the model source respectively.

In order to produce model nebulae with extended crescent morphology, two firm constraints were found to obtain. Firstly, X_{stb} must take values exceeding $\pi/4$ (C-facing nebula); only in this geometry can the required concave profiles be produced. Secondly, binary separations must subtend an angle on the plane of the sky of approximately the same scale as that of the observed emission. From a purely geometric point of view, the correct morphology could be produced with smaller separations; in practice however, intensity profiles become sharply peaked at smaller separations and very little flux density is left in the crescent wings. For the model shown in Figure 5.5, a binary separation of $a = 2000D_{\text{kpc}}$ [AU] has been used. Best estimates of distances to He 2-106 and BI Cru are ~ 3 kpc (table 4.3), implying that binary separations on the order of 6000 AU are required. Such large binary separations may present problems if the hot component is a WD or MS star. Hot components



$$\dot{M}/v = 6.2 \times 10^{-8} D_{\text{kpc}}^{3/2} [M_{\odot} \text{ yr}^{-1}]$$

$$a = 2000 D_{\text{kpc}} [\text{AU}] = 2''$$

$$L_{\text{ph}} = 3.1 \times 10^{45} D_{\text{kpc}}^2 [\text{s}^{-1}]$$

$$\text{Viewing Angle} = 90^{\circ}$$

C-Facing Nebula

$$X_{\text{stb}} = 10$$

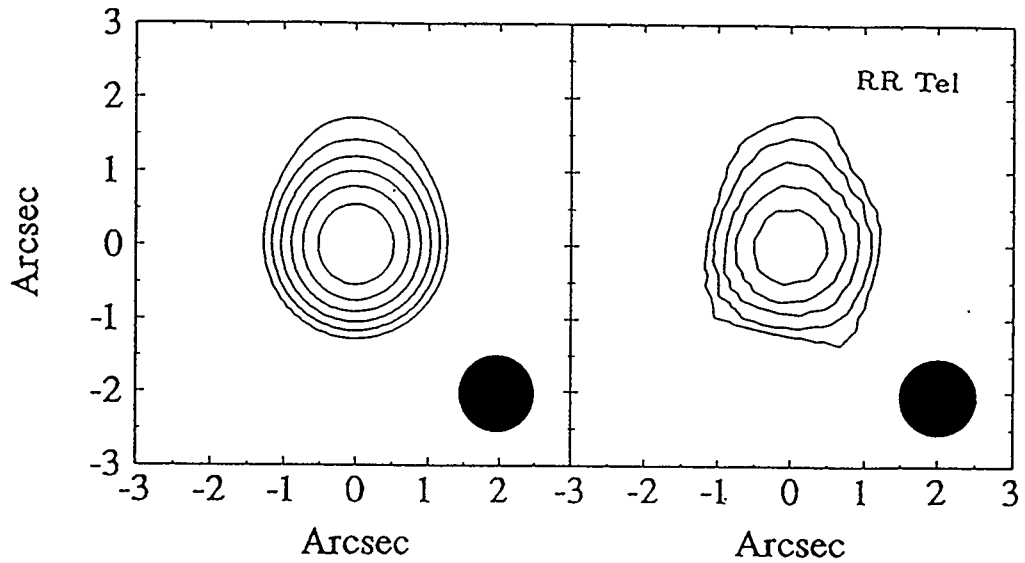
$$\text{Flux Density (8.6 GHz)} = 5 [\text{mJy}]$$

$$\text{Depletion Cone Angle} = 32^{\circ}$$

$$\text{Ionized Mass} = 92 \% \text{ of } \dot{M}$$

Figure 5.5: STB Model: Crescent Morphology

A model intensity distribution is shown resembling the observed distribution of He 2-106. The model beam and contour levels are consistent with those of the observed image shown. The “depletion cone angle” is the opening angle of the conical region of neutral nebular matter.



$$\dot{M}/v = 1.2 \times 10^{-7} D_{\text{kpc}}^{3/2} [M_{\odot} \text{ yr}^{-1}]$$

$$a = 20 D_{\text{kpc}} [\text{AU}] = 0.''02$$

$$L_{\text{ph}} = 4.2 \times 10^{46} D_{\text{kpc}}^2 [\text{s}^{-1}]$$

$$\text{Viewing Angle} = 90^{\circ}$$

H-Facing Nebula

$$X_{\text{stb}} = 0.36$$

$$\text{Flux Density (8.6 GHz)} = 25 [\text{mJy}]$$

$$\text{Ionization Cone Angle} = 30^{\circ}$$

$$\text{Ionized Mass} = 7 \% \text{ of } \dot{M}$$

Figure 5.6: STB Model: Unipolar Morphology

A model intensity distribution is shown resembling the observed distribution of RR Tel. The model distribution has been convolved with a $1''$ beam, characteristic of the observations. Contours in both images have been plotted at similar percentage levels of the maximum intensity, with intensities changing by a factor of 2 between contour lines.

are thought to be maintained in a state of high temperature through accretion from the cool component wind. Accretion power may be ineffective if binary separations greatly exceed ~ 20 AU (Kenyon 1986). The system $\alpha + \text{VZ Cet}$ is only “marginally symbiotic” in terms of its nebular emission and variability (Yamashita, Maehara and Norimoto 1978; Hoffmeister, Richter and Wenzel 1985, p.131) and yet its binary separation (100 AU; Whitelock 1988) is much closer than the values of $\sim 2000D_{\text{kpc}}$ AU suggested here.

The discrepancies in binary separation for BI Cru and He 2-106 may be resolved to a certain extent if the systems are much closer than previously suggested, *i.e.* a few hundred pc rather than several thousand pc. Such a possibility may not be ruled out since determinations of distances to these systems are quite tentative (table 4.3), particularly those which depend upon estimates of circumstellar extinction. Further, evidence of orbital motion in HM Sge (Section 8.7) supports the suggestion that standard methods of distance determination in D type systems produce results which are systematically high.

The model image in Figure 5.6 presents an elongated morphology similar to that observed in RR Tel. The model system parameters shown in the figure are consistent with our understanding of symbiotic systems. The egg-shaped morphology requires very restricted values of the geometry factor X_{stb} : values < 0.30 produce model nebulae which are not sufficiently extended, and values > 0.38 result in “blunt-headed” nebulae. The binary separation is also reasonably well-fixed: values of $a < 10D_{\text{kpc}}$ [AU] result in relatively larger optically thick regions, leaving little flux density for extended emission; values of $a > 100D_{\text{kpc}}$ [AU] result in sharply peaked intensity profiles which again leave little flux density for extended emission. Having

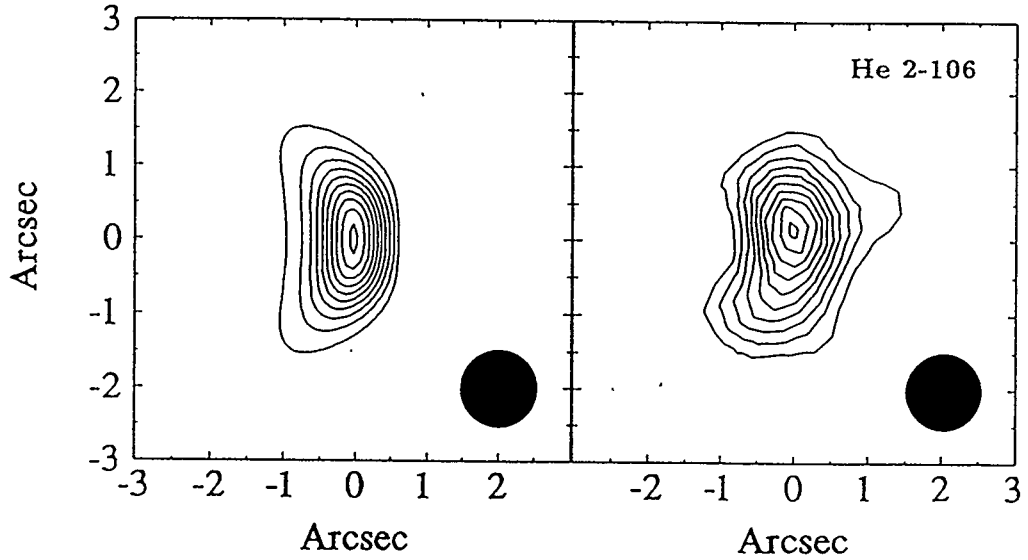
fixed the other two parameters, \dot{M}/v is strongly constrained by the observed flux density; its relative uncertainty is approximately that of a . Although the STB model is quite successfully applied to RR Tel, it is incapable of producing model nebulae whose elongation is as exaggerated as that of HD 149427.

5.2.2 CWb Model

The CWb model is also capable of producing crescent shaped and unipolar nebulae, and examples are shown in Figures 5.7 and 5.8.

The CWb model may be reduced to a 3 parameter problem by holding the wind velocities fixed. A value of 10 km s^{-1} was selected for v_2 , consistent with observed velocities of late-type winds. A value of 1000 km s^{-1} was selected for v_1 , consistent both with WD escape velocities, and the observed velocities of ejecta from systems in outburst (Section 2.2.4). The remaining physical parameters are a , \dot{M}_2 , and $m \equiv \dot{M}_1/\dot{M}_2$. The binary separation, a , and the cool component mass loss rate, \dot{M}_2 , play the same roles in the CWb model as in the STB model: *i.e.* they primarily affect the angular scale of observed emission and the associated flux density, respectively. In the STB model, the geometry is principally established by X_{stb} , and this role is assumed by m (or equivalently X_{cwb} , Section 3.1.2) in the CWb model.

The CWb model produces crescent nebulae resembling He 2-106 and BI Cru with approximately equal success as the STB model. As for the STB model, this model predicts large binary separations, *i.e.* $\sim 4000D_{\text{kpc}}$ AU. The crescent image shown in Figure 5.7 corresponds to a C-facing nebula, however, the model is capable of producing similar images in H-facing geometry. In H-facing geometry, the binary separation is reduced slightly to $\sim 1000D_{\text{kpc}}$, m is decreased to ~ 0.02 , and \dot{M}_2 is



$$\dot{M}_1 = 8.0 \times 10^{-7} D_{\text{kpc}}^{3/2} [M_{\odot} \text{ yr}^{-1}]$$

$$\dot{M}_2 = 6.6 \times 10^{-7} D_{\text{kpc}}^{3/2} [M_{\odot} \text{ yr}^{-1}]$$

$$v_1 = 1000 \text{ km s}^{-1}$$

$$v_2 = 10 \text{ km s}^{-1}$$

$$a = 4000 D_{\text{kpc}} [\text{AU}] = 4''$$

$$\text{Viewing Angle} = 90^\circ$$

C-Facing Nebula

$$m = 1.2$$

$$\text{Flux Density (8.6 GHz)} = 5 \text{ [mJy]}$$

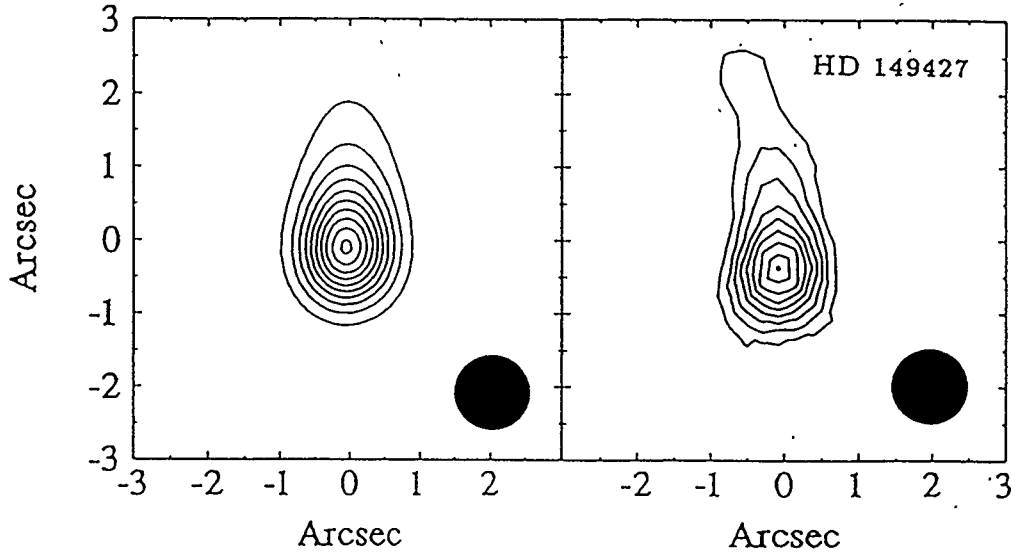
$$\text{Interaction Cone Angle} = 40^\circ$$

$$\text{Interaction Stream Mass} = 12 \% \text{ of } \dot{M}_1$$

$$+ 88 \% \text{ of } \dot{M}_2$$

Figure 5.7: CWb Model: Crescent Morphology

A model intensity distribution is shown resembling the observed distribution of He 2-106. The model beam and contour levels are consistent with those of the observed image shown.



$$\dot{M}_1 = 4.3 \times 10^{-4} D_{\text{kpc}}^{3/2} [M_{\odot} \text{ yr}^{-1}]$$

$$\dot{M}_2 = 2.1 \times 10^{-6} D_{\text{kpc}}^{3/2} [M_{\odot} \text{ yr}^{-1}]$$

$$v_1 = 1000 \text{ km s}^{-1}$$

$$v_2 = 10 \text{ km s}^{-1}$$

$$a = 20 D_{\text{kpc}} [\text{AU}] = 0.''02$$

$$\text{Viewing Angle} = 90^{\circ}$$

C-Facing Nebula

$$m = 210$$

$$\text{Flux Density (8.6 GHz)} = 25 \text{ [mJy]}$$

$$\text{Interaction Cone Angle} = 7^{\circ}$$

$$\text{Interaction Stream Mass} = 0.4 \% \text{ of } \dot{M}_1$$

$$+ 99.6 \% \text{ of } \dot{M}_2$$

Figure 5.8: CWb Model: Unipolar Morphology.

A model intensity distribution is shown resembling the observed distribution of HD 149427. The model beam and contour levels are consistent with those of the observed image shown.

increased to $\sim 2 \times 10^{-6} M_{\odot} \text{yr}^{-1}$.

The CWb model is able to produce elongated nebulae resembling RR Tel for reasonable system parameters ($m \sim 1$, $a \sim 20D_{\text{kpc}}$ [AU], $\dot{M}_1 \sim 10^{-6} D_{\text{kpc}}^{3/2} M_{\odot} \text{yr}^{-1}$). It is also able, to a much greater extent than the STB model, to produce highly elongated nebulae resembling HD 149427, as shown in Figure 5.8. In order to produce model nebulae of this type, however, the interaction cone must be strongly C-facing, and this implies that the hot component mass loss rate must be very high for reasonable estimates of distance, *i.e.* $\dot{M}_1 = 4.3 \times 10^{-4} D_{\text{kpc}}^{3/2} M_{\odot} \text{yr}^{-1}$ in Figure 5.8. Mass loss rates of this magnitude would only be expected during major outbursts. It is by no means impossible that HD 149427 is in an outbursting state, especially if a cool component exists distinct from the observed G-type spectrum (Tylenda *et al.* 1989). If the system is in outburst, however, other explanations for the extended feature (*e.g.* jets, *cf.* CH Cyg, R Aqr) might also be considered.

5.2.3 CWo Model, and Equatorially Enhanced Mass Loss

The CWo model has not been considered in image analysis since it does not predict the observed morphologies. Further, since the systems are all of D-type, their periods are likely to exceed the limit for observing CWo phenomena (Equation 3.60). For $\theta \sim 1''$ and $v_{\text{sp}} \sim 200 \text{ km s}^{-1}$, the critical period is $24D_{\text{kpc}} \text{ yr}$. This value may be compared to values of $1.8 \times 10^5 D_{\text{kpc}}^{3/2} \text{ yr}$ (crescent morphology) and $65D_{\text{kpc}}^{3/2} \text{ yr}$ (unipolar morphology) derived from the CWb model for a total system mass of $2 M_{\odot}$.

In the present study, attention has been confined to the simplest configurations involving CW and ionization phenomena. It has been demonstrated that these mod-

els are plausible only if the hot component is heated by some mechanism other than accretion (as understood at present). This failure may suggest that more sophisticated models are appropriate. Very successful model imaging of planetary nebula has been conducted by a number of authors (*e.g.* Kahn and West 1985; Icke 1988; Stoker and Livio 1989; Mellema 1993; see also Kwok 1993, 1994) assuming modest density variations as a function of latitude (equatorially enhanced mass loss). Such an approach might also be fruitfully investigated in the present context.

5.2.4 Conclusions

The AT observations of RR Tel, HD 149427, He 2-106 and BI Cru have resulted in flux density measurements as well as marginally resolved images. The flux density obtained for HD 149427 is consistent with earlier measurements. The values obtained for He 2-106 and BI Cru are substantially less than suggested by previous observations, and the excess flux density may have been “resolved-out” by the AT beam. The flux density obtained for RR Tel is slightly lower than expected on the basis of previous spectra, and the shortfall may reflect decline from the 1944 symbiotic nova outburst.

Both the STB and CWb models are capable of reproducing the crescent morphologies observed in He 2-106 and BI Cru. In both models, however, the large binary separations suggested make it difficult to understand the powering of the hot component. Both models can also produce unipolar nebulae resembling RR Tel for reasonable input parameters. The STB model is unable to reproduce the morphology observed in HD 149427, and the CWb model is successful only for very large values of m .

Chapter 6

Z ANDROMEDAE

6.1 Observations

Z And was first detected in radio emission in 1982 by Seaquist, Taylor and Button (1984). This detection led to a radio monitoring program, the results of which are reported by Seaquist and Taylor (1990) and Fernández-Castro *et al.* (1995). Further radio observations are reported by Torbett and Campbell (1989) and Ivison *et al.* (1991). Radio light curves for Z And at 1.5, 4.9 and 15 GHz, including all published data from observations between 1982 and 1987, are plotted in Figure 6.1.

The new observations reported here (table 4.10) include near simultaneous observations at the VLA and MERLIN. The observations are spaced by 0.56 in orbital phase: 0.93 (VLA, August 1991) and 0.37 (MERLIN, July 1992) according to the ephemeris of Kenyon and Webbink (1984). Despite this separation, the total flux densities from the two sets of observations are in good agreement: 1.34 ± 0.05 mJy (VLA) and 1.3 ± 0.1 mJy (MERLIN).

6.1.1 Flux Density Variations

The radio light curves plotted in Figure 6.1 suggest that radio flux density variations may be correlated with orbital phase. To more clearly illustrate the suggested correlation, the data at 1.5 and 5 GHz has been plotted against orbital phase in Figure 6.2. Flux densities at 5 GHz measured after July 1987 (Fernández-Castro

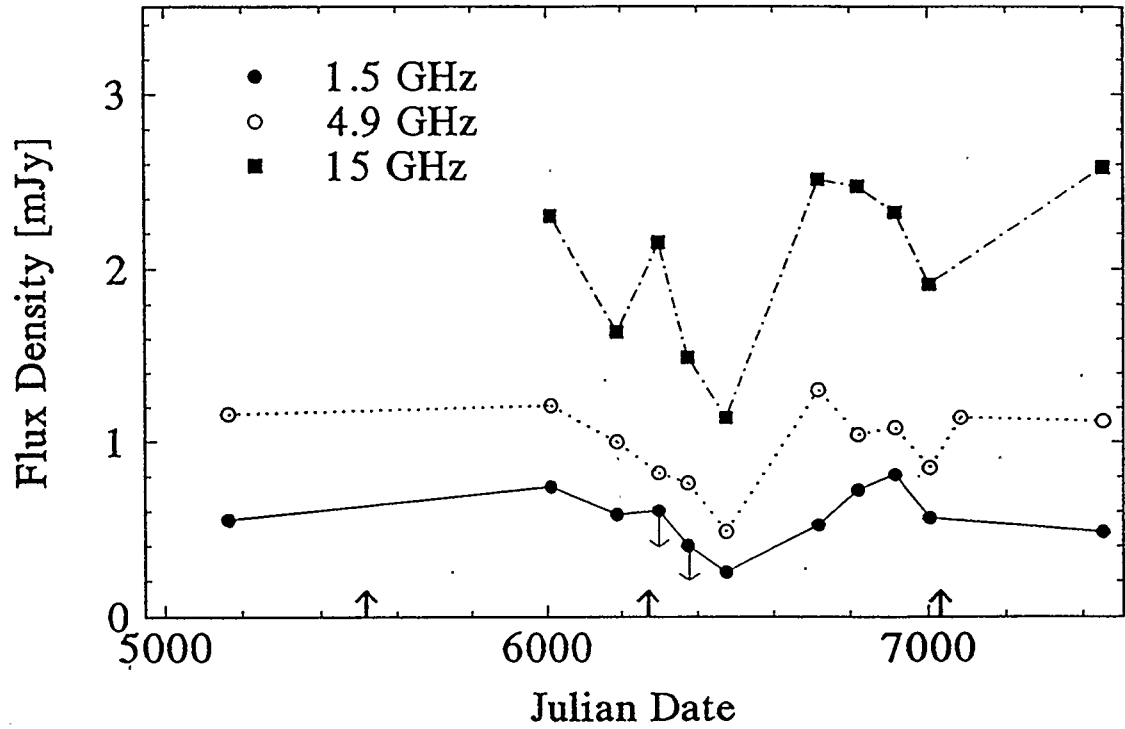


Figure 6.1: Z And: Radio Light Curve, 1982 - 1987

Upward arrows along the x-axis indicate times of visual minima according to the ephemeris of Kenyon and Webbink (1984): $\text{Min}(m_v) = \text{JD } 2,421,298 (\pm 15) + 756.85 (\pm 0.99) \text{ E}$.

et al. 1995; Torbett and Campbell 1989; Ivison *et al.* 1991; new results from this work) are plotted with filled squares and appear to be generally higher than values obtained during the monitoring program. The enhancement of recently measured flux densities is presumably related to the active phase which began in 1984 (Fernández-Castro *et al.* 1995). The delay between the active phase and the observed radio enhancement would represent the time required for the newly expelled material to expand beyond the quiescent optically thick limits. Flux densities measured prior to July 1987 exhibit a distinctive pattern of variation with orbital phase at both 1.5 and 4.9 GHz. The pattern exhibited by phased light curves at 15 and 22.5 GHz are similar to those at lower frequencies, although they are somewhat less well-defined.

6.1.2 Spectral Index Variations

Multifrequency data for Z And has been given by Seaquist, Taylor and Button (1984), Seaquist and Taylor (1990), and Fernández-Castro *et al.* (1995). From this data, spectral indices have been computed by epoch and are listed in table 6.1.

The spectral indices listed in table 6.1 include values from fits across the range of observed frequencies (α), as well as between pairs of frequencies: α_{LC} (1.5 - 4.9 GHz); α_{CU} (4.9 - 14.9 GHz); α_{UK} (14.9 - 22.5 GHz). Values of α are generally near 0.6, the value expected for wind-like density distributions (Wright and Barlow, 1975). Significant variations occur, however, and it will be noted that these variations tend to be more pronounced at low frequencies (α_{LC}) than at high frequencies (α_{CU} , α_{UK}).

For most of the epochs represented in table 6.1 the spectrum is “linear” across the measured frequencies, *i.e.* well-characterized by a single spectral index. The χ^2 merit function for linear least squares fits typically took a value of $\sim 0.3/\text{point}$. A

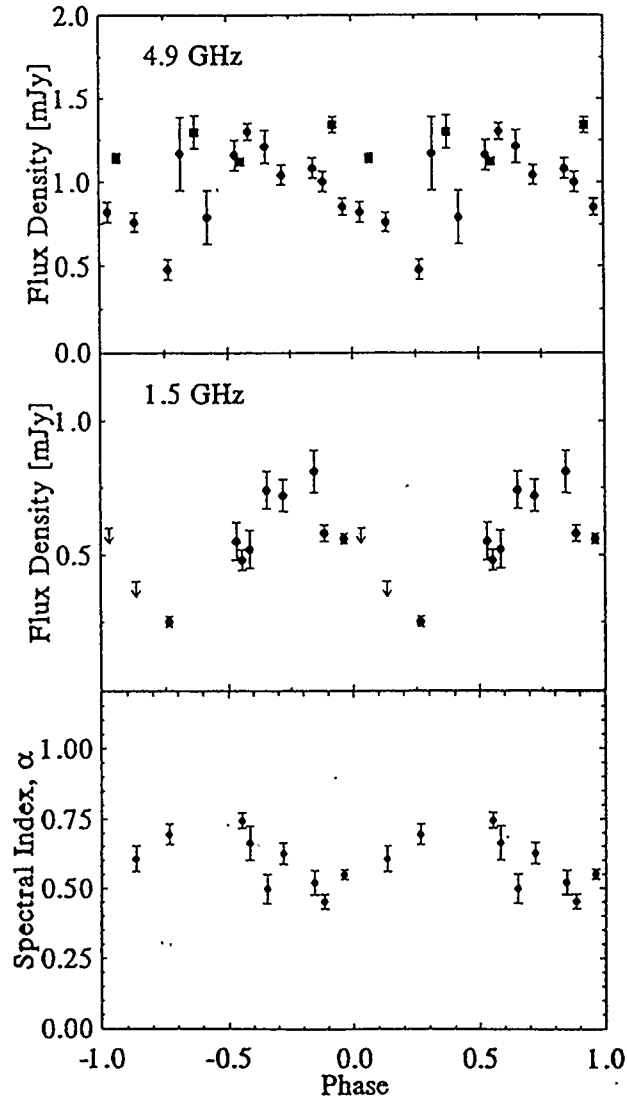


Figure 6.2: Z And: Variations with Optical Phase

Flux densities and spectral indices are plotted by orbital phase according to the ephemeris of Kenyon and Webbink (1984): $\text{Min}(m_v) = \text{JD } 2,421,298 (\pm 15) + 756.85 (\pm 0.99) \text{ E}$. Data is taken from Seaquist, Taylor and Button (1984), Torbett and Campbell (1989); Ivison *et al.* (1991); Seaquist and Taylor (1990); Fernández-Castro *et al.* (1995); and this work. Data at 5 GHz obtained after July 1987 has been plotted as filled squares.

Date	Julian 244+	Spectral Index			α
		α_{LC}	α_{CU}	α_{UK}	
13 Jul 82	5164	0.62 ± 0.28	-	-	0.62 ± 0.28
08 Nov 84	6012	0.416 ± 0.11	0.578 ± 0.11	-	0.498 ± 0.057
03 May 85	6188	0.460 ± 0.052	0.445 ± 0.039	-	0.451 ± 0.025
21 Aug 85	6299	-	0.87 ± 0.22	1.46 ± 0.98	0.91 ± 0.18
07 Nov 85	6376	-	0.606 ± 0.047	-	0.606 ± 0.047
14 Feb 86	6475	0.551 ± 0.079	0.778 ± 0.056	-	0.699 ± 0.039
13 Oct 86	6717	0.77 ± 0.14	0.59 ± 0.10	0.72 ± 0.44	0.666 ± 0.055
25 Jan 87	6820	0.311 ± 0.089	0.778 ± 0.067	1.36 ± 0.32	0.647 ± 0.042
30 Apr 87	6915	0.24 ± 0.10	0.688 ± 0.068	-0.48 ± 0.72	0.527 ± 0.047
27 Jul 87	7003	0.353 ± 0.043	0.728 ± 0.042	-	0.555 ± 0.021
16 Oct 88	7450	0.716 ± 0.075	0.751 ± 0.033	-	0.744 ± 0.028

Table 6.1: Z And: Spectral Indices from Monitoring Program

The spectral index across the range of measured frequencies is designated, α . Spectral indices between pairs of adjacent frequencies are also listed: α_{LC} (1.5 - 4.9 GHz); α_{CU} (4.9 - 14.9 GHz); α_{UK} (14.9 - 22.5 GHz). Flux densities used to compute spectral indices are taken from Seaquist, Taylor and Button (1984), Seaquist and Taylor (1990) and Fernández-Castro *et al.* (1995).

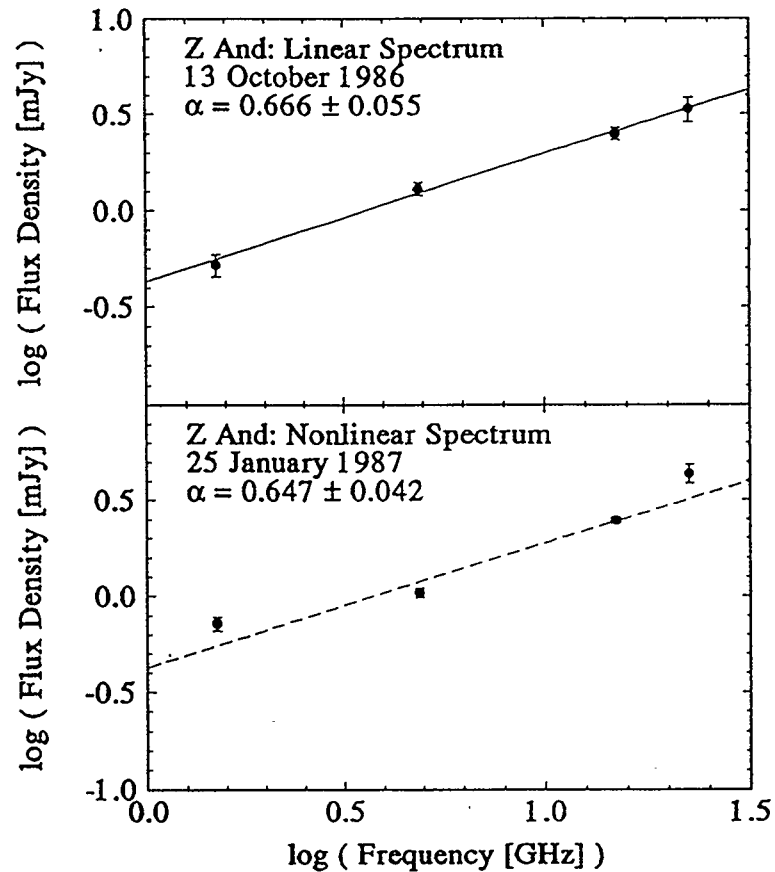


Figure 6.3: Z And: Examples of Linear and Non-Linear Spectra
(Data from Fernández-Castro *et al.*, 1995.)

spectrum of this type is plotted in the upper panel of Figure 6.3. For the three epochs in 1987 however, the spectrum departed significantly from linearity and developed the profile shown in the lower panel of Figure 6.3. The values of χ^2/point were 4.8, 4.4 and 9.7 for the January, July and April observations respectively. By 16 October 1988, the spectrum resumed its previous linear profile, with χ^2/point taking a value of 0.06.

In the lower panel of Figure 6.2, spectral indices are plotted against orbital phase according to the ephemeris of Kenyon and Webbink (1984). A well-defined correla-

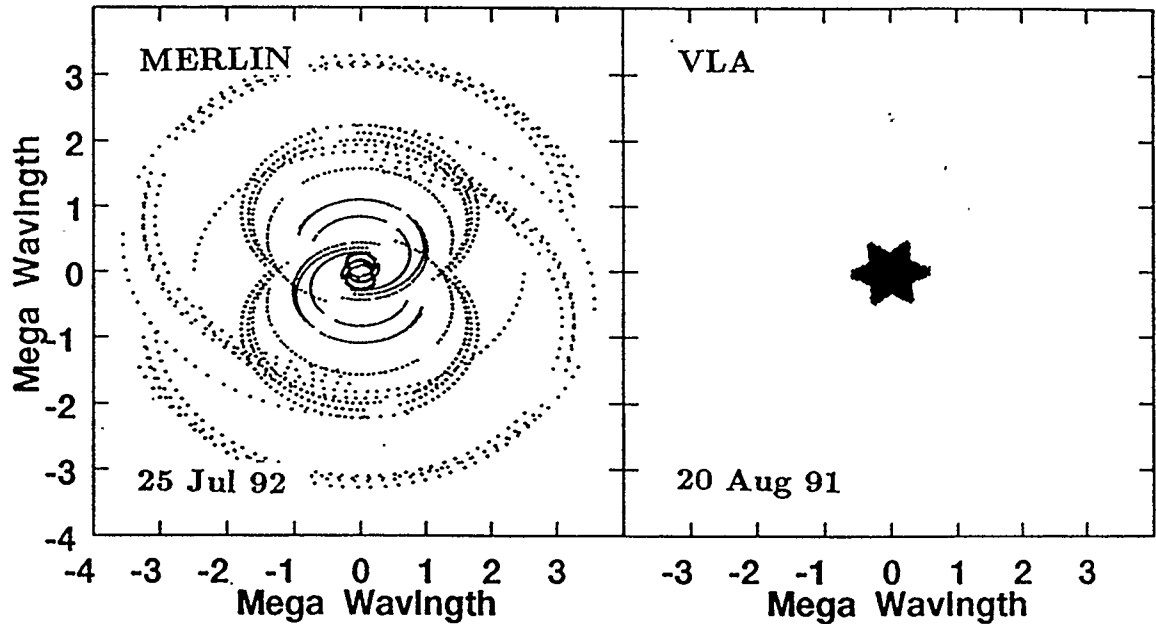


Figure 6.4: Z And: uv Tracks

tion is apparent, indicating that spectral index variations are in antiphase with flux density variations, *i.e.* when the flux density is at a minimum ($0.25 < \text{phase} < 0.5$) the spectral index is at a maximum.

6.1.3 MERLIN/VLA Imaging

The new observations of Z And reported in this thesis have resolved the radio emission for the first time. Data from MERLIN and the VLA were combined to image the system, and the “ uv -tracks” of both arrays are shown in Figure 6.4. It will be noted that some uv regions were shared by both arrays.

The data sets were combined in such a way that visibility points were treated equally regardless of the array at which they were measured (“natural weighting”). In Figure 6.5 the real visibility amplitudes corresponding to the combined data set is

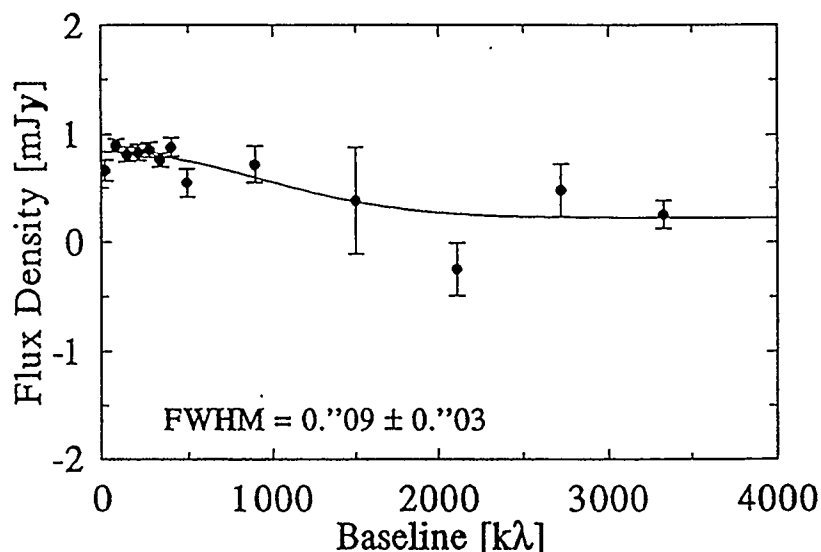


Figure 6.5: Z And: Real Visibility Curve

The fitted line corresponds to a simple Gaussian function with FWHM of $0.''09$.

shown. The data has been shifted in the uv plane to position the source at the combined array phase center. Imaginary visibilities were zero to a good approximation (0.055 ± 0.027 mJy), which suggests that the source is approximately symmetric through its center, and that essentially all of the flux density is contained within the real visibilities. The uncertainties associated with the VLA data (short baselines) are much smaller than those associated with the MERLIN data (long baselines) since baselines were more tightly sampled at the VLA (Figure 6.4). The uncertainties per visibility point are similar for the two arrays.

The real visibility curve of Figure 6.5 would suggest that the source has been resolved, *i.e.* a significant decrease in flux density toward long baselines is apparent. Although the observations were not strictly simultaneous, the total flux density from observations at the individual arrays were in strong agreement (~ 1.3 mJy), and hence the decrease in flux density toward long baselines is not the effect of source

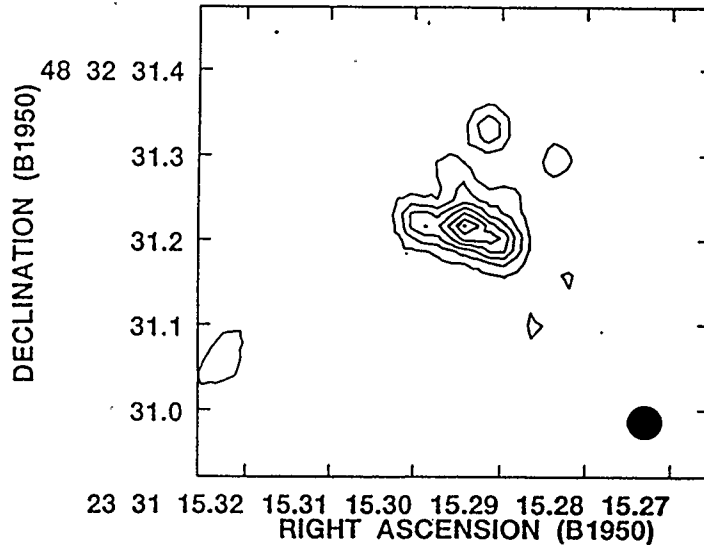


Figure 6.6: **Z And: Near Simultaneous VLA/MERLIN Observations**
 Data at 5 GHz, taken from the MERLIN array (25 July 92) and the VLA (20 Aug 91), have been combined to produce this image of Z And. Contour lines are evenly spaced in intensity. The image has been restored with a beam size characteristic of the MERLIN array (0."04 FWHM).

variability. The distribution in Figure 6.5 has been fitted by a Gaussian function with a FWHM of $0."09 \pm 0."03$. This characteristic size is in good agreement with the average value of the deconvolved, two dimensional, Gaussian fit performed in the intensity domain: $0."12 \times 0."05$ at a position angle of 75° .

The combined image of Z And is shown in Figure 6.6. A bipolar structure has been resolved with a central emission peak. There is also the suggestion of a weaker unresolved source (~ 0.2 mJy) lying $\sim 0."1$ to the north of the dominant emission.

6.2 Discussion

6.2.1 Flux Density and Spectral Index

The observed variations in flux density and spectral index place strong constraints upon models of radio emission from Z And. It is not immediately obvious that either the STB or CW models are capable of reproducing these results. The primary difficulty lies in producing a pattern which peaks once rather than twice per orbital cycle.

In both the STB and CW models, the primary emitting zone consists of a conical region which changes orientation with the orbital phase. Small changes in flux density and spectral index occur as a result of the orientation changes (CWb - see Figure 3.8; STB - Taylor and Seaquist 1984). In the absence of additional regions of emission and/or absorption, the observed characteristics of the system should be identical at inferior and superior conjunction of the hot component about the cool component. Flux density and spectral index should therefore peak twice every orbital cycle. Observations indicate however that variations are single peaked (Figures 6.2).

The STB or CW models may produce single peaked profiles if the cool component is able to eclipse a significant fraction of the radio emitting region. This possibility may be ruled out, however, by simple arguments. For a cool component of radius $150 R_{\odot}$ to eclipse the variable component of emission (~ 0.5 mJy, Figure 6.2) implies a radio emitting region with a brightness temperature of 2×10^7 K. Temperatures of this order have not been observed in the system and are not expected in either the STB model or the CWb model (Equations 3.17 and 3.18).

A more successful possibility, which follows from the STB model, is illustrated

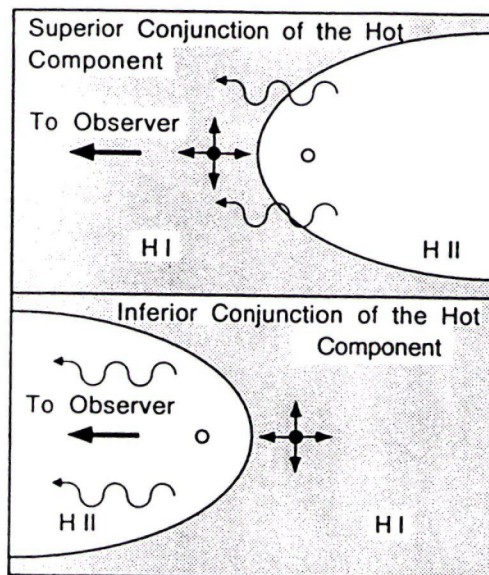


Figure 6.7: **Flux Density Modulation with Orbital Phase: STB Geometry**
 Top: At superior conjunction of the hot component about the cool component, radio waves from the ionized nebula must pass through the “neutral” portion of the cool component wind (ionization fraction $\sim 10^{-5}$) to reach the observer, and may suffer significant attenuation (radio flux density minimum). Bottom: At inferior conjunction of the hot component about the cool component, radio waves from the ionized nebula may proceed to the observer unattenuated by passage through “neutral” cool component wind (radio flux density maximum).

in Figure 6.7. Here, the radio emission is attenuated in passage through the neutral component of the cool component wind. It is assumed that some small fraction of the “neutral” wind is in fact ionized, and equilibrates to the temperature of the cool component wind ($\sim 10^3$ K). This portion of the “neutral” wind may then act as a low temperature absorbing medium for radio emission produced within the “ionization cone”. In this way, the cool component is able to extend its influence to much larger scales than it physically occurs.

In the STB model, the ionization boundary changes orientation with orbital

phase. Therefore, at superior conjunction of the hot component (*i.e.* cool component in front), the cool thermal plasma will lie maximally between the earth and the radio emitting region. The observed radio flux density will therefore be at a minimum. At inferior conjunction (hot component in front), the line of sight to the radio emitting region will be minimally obstructed by the cool thermal plasma and therefore the observed flux density will be at a maximum. The resulting radio light curve will peak only once per orbital cycle.

The coefficient for bremsstrahlung absorption by a thermal plasma scales with $\nu^{-2.1}$. Radiation should therefore be more efficiently attenuated at low frequencies than at high frequencies. This selective absorption of low frequency radiation will have the effect of steepening the spectrum. Therefore spectral index will increase with increasing absorption (decreasing flux density). This prediction is in agreement with the observed anti-phase relationship between flux density and spectral index (Figures 6.2).

The fractional ionization in the cool component wind required to produce the observed attenuation is relatively low. Consider a line of sight passing through the cool component wind with an "impact parameter" of one binary separation. The optical depth scales linearly with the ionization fraction, and must take a value approaching 1 at 5 GHz in order to produce variations of the observed amplitude (Figure 6.2). Using a value of $1 \times 10^{-8} [M_{\odot}\text{yr}^{-1}][\text{km s}^{-1}]^{-1}$ for \dot{M}/v (Figure 6.9), a binary separation of 2 AU (total mass $\sim 2 M_{\odot}$, orbital period = 756 d), and a temperature of 10^3 K, an ionization fraction of 3.5×10^{-6} is obtained for a hydrogen nebula. Such a value does not seem unreasonable, and is also consistent with the observed correlation between infrared and radio luminosities in the general symbiotic

population (Seaquist and Taylor 1990).

Further support of the STB interpretation of radio variability arises from the light curve in UV magnitudes. In Figure 6.8, data from Yudin (1985), for observations between 1974 and 1983 has been plotted by phase. The pattern of variations is in strong agreement with that of the flux density variations (Figure 6.2): *i.e.* minima are observed at \sim phase 0.25, while maxima are observed at \sim phase 0.75. The U magnitudes are most closely associated with the hot component, and Yudin (1985) interprets the light curve in terms of an eclipsing system. Fernández-Castro *et al.* (1995) suggest that the “eclipses” do not represent the physical blockage of the hot component radiation by the cool component, but rather arise due to Rayleigh scattering in the cool component wind. In either case, the required configuration is consistent with the STB description of radio variability. At superior conjunction of the hot component (eclipse, minimum U), the amount of thermal plasma lying between the hot component and the earth will be at a maximum (maximum absorption, minimum radio flux density).

While the characteristics of observed radio flux density are generally well explained by the STB model, some further explanation is required for the development of a nonlinear radio spectrum in 1987. The observed spectral changes are explained if new components of emission were ejected sometime before 1987 (Fernández-Castro *et al.* 1995). When ejection takes place from within a wind-like radio emitting region, it will be first detected at high frequencies. At these frequencies the undisturbed optically thick region has a smaller angular size, and therefore the newly ejected material will expand beyond the previous optically thick limits more quickly.

According to this picture, the observed spectral evolution is understood as follows.

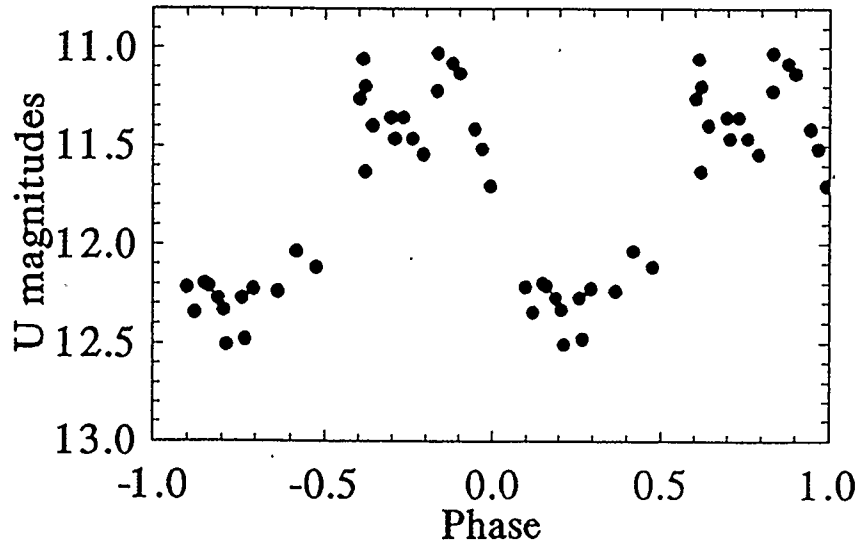


Figure 6.8: Z And: U Magnitude Variations with Optical Phase

Data from Yudin (1985), has been plotted against orbital phase according the ephemeris of Kenyon and Webbink (1984): $\text{Min}(m_v) = \text{JD } 2,421,298 (\pm 15) + 756.85 (\pm 0.99) \text{ E}$. The data was taken between 1974 and 1983, *i.e.* previous to the most recent active phase.

The ejected material is first detected at 22.5 and 15 GHz in June 1987, and the spectrum is steepened at these frequencies. Later, when the ejecta move to larger separations, it becomes detectable at the lower frequencies as well, and spectral linearity is therefore restored at a higher absolute level of flux density. As previously discussed, flux densities at 5 GHz have been observed to be systematically high since July 1987. The new observations reported here exceed the values expected for their respective orbital phases (Figure 6.2) by ~ 0.3 mJy.

An expansion velocity may be calculated using the time required for the newly ejected material to appear at 15 GHz. At the point of first appearance (January 1987), the ejecta must have expanded beyond the optically thick radius which is normal for the corresponding orbital phase. The quiescent flux density at this phase is ~ 2 mJy, and assuming complete optical thickness, the quiescent source would have

an angular radius of $0.''02$, and an associated linear radius of 3.3×10^9 km (assuming a distance of 1.1 kpc, table 4.3). Assuming that the newly expelled material was associated with the eruptions of December 1985 (Fernández-Castro *et al.* 1995), the expansion time to January 1987 is 420 d. The inferred expansion velocity of the ejecta is ~ 90 km s $^{-1}$, which is within a factor of three of the value of 250-300 km s $^{-1}$ obtained by Fernández-Castro *et al.* (1995).

6.2.2 Image Interpretation

The morphology of the MERLIN/VLA image (Figure 6.6) may be modelled with various combinations of system parameters within the context of both the STB and CW models. Treatments in terms of the CW models would have to be coupled with the STB model, however, in order to explain the observed fluctuations in flux density and spectrum as described above. In a combined CW/STB model, the interaction and ionization cones would corotate and the “unilluminated” portion of the CWo nebula could begin to recombine and act as an absorbing medium for radiation from the CWb component. The combined model is much more complex, and is not favored since there is no evidence for the existence of a quiescent hot component wind in the system. Therefore, only the STB model will be considered here.

STB model imaging for Z And is relatively straight forward since the binary separation is already known with reasonable accuracy, *i.e.* ~ 2 AU. For a fixed binary separation, the STB model is reduced to a problem of two parameters: *i.e.* X_{stb} (geometry factor) and \dot{M}/v . The value of X_{stb} is strongly constrained by the image morphology, and for a given value of X_{stb} the value of \dot{M}/v is uniquely determined by the observed flux density.

Some preliminary interpretation of the features in the observed image is useful. The features include (figure 6.6): an unresolved object at the point of peak emission at the center of the map (~ 0.4 mJy); a “bipolar feature” extending on either side of the unresolved object ($\sim 0.''15$, ~ 0.6 mJy); and possibly an additional unresolved feature $\sim 0.''12$ to the north of the main emission (~ 0.2 mJy). The morphological symmetry of the image suggests that the binary system is likely to be located within the central unresolved feature; at a distance of 1.1 kpc, a binary separation of 2 AU would subtend an angle of ~ 2 mas, which is below the resolution of the image. The observed periodic flux density variations are likely to arise in the vicinity of the binary system and therefore to be associated with the unresolved feature. The flux density of the bipolar feature (~ 0.6 mJy) is in good agreement with that of the lower level of the 5 GHz light curve (Figure 6.2), perhaps suggesting that it represents a constant component of flux density.

The compact northern feature, although near the limits of sensitivity, might be associated with the 1984/1985 ejection (Fernández-Castro *et al.* 1995). Its flux density, for instance, corresponds to the amount by which the total measured flux density exceeds the “quiescent” value for the phases of interest (~ 0.2 mJy, phases 0.37 and 0.93, Figure 6.2). Its location, $\sim 0.''12$ from the apparent system center, is also consistent with that expected for the ejecta: at a distance of 1.1 kpc, the linear separation is $130/\sin i$ where i is the inclination of the ejection axis to the line of sight; this separation implies an expansion velocity of $100/\sin i$ km s⁻¹ in reasonable agreement with the value obtained from the evolution of the radio spectral data in the previous section.

STB Model

Within the context of the STB model, bipolar morphology resembling that observed for Z And may be obtained in two ways: *i.e.* $X_{\text{stb}} \sim \pi/4$ and $X_{\text{stb}} \sim 0.36$. Either possibility is consistent with the widely varying values of X_{stb} inferred by Mürset *et al.* (1991) from IUE observations between 1979 and 1987, *i.e.* $< 1/3$ to 2.5.

If X_{stb} is near the critical value of $\pi/4$, the ionization boundary is roughly linear, giving rise to an elongated emitting region. A model image of this type is shown in the upper panel of Figure 6.9. In order to obtain the observed flux density of ~ 1.0 mJy, a value for \dot{M}/v of $8.5 \times 10^{-9} [M_{\odot}\text{yr}^{-1}][\text{km s}^{-1}]^{-1}$ is required, which is typical of late-type stars. The implied value of ionizing photon luminosity, $4.6 \times 10^{45} \text{ s}^{-1}$, is consistent with values expected for excited WDs; a hot component radius of $\sim 0.03 R_{\odot}$ is obtained for a temperature of 10^5 K. The spectral index for these model parameters is 0.64, in very good agreement with the range of observed values (Figure 6.3). The optically thin turnover of the model occurs at 750 GHz, consistent with the mm observations of Ivison *et al.* (1995).

A weakness of this first model is that it would predict relatively large changes in flux density, doubly peaked with orbital phase. Using the model parameters discussed above, the 5 GHz flux density would change from 1.0 to 1.3 mJy as the viewing angle changed from 90° to 0° . The observed light curve (Figure 6.2) is not consistent with variation of this type. The model spectral index is stable with orbital phase to within a few percent.

A second possibility within the context of the STB model involves two components of emission: an STB nebula with a narrow ionization cone opening angle ($\theta_a \sim 30^{\circ}$, $X_{\text{stb}} \sim 1/3$); and an NR-shell ("no-recombination") as discussed in Sec-

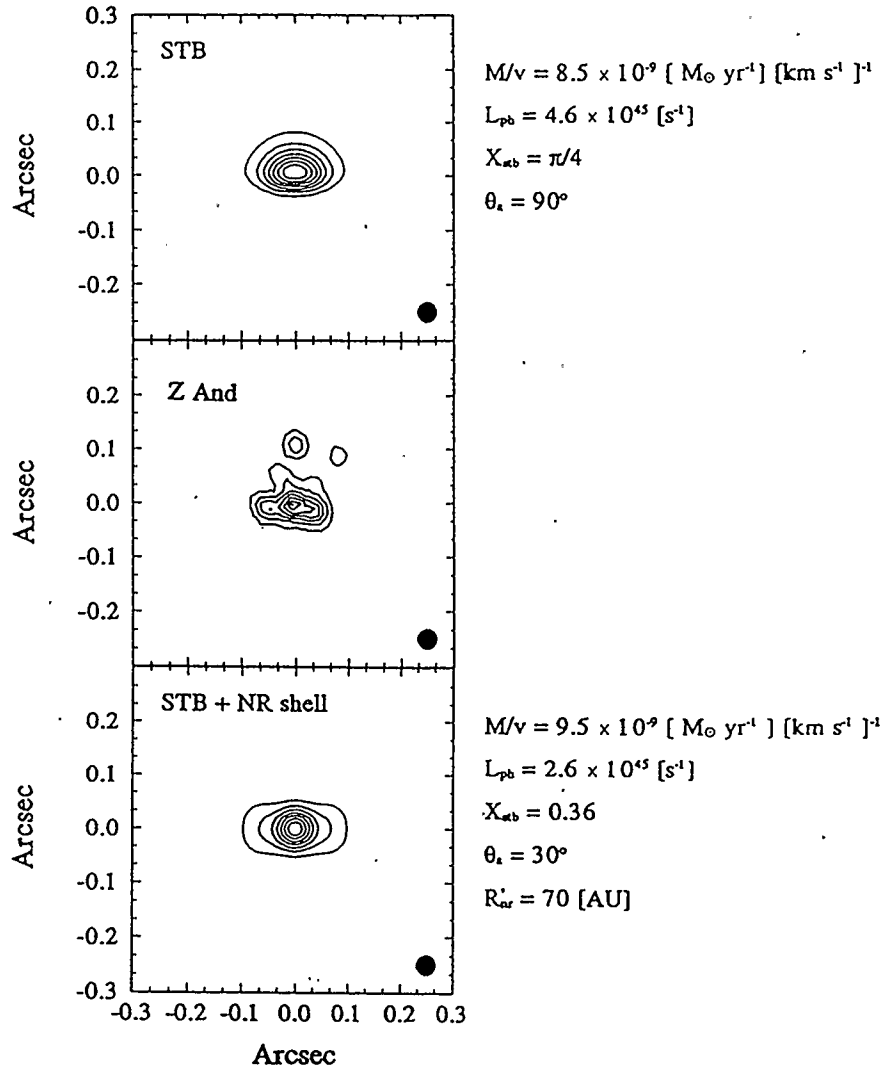


Figure 6.9: Z And: STB Model Images at 5 GHz

Model beam sizes and contour intervals are consistent with the observed image (central panel). In both models, the assumed values of binary separation and distance are 2 AU and 1.1 kpc respectively, and the model flux density is 1.0 mJy. The parameter θ_a is the opening angle of the cone of ionized material. R'_{nr} is the “no-recombination” radius, corrected to include the orbital ionization trail (Section 2.1.3). The viewing angle to the STB nebula is 90° in the upper panel and 0° in the lower panel. The orbital plane lies perpendicular to the plane of sky in both models. In the upper panel, the projected orbital plane lies in the NS direction, while in the lower panel it lies in the EW direction.

tion 2.1.3. An example of this type is shown in the lower panel of Figure 6.9. The NR radius, R_{nr} , computed from Equation 2.8 is ~ 140 AU, however, an “effective” value of $R'_{\text{nr}} = 70$ AU has been used here to account for the additional “ionization trail” discussed in Section 2.1.3, and to produce better agreement with the observed morphology. The values obtained for \dot{M}/v and L_{ph} are very close to those suggested by the first model, *i.e.* $\sim 1 \times 10^{-8} [M_{\odot}\text{yr}^{-1}][\text{km s}^{-1}]^{-1}$ and $\sim 3 \times 10^{45} \text{ s}^{-1}$ respectively. The spectral index is 0.51, in agreement with the observed range of values (Figure 6.3). The optically thin turnover frequency, 680 GHz, is again consistent with mm observations (Ivison *et al.* 1995).

Unlike the first model, the STB + NR shell model does not produce significant bi-periodic variability of flux density and spectral index. It is therefore consistent with the observed variability of these quantities. Further, the STB + NR shell model suggests that the orbital plane lies along the major axis of the bipolar feature. This orientation would allow polar ejecta to be observed to the north of the main emission, as is hinted in the observed image (Figure 6.6).

6.3 Conclusions

The discussion of new and previously published radio observations of Z And has led to a number of conclusions.

- Radio flux densities vary with orbital phase in close correspondence with the light curve of the hot component (U magnitudes).
- Radio spectral indices vary with orbital phase, and are in antiphase with the flux density variations.

- The recent active phase has led to increased flux densities appearing first in January 1987.
- The nebular region associated with Z And is composed of several components: an unresolved central object; a bipolar nebula; and a possibly a further unresolved feature to the north of the system.

The general characteristics of observed radio emission are well-explained in the context of the STB model. System parameters derived from this model include a value of $\dot{M}/v \simeq 1 \times 10^{-8} [M_{\odot}\text{yr}^{-1}][\text{km s}^{-1}]^{-1}$, and $L_{\text{ph}} \simeq 3.5 \times 10^{45} \text{ s}^{-1}$. From the ionizing photon luminosity, it may be demonstrated that the hot component radius is of the order expected for an excited WD, *i.e.* $0.025 R_{\odot}$ for a temperature of 10^5 K. The observed variations in flux density and spectral index are well explained as thermal absorption in the “unilluminated” portion of the cool component wind (fractional ionization $\sim 4 \times 10^{-6}$).

Chapter 7

AG PEGASI

7.1 Observations

Observations of AG Peg include four epochs of high-resolution, high-sensitivity VLA imaging at 5 GHz (table 4.10). The final set of observations was scheduled to coincide with observations at MERLIN. The MERLIN data is presented with the permission of Dr. Richard Davis and Stewart Eyres of the University of Manchester in the UK.

Images from the VLA observing sessions are shown in Figure 7.1. Two primary components of emission are observed in each image: a central unresolved object; and a resolved nebulosity on the scale of $\sim 2''$. The resolved nebulosity is referred to by Kenny (1989) as the “inner nebula” to distinguish it from larger scale structure observed at lower frequencies (Figure 4.4).

The inner nebula appears to evolve in a number of ways. Firstly, a systematic increase in size with increasing epoch is apparent. Further, although the inner nebula is relatively circular in all epochs, a significant global departure from circularity is observed in 1987 along a NS axis. It is of interest that circularity is restored in later epochs. Finally, lobe enhancements within the inner nebula change in appearance and position with time.

The near-simultaneous observations at MERLIN and the VLA (1991/1992) resulted in uv coverages as shown in Figure 7.2. The upper image in Figure 7.3 has been restored with a $0.''3$ beam, characteristic of the combined data set. The lower

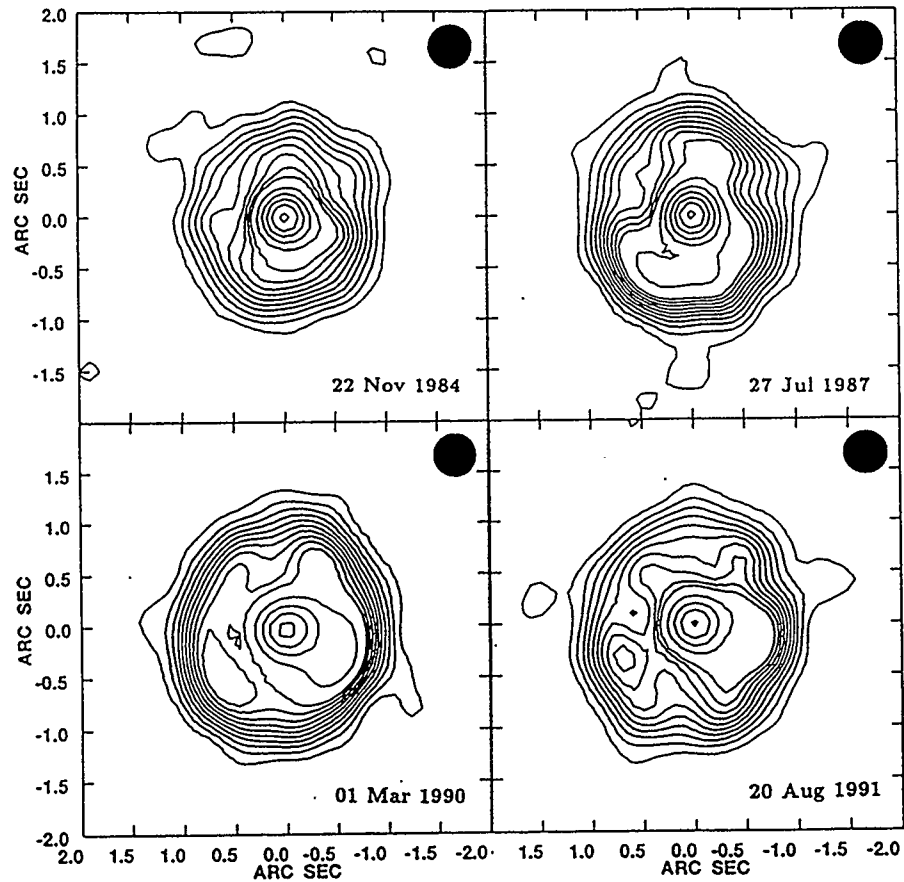


Figure 7.1: AG Peg: VLA Images in Four Epoches, 5 GHz.

All maps have been produced with natural weighting of the visibility data, and have been restored with a $0.''45$ beam. The base contour in each plot is at an intensity of $60 \mu\text{Jy}/\text{beam}$. The contour interval in each plot is $60 \mu\text{Jy}/\text{beam}$ below $600 \mu\text{Jy}/\text{beam}$, and $180 \mu\text{Jy}/\text{beam}$ above $600 \mu\text{Jy}/\text{beam}$. Peak flux densities, in order of epoch, are: 1.57, 1.74, 1.36, and 1.35 mJy/beam.

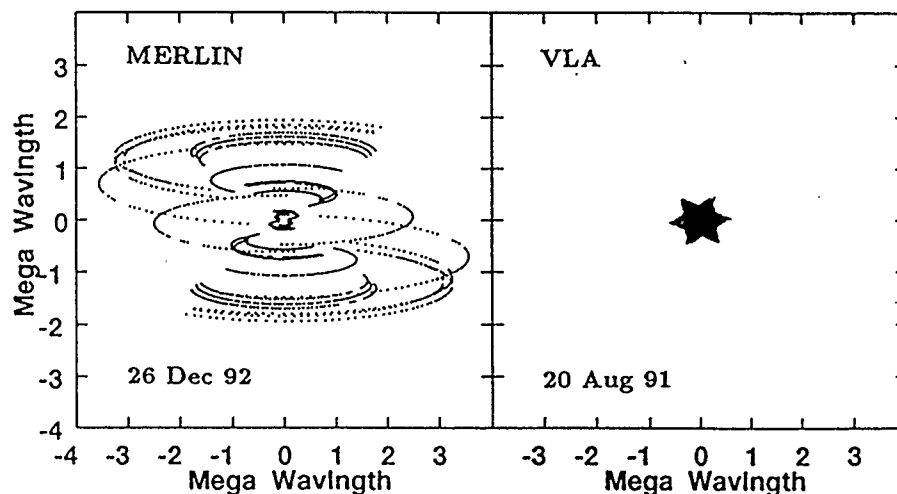


Figure 7.2: AG Peg: uv Tracks
(Near-Simultaneous MERLIN/VLA Observations)

Vertical and horizontal axes correspond to components of antenna separation (u and v) for which visibilities were obtained during the observations indicated.

image has been restored with a $0.''05$ beam, characteristic of the MERLIN array alone.

The upper image in Figure 7.3 may be compared to the image produced from the 1991 VLA data alone (lower right of Figure 7.1). The primary difference is an improvement of resolution from $0.''45$ to $0.''3$. It is of interest that, the westward lobe enhancement is less strongly dominant in the combined image, and appears detached from the central object.

The very high resolution image in the lower panel of Figure 7.3 resolves the central object. The flux density is 0.92 ± 0.09 mJy. Emission is extended at a position angle of $-35^\circ \pm 3^\circ$, and has a “blobby” appearance. The position angle of elongation is in substantial agreement with the position angle of the the outer nebular ($-40^\circ \pm 10^\circ$,

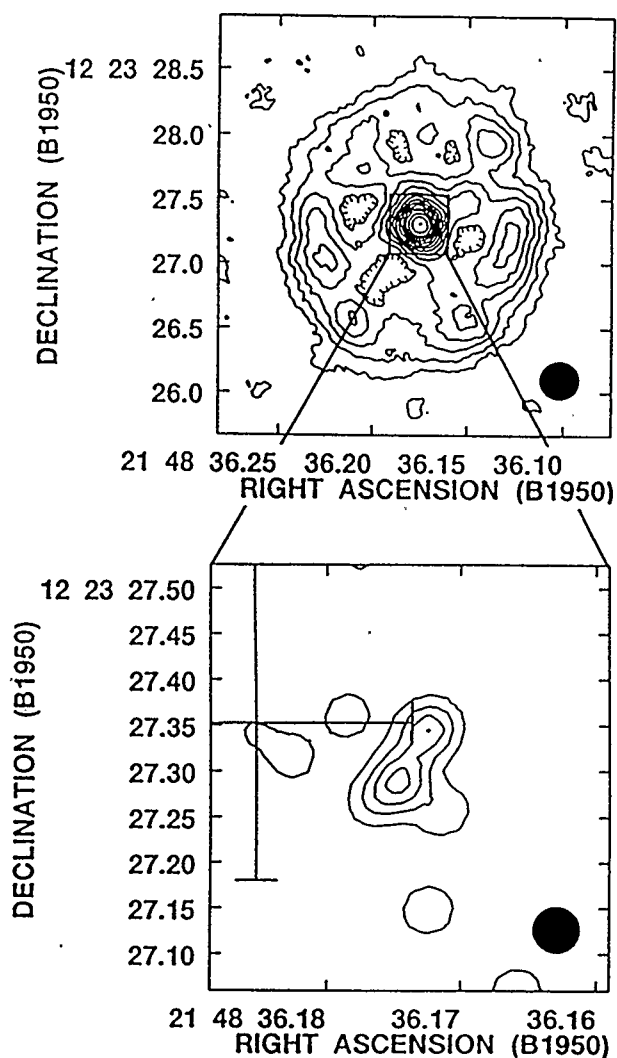


Figure 7.3: AG Peg: Combined Array Images, MERLIN/VLA

Natural weighting has been applied in both images. The upper image has been restored with a $0.''3$ beam, while the lower image has been restored with a $0.''05$ beam. The contour interval in both images is $70\mu\text{Jy}/\text{beam}$. The peak intensity is $1.1\text{ mJy}/\text{beam}$ in the upper plot and $0.32\text{ mJy}/\text{beam}$ in the lower plot. The error bars in the lower plot indicate the optical position as given in the SAO catalogue.

Epoch	Total [mJy]	Central Object [mJy]	Inner Nebula [mJy]
22 Nov 84	6.3 ± 0.1	1.17 ± 0.04	5.2 ± 0.1
27 Jul 87	9.0 ± 0.1	1.31 ± 0.04	7.7 ± 0.1
01 Mar 90	9.9 ± 0.1	0.96 ± 0.02	9.0 ± 0.1
19 Aug 91	9.1 ± 0.1	1.02 ± 0.03	8.1 ± 0.2

Table 7.1: AG Peg: 5 GHz Flux Densities by Component

Figure 4.4).

7.2 Central Source Variations

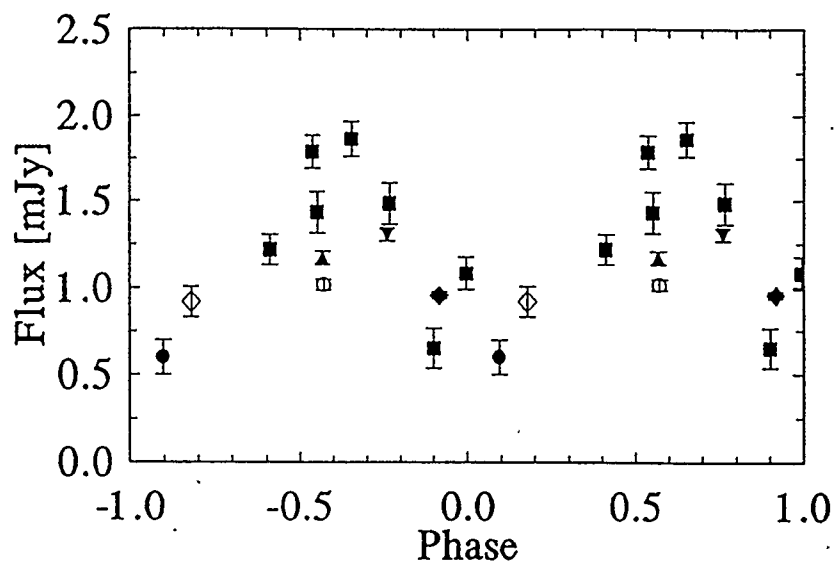
The technique of visibility modelling has been used to separate the emission from AG Peg into resolved (inner nebula) and unresolved (central source) components in the four epochs of VLA data (Section 7.3). Values of central source flux density are listed in table 7.1.

Kenny (1989) analyzed VLA observations of AG Peg from nine epochs between 1984 and 1987, and noted that the central source flux density appears to vary with orbital phase. The 5 GHz minimum occurs near phase zero (UBV minimum), which is thought to coincide with orbital opposition of the hot component (Formiggini and Leibowitz 1990). These characteristics are highly reminiscent of those observed in Z And (Section 6.1.1).

The new values of central component flux density reported here do not strongly support the earlier periodicity. Instead, they are consistent with a constant level of

emission, despite the fact that they are separated widely in phase (ephemeris from Belyakina 1985): VLA, March 1990, 0.96 ± 0.02 mJy, phase 0.92; VLA August 1991, 1.02 ± 0.03 mJy, phase 0.57; MERLIN, December 1992, 0.92 ± 0.09 mJy, phase 0.18. Evidence to be discussed below will suggest that a period of enhanced activity on the hot component occurred previous to 1987. It would appear that deeper fluctuations in flux density occur during active periods, as is also observed in the optical fluctuations of Z And.

In Figure 7.4, central source flux densities from newly reported and previous observations are plotted against orbital phase. The pattern of variation with phase remains apparent, however, it is equally apparent that significant variations also occur from cycle to cycle. The periodic variability may arise from the same mechanism discussed for Z And, *i.e.* the attenuation of radio emission in passage through a cool thermal plasma embedded in the “neutral” cool component wind (Figure 6.7). For Z And, the periodicity of attenuation was interpreted in terms of changes in the optical depths through the “neutral” wind with orbital phase (STB model). Since AG Peg supports a hot component wind as well as a cool component wind (*e.g.* Penston and Allen 1985; Kenny, Taylor and Seaquist 1991) a combined CW/STB model must be considered. The essential characteristics of the attenuation mechanism are essentially unchanged by the presence of colliding winds. The interaction and ionization cones would corotate and the “unilluminated” portion of the CWo nebula could begin to recombine and act as an absorbing medium for radiation from the CWb component.



- Hjellming (1985)
- Kenny (1989)
- ▲ 22 Nov 1984, VLA
- ▼ 27 Jul 1987, VLA
- ◆ 02 Mar 1990, VLA
- 19 Aug 1991, VLA
- ◇ 29 Dec 92, MERLIN

Figure 7.4: AG Pegasi: Central Flux Density Variations, 5 GHz
 Flux density measurements are plotted by orbital phase for observations as shown. The ephemeris of Belyakina (1985) has been used to compute phases: $\text{Min(UBV)} = 2439000 + 820\text{E}$.

7.3 The Inner Nebula: Visibility Analysis

Kenny, Taylor and Seaquist (1991) argue that the inner nebula represents the interaction front between colliding winds. This interpretation is consistent with the observed expansion velocity, mass and morphology of the inner nebula, as well as the observed simultaneous presence of both a Wolf-Rayet wind and a late-type wind (*e.g.* Penston and Allen 1985). The present observations support the earlier conclusions, as will be discussed, and permit the refinement of the earlier model.

Modelling of the inner nebula has been performed in the visibility domain. As previously noted (Section 4.1.4), this technique is preferred for sources, like AG Peg, which possess a high degree of circular symmetry. The resulting analysis provides azimuthally average quantities. The configuration assumed is that illustrated in Figure 7.5. The emitting region consists of a homogeneously filled, spherically symmetric shell. The free parameters include: the inner and outer radii of the shell, θ_o and θ_i respectively; the electron number density within the shell, n_e ; and the flux density, m , of the unresolved central component of emission. A distance of 0.6 kpc is assumed, consistent with commonly quoted values (table 4.3).

A spherically symmetric source will present a circularly symmetric intensity distribution on the plane of the sky. Visibilities may therefore be characterized by the absolute value of the associated antenna separation, regardless of the orientation of the observing antenna pair with respect to the source. For the purposes of modelling, therefore, data were binned by antenna separation ("baseline"). The fitted real visibility curve for the 01 Mar 1990 observations is shown in Figure 7.6, and its shape is reasonably typical of the other epochs of VLA observations as well. Fitted curves

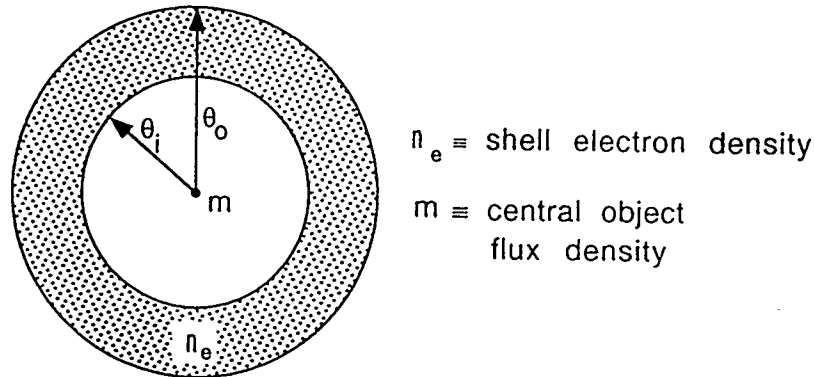


Figure 7.5: Spherical Shell Model

A spherical shell of ionized material has outer radius θ_o , inner radius θ_i , and a density of n_e . An unresolved source, with a flux density m , is located at the center of the shell.

are in good agreement with observed data, and values of the χ^2 merit function per point, for fits in the four epochs 1984, 1987, 1990, and 1991 were 0.7, 1.0, 1.7 and 1.2 respectively.

Fitted model parameters for the four epochs are shown in table 7.2. Values for the flux density of the unresolved component have been previously listed in table 7.1. The θ_i variations shown in table 7.2 reflect changes in the internal structure of the inner nebula (*cf.* Figure 7.1), and decreases in θ_i should not be strictly interpreted as inward movement.

The values of outer radius listed in table 7.2 have been plotted in Figure 7.7, and provide quantitative confirmation of the expansion of the inner nebula. The nominal expansion rate is $72 \pm 9 \text{ km s}^{-1}$ (for a distance of 0.6 kpc). The nonlinearity of the data in Figure 7.7 might suggest that an acceleration has taken place between 1990 and 1991, and may be related to the observed changes in lobe enhancements. If a “centre of mass radius”, $\theta_c \equiv 1/M \int_{\theta_i}^{\theta_o} \theta dM$, is used in place of θ_o , a much more linear expansion is suggested at a rate of $53 \pm 4 \text{ km s}^{-1}$ ($\chi^2/\text{point} = 0.89$). In

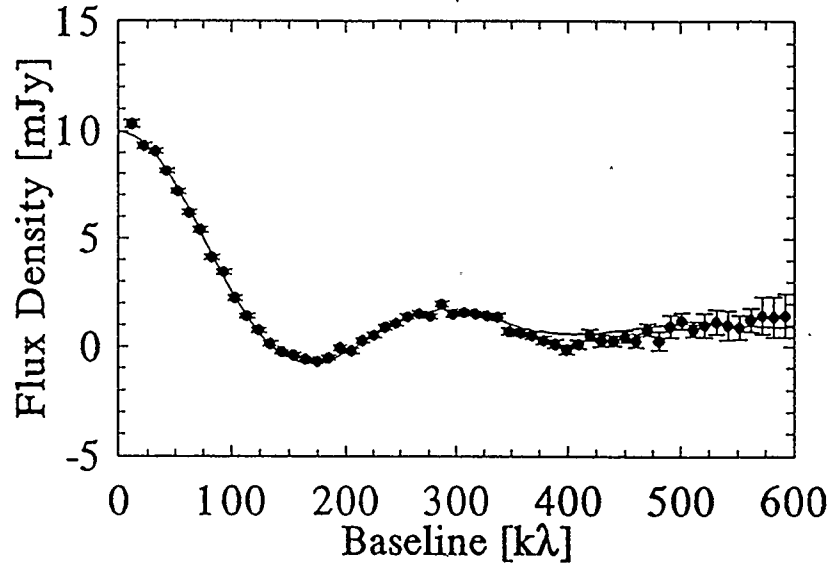


Figure 7.6: Fitted Visibility Curve: AG Pegasi, 01 Mar 1990, 5 GHz
 Real visibilities are plotted along with a fitted curve derived from the spherical shell model (Figure 7.5). Model parameters are shown in table 7.2.

Epoch	θ_o ["]	θ_i ["]	n_e [10^4 cm^{-3}]
22 Nov 1984	0.934 ± 0.020	0.536 ± 0.032	1.78 ± 0.073
27 Jul 1987	0.978 ± 0.015	0.646 ± 0.019	2.26 ± 0.083
02 Mar 1990	1.018 ± 0.010	0.681 ± 0.011	2.22 ± 0.067
19 Aug 1991	1.120 ± 0.013	0.592 ± 0.035	1.66 ± 0.045

Table 7.2: Nebular Shell Model: Fitted Parameters for AG Pegasi
 The uncertainties indicated are formal fitting errors.

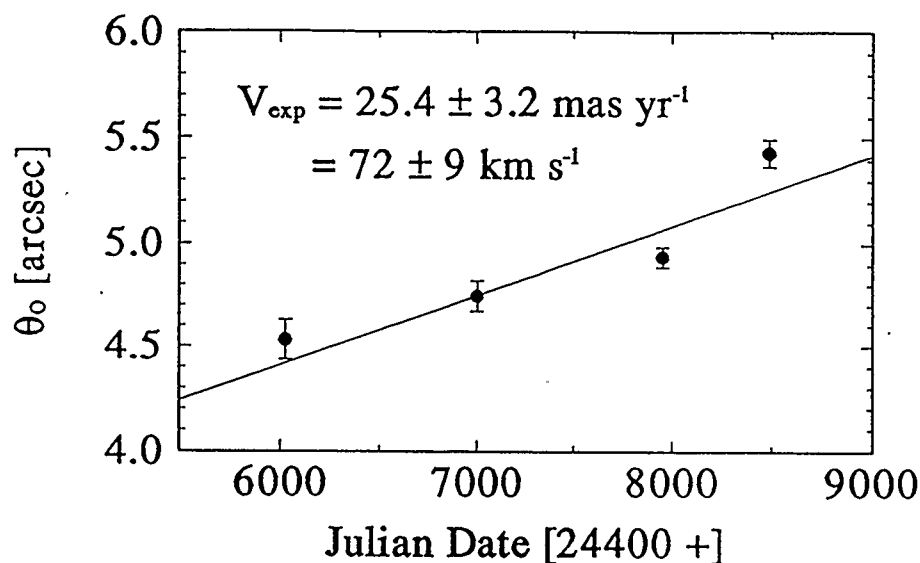


Figure 7.7: AG Pegasi, Expansion of the Inner Nebula

Values of θ_0 from table 7.2 have been plotted by epoch. The solid line represents a linear least squares fit, whose slope is given by the velocities indicated.

the next section, a model will be discussed which postulates an episode of increased hot component mass loss beginning sometime slightly before 1984. The effects of this increased mass loss would reach the inner nebula ~ 1991 , consistent with the acceleration suggested in Figure 7.7. An expansion velocity of 72 km s^{-1} implies a kinematic age of $\sim 36 \text{ yr}$ for the inner nebula, and points back to the epoch of the secondary outburst (Figure 4.3).

It should be emphasized that the expansion of the inner nebula is a model independent result. The physical expansion of an arbitrary nebula is observed in radio interferometric data as an inward scaling of the characteristic visibility curve with baseline. Figure 7.8 demonstrates that this type of scaling is exhibited by the inner nebula between 1984 and 1991.

A further quantity of interest which may be derived from the spherical shell model

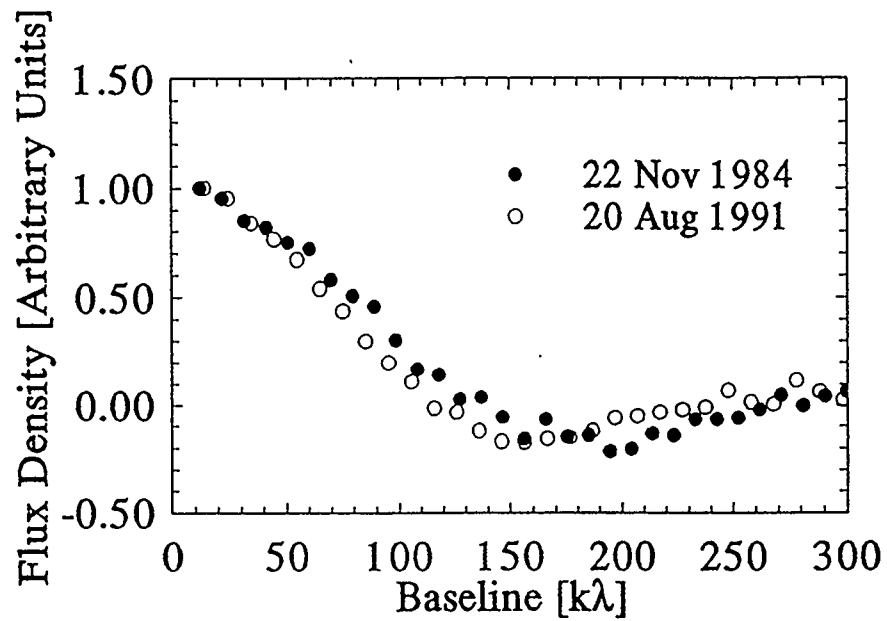


Figure 7.8: AG Pegasi: Evolution of Real Visibility Curves

Real visibility data corresponding to the inner nebula in 1984 and 1991 are plotted to demonstrate the inward scaling of the profile with time. Uncertainties on data points are smaller than the size of the plotted points.

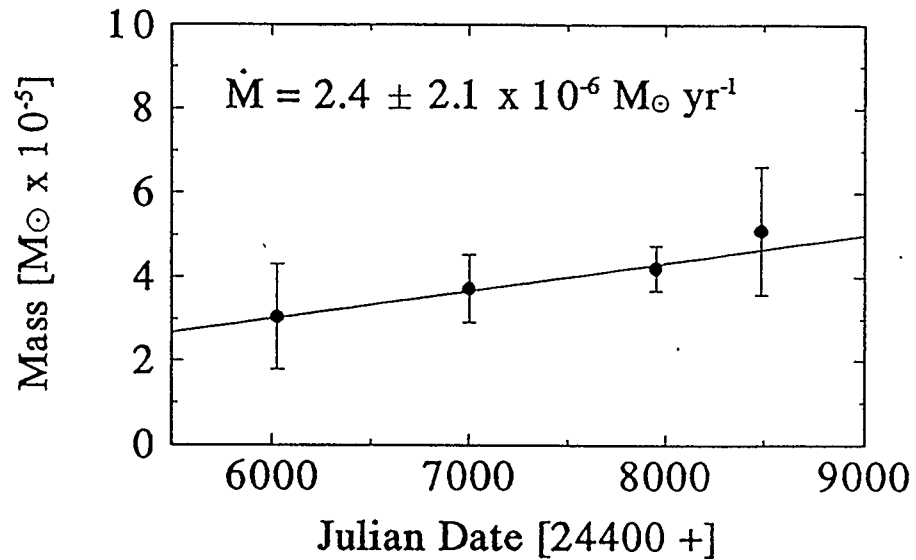


Figure 7.9: **AG Pegasi: Mass of the Inner Nebula by Epoch**
 Values of mass for the inner nebula have been computed from the fits given in table 7.2.

is the nebular mass. Computed values are plotted in Figure 7.9 by epoch. Although uncertainties are very large, there is a suggestion of net mass accumulation in the shell at the nominal rate of $2.4 \times 10^{-6} M_{\odot} \text{yr}^{-1}$. The average value of mass over the four epochs is $4.0 \pm 0.5 \times 10^{-5} M_{\odot}$.

7.4 Lobe Enhancements of the Inner Nebula

The above discussion has provided a consistent explanation for the inner nebula as an interaction shell that expands globally ($60\text{-}70 \text{ km s}^{-1}$), and sweeps up mass from the pre-existing cool component wind. Further structure within the inner nebula indicates refinements of this picture.

The images of Figure 7.1 reveal that the structure within the inner nebula evolves with time. In 1984 it appeared that elongation was developing from the central region

toward the north and south, and perhaps also to the west. By 1987, the NS features had progressed significantly, and the southern component appeared to be broadening. In 1990, the NS enhancements were no longer evident, and the regions which they previously occupied were relatively devoid of emission; this apparent evacuation was offset by significant growth to the west. The 1990 pattern continued through 1991: the NS voids widened further, and the western enhancement expanded.

In Figure 7.10, the images of Figure 7.1 have been reproduced with the central point source subtracted from the visibility data. The flux density subtracted in each epoch is that obtained from the visibility analysis of the previous section (table 7.2). The morphological evolution described in the previous paragraph is more easily seen in these images. Here, the dotted lines have been drawn to illustrate the CW interpretation to be described below. At this point they may serve to indicate an axis of "symmetry", defined largely by the NS enhancements in 1987, at a position angle of $\sim -15^\circ$.

With the benefit of having removed the central object, the dynamics of the lobe enhancements is clarified. Ignoring for the moment the western enhancement in the 1984 image, it would appear that some form of outflow in the NNW-SSE direction has begun in 1984; the separation of enhancements along this axis is $1.''05$. The same features persist in 1987, but the separation has increased to $1.''30$, indicating an outflow velocity from the center of approximately 50 mas/yr. At a distance of 0.6 pc this corresponds to a velocity of 133 km s^{-1} , or about twice as fast as the average expansion rate of the entire nebula.

By 1987 the southern component of outflow has begun to flare to east and west. This process is further advanced in 1990; the southern lobe has apparently divided

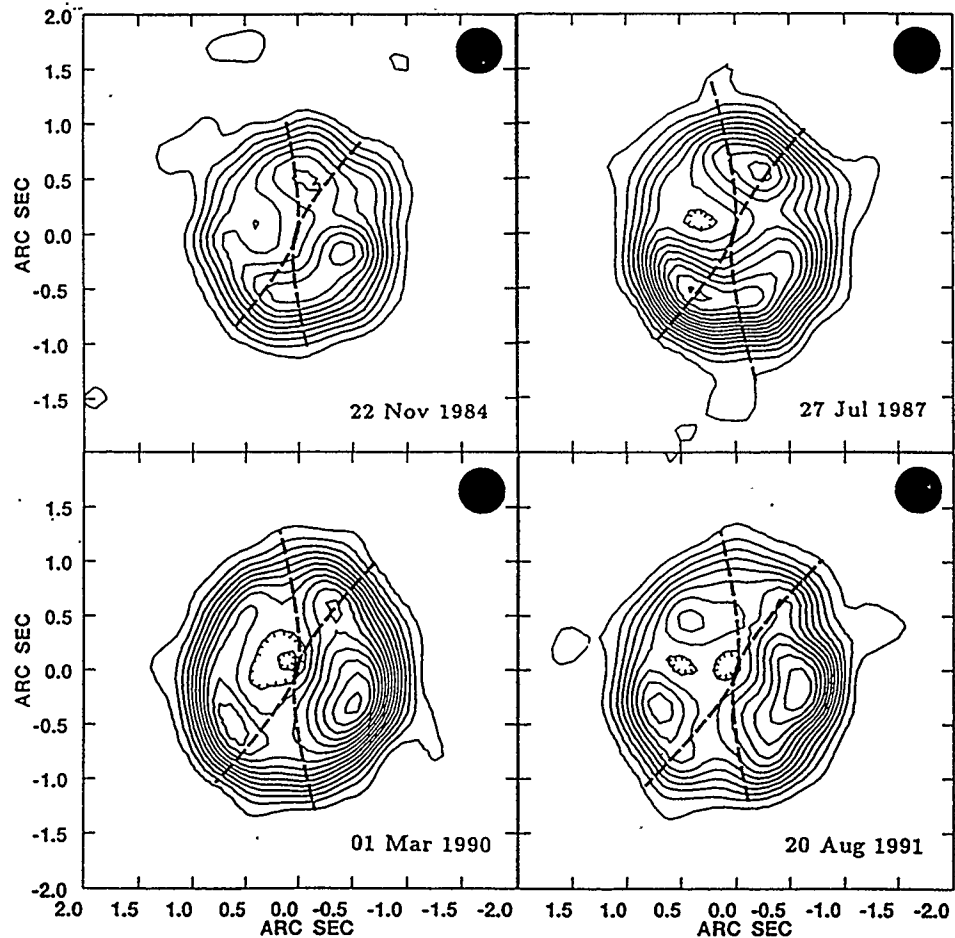


Figure 7.10: AG Peg: 5 GHz Images with Central Source Subtracted
 Plotted images correspond to the same observations as shown in Figure 7.1, with the central point source subtracted. Hatched contour lines designate depressions. The dashed curves in each image represent the interaction boundary, rotated about the orbital axis, in accordance with the CWo model (Section 7.5, C-facing geometry).

into an eastern and western component, leaving the southern region relatively evacuated. By 1991 the new eastern and western components have separated still further so that the southern void is more pronounced. In 1991 it is also apparent that a similar process has taken place in the north: the original direction of outflow has become relatively devoid of emission, while new features are becoming evident in the east and the west. During this process the entire nebula has continued to expand (Figure 7.7).

The processes observed in Figure 7.10 may be understood in terms of a CW system with *variable hot component mass loss*, as illustrated in the schematic diagram of Figure 7.11. In this model, the inner nebula represents the interaction front between the CWo nebula and the remnant cool component wind (Section 3.3.4). If the interaction cone is H-facing in the epoch preceding the 1984 observations, no polar interaction caps will form. Cool component wind will flow freely into the polar directions.

Suppose now that the hot component mass loss rate becomes enhanced so that the geometry in the inner system becomes C-facing. The polar directions will now be subjected to hot component wind as shown in panel II of Figure 7.11. Polar interaction caps will begin to develop as the hot component wind contacts the cool component wind previously occupying these directions.

If the mass loss rate from the hot component subsequently returns to its pre-excitation level, the central interaction will return to an H-facing configuration, and the hot component wind will again be excluded from the polar directions. The time scale upon which the hot component wind is excluded from the poles is roughly the time required for the asymptotic cone angle to be reestablished in the inner system;

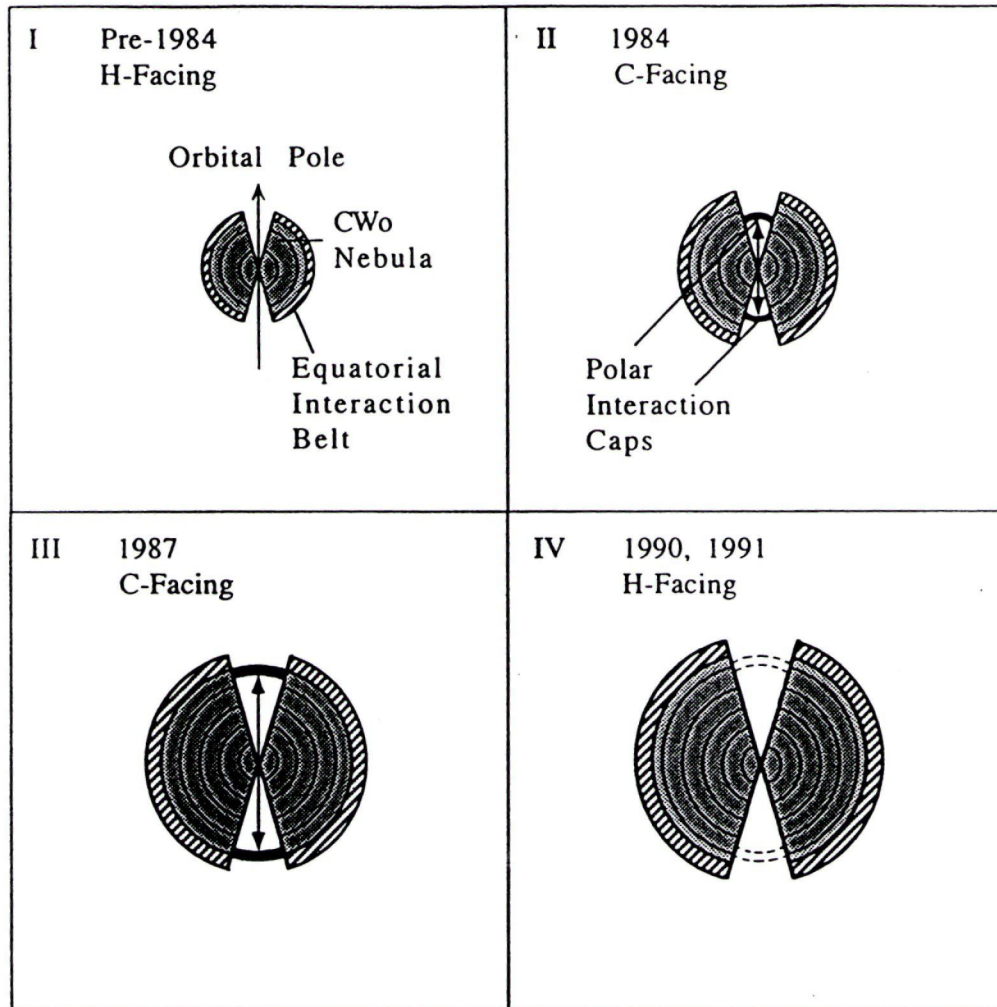


Figure 7.11: A Model of Lobe Enhancements of the Inner Nebula

- I) A CW system with central H-facing geometry, including binary motion.
- II) Increased hot component mass loss leads to C-facing geometry and the development of polar interaction caps.
- III) Polar interaction caps advance more quickly than the equatorial interaction belt (Section 3.3.4).
- IV) The hot component mass loss rate returns to pre-enhancement levels, and H-facing geometry is restored.

Evolutionary stages of the model may be compared to the morphologies observed in epoches as labelled (Figure 7.10).

this time scale may be approximated by the time required for the cool component wind ($v_2 \sim 10 \text{ km s}^{-1}$) to travel a binary separation ($\sim 2.5 \text{ AU}$), *i.e.* $\sim 1.2 \text{ yr}$. Since the polar interaction caps are no longer driven by the hot component wind, they will fade on a thermal time scale. For the model parameters to be discussed in the next section, the polar interaction caps have a thickness of $\sim 15 \text{ AU}$; at a thermal velocity of $\sim 10 \text{ km s}^{-1}$, *i.e.* $T \sim 10^4 \text{ K}$, the cap thickness will increase by a factor of ~ 1.33 in the 2.6 period between the 1987 and 1990 observations, implying a decrease in optically thin flux density by a factor of ~ 2 .

The postulated fluctuations in hot component mass loss rate will also affect the CWo nebula. As the rate increases, spiral walls will become more highly compressed and more widely spaced. For the model parameters discussed in the next section, v_{sp} increases from 150 to 250 km s^{-1} , and the “steady-state” spacing between spiral walls (*i.e.* Pv_{sp} where P is the orbital period) increases by a factor of 1.7. The further interaction of the spiral walls with the pre-existing cool component wind will give rise to the inner nebula, moving considerably slower than v_{sp} (Section 7.5).

The model introduced here includes a single new requirement: *i.e.* the variability of the hot component mass loss rate. This possibility appears to be supported by the fact that the flux density of the central component is observed to vary strongly from cycle to cycle (Figure 7.4). Further, fluctuations are also observed in the flux density and expansion rate of the inner nebula (table 7.1, Figure 7.7), as might be expected since increased momentum of the hot wind would also accumulate in the shell. Finally, fluctuations in the hot component wind are suggested by observed UV variability (*e.g.* Choccol, Komárek and Vittone 1988, C IV 1458, 1550 Å line fluxes).

7.5 CW Model Images and Spectra

The CW model proposed in the previous section (Figure 7.11) is in qualitative agreement with the morphology and evolution of the inner nebula. The quantitative aspects of the model will now be examined.

The primary input parameters for all CW models include: distance; binary separation; and mass loss rates and velocities from the stellar components. Many of these parameters are reasonably well known for AG Peg, and therefore the present modelling problem is somewhat simplified. The orbital period is known from both photometric and spectroscopic studies (*e.g.* Belyakina 1985; Garcia and Kenyon 1988), and has a value of 820 ± 5 d. This period implies a binary separation of 2.5 AU for a total system mass of $\sim 3 M_{\odot}$ (table 4.6). A distance of 0.6 kpc will be assumed, consistent with published values shown in table 4.3. A value of 10 km s^{-1} will be assumed for the velocity of the cool component wind, which is reasonable for late-type stars. A value of 900 km s^{-1} will be used for the hot component wind velocity, consistent with the UV observations of Penston and Allen (1985). The undetermined parameters are the mass loss rates from the hot and cool components. The ratio of the mass loss rates follows immediately from X_{cwb} (Equation 3.29), which may be well estimated from the observed image morphology. For a given value of X_{cwb} , the individual mass loss rates are uniquely determined by the observed flux density.

In Figure 7.12 two examples of model nebulae are shown. Model parameters for the upper image have been selected to reproduce, as best as possible, the 1987 morphology. C-facing geometry is required in order to produce polar interaction caps, and the relative extent of the observed polar enhancements suggest an interaction

cone opening angle of 70° , or equivalently $X_{\text{cwb}} = 11$.

The individual mass loss rates required to obtain a flux density of 9 mJy were: $\dot{M}_1 = 6.0 \times 10^{-8} M_\odot \text{yr}^{-1}$ and $\dot{M}_2 = 2.1 \times 10^{-7} M_\odot \text{yr}^{-1}$. The value of $\dot{M}_2 = 2.1 \times 10^{-7} M_\odot \text{yr}^{-1}$ for the cool component mass loss rate is in reasonable agreement with the value of $\dot{M}_2 = 3 \times 10^{-7} M_\odot \text{yr}^{-1}$ obtained by Kenny, Taylor and Seaquist (1991) from the known density of the intermediate nebula (Kenny, Taylor and Seaquist 1991, Figure 4.4). In order to obtain polar interaction caps of appropriate flux density, it was necessary to assume a filling factor of 0.6 in the polar directions; this assumption may be reasonable in view of the long refilling times of the polar regions between episodes of enhanced hot component mass loss (*e.g.* 600 AU at $10 \text{ km s}^{-1} = 285 \text{ yr}$). A polar cap radius of $0.''8$ has been used. The model image for C-facing geometry in Figure 7.12 is in reasonable agreement with the 1987 morphology (Figure 7.10). In particular it exhibits a roughly circular appearance while maintaining internal bipolar enhancements, and a central depression. The dotted lines in the observed images in Figure 7.10 represent the interaction boundary, in C-facing geometry, for the parameters derived here.

The lower model image in Figure 7.12 uses the same parameters as the upper image, with the exception that the hot component mass loss rate has been reduced by a factor of 3 to $2.1 \times 10^{-8} M_\odot \text{yr}^{-1}$. The result of this decrease is that the interaction cone widens to an opening angle of 110° , so that the configuration is now H-facing. Since the hot component wind is now excluded from the polar regions, no interaction occurs in the polar direction. The lower image in Figure 7.12 represents a "steady state" (apart from the shell expansion), and so no interaction caps are shown. In the absence of interaction caps, the flux density is reduced to 6.9 mJy.

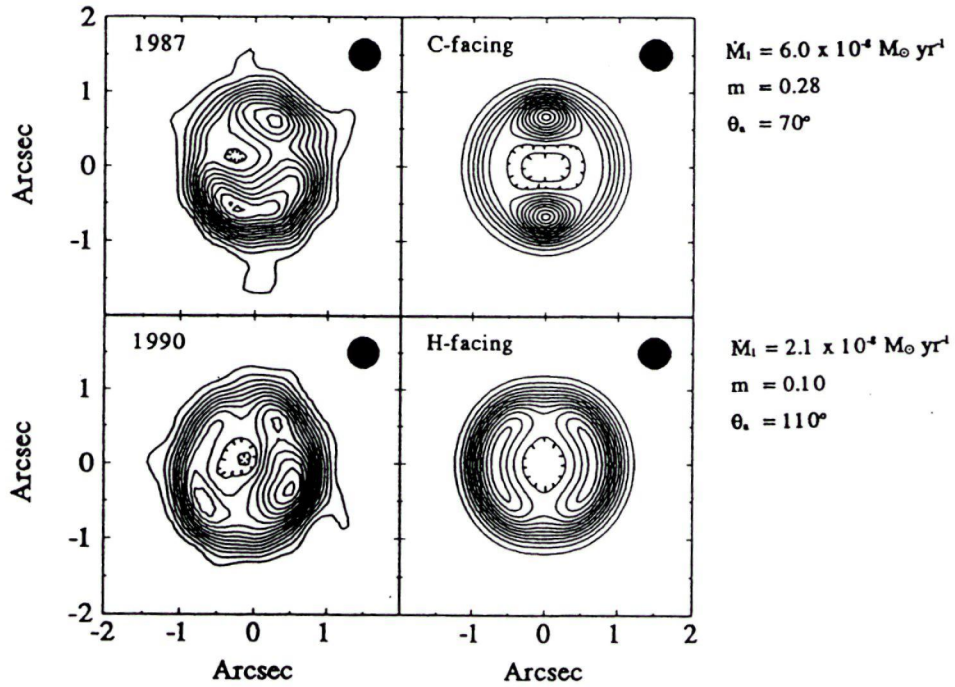


Figure 7.12: AG Peg: CW Model Images for the Inner Nebula

Model images are shown next to observed images with which they may be compared. Parameters common to both model images include: a distance of 0.6 kpc; a binary separation of 2.5 AU; a hot component mass loss velocity of $v_1 = 900 \text{ km s}^{-1}$; a cool component mass loss velocity of $v_2 = 10 \text{ km s}^{-1}$; a cool component mass loss rate of $\dot{M}_2 = 2.1 \times 10^{-7} M_{\odot} \text{ yr}^{-1}$; an inclination of 65° ; and a projected position angle of the polar axis of -15° . Model beam sizes and contour levels are consistent with values in the observed images. Hatched contour lines represent depressions.

The morphology shown in this image is in reasonable agreement with the observed morphologies in 1990 and 1991. The overall intensity distribution is highly circular, while ridges corresponding to the equatorial interaction belt give internal structure to the nebula.

The C-facing model suggests a polar cap velocity of 70 km s^{-1} and an equatorial belt velocity of 46 km s^{-1} , in reasonable agreement with the measured expansion velocity of the inner nebula of $72 \pm 9 \text{ km s}^{-1}$, and the “center of mass” expansion velocity of $53 \pm 4 \text{ km s}^{-1}$. The spiral wall velocity in H-facing geometry is 150 km s^{-1} implying the existence of 8.5 spiral wrappings within the CWo nebula out to $1''$ (600 AU at 0.6 kpc). The velocity in C-facing geometry is increased to 250 km s^{-1} , and the number of spiral wrappings is decreased to 5. As the C-facing configuration establishes itself, a density wave will travel outward in the CWo nebula and sweep the excess 3.5 spiral wrappings into the equatorial interaction belt, giving rise to enhanced emission in the inner nebula (*cf.* Figure 7.10, 1990 and 1991). The total mass contained within the model interaction belt and interaction caps is $4.0 \times 10^{-5} M_{\odot}$, in agreement with the average value across the four epoches obtained in Section 7.3 ($4.0 \pm 0.5 \times 10^{-5} M_{\odot}$) from a simple shell model.

A consistent treatment of the CW configuration must also include the central contribution of the CWb interaction. In Figure 7.13, spectra for the CWb nebula corresponding to the model parameters discussed above are plotted against the observed spectrum of the central source. The model curves correspond to the C-facing geometry (upper panel, Figure 7.12) at a viewing angle of 0° , and the H-facing geometry (lower panel, Figure 7.12) at a viewing angle of 90° . Model curves corresponding to C-facing geometry at 90° , and H-facing geometry at 0° , lie between the plotted

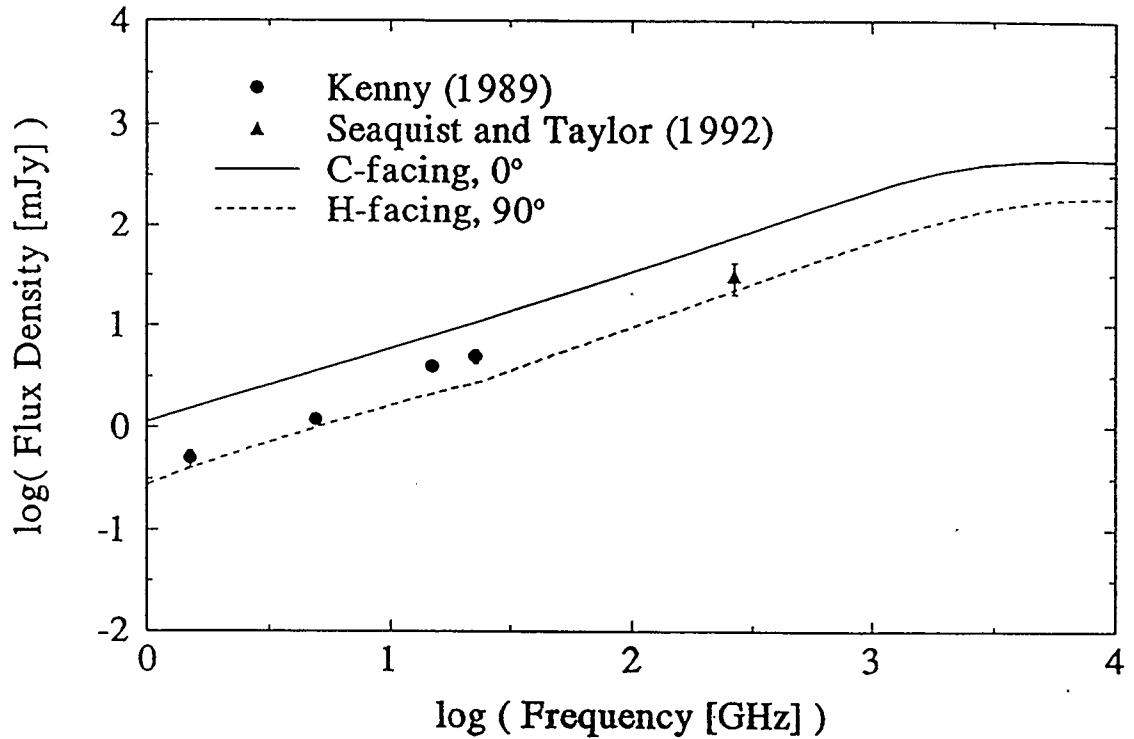


Figure 7.13: AG Peg: Model Spectra of the Central Object

Model spectra are plotted for a CWb nebula with model parameters corresponding to those of Figure 7.12. The geometries and viewing angles of the model curves are shown in the plot. The radio data points represent an “average spectrum” between 1984 and 1987, from the multi-epoch study of Kenny (1989).

curves, and correspond fairly closely to the observed spectrum of the central object. It may be concluded that both the flux density and spectral index of the central object are consistent with those of the suggested by the CW model. This is especially convincing support of the model since parameters have been selected to reproduce the characteristics of the inner nebula, and not those of the central component.

Figure 7.14 shows a model image of the CWb nebula (the central component) with C-facing geometry and a viewing angle of 90° for the model parameters derived above. Although the model morphology is crescent shaped, and the observed morphology is bipolar (Figure 7.3), the agreement is reasonable given the noise level

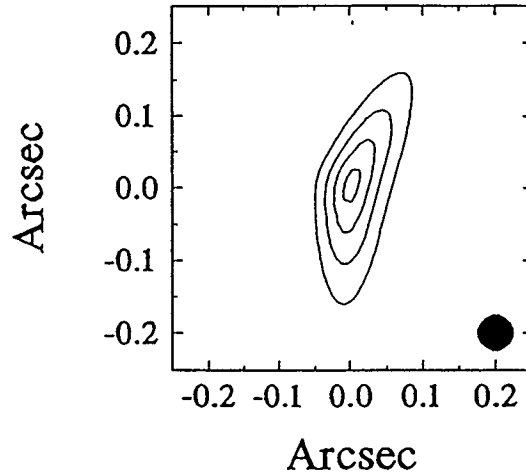


Figure 7.14: AG Peg: Model Image of the Central Object

The model parameters used are those selected to reproduce the observed characteristics of the inner nebula (C-facing case, upper panel of Figure 7.12). The CWb component is plotted here, while the CWo/CWc components are plotted in Figure 7.12. The position angle of the orbital pole projected on the plane of the sky is -15° . Contours are drawn with linear spacing.

of the observed image. If the central object is truly bipolar in the present epoch, this may suggest the additional presence of discrete polar ejection, similar to that giving rise to the outer nebula (Figure 4.4).

7.6 Aspects of the Binary System

In the context of the CW model proposed in the previous sections (Figure 7.11), it is possible to investigate further fundamental properties of the symbiotic system.

The model would suggest that the orbital pole has a position angle of $-15^\circ \pm 10^\circ$ on the plane of the sky. This is the direction in which lobe enhancements appear to grow in 1984 and 1987, and the direction in which voids of emission appear in 1990 and 1991. The orientation of outer nebula ($-40^\circ \pm 10^\circ$, Figure 4.4) is also in rough

agreement with the suggested polar direction. Kenny, Taylor and Seaquist (1991) suggest that the outer nebula is the remnant of a bipolar ejection associated with the 1850 symbiotic outburst of the system. Under this interpretation, its bipolar axis might be expected to be approximately aligned with the orbital pole.

The orbital inclination may also be investigated. An upper limit of inclination may be derived from the absence of observed optical eclipses. For a binary separation of 2.5 AU, and a cool component radius of $\sim 120 R_{\odot}$, eclipses will be observed unless $i \lesssim 77^{\circ}$. A somewhat stronger constraint ($i < 70^{\circ}$) may be inferred in the context of the CW model since the inner nebula exhibits an overall circularity in the presence of polar voids. For values of inclination exceeding 70° , the outer contour lines of the model inner nebula dip significantly toward the nebular centre, and the overall circular symmetry is broken. A value of $i \sim 65^{\circ}$ was found best for model imaging (Figure 7.12), and is in agreement with the lower limit of inclination given by Hutchings *et al.* (1975; $i > 45^{\circ}$) on the basis of the deep photometric and spectroscopic variations which are observed. The true value must be bracketed by the identified limits, *i.e.* $i \sim 45 - 70^{\circ}$.

The circularity of the inner nebula is also a strong indicator of the nature of mass loss from the stellar components. In particular, it would appear unlikely that the cool component mass loss is significantly equatorially enhanced. If the cool component wind was concentrated toward the equator, the interaction shell would proceed more slowly on the equatorial plane. An hour glass morphology would then develop, in contrast to the observed circular distribution. Similarly, a nonsymmetric hot component wind might lead to noncircular intensity profiles for $45^{\circ} < i < 70^{\circ}$.

7.7 Conclusions

This study of AG Pegasi has led to a number of model independent conclusions:

- The inner nebula is expanding.
- Lobe enhancements within the inner nebula evolve on the time scale of years.
- A preferred axis in the inner nebula exists to the NNW and SSE, along which lobe enhancements and voids of emission are alternately observed.
- The central object in the MERLIN/VLA image (Figure 7.3, lower panel) exhibits elongation along an axis which coincides with the bipolar axis of the outer nebula (Figure 4.4).
- The central object is variable. Although variability appears to correlate with orbital phase, significant changes from cycle to cycle are also observed.

Modelling of the inner nebula suggests further detail.

- The average expansion velocity of the inner nebula between November 1984 and August 1991 is $72 \pm 9 \text{ km s}^{-1}$, and an acceleration may have been experienced beginning in ~ 1990 .
- The inner nebula is well modelled as a spherical shell, and may be understood as the interface between colliding winds. Its mass is $4.0 \pm 0.5 \times 10^{-5} M_{\odot}$, and appears to be increasing.
- The mass loss rate of the cool component is $\sim 2 \times 10^{-7} M_{\odot} \text{ yr}^{-1}$.

- The mass loss rate of the hot component appears to be variable, and may take values in the range of $\sim 2 - 6 \times 10^{-8} M_{\odot}\text{yr}^{-1}$.
- The dynamics of lobe enhancements in the inner nebula may be understood qualitatively and quantitative in terms of an episode of increased hot component mass loss.
- The position angle of the orbital pole, projected on the plane of the sky is $-15^{\circ} \pm 10^{\circ}$.

The CW model proposed for AG Peg, including variable hot component mass loss, is successful in many ways. It is able to explain the overall circular symmetry of the inner nebula as well as the internal development of bipolar emission features and voids. It also suggests a mechanism through which circular symmetry may be broken and subsequently reestablished (inner nebula, 1987, Figure 7.10). The model parameters selected to reproduce the characteristics of the inner nebula also predict a central component of emission (CWb nebula), whose flux density and spectrum are in agreement with the observed properties of the central source.

Chapter 8

HM SAGITTAE and V1016 CYGNI

8.1 Images

Observations of HM Sge and V1016 Cyg included high-resolution, high-sensitivity observations at the VLA, at 5 GHz as listed in table 4.10. Near-simultaneous observations were also scheduled at 5 GHz at MERLIN (Eyres *et al.* 1995, and Eyres 1995).

HM Sge

Figure 8.1 shows the MERLIN and VLA images for HM Sge. At the center of the MERLIN image there exists a depression in intensity which is bracketed by ridges of emission. These ridges are separated by $\sim 0.''15$, are roughly parallel to each other, and have peak brightness temperatures of $\sim 4.5 \times 10^4$ K. The outer structure of the nebula ($\sim 0.''6$) is highly elongated along a \sim NS axis which coincides with the axis of separation of the inner ridges.

The VLA image displays the structure on larger scales. Although the intensity distribution is more circularly symmetric than that of the MERLIN image, significant departures from circular symmetry are also apparent. The dominant axis of elongation is in approximate agreement with that of the outer structure in the MERLIN image.

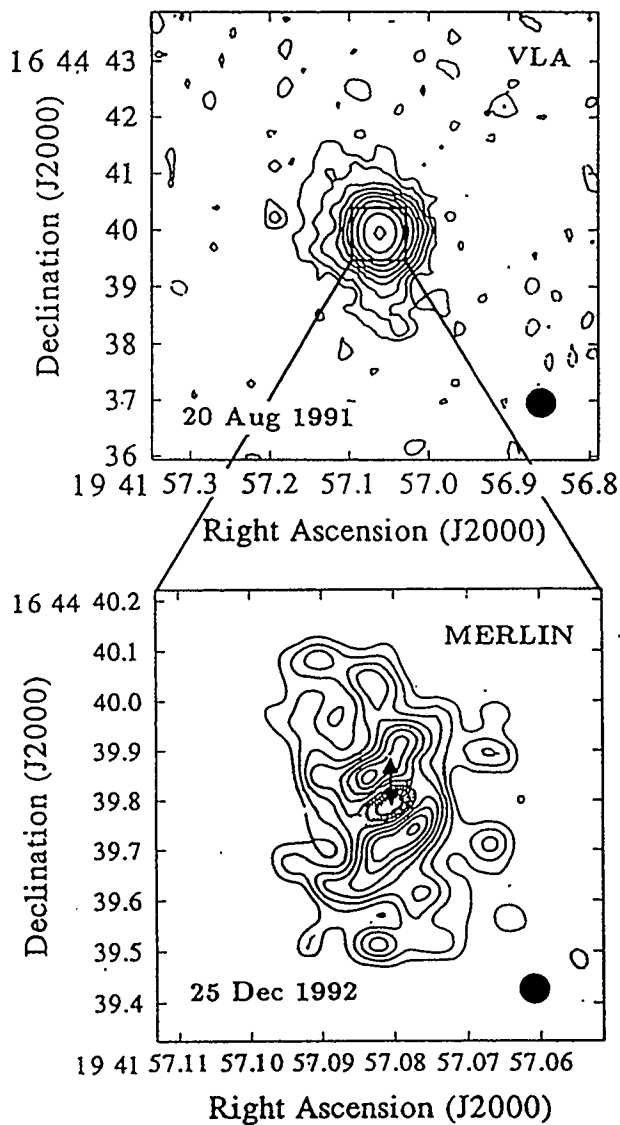


Figure 8.1: HM Sge: 5 GHz Images

Contours in the MERLIN image are evenly spaced at intervals of $270 \mu\text{Jy}/\text{beam}$. Intensities in the VLA image change by a factor of 2 between lines. Peak intensities are $31 \text{ mJy}/\text{beam}$ and $2.3 \text{ mJy}/\text{beam}$ for the VLA and MERLIN images respectively. The double headed arrow (\longleftrightarrow) in the MERLIN image is used to indicate the positions of the hot (south) and cool (north) components according to the model discussed in Section 8.6. VLA data are from Kenny *et al.* 1993. MERLIN data are from Eyres *et al.* 1995.

V1016 Cyg

Figure 8.2 shows the MERLIN and VLA images for V1016 Cyg; the similarities with HM Sge are striking. The MERLIN image of V1016 Cyg, like that of HM Sge, is dominated by two parallel ridges. The VLA image of V1016 Cyg, like that of HM Sge, shows structure on the scale of $\sim 4''$, which is elongated along an axis which coincides roughly with the axis of separation of the ridges.

8.2 Preliminary Discussion

HM Sge

Eyres *et al.* (1995) interpret the outer structure of the MERLIN image as preoutburst, cool component mass loss. The observed elongation is explained in terms of equatorial enhancement of mass loss, observed at high inclination. Both equatorial enhancement of mass loss and high inclination have been previously suggested from the radial velocity analysis of Solf (1984, Section 4.2.3, Figure 4.5). Under this interpretation, the polar axis should lie roughly at right angles to the axis of elongation of the outer MERLIN structure. That direction coincides with the axis of extension of a second circumstellar feature at 1.5 GHz ($\sim 1.''5$), also imaged by Eyres *et al.* (1995) with MERLIN.

Eyres *et al.* (1995) interpret the inner ridge features in Figure 8.1 in terms of a CW configuration. The hot component wind sweeps up a CWc shell as it overtakes the cool component wind, and the primary emission from this feature arises from the material swept up on the equatorial plane ("disk"). An equatorial disk viewed edge on may produce the observed ridge-and-hollow morphology if the center is

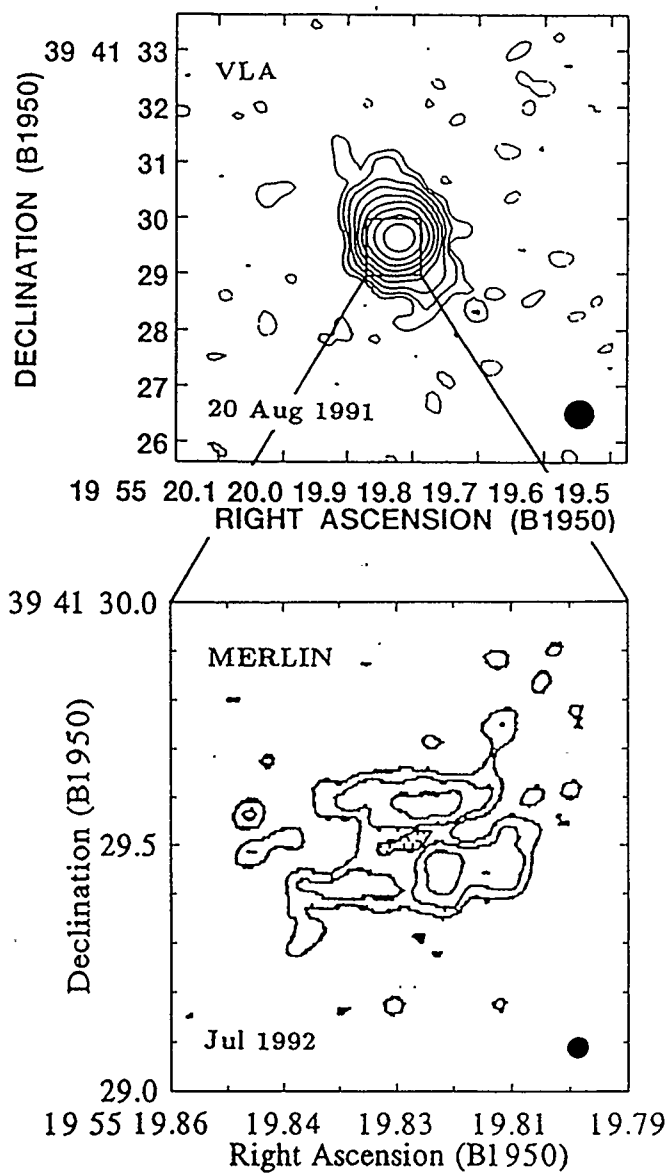


Figure 8.2: V1016 Cygni: 5 GHz Images

In both images, contours are drawn at intensities which change by a factor of 2 between lines. Peak intensities are 19 mJy/beam and 0.96 mJy/beam for the VLA and MERLIN images respectively. VLA data are from Kenny *et al.* 1993. MERLIN data are from Eyres 1995.

optically thin along the line of sight, and the extremities are optically thick. This interpretation of the observed ridge features is the same as that offered by Solf (1984) for his [N II] 'A' features. The orientation suggested by the radio morphology is also the same as that indicated by Solf (1984). Eyres *et al.* (1995) further point out that the location of the central depression in the MERLIN image corresponds closely with the location of peak emission in the UV (1880 Å) image of Hack and Paresce (1993). This correspondence is expected if the depression is filled with low density, highly ionized material, as assumed by the above model (hot component wind).

The new analysis of HM Sge offered in this work is generally in agreement with the model proposed by Eyres *et al.* (1995). It will be further suggested, however, that while the hot component may lie in the central depression, the cool component must be embedded in the northern ridge feature. That feature would then include emission not only from the elements of cool component wind swept up by the hot component wind, but also the ionized portion of free flowing cool component wind. This modified model suggests that the northern feature should remain optically thick to higher frequencies than the southern feature, as is in fact observed (Figure 8.4, Section 8.4).

The highly bipolar nature of the outer structure in the MERLIN image, contrasts with the more circular appearance of the VLA image in Figure 8.1. It may be suggested that mass loss in the epoch immediately preceding outburst was more highly equatorially enhanced. The development of equatorial enhancement would have the effect of increasing accretion onto the hot component (for constant mass loss rate), and might thereby encourage the initiation of an outburst.

V1016 Cyg

V1016 Cyg has also been previously modelled in terms of equatorially enhanced mass loss and high inclination (Solf 1983), and the images in Figure 8.2 are consistent with this interpretation. The parallel ridges in the MERLIN image, like those of HM Sge, would represent an interaction disk plus emission from the ionized portion of the free flowing cool component wind. The elongated structure in the VLA image would correspond to the undisturbed cool component halo, with the axis of extension representing the equatorial plane, projected on the plane of the sky.

8.3 Visibility Analysis

The 5 GHz VLA observations of HM Sge and V1016 Cyg show large scale nebular structure which is likely to correspond to the pre-outburst mass loss of the cool component, as noted above. Estimates of mass loss parameters have been obtained through the analysis of the real visibilities. Imaginary visibilities for both systems contained less than 1% of the flux density of the real components, justifying the approach taken.

The visibility analysis was performed using a spherical wind-shell model ($1/r^2$ density distribution) as described in Section 7.3. For neither of the systems were fits improved by placing a finite inner radius on the shell, and therefore a value of zero was assumed. Fitted parameters represent azimuthally averaged quantities.

The fitted curves for HM Sge and V1016 Cyg are shown in Figure 8.3, and are in good agreement with the data. The discrepancies at long baselines for HM Sge correspond to fine scale structure, and do not effect the general conclusions of

the analysis. V1016 Cyg was fitted straight forwardly by a simple spherical wind-shell. HM Sge could not be well fitted by a model of this type, and therefore a two component model was assumed in which the outer radius of the inner shell coincided with the inner radius of the outer shell. For both systems, the flux density of a central unresolved source was also included as a fitted parameter.

An electron temperature of 10^4 K has been assumed in this analysis and will be used as a standard throughout this chapter. In the outer regions, as being discussed in this section, 10^4 K is a reasonable estimate of the true electron temperature. Although higher temperature are likely to exist in the inner region of HM Sge (*e.g.* $\sim 45,000$ Eyres *et al.* 1995; $\sim 15,000$ Mürset *et al.* 1991; $\sim 25,000$ Li 1993), the results to be derived here are relatively insensitive to such departures. According to the stellar winds formulation of Wright and Barlow (1975), equivalent results are obtained for all models in which $n_e^2 T^{-1/2}$ is constant. Consequently, the fitted values of density (or \dot{M} for given v) may be multiplied by $\sqrt[4]{(T/10^4)}$ to obtain the values corresponding to some different temperature, T .

Table 8.1 lists the fitted model parameters. For HM Sge, the angular radius of the inner shell ($0.''31 \pm 0.''04$) is in rough agreement with that of the outer structure in the MERLIN image (lower panel, Figure 8.1). The requirement for a two component model to fit the visibilities is therefore in agreement with the observed existence of two distinct components in the halo. It is also of interest that the fitted value of \dot{M}/v for the inner component is a factor of four larger than that for the outer component. It may be suggested that, in the epoch immediately preceding outburst, the cool component wind was not only equatorially enhanced (see above), but also more massive.

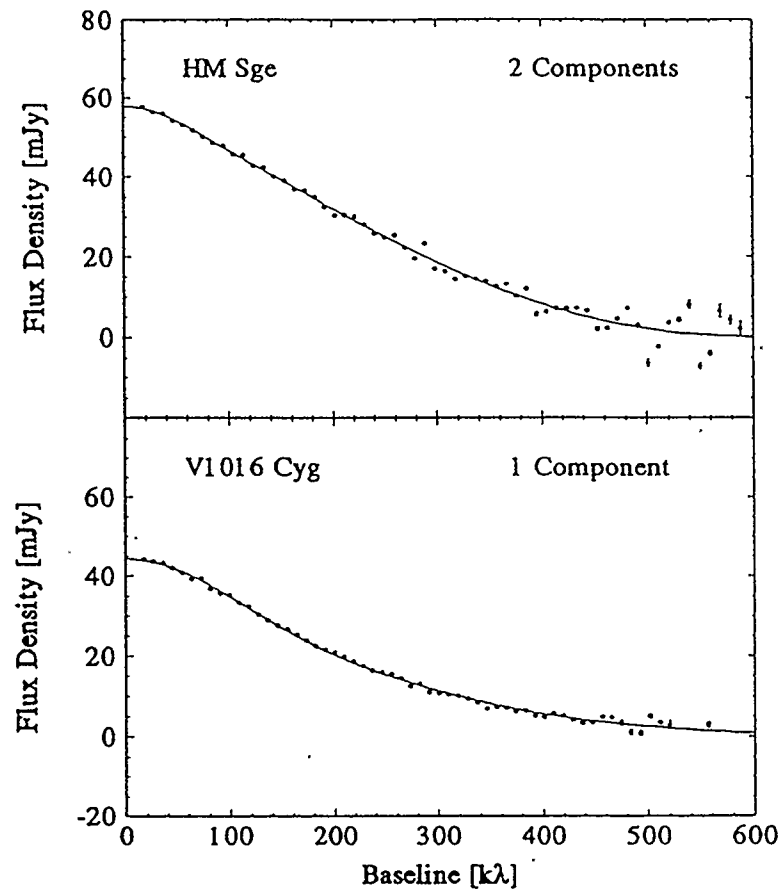


Figure 8.3: Real Visibility Fits: HM Sge and V1016 Cyg

Real visibilities for the 5 GHz VLA observations of HM Sge and V1016 Cyg (Figures 8.1 and 8.2) are plotted with fitted curves corresponding to a spherical wind-shell model (Figure 7.5). For both systems, the flux density of a central unresolved source was also included as a fitted parameter. The fitted model parameters are given in table 8.1.

	θ_{radius} ["]	\dot{M}/v [$M_{\odot}\text{yr}^{-1}$][km s^{-1}] $^{-1}$	Flux Density [mJy]
HM Sge			
Unresolved	-	-	5.0 ± 0.3
Inner	0.31 ± 0.04	$1.9 \pm 0.9 \times 10^{-7} D_{\text{kpc}}^{3/2}$	41 ± 1
Outer	1.8 ± 0.2	$5.1 \pm 0.3 \times 10^{-8} D_{\text{kpc}}^{3/2}$	15 ± 2
V1016 Cyg			
Unresolved	-	-	1.00 ± 0.03
Inner	1.0 ± 0.2	$6.62 \pm 0.02 \times 10^{-8} D_{\text{kpc}}^{3/2}$	43.4 ± 1.3

Table 8.1: Fitted Visibility Parameters: HM Sge and V1016 Cyg

Fitted visibility curves provide values of flux density through the extrapolation of real visibilities to zero baseline. Flux densities are listed by component in table 8.1, and the total flux densities for HM Sge and V1016 Cyg are 57.8 ± 0.4 mJy and 44.3 ± 1.4 mJy respectively. The value obtained for HM Sge is in close agreement with the value of 58 ± 3 mJy reported for 18 September 1987 by Li (1993). It would appear that the flux density did not change significantly in the four year period between 1987 and 1991. This conclusion is of interest since the results of Li (1993) indicate that the flux density was steadily increasing by ~ 2.3 mJy/yr between 1981 and 1987.

Date	Major Feature [mJy]	Minor Feature [mJy]	Separation ["]	Position Angle [°]
16 Feb 82	134.03	25.00	0.062 ±0.010	151 ±1
10 Nov 83	132.26	69.71	0.064 ±0.010	158 ±1
18 May 86	143.85	31.21	0.102 ±0.010	162 ±1
20 Sep 87	148.24	22.92	0.108 ±0.010	170 ±1
18 Dec 88	145.56	22.22	0.122 ±0.010	172 ±1

Table 8.2: Binary Nebular Features of HM Sge at 22.5 GHz

8.4 HM Sge: Expansion and Position Angle Rotation

Figure 8.4 shows 22.5 GHz images of HM Sge from 5 epochs between 1982 and 1988 (Li 1993). Binary nebular features are observed in the inner regions of each image, and Li (1993) notes that the separation between the features is increasing with time. The position angle between the features is also advancing, as indicated.

Separations and position angles of the nebular features are listed by epoch in table 8.2, and are plotted in Figure 8.5. A secular increase in both of these quantities is suggested, at the rates shown in the plots. The position angle rotation is expressed both as a rate of change of angle, and as an “apparent period” (assuming a constant rate of change through 360°).

Flux densities of the nebular features from Li (1993) are also listed in table 8.2 from Li (1993). The major component (~ 140 mJy) is very much stronger than the minor component (20 - 70 mJy) and appears of be slowly increasing in flux density. The minor component, following an initial increase in flux density, has subsequently

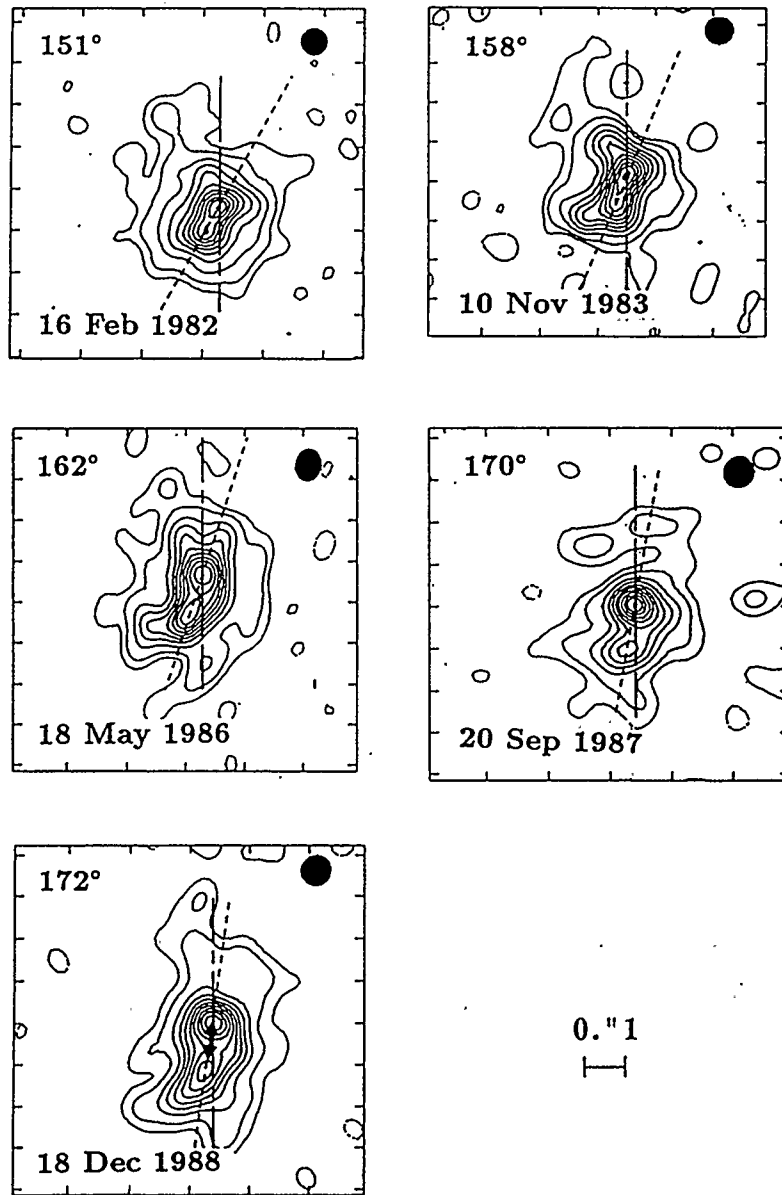


Figure 8.4: HM Sge: 22.5 GHz VLA Images between 1982 and 1988
(Data from Li, 1993.)

Solid lines are drawn in the NS direction, and dotted lines are drawn joining the major and minor nebular features in the images. Position angles between the lines are indicated in each image. The double headed arrow (\longleftrightarrow) in the December 1988 image is used to indicate the positions of the hot (south) and cool (north) components according to the model discussed in Section 8.6.

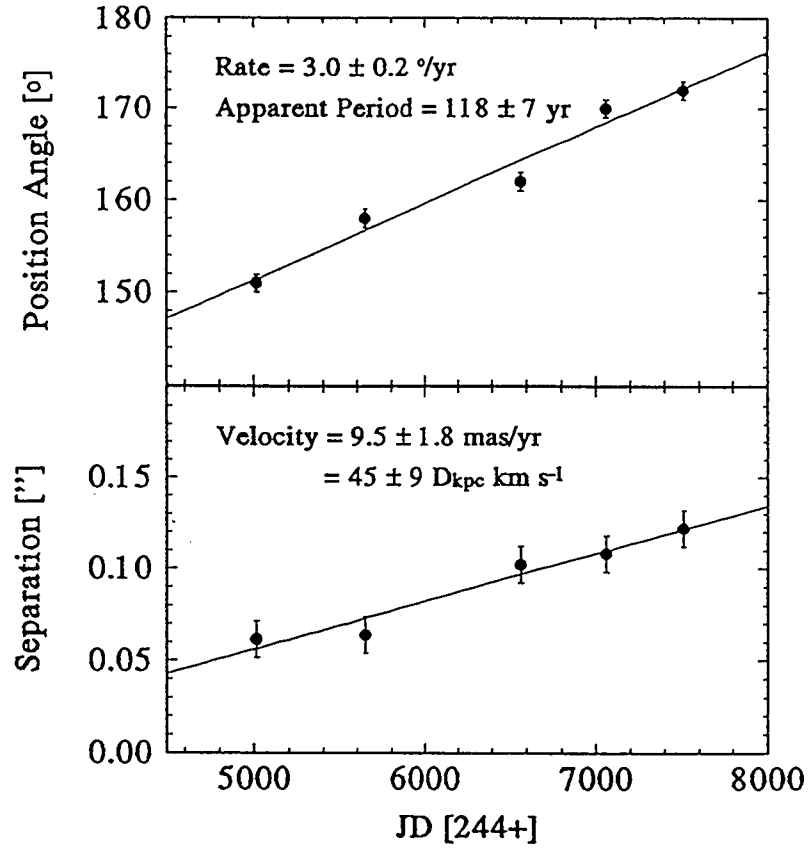


Figure 8.5: HM Sge: Evolution of Binary Nebular Features

Data from table 8.2 is plotted by epoch. Solid lines correspond to linear least squares fits, and the fitted slopes are indicated in each plot. The position angle rotation is expressed both as a rate of change of angle, and as an “apparent period” (assuming a constant rate of change through 360°).

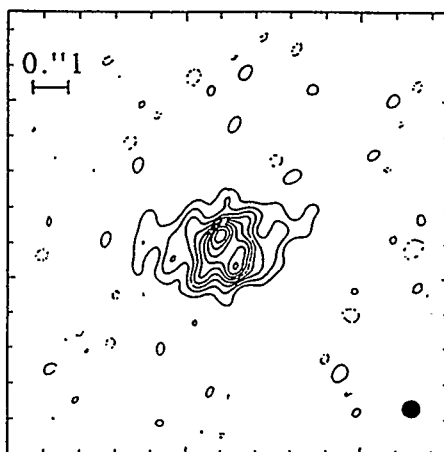


Figure 8.6: V1016 Cygni: 22.5 GHz VLA Image
(Data from Newell and Hjellming, 1981.)

begun to decrease.

Figure 8.6 presents an image of V1016 Cyg at 22.5 GHz (Newell and Hjellming 1981). The morphology of this image is strongly reminiscent of the 22.5 GHz images of HM Sge (Figure 8.4). In particular, the inner region consists of binary nebular features, one of which is very much stronger than the other. This close correspondence, together with the close correspondence of the 5 GHz images (Figures 8.1 and 8.2), suggests a similar physical configuration for both systems. If the ridges in the MERLIN image of V1016 Cyg (Figure 8.2) are the extremities of an equatorial disk as suggested by Eyres *et al.* 1995 for HM Sge, then the outer structure in Figure 8.6 is elongated along the polar axis. Polar ejection from the system has been previously inferred from optical emission line profiles (Solf 1983). No multi-epoch images at 22.5 GHz are available to investigate whether the binary nebular features of V1016 Cyg are in relative motion as observed for HM Sge.

8.5 STB/CW Model for HM Sge

A number of models have been previously proposed for the nebular regions associated with HM Sge. None of these models are able to accommodate the combination of position angle rotation and separation of the 22.5 GHz nebular features identified in the previous section. Li (1993) interpreted the major feature as the apex of a CWb interaction cone, and the minor feature as the CWc interaction zone between the hot component wind and the pre-outburst cool component wind. This model is capable of explaining the nebular expansion, but it does not immediately suggest a mechanism for position angle rotation. Hack and Paresce (1993) propose a model for their UV image (Figure 4.7, resolution similar to the 22.5 GHz images) involving a precessing jet. Although a precessing jet involves both a rotating position angle, and an outward progression of ejecta, the ejecta follow ballistic trajectories once expelled. The motion of the minor nebular feature about the major feature in the 22.5 GHz images of Figure 8.5 does not appear to be ballistic.

A model which is capable of producing both expansion and position angle rotation is illustrated in Figure 8.7. The model represents a synthesis of STB and CW characteristics, and will be referred to as the STB/CW model. The hot component provides ionizing photons to support an STB nebula, and also provides a high velocity wind to generate CW phenomena. Emission from the STB nebula is expected to dominate strongly for most combinations of input parameters (Section 3.1.7, Figure 3.9).

As applied to HM Sge, the STB/CW model would suggest that the major nebular feature observed at 22.5 GHz represents the STB nebula, while the minor feature is

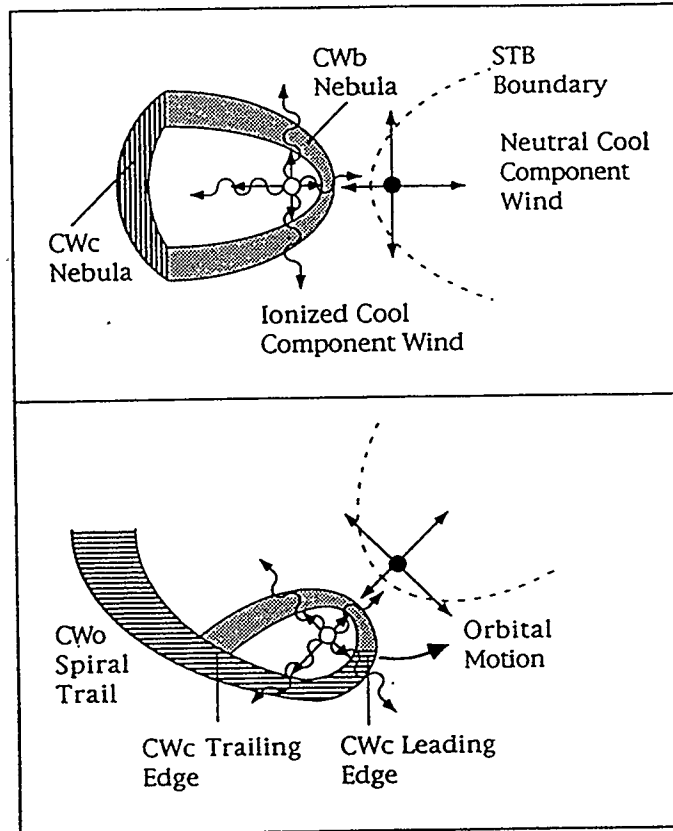


Figure 8.7: STB/CW Model for HM Sge

Top: The hot component (o) in a symbiotic system acts as the source of high energy photons and a high velocity wind. The high energy photons ionize a portion of the wind from the cool component (•) in accordance with the STB model. Bottom: Orbital motion of the stars leads to a rotation of the position angle between the nebular features. Projection effects due to orbital inclination may cause the observed separation between nebular features to change with time.

the CWc nebula swept up by the hot component wind. The primary emission from the CWb nebula occurs at the interaction apex, and is effectively merged with the emission peak from the STB nebula.

The model predicts apparent motion of the nebular features as illustrated in the lower panel of Figure 8.7. Each of the nebular features is closely associated with one of the stars and hence the emission peaks follow the stars in their orbital motion. The observed changes in separation of the nebular features arise due to the orbital inclination.

Some component of the observed increase in nebular separation may also arise from real expansion of the CWc nebula. Activity on the hot component was initiated relatively recently, and the orbital motion is apparently quite slow (apparent period ~ 120 yr). If a “steady state” has not yet been achieved, the minor feature (CWc nebula) may still be separating from the hot component.

It is important to note that the suggested configuration is not that described by the CWo model. The CWo model is concerned with the large scale structure after many spiral wrappings, and the apparent orbital motion observed in HM Sge suggests that less than one orbital cycle has taken place since the outburst began. Since a CWo nebula is in the process of developing, however, a “CWo spiral trail” should be observed on the trailing edge of the CWc nebula (Figure 8.7). Observational evidence for such a trail is arguably present in the “tear-spaced” morphology of a number of the 22.5 GHz images (*e.g.* 18 December 1988, Figure 8.4) and in the curvature of the southern extension of the UV image of Hack and Paresce (1993, Figure 4.7).

A model image (22.5 GHz), exhibiting a morphology very similar to that observed, is shown in the upper panel of Figure 8.8. The arrows in this plot locate the hot

(south) and cool (north) components with respect to the nebular structure, using the binary separation to be derived in Section 8.9. Various simplifying assumptions have been made to facilitate model imaging. The cool component wind has been assumed fully ionized, which is a reasonable approximation given the nearly circularly symmetric distribution observed in the 5 GHz VLA image (Figure 8.1). An H-facing CWb geometry has been assumed, as is necessary from spectral considerations (Section 8.6). The curvature at the interaction cone apex has been ignored, and the density and thickness of the CWc feature have been determined assuming a common center for the hot and cool component winds.

The model parameters used in Figure 8.8 are generally consistent with observational constraints. Values of 10 km s^{-1} and 2000 km s^{-1} have been used for v_2 and v_1 respectively (*e.g.* Wallerstein 1978). A value of $9 \times 10^{-7} D_{\text{kpc}}^{3/2} [M_{\odot} \text{yr}^{-1}] [\text{km s}^{-1}]^{-1}$ has been used for \dot{M}_2 , in agreement with average determinations in tables 8.1 and 8.3. Various constraints apply to \dot{M}_1 (once \dot{M}_2 , v_1 and v_2 have been set) and a value of $1 \times 10^{-8} D_{\text{kpc}}^{3/2} [M_{\odot} \text{yr}^{-1}]$ has been used. Lower values of \dot{M}_1 result in excessively weak CWc features, while higher values lead to excessively high optically thin turnover frequencies (Section 8.6). For the CWc feature, an angular separation from the center of mass loss is also required as input: a value of $0.''1$ was used. The individual flux densities of the model features are in close agreement with the observed values, *i.e.* ~ 150 and ~ 25 mJy.

Figure 8.8 also shows a model image at 5 GHz. The same model parameters have been used as for the 22.5 GHz model image, except that a value of $0.''15$ has been used for the separation of the CWc feature from the center of mass loss. This value is somewhat larger than the value of $0.''1$ used at 22.5 GHz and may be appropriate

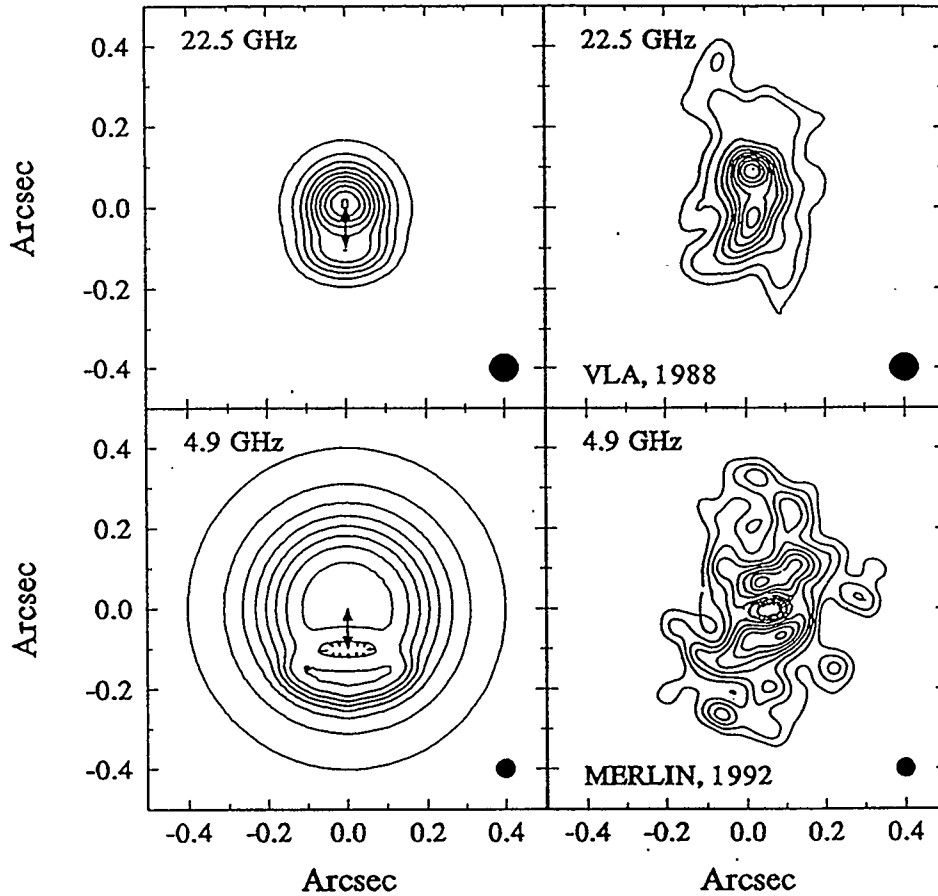


Figure 8.8: HM Sge: STB/CW Model Images

Model parameters: $v_1 = 2000 \text{ km s}^{-1}$; $v_2 = 10 \text{ km s}^{-1}$; $\dot{M}_1 = 1 \times 10^{-8} D_{\text{kpc}}^{3/2} M_{\odot} \text{ yr}^{-1}$; $\dot{M}_2 = 9 \times 10^{-7} D_{\text{kpc}}^{3/2} M_{\odot} \text{ yr}^{-1}$. Model beams and contour levels are consistent with those of the observed images. A viewing angle of 90° has been assumed. Nebular separations (between STB and CWc features) of $0.''1$ and $0.''15$ have been assumed in the upper and lower plots respectively. The double headed arrows (\longleftrightarrow) are used to locate the hot (south) and cool (north) components with respect to the model nebular structure.

due to the evolution in the four years between the final 22.5 GHz image and the 5 GHz MERLIN observation. The morphology exhibited in the 5 GHz model image may be compared to that observed in the MERLIN image (Figure 8.1, reproduced in Figure 8.8). Despite obvious differences, the images also possess several qualitative similarities. The primary characteristic of both observed and model images is the existence of a central depression bracketed by ridges of equal intensity (optically thick). Further, the model image includes a diffuse halo on the same angular scale as the major axis of the observed morphology. The absence of observed emission in the E-W directions may be attributed to equatorial enhancement of mass loss (*e.g.* Eyres *et al.* 1995), or the sweeping clear of these directions by high velocity “polar” ejecta (see 1.5 GHz image of Eyres *et al.* 1995).

The model suggests that the northern ridge contains the cool component and therefore remains optically thick to higher frequencies than the southern ridge (CWc feature). This arrangement explains the differences in morphology observed at 5 and 22.5 GHz. Since the southern feature is optically thin at 22.5 GHz, its flux density at this higher frequency is greatly reduced relative to that of the northern feature which remains optically thick.

As a test of consistency, it is necessary to investigate the depletion of ionizing photons in passing through the CW features. As long as no substantial depletion occurs, ionization in the circumstellar halo will be well approximated by the STB model. The most extreme conditions exist at the interaction cone apex, and hence the value of L_{ph} required for penetration at this point represents an upper limit. For the model parameters used in Figure 8.8, and a binary separation of $100D_{\text{kpc}}$ AU (Section 8.6), the interaction apex is located $50D_{\text{kpc}}$ AU from the hot component,

has a thickness of $6D_{\text{kpc}}$ AU, and a density of $7.6 \times 10^6 D_{\text{kpc}}^{-1/2} \text{ cm}^{-3}$. The required value of L_{ph} to ionize through the apex is $1.1 \times 10^{46} D_{\text{kpc}}^2 \text{ s}^{-1}$, ~ 15 times less than the value required to ionize the halo of the nebula for $X_{\text{stb}} = 10$ (see Section 8.6, table 8.3). Therefore, the existence of CW features does not appear to substantially alter the ionization structure of the circumstellar envelope.

The STB/CW model appears to be broadly consistent with observation. Certain alternative models of emission have also been examined and ruled out. One such model would suggest that the minor nebular feature at 22.5 GHz (Figure 8.4) represents the CWb emission peak (interaction apex) rather than the CWc nebula. This model has many failings: it fails to produce 22.5 GHz emission features which are sufficiently compact; fails to produce the observed spectrum without additional assumptions; and suggests a distance of ~ 100 pc, which is inconsistent for reasons discussed in the next paragraph. Another emitting component of potential importance is the free flowing hot component wind. According to the theory of Wright and Barlow (1975), the flux density of an ionized stellar wind scales with $v^{-4/3}$. The ratio of hot component to cool component mass loss velocities for HM Sge is $\sim 2000:10$, as discussed above, and hence the ratio of flux densities from the free flowing winds is $\sim 1:1200$ (assuming equal mass loss rates). The free flowing hot component wind will therefore make an insignificant contribution to the total observed flux density ($\dot{M}_1 < \dot{M}_2$, Section 8.6).

In the context of the STB/CW model, a lower limit of distance may be inferred. Using the wind parameters from Figure 8.8, a CWc expansion velocity of 19 km s^{-1} is obtained. Since the hot component wind appears to have been stronger in the early stages of outburst (*e.g.* Stauffer 1984), this velocity may be taken as a lower

limit to the average velocity. At 19 km s^{-1} , a distance of 56 AU would be travelled between 1975 (initiation of outburst) and 1988 (22.5 GHz image, Figure 8.4). Using $0.''3$ as an upper limit to angular binary separation (1988 image in Figure 8.4), a lower limit of distance of 185 pc is obtained.

The observed evolution of flux densities at 22.5 GHz is also consistent with the STB/CW model. Table 8.2 shows that the major component has been slowly increasing since 1982, while the minor component, following an initial rise, has been decreasing. If activity on the hot component has been declining since the initial outburst (*e.g.* Stauffer 1984), then the CWc feature (minor component) would naturally decrease. The major component, which is primarily constituted by the STB nebula, might then increase as the cool component wind reestablished itself in the near environment of the binary system. Orbital motion may offer another source of flux density variability in the radio emitting features, since viewing angles to the features will change with orbital phase.

One of the strongest supports of the STB/CW model is its ability to reproduce the observed spectrum of HM Sge. Spectral fitting will now be discussed.

8.6 Spectra

For the model parameters of interest to HM Sge (Figure 8.8), the model spectrum of the STB/CW model is essentially identical to that of a simple STB model. The reasons for this extremely close correspondence are several. Firstly, the flux density from the STB nebula strongly dominates the total model flux density. Secondly, although wind collision may increase flux density in some regions by virtue of com-

pression (Equation 3.63), it may also reduce the flux density if emitting material is moved from optically thin to optically thick regions. Finally, for the low levels of hot component mass loss found appropriate for HM Sge ($\sim 10^{-8} D_{\text{kpc}}^{3/2} M_{\odot} \text{yr}^{-1}$, Figure 8.8), the optically thin turnover of the CWb nebula (~ 20 GHz) occurs at a somewhat lower frequency than the STB turnover (~ 60 GHz, see below). The observed optically thin turnover is therefore governed by STB rather than CWb processes.

STB model fits to the spectra of HM Sge and V1016 Cyg are shown in Figure 8.9. The fitted data was not all obtained simultaneously, however, it may be argued that the spectra have reached a post-outburst quasi-steady-state (*e.g.* Seaquist and Taylor 1992). The model curves provide a good overall characterization of the data, although certain discrepancies will be discussed below.

As an additional constraint in fitting, the geometry factor (X_{stb}) was held at a value of 10, consistent with the observed VLA morphologies (Figures 8.1 and 8.2). Mürset *et al.* (1991) have obtained values of X_{stb} , from fits to IUE spectra between 1978 and 1990, which are in reasonable agreement with the value adopted here: *i.e.* 1-4 for HM Sge, and 2-4 for V1016 Cyg. Binary separations in the STB model are relatively insensitive to the assumed value of X_{stb} (Equation 2.6). The parameters used for the model spectra of HM Sge are consistent with those used for the model images (Figure 8.8), except that complete ionization was assumed for convenience in model imaging.

Significant discrepancies between model and data occur near 15/22.5 GHz in both systems. It is possible that these discrepancies are related to the CW features, even though the simplified implementation of the STB/CW model employed here suggests

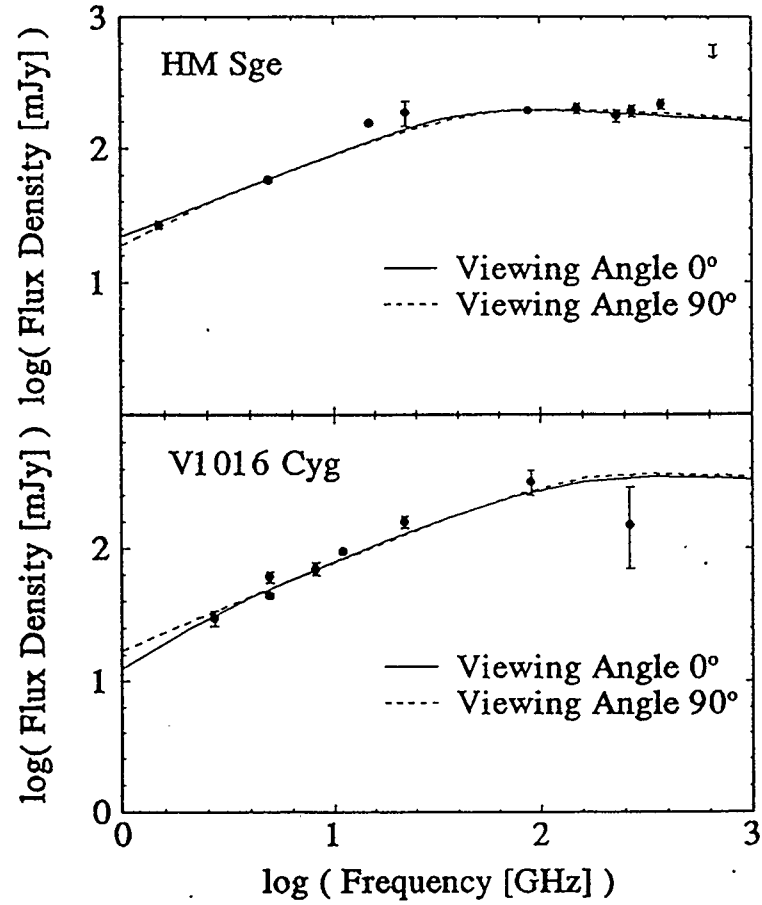


Figure 8.9: STB Spectral Fits: HM Sge and V1016 Cyg

Data for HM Sge is from Li (1993), Ivison *et al.* (1995) and this work. Data for V1016 Cyg is from Purton *et al.* (1982), Becker and White (1985), Seaquist and Taylor (1992), and this work. Model parameters for fitted curves are given in table 8.3.

that the spectrum should depart minimally from that of a simple STB model. If any distinct contribution is going to be made by the CW features, it is likely to occur at the intermediate frequencies being considered here: at low frequencies, the optically thick surface of the STB nebula conceals the CW features, while at high frequencies the STB nebula again dominates because it remains optically thick to higher frequencies. The discrepancies between model and data are of the order of the flux density of the minor nebular features (CWc nebulae, ~ 20 mJy at 22.5 GHz).

Whatever the nature of the additional emitting component, it must pass to optical thinness in the neighborhood of $\lesssim 60$ GHz since there is no evidence for optically thick emission at substantially higher frequencies. In order for the interaction apex to pass to optical thinness at this frequency, a relatively low value of hot component mass loss rate is required, *i.e.* $\dot{M}_1 < 8 \times 10^{-8} D_{\text{kpc}}^{3/2} [M_{\odot} \text{yr}^{-1}]$ (Equation 3.38), $m < 0.1$. The CWb nebula is therefore necessarily H-facing as noted in the previous section. Using \dot{M}_2/v_2 and a from spectral fits (table 8.3), $v_1 = 2000 \text{ km s}^{-1}$ and $v_2 = 10 \text{ km s}^{-1}$, and $\dot{M}_1 = 10^{-8} D_{\text{kpc}} [M_{\odot} \text{yr}^{-1}]$ (Figure 8.8), the turnover frequency for the STB nebula is ~ 60 GHz, and that of the CWb nebula ~ 20 GHz.

The spectrum of V1016 Cyg is subject to the same interpretation as that of HM Sge. Again, the optically thin turnover occurs near 60 GHz, implying a low rate of mass loss from the hot component and an H-facing CWb nebula. The model parameters obtained for the fits shown in Figure 8.9 are given in table 8.3. It will be noted that the fitted parameters for both HM Sge and V1016 Cyg are relatively insensitive to viewing angle.

The values obtained for \dot{M}/v in table 8.3 are consistent with those expected for late-type stars at reasonable distances. They are also consistent with the values

Name/Viewing Angle	\dot{M}/v [$M_{\odot}\text{yr}^{-1}$][km s^{-1}] $^{-1}$	Binary Separation [AU]	L_{ph} [s^{-1}]
HM Sge			
0°	$9.0 \pm 0.2 \times 10^{-8} D_{\text{kpc}}^{3/2}$	$90 \pm 5 D_{\text{kpc}}$	$1.7 \pm 0.1 \times 10^{47} D_{\text{kpc}}^2$
90°	$9.1 \pm 0.2 \times 10^{-8} D_{\text{kpc}}^{3/2}$	$108 \pm 6 D_{\text{kpc}}$	$1.7 \pm 0.2 \times 10^{47} D_{\text{kpc}}^2$
V1016 Cyg			
0°	$8.7 \pm 0.2 \times 10^{-8} D_{\text{kpc}}^{3/2}$	$50 \pm 20 D_{\text{kpc}}$	$2.8 \pm 0.2 \times 10^{47} D_{\text{kpc}}^2$
90°	$9.1 \pm 0.3 \times 10^{-8} D_{\text{kpc}}^{3/2}$	$47 \pm 20 D_{\text{kpc}}$	$3.2 \pm 0.3 \times 10^{47} D_{\text{kpc}}^2$

Table 8.3: STB Fits to HM Sge and V1016 Cyg

Spectral fits were performed with X_{stb} held at a value of 10. Model spectra corresponding to the listed parameters are plotted in Figure 8.9.

obtained from the visibility analysis of the 5 GHz VLA observations in Section 8.3 (table 8.1).

The values of ionizing photon luminosity, L_{ph} , in table 8.3 are difficult to criticize since the nature of the hot component in symbiotic systems is ill-understood. It may be noted, however, that a WD of normal radius ($\sim 0.01 R_{\odot}$, Hopkins 1980) at a temperature of 200,000 K (*cf.* Mürset *et al.* 1991) will have an ionizing photon luminosity of $5 \times 10^{45} \text{ s}^{-1}$. The values of L_{ph} in table 8.3 are consistent with this value for distances of $\sim 200 \text{ pc}$.

The angular binary separation for HM Sge is reasonably well determined by the fits in table 8.3, *i.e.* to within $\sim 5\%$. The angular scale suggested, *i.e.* $\sim 0.''1$, is of the order of the separation of the major and minor nebular features at 22.5 GHz (Figure 8.4), in agreement with the suggested association of nebular features and

stellar components (Section 8.5, Figure 8.7). The suggested locations of hot and cool components are plotted with respect to the nebular features in Figures 8.1, 8.4, and 8.8.

The suggested binary separation plotted with the MERLIN image of HM Sge (Figure 8.1) assists in interpreting the morphology. The symmetry of the ridge-and-hollow complex suggests that the hot component should be positioned within the hollow, where it can effectively “blow a bubble”. This inference is also supported by the fact that the peak of UV emission 1980 \AA , which is likely to indicate the position of the hot component, lies in the centre of the hollow (Hack and Paresce, 1993; Eyres *et al.* 1995). If the hot component lies at the centre of the hollow, the cool component must be situated no closer than the angular radius of the hollow ($\sim 0.''04$); otherwise the hollow would be filled by STB emission. It might be possible to conceal the cool component within the hollow if the CWb interaction is strongly C facing, however this possibility is ruled out by the observed optically thin turnover frequency of $\lesssim 60$ GHz (see above). It may therefore be concluded that an angular binary separation of $\gtrsim 0.''04$ is required.

The binary separation for V1016 Cyg is somewhat less well determined from the spectral analysis (table 8.3), *i.e.* to within $\sim 40\%$. As for HM Sge, however, the associated angular scale ($\sim 0.''05$) is of the order of the observed separation of major and minor features at 22.5 GHz (Figure 8.4). This agreement provides further evidence for a common interpretation of both HM Sge and V1016 Cyg in terms of the STB/CW model.

8.7 Binary Separations and Distances

The STB/CW model appears capable of explaining a large number of the observed characteristics for both HM Sge and V1016 Cyg. An important implication of this model is the close association of the binary nebular features at 22.5 GHz with the stellar components (Figure 8.4). For HM Sge, the fact that relative motion has been measured between the nebular features (Figure 8.5) facilitates the determination of the binary separation and the distance.

In Figure 8.10, relative positions of the nebular features of HM Sge at 22.5 GHz are plotted (*cf.* Figure 8.4). The central filled circle in the plot indicates the position of the major feature, while the relative positions of the minor feature in the various epoches are indicated by open circles. The fitted orbital path is also plotted, with arrows indicating the orbital direction. A circular orbit has been assumed, and therefore the elliptical shape of the apparent path is a result of the orbital inclination. The model positions for the minor feature in the epoches of observation are marked by crosses (+), and agree with observed positions within uncertainties. A more recent 22.5 GHz observation by Eyres (1995) indicates that the position angle has continued to increase since 1988 (*i.e.* $185^\circ \pm 1^\circ$ in 1994).

The orbital model includes five free parameters: the orbital inclination, i ; the position angle of the orbital pole on the plane of the sky, θ ; the orbital phase of the first observation, ϕ ; the orbital period, P ; and the angular separation of nebular features, a' . Both ϕ and θ were measured counterclockwise from north.

Three of the model parameters were reasonably well determined: *i.e.* $71^\circ < i < 79^\circ$; $87^\circ < \theta < 101^\circ$; and $0.28 < \phi < 0.32$. The requirement for a high inclination

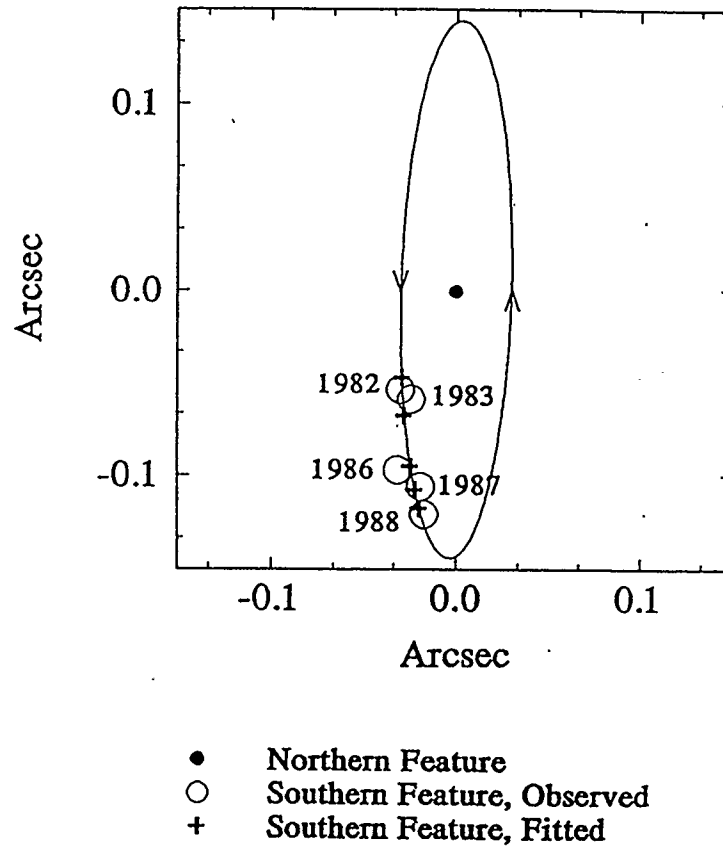


Figure 8.10: Orbital Solution for HM Sge

Data from table 8.2 has been plotted indicating the relative positions of the nebular features of HM Sge (Figure 8.4). The location of the major feature (northern) is indicated by the central filled circle (•). Open circles (○) represent the positions of the minor nebular feature (southern) in the epochs indicated. The size of the open circles is characteristic of measurement uncertainties. The plotted ellipse through the positional points corresponds to the orbital path projected on the plane of the sky: $\phi = 0.31$, $i = 77^\circ$, $\theta = 88^\circ$, $P = 65$ yr, $a = 0.''134$. Arrows indicate the direction of orbit. Fitted orbital positions for the epochs of observation are indicated by crosses (+).

system, $i > 71^\circ$, is in agreement with the radial velocity data of Solf (1984), and the interpretation of the outer bipolar structure of the MERLIN image (Figure 8.1) as equatorially enhanced mass loss (Eyres 1995).

The separation and period were not individually well constrained when all parameters were fitted freely. It was possible, however to place an upper limit of $0.''15$ on the separation on the basis that larger values lead to distance estimates below the lower limit of 185 pc obtained in Section 8.5. Taking $a' = 0.''134$, which was a local fitting minimum, an orbital period of 65 ± 10 yr was obtained. This period yields a linear binary separation of 20 ± 2 AU for an assumed total system mass of $2 M_\odot$.

An alternative approach to estimating the binary separation is to assume that while the position angle rotation is associated with orbital motion, that the observed increase in nebular separation arises in part from a true expansion of nebular dimensions. Under this assumption, orbital periods approach the apparent period of 118 yr (Figure 8.5). The corresponding upper limit to binary separation is 30 AU. Taking an average of this result with that obtained from the orbital analysis, a binary separation of 25 ± 5 AU may be quoted.

Orbital periods are not available for any D-type systems from spectroscopic analysis or direct imaging. However, it has been argued on theoretical grounds that separations should be on the order of ~ 20 AU. Smaller binary separations may be ruled out on the basis of the failure to detect orbital variations in radial velocity (*e.g.* Kenyon 1986). Larger binary separations are unlikely since accretion onto the hot component may then be insufficient to satisfy the energy budget of nebular emission (*e.g.* Kenyon 1986). The one D-type system for which a convincing period has been published (R Aqr: Willson, Garnavich and Mattei 1981) gives a binary

separation of 14-18 AU for a total system mass of 1.5-3 M_{\odot} (eclipse period 44 yr).

The linear binary separation of HM Sge (25 ± 5 AU) may be used, together with the angular binary separation ($0.''10 \pm 0.''01$, Section 8.6) to obtain a distance of 250 ± 40 pc. This value is substantially lower than most published estimates; the average value of distance shown in table 4.3 is almost an order of magnitude higher, *i.e.* 1.7 ± 0.8 kpc. It should be noted however that nearly all published values depend upon estimates of circumstellar extinction, which are highly uncertain (Section 4.2.3). Apart from the present work, the most reliable distance determination is that of Solf (1984, Section 4.2.3). Solf's observations include high spectral and spatial resolution data in [N II] and [O III] emission lines. A conical outflow model applied to his 'B' features suggests a distance of less than 400 pc. An independent distance estimate obtained from the velocity width and angular extent of his 'C' feature yields a distance of 385 ± 150 pc. Solf's values of distance are in agreement with the present determination.

As noted above, it is natural to assume that HM Sge and V1016 Cyg represent similar physical configurations. If they are also similar in binary separation, *i.e.* $a \sim 25$ AU, then the angular binary separation obtained for V1016 Cyg in the previous section ($0.''05 \pm 0.''02$) yields a distance of 500 pc. This distance is again considerably lower than values commonly quoted in the literature (*e.g.* 1.3 kpc, Feibelman 1982a; 2.2 kpc, Nussbaumer and Schild 1981; 7.0 kpc, Kenyon and Cahn 1979). If both HM Sge and V1016 Cyg lie at ~ 300 kpc, this would imply that their requirements for ionizing photon luminosity (table 8.3) may be satisfied by excited WDs ($T \sim 200,000$ K).

8.8 Conclusions

An analysis of various observational evidence has led to a new model of radio emission from HM Sge. This model synthesizes elements of the STB and CW models, and is consistent with many observed characteristics including: the radio spectrum; the morphologies of radio and UV images; and the evolution of imaged nebular features. The model involves a hot component which simultaneously provides high energy photons and a high velocity wind. The high energy photons ionize the majority of the cool component wind (STB nebula), and the high velocity wind results in an H-facing CW geometry. The orbital motion of the stars produces an apparent rotation of position angle between nebular features, as observed. The system orientation inferred from the model is in agreement with previous determinations (*e.g.* Solf 1984, Eyres 1995).

Using radio spectral information, together with the observed changes in nebular orientation, it has been possible to derive a binary separation of 25 ± 5 AU for HM Sge, and a distance of 250 ± 40 pc. At 250 pc, the derived value of cool component mass loss rate is $1 \times 10^{-7} M_{\odot} \text{yr}^{-1}$ (for a velocity of 10 km s^{-1}), in good agreement with values expected for late-type stars. The inferred value of ionizing photon luminosity is consistent with values expected for excited WDs.

Since the STB/CW model requires no new assumptions, but only a consistent treatment of known nebular processes, it is likely that other examples will be identified among the symbiotic population. It is especially likely that V1016 Cyg is of this type. The spectral determination of angular binary separation for V1016 Cyg indicates a scale in agreement with the observed separation of binary nebular features at

22.5 GHz. Further, the many similarities between HM Sge and V1016 Cyg make it difficult to imagine that their physical configurations could differ significantly. Those similarities include: similar outburst histories; similar radio spectra; similar scales of flux density; and similar radio images in terms of both morphology and angular size.

The fact that HM Sge may be much closer than previously suggested has implications for distance determinations of D-type systems in general. Frequently quoted values may be systematically high due to an inadequate knowledge of circumstellar extinction.

Chapter 9

DISCUSSION OF THE SYMBIOTIC PHENOMENON

The introductory chapter of this thesis concluded with a list of general questions concerning the symbiotic phenomenon. A number of those questions may now be addressed.

9.1 The Cool Component

- Why do late-type stars in symbiotic systems, even in wide configurations, appear to systematically lose mass at higher rates than their single counterparts?

The existence of orbital wind interactions in some systems may produce nebular compression. Such compression may lead to an overestimate of mass loss rate by a factor of $1/\sqrt{\epsilon}$, where ϵ is the ratio of the compressed volume to the uncompressed volume (Section 3.3.3, Equation 3.63). The value of ϵ is not normally known.

9.2 The Hot Component

- What are the physical properties of the hot component?

STB modelling of the radio nebulae observed in this work has yielded parameters (*i.e.* ionizing photon luminosities) consistent with the assumption that hot components are hot WDs. The required temperatures ($T \sim 10^5$ K) are achievable through thermonuclear outburst (*e.g.* AG Peg, HM Sge, V1016 Cyg) or mass accretion (*e.g.* Z And). Other types of hot component (*e.g.* MS stars with an accretion disks) can not be ruled out. Where hot component winds have been identified (AG Peg, HM Sge, V1016 Cyg), mass loss rates have been suggested on the order of $10^{-9} - 10^{-8} M_{\odot}\text{yr}^{-1}$; such rates are substantially lower than the associated cool component mass loss rates, *i.e.* $0.01 < m < 0.3$. Hot component mass loss among the outbursting systems may be variable; the hot component mass loss rates for HM Sge and V1016 Cyg appear to be decreasing (Section 4.2.3), while that of AG Peg may be fluctuating (Section 7.5).

9.3 The Nebular Component

- Is asymmetry a normal characteristic of all symbiotic nebulae?

Asymmetry has been observed in all of symbiotic nebulae studied in this work, and appears to arise in many different ways. The unipolar and crescent shaped morphologies observed in the southern symbiotic sources are consistent with either a simple STB model, or a simple CWb model. The bipolar morphology of Z And was found consistent with a simple STB model, or a modified STB model including a “no-recombination” (NR) shell. The asymmetry in the “inner nebula” of AG Peg was interpreted in the context of the CWo model, modified

to include variable hot component mass loss; the bipolar central source of AG Peg was interpreted as a CWb feature. The strong asymmetries of the 22.5 GHz images of HM Sge and V1016 Cyg were found consistent with a combined STB/CW model. The many diverse ways in which asymmetry may arise in interacting binary systems suggests that this characteristic may be widespread among the general population of symbiotic stars.

- Is cool component mass loss equatorially enhanced? If so, does this enhancement arise from binary influences or normal mass loss processes?

The circularity of the inner nebula of AG Peg, coupled with the requirement for relatively high inclination (Section 7.6) suggests that cool component mass loss cannot be significantly equatorially enhanced in this system.

In HM Sge and V1016 Cyg, the large scale structure revealed in the VLA images at 5 GHz (Figures 8.1 and 8.2) suggests that mass loss in these systems may have been asymmetric in the epoch preceding their outbursts. In the case of HM Sge, this suggestion is reinforced by the 5 GHz MERLIN image (Figure 8.1) which shows elongated structure on a smaller scale $\sim 0.''6$, aligned in the same direction as that of the VLA structure. The hypothesis of equatorially enhanced mass loss for HM Sge is strengthened by additional observations which suggest the same system orientation for HM Sge. The 1.5 GHz MERLIN image of Eyres *et al.* (1995) suggests a “polar” axis which coincides with the polar direction required by the “equatorial enhancement” hypothesis. Detailed kinematic information from high spectral and spatial resolution spectroscopy

(Solf 1984, Section 4.2.3) also suggests both equatorial enhancement of mass loss and polar ejection. The inferred system orientation is in agreement with that deduced from the radio images.

Equatorial enhancements need not always arise from mass loss asymmetries. In the STB model, orbital motion may give rise to an equatorial “doughnut”, as suggested for Z And. The CWo model may also produce equatorial structures including equatorial spiral walls, and equatorial interaction belts (*e.g.* AG Peg, Section 7.4). It may be significant that systems for which equatorial enhancement seems most likely (*e.g.* HM Sge, V1016 Cyg) are D-type systems, known to contain Mira variables. The observed S-type systems, whose cool components are “normal” late-type stars (*e.g.* AG Peg, Z And), are consistently explained without the assumption of equatorially enhanced mass loss.

- How do gradients in nebular density and velocity develop and propagate? What is the role of wind interactions in shaping and exciting the nebular matter?

CW models produce many diverse domains of velocity and density within a single binary system. Three such domains will exist in the neighborhood of the stellar components: the free flowing cool component wind; the free flowing hot component wind; and the interaction flow (CWb nebula). When orbital motion is considered (CWo model), a series of spiral walls will develop, representing a new domain of velocity and density. The filling of the interwall regions will depend upon the stellar wind parameters, the orbital period, and the distance scales of interest. Further distinct domains of velocity and density may occur

as CWo features come into contact with an external cool component wind. An “equatorial interaction belt” may develop at the contact surface with the spiral wall stream. “Polar interaction caps” may develop where the external cool component wind is contacted by the free flowing hot component wind (C-facing geometry only).

Density gradients (of ionized material) may also arise in the STB model. In the absence of orbital motion, a well defined ionization boundary will separate ionized and neutral portions of the cool component wind. When orbital motion is considered, a “no-recombination” (NR) shell may also exist (Chapter 2), and the “neutral” portion of the cool component wind may support a small fractional ionization ($\sim 10^{-5}$, Z And). The ionization cone will follow the hot component in its orbital motion.

9.4 Outbursts

- What are the physical requirements for quiescent behavior? How is the quiescent environment affected by outburst? How does the environment evolve following outburst?

There exists no evidence that hot components in symbiotic systems support high velocity winds outside of outburst. A typical quiescent environment may therefore consist essentially of cool component wind. When an outburst is initiated, the increased temperature and luminosity of the hot component will affect the ionization structure of the environment in accordance with the STB

model. When a sustained wind is maintained from the hot component, the various forms of wind interaction described by the CWb, CWc and CWo models may occur.

Assuming a hot component wind which is initially relatively massive, a C-facing CWb interaction will develop at the system center, and the cool component wind will be confined to a narrow conical region. The configuration will resemble that in Figure 3.10, with a CWc nebula developing at the interface between the hot component wind and the external cool component wind. Some time may be required before these CW features become apparent in radio emission. The expansion velocity will be on the order of $50 - 100 \text{ km s}^{-1}$, and the typical radius for the optically thick surface of a fully ionized cool component wind may be $\sim 100 \text{ AU}$ (5 GHz, Wright and Barlow 1975). The implied time scale for appearance of the CW features is then $\sim 6 \text{ yr}$. The central "bubble" blown by the hot component wind may appear earlier.

As the mass-losing objects move in mutual orbit, the CWb interaction cone will be swept into an Archimedean spiral structure (CWo model). The spiral walls may eventually absorb the free flowing elements of hot and cool component winds lying between them. The CWc interaction will continue at the poles, giving rise to "polar interaction caps". The interaction between the spiral walls and the external cool component wind will produce an "equatorial interaction belt". The polar caps and equatorial belt will expand outward, becoming optically thin (*e.g.* inner nebula of AG Peg), and will eventually fade below sensitivity limits. The remaining radio emitting components will then

include the spiral wall structure (CWo nebula) and the central CWb feature; the observed morphology will be strongly dependent upon the orbital period (Equation 3.60). The ionization structure within these features will be governed by a modified STB model, and the observed emission may be modulated with orbital phase if the “neutral” component of the surrounding medium includes some small but finite fractional ionization (*e.g.* AG Peg).

As the hot component mass loss rate decreases following outburst, the CWb interaction may become H-facing (*e.g.* HM Sge). Polar interaction caps will then no longer be driven by the hot component wind. Episodes of enhanced hot component mass loss may occur, however, resulting in transitions from H to C-facing geometries, and the transient reappearance of polar features (*e.g.* AG Peg). Further decreases in hot component mass loss rate will lead to the collapse of the CWb interaction cone around the hot component, and the reestablishment of a quiescent configuration.

The time scale upon which the quiescent environment will be reestablished is governed primarily by the velocity of the cool component wind ($\sim 10 \text{ km s}^{-1}$). Using the optically thick radius of a completely ionized cool component wind (~ 100 at 5 GHz, Wright and Barlow 1975) as a characteristic distance scale, the inferred time scale for the reestablishment of the quiescent environment is ~ 50 yr. Spiral wall features will fade quickly, since they move outward with a velocity substantially higher than that of the cool component wind (*i.e.* $\sim 200 \text{ km s}^{-1}$).

High velocity outflows from the hot component appear typical of symbiotic novae (*e.g.* AG Peg, HM Sge, V1016 Cyg). It has not been demonstrated that such outflows are typical of outbursts in classical symbiotic systems. Z And, the only classical symbiotic star examined in this work, has shown evidence for high velocity ejection in its most recent outburst (Fernández-Castro *et al.* 1995), albeit at a much lower velocity ($\sim 100 - 300 \text{ km s}^{-1}$).

9.5 Radio Statistics

Various configurations for radio emission from symbiotic stars appear possible: STB, STB + NR shell, CWb, CWc, and CWo, as well as various combinations of these simple configurations. Not all of these possibilities are equally likely to be observed among the general symbiotic population.

Among CW systems, domains of orbital period were identified for observed CWo and CWb morphologies (Equation 3.60). For a resolution of $0.''1$, a system of typical flow parameters located at 1 kpc will not exhibit a CWo nebula unless its period is less than 2.4 yr. It may be inferred that D-type systems ($P \gtrsim 20 \text{ yr}$; Kenyon 1986), are more likely to exhibit CWb than CWo morphologies.

There is no evidence that quiescent systems support high velocity winds from the hot component, and hence the applicability of the CW models is likely to be confined to outbursting systems. Even in outburst, however, the “quiescent” component of emission from the cool component envelop may continue to dominate the observed radio flux density. The relative emission from STB (“quiescent”) and CWb (“outbursting”) features was discussed in Section 3.1.7, and it was concluded that

the STB emission should strongly dominate in most cases. CWb emission becomes increasingly important for large values of hot component mass loss rate, where the cool component wind is confined to a narrow cone on the equatorial plane.

It is instructive that the radio spectrum of HM Sge appears relatively unaffected by the recent outburst. The outer cool component envelop has not suffered disruption, and dominates emission at low frequencies. At high frequencies, including the optically thin turnover frequency, flux densities are also apparently governed by the quiescent (STB) model due to the low relative mass loss rate of the hot component ($m \sim 0.01$). This may suggest that quiescent models are meaningfully applied, in a statistical sense, to the general class of radio emitting symbiotics.

Finally, the study of HM Sge suggests that previous distance determinations have been systematically high. If distance estimates for other highly reddened D-type systems are similarly in error, there may exist more D-type systems in the Galaxy than previously predicted from observational evidence.

9.6 New Questions

In addition to providing comment concerning previously posed questions, this work has raised a number of new ones.

- Hot component variability. What factors affect the mass loss rate of the hot component during decline from outburst? AG Peg experienced a secondary outburst ~ 1940 , and appears to have gone through a more recent episode of enhanced mass loss (1984 - 1987). Is HM Sge likely to exhibit renewed hot component activity?

- Are distance estimates to D-type symbiotic systems systematically in error? The distance to HM Sge determined from apparent orbital motion is 250 ± 40 pc, almost an order of magnitude lower than values commonly quoted in the literature.
- What are the typical binary separations of D-type systems? The value obtained for HM Sge from apparent orbital motion is 25 ± 5 AU, however both STB and CWb models suggest much higher values for BI Cru and He 2-106 ($\sim 3000 D_{\text{kpc}}$ AU).

Chapter 10

CONCLUSIONS

10.1 Summary

In this study of symbiotic stars, both theoretical and observational problems have been addressed. The physics of colliding winds (CW) has been examined, and models have been reformulated, expanded, and applied to the problem of radio structure and spectra from symbiotic stars. It has been shown that thermal pressure within the cool component wind must be considered in determining the geometry of the interaction surface, and a new set of differential equations has been derived to include this effect (CWb model, Appendix A). CW models have also been expanded to include interaction zones of finite thickness; in this way it has been possible to solve the radiative transfer problem and produce model images for given wind parameters. Conditions at the static point between opposing winds have been examined, and analytic expressions have been derived for potentially observable quantities such as the static point density and the optically thin turnover frequency. A new model, the CWo model, has been formulated to describe the “steady state” nebular structure arising when mass losing objects are in mutual orbit. Domains of applicability for the CWo and CWb models have been identified (Equation 3.60). The role of colliding winds in enhancing emission through compression has also been examined, and it has been shown that standard techniques of estimating mass loss rates may overestimate actual rates by a factor of $1/\sqrt{\epsilon}$ where ϵ is the ratio of compressed to uncompressed

volumes.

The observational component of this thesis has included high resolution radio imaging of selected objects with the VLA and MERLIN in the northern hemisphere, and with the AT in the southern hemisphere. The morphologies have been interpreted in terms of various combinations of the STB model and CW models.

The southern sources have been resolved (albeit marginally) for the first time in this work, and the observed morphologies (“crescent shaped” and “elongated”) are consistent with simple STB or CWb models. Estimates of binary separations from both models were in close correspondence. For RR Tel and HD 149427, separations of $\sim 20D_{\text{kpc}}$ AU were obtained, consistent with theoretical predictions of some authors for D-type systems (*e.g.* Kenyon 1986). For BI Cru and He 2-106, the separations obtained were very much larger, *i.e.* $\sim 3000 D_{\text{kpc}}$ AU, far exceeding the limits to which known processes of accretional heating are effective (*e.g.* Kenyon 1986).

Z And has also been resolved for the first time in this work, in this case through the combination of near-simultaneous data obtained at MERLIN and the VLA. The observed morphology has been found consistent with a simple STB model, or a modified STB model including a “no-recombination” (NR) shell. The radio light curve of Z And since 1982 has been analyzed, and flux densities have been shown to vary with orbital phase. A model is proposed in which the radio emission is attenuated in passage through the “neutral” portion of the cool component wind (ionization fraction $\sim 10^{-5}$), whose optical depth varies with orbital phase. A similar interpretation for the observed modulation of flux densities for AG Peg is also proposed, although in this case the STB model must be coupled with CW models.

Observations of AG Peg have included four epoches of high resolution, high sen-

sitivity VLA images at 5 GHz. The dominant feature in these images is the “inner nebula” with an angular diameter of $\sim 2''$. This feature has been observed to expand at a rate of 25.4 ± 3.2 mas/yr (72 ± 9 km s $^{-1}$ at 600 pc) and to contain a mass of $4.0 \pm 0.5 \times 10^{-5} M_{\odot}$. The nature and evolution of the inner nebula is interpreted in terms of the CWo model, including variable hot component mass loss. Combined MERLIN/VLA imaging has resolved the central component of emission (0.92 ± 0.9 mJy at 5 GHz) for the first time, revealing a bipolar structure whose axis of elongation coincides with the bipolar axis of the “outer” nebulosity ($\sim 1'$, 1.5 GHz, Figure 4.4). AG Peg is the only symbiotic system known to support both a high velocity wind and a short period orbit (S-type system), as required by the CWo model.

The analysis of HM Sge and V1016 Cyg have suggested an H-facing CW configuration for both systems. Multi-epoch VLA imaging of HM Sge at 22.5 GHz (Li 1993) has apparently revealed the effects of orbital motion. Analysis of this motion suggests a period of 65 ± 10 yr, and a binary separation of 25 ± 5 AU for a total system mass of $2 M_{\odot}$. The only other D-type system for which a reliable binary separation has been published is R Aqr (Willson, Garnavich, and Mattei 1981), and the value obtained (14-18 AU) is of the same order as obtained here for HM Sge. It is believed that the present work represents the first direct determination of an orbital period from radio images. The derived linear binary separation has been used together with the angular binary separation, $0.''10 \pm 0.''01$, to obtain a distance for HM Sge of 250 ± 40 pc.

10.2 Further Work

Since the southern symbiotic systems have been resolved, it will be possible to monitor their morphological evolution with time. Both the STB and CWb models indicate that the observed morphologies should change with orbital phase, and hence imaging in the present epoch may provide evidence of orbital motion. The most extreme morphology among the southern sources is that of HD 149427, and in this case multifrequency imaging is warranted in order to establish the nature of the extended emission (jet?). Particular attention to HD 149427 may be appropriate since it is the first D' system to be resolved in radio emission.

The observed nebular morphology of Z And is consistent with two models (STB model; STB model plus NR shell), each of which predicts different evolution with orbital phase. Further imaging observations at different orbital phases may therefore distinguish between the models. New MERLIN/VLA images of Z And may also suggest whether the marginally detected northern feature in Figure 6.6 is ejecta from the 1984/5 optical outburst; if so, its motions may be monitored. A new multi-frequency monitoring program, similar to the one between 1984 and 1987, may be worthwhile to establish whether the previous pattern of orbital variation in flux density and spectral index continues following the recent outburst. The model proposed for these variations, *i.e.* the modulation of radio emission in passing through the "neutral" portion of the cool component wind, may be tested in this way. Other systems with known spectroscopic or photometric periods may also be examined for similar behavior.

The structure of the "inner nebula" of AG Peg has proven highly informative of

the central activity in this system. Since the morphology of the inner nebula evolves on the time scale of years, new observations are appropriate in the present epoch. The CW model proposed for AG Peg suggests that the hot component mass loss rate is variable, and new images may serve to test and refine this model. The central source of AG Peg also warrants further attention. The resolved image presented in this work (combined MERLIN/VLA data; Figure 7.3) exhibits bipolar structure along an axis which coincides with the axis of high velocity ejection during the 1850 outburst ("outer nebula", Kenny 1989). Further combined array imaging may clarify whether the present morphology is related to the CWb interaction or discrete polar ejection.

The determination of an orbital period and a distance for HM Sge, from the apparent motion of nebular features, is of considerable importance. Reliable orbital periods for D-type systems have not been previously reported, and the distance to HM Sge appears to be almost an order of magnitude lower than previously suggested (table 4.3). Confirmation of the orbital motion through further 22.5 GHz images is clearly recommended.

The STB/CW model, proposed for HM Sge, requires no new assumptions but only a consistent treatment of ionization and CW processes. It is therefore possible that other systems will be found for which this model is also appropriate. V1016 Cyg exhibits a 22.5 GHz morphology very similar to that of HM Sge, and is an obvious candidate; H1-36 is another (Taylor 1988a). The model indicates that orbital motion is potentially observable, and hence multi-epoch, 22.5 GHz imaging of these systems may be useful in testing the model and in determining their orbital periods.

Bibliography

- [1] Aaquist, O. B. 1990, PhD Thesis, University of Calgary.
- [2] Acker, A., Köppen, J., Stenholm, B., and Jasniewicz, G. 1989, *Astron. Astrophys. Supp. Ser.*, **80**, 201.
- [3] Ahern, A. 1975, *Ap. J.*, **197**, 639.
- [4] Ahern, F. J., Fitzgerald, M. P., Marsh, K. A., and Purton, C. R. 1977, *Astr. Ap.*, **58**, 35.
- [5] Allen, D. A. 1974a, *M.N.R.A.S.*, **168**, 1.
- [6] Allen, D. A. 1974b, *Inf. Bull. Var. Stars*, No. 911.
- [7] Allen, D. A. 1979, in *IAU Colloquium 46: Changing Trends in Variable Star Research*, ed. F. M. Bateson, J. Smak, and I. H. Urch, (Hamilton, NZ: University of Waikoto), 125.
- [8] Allen, D. A. 1980a, *M.N.R.A.S.*, **192**, 521.
- [9] Allen, D. A. 1980b, *M.N.R.A.S.*, **190**, 75.
- [10] Allen, D. A. 1981a, *M.N.R.A.S.*, **197**, 739.
- [11] Allen, D. A. 1981b, in *Proceedings of the North American Workshop on Symbiotic Stars*, ed. R. E. Stencel (JILA, Boulder), 12.
- [12] Allen, D. A. 1982, in *IAU Colloquium 70: The Nature of Symbiotic Stars*, ed. M. Friedjung and R. Viotti, (Dordrecht: Reidel), 27.
- [13] Allen, D. A. 1983, in *Astrophysics and Space Science Library*, **99**, 102.
- [14] Allen, D. A. 1984a, *Proc. ASA*, **5**, 369.
- [15] Allen, D. A., 1984b, *Ap. Space Sci.*, **99**, 101.
- [16] Allen, D. A. 1988, in *IAU Colloquium 103: The Symbiotic Phenomenon*, ed. J. Mikolajewska, M. Friedjung, S. Kenyon, and R. Viotti, (Dordrecht: Kluwer), 3.
- [17] Allen, D. A., and Glass, I. S. 1974, *M.N.R.A.S.*, **167**, 337.
- [18] Allen, D. A., and Wright, A. E. 1988, *M.N.R.A.S.*, **232**, 683.

- [19] Allen, D. A., Beattie, D. H., Lee, T. J., Stewart, J. M., and Williams, P. M. 1978, *M.N.R.A.S.*, **182**, 601.
- [20] Altamore, A., Baratta, G. B., and Viotti, R. 1979, *Inf. Bull. Var. Stars.*, No. 1636.
- [21] Altamore, A., Baratta, G. B., Cassatella, A., Friedjung, M., Griangrand, A., Ricciardi, O., and Viotti, R. 1981, *Ap. J.*, **245**, 630.
- [22] Andrillat, Y. 1982, in IAU Colloquium 70, *Nature of Symbiotic Stars*, ed. M. Friedjung and R. Viotti (Dordrecht: Reidel), p. 173.
- [23] Andrillat, Y., and Houziaux, L. 1986, *Astr. Ap.*, **52**, 119.
- [24] Andrillat, Y., Ciatti, F., and Swings, J. P. 1982, *Ap. Space Sci.*, **83**, 423.
- [25] Arkhipova, V. P., and Dokachaeva, O. D. 1962, *Soviet Astr.*, **6**, 483.
- [26] Arons, J. 1973, *Ap. J.*, **184**, 539.
- [27] Arnett, D., Fryell, B., and Muller, E. 1989, *Ap. J. Letters*, **341**, L63.
- [28] Baratta, G. B., Cassatella, A., and Viotti, R. 1974, *Ap. J.*, **187**, 651.
- [29] Bath, G. T. 1977, *M.N.R.A.S.*, **178**, 203.
- [30] Bath, G. T., and Shaviv, G. 1976, *M.N.R.A.S.*, **175**, 305.
- [31] Bath, G. T., and Wallerstein, G. 1976, *P. A.S.P.*, **88**, 759.
- [32] Becker, R. H., and White, R. L. 1985, in *Radio Stars* ed. R. M. Hjellming, and D. M. Gibson, (Dordrecht: Reidel), 139.
- [33] Belyakina, T. S. 1970, *Astrofizika*, **6**, 49.
- [34] Belyakina, T. S. 1985, *Inf. Bull. Var. Stars*, No. 2697.
- [35] Belyakina, T. S., Gershberg, R. E., and Shakhovskaya, N. I. 1978, *Sov. Astron. Letters*, **5(6)**, 349.
- [36] Bianchini, A. 1990, *Astron. J.*, **99**, 1941.
- [37] Blair, W. P., Stencel, R. E., Shaviv, G., and Feibelman, W. A. 1981, *Astr. Ap.*, **99**, 73.
- [38] Blair, W. P., Stencel, R. E., Feibelman, W. A., and Michalitsianos, A. G. 1983, *Ap. J. Sup*, **53**, 573.

- [39] Boggess, A., Feibelman, W. A., McCracken, C. W. 1981, in *The Universe at Ultraviolet Wavelengths*, ed. R. D. Chapman, NASA CP-2171, 663.
- [40] Bopp, B. W. 1981, in *Proceedings of the North American Workshop on Symbiotic Stars*, edited by R. E. Stencel (JILA, Boulder), 11.
- [41] Bowen, G. H., and Beach, T. E. 1987, in *Late Stages of Stellar Evolution*, ed. S. Kwok, and S. R. Pottasch, (Dordrecht: Reidel), 275.
- [42] Bowen, G. H., and Willson, W. A. 1991, *Ap. J.*, **375**, L53.
- [43] Boyarchuk, A. A. 1968, *Soviet Astr.*, **11**, 818.
- [44] Boyarchuk, A. A. 1968b, *Astrophysics*, **4**, 109.
- [45] Boyarchuk, A. A. 1969, in *Non-Periodic Phenomena in Variable Stars*, ed. L. Detre (Budapest: Academic Press), p.395.
- [46] Boyarchuk, A. A. 1975, in *IAU Symposium 67: Variable Stars and Stellar Evolution*, ed. V. E. Sherwood, and L. Plant, (Dordrecht: Reidel), 377.
- [47] Boyarchuk, A. A., Esipov, V. F., and Morov, V. I. 1966, *Soviet Astr.*, **10**, 331.
- [48] Brocka, B. 1979, *P. A.S.P.*, **91**, 519.
- [49] Brown, L. W., Feibelman, W. A., Hobbs, R. W., and McCracken, C. W. 1978, *Astrophys. Letters*, **19**, 75.
- [50] Bryan, G. L., and Kwok, S. 1991, *Ap. J.*, **368**, 252.
- [51] Burbidge, G. R., and Burbidge, E. M. 1954, **120**, 76.
- [52] Calabretta, M. R. 1982, *M.N.R.A.S.*, **199**, 141.
- [53] Cannizzo, J. K., and Kaitchuck, R. H. 1992, *Scientific American*, January, 92.
- [54] Cassatella, A., Fernandez-Castro, T., and Olivesen, N. 1988, in *IAU Colloquium 103: The Symbiotic Phenomenon*, ed. J. Mikolajewska, M. Friedjung, S. Kenyon, and R. Viotti, (Dordrecht: Kluwer), 181.
- [55] Chochol, D. 1988, in *IAU Colloquium 103: The Symbiotic Phenomenon*, ed. J. Mikolajewska, M. Friedjung, S. Kenyon, and R. Viotti, (Dordrecht: Kluwer), 251.

- [56] Chochol, D., Komárek, Z, and Vittone, A. 1988, in *IAU Colloquium 103: The Symbiotic Phenomenon*, ed. J. Mikolajewska, M. Friedjung, S. Kenyon, and R. Viotti, (Dordrecht: Kluwer), 263.
- [57] Ciatti, F., Mammano, A., and Vittone, A. 1978, *Astr. Ap.*, **68**, 251.
- [58] Ciatti, F., Mammano, A., and Vittone, A. 1979, *Astr. Ap.*, **79**, 247.
- [59] Clements, E. D., and Argyle, R. W. 1984, *M.N.R.A.S.*, **209**, 1.
- [60] Costa, E., and Loyola, P. 1991, *Astr. Ap. Suppl.*, **89**, 411.
- [61] Cowley, A. P., and Stencel, R. 1973, *Ap. J.*, **184**, 687.
- [62] Crampton, D., Grygar, J., Kohoutek, L., and Viotti, R. 1970, *Astrophys. Lett.*, **6**, 5.
- [63] Davidson, K., Humphreys, R. M., and Merrill, K. M. 1978, *Ap. J.*, **220**, 239.
- [64] de Freitas Pacheco, J. A., Codina-Landaberry, S. J., and Lopes, D. F. 1989, **337**, 520.
- [65] Dokuchaeva, O. D. 1976, *Inf. Bull. Var. Stars*, No. 1189.
- [66] Dolidze, M. V., and Dzhimsheljsvili, G. N. 1966, *Izv. Abast. Astrofiz. Obs.*, No. 34, p.27.
- [67] Dupree, A. K. 1986, *Ann. Rev. Astr. Ap.*, **24**, 377.
- [68] Dyson, J. E., and Williams, D. A. 1980, *The Physics of the Interstellar Medium*, (London: Manchester University Press).
- [69] Eyres, S. P. S. 1995, PhD Thesis, University of Manchester, in preparation.
- [70] Eyres, S. P. S., Kenny H. T., Cohen, R. J., Lloyd, H. M., Dougherty, S. M., Bode, M. F., and Davis, R. J. 1995, *M.N.R.A.S.*, January.
- [71] Feast, M. W., and Whitelock, P. A. 1987, in *Late Stages of Stellar Evolution*, ed. S. Kwok, and S. R. Pottasch, (Dordrecht: Reidel), 33.
- [72] Feast, M. W., Catchpole, R. M., Whitelock, P. A., Carter, B. S., and Roberts, G. 1983a, *M.N.R.A.S.*, **203**, 383.
- [73] Feast, M. W., Whitelock, P. A., Catchpole, R. M., Roberts, G., and Carter, B. S. 1983b, *M.N.R.A.S.*, **202**, 951.

- [74] Feibelman, W. A. 1982a, *Ap. J.*, **258**, 548.
- [75] Feibelman, W. A. 1982b, *Ap. J. (Letters)*, **263**, L69.
- [76] Feibelman, W. A., 1983, *Astr. Ap.*, **122**, 335.
- [77] Feibelman, W. A., Boggess, A., Hobbs, R. W., and McCracken, C. W. 1980, *Ap. J.*, **214**, 725.
- [78] Feldman, P., A. 1977, *IAU Circ.*, 3094.
- [79] Feldman, P. A., and Kwok, S. 1979, *J. Roy. Astron. Soc. Canada*, **73**, 271.
- [80] Feldman, P. A., Purton, C. R., Ryle, M., and Seaquist, E. R. 1978, *Bull. AAS*, **9**, 600.
- [81] Fernández-Castro, T., Cassatella, A., Giménez, A., and Viotti, R. 1988, *Ap. J.*, **324**, 1016.
- [82] Fernández-Castro, T., González-Riestra, R., Cassatella, A., Taylor, A. R., and Seaquist, E. R. 1995, *Ap. J.*, 20 March.
- [83] Fernie, J. D. 1985, *P. A.S.P.*, **97**, 653f.
- [84] Fitzgerald, M. P., and Houk, N. 1970, *Ap. J.*, **159**, 963.
- [85] Fitzgerald, M. P., and Pilavaki, A. 1974, *Ap. J. Suppl.*, **28**, 147.
- [86] Fitzgerald, M. P., Houk, N., McCuskey, S. W., and Hoffleit, D. 1966, *Ap. J.*, **144**, 1135.
- [87] Fitzgerald, M. P., Purton, C. R., Marsh, K., and Ahern, F. 1975, *Bull. AAS*, **8**, 372.
- [88] Flower, D. R., Nussbaumer, H., and Schild, H. 1979, *Astr. Ap.*, **72**, L1.
- [89] Formiggini, L., Leibowitz, E. M. 1990, *Astr. Ap.*, **227**, 121.
- [90] Friedjung, M. 1988, in *IAU Colloquium 103: The Symbiotic Phenomenon*, ed. J. Mikolajewska, M. Friedjung, S. Kenyon, and R. Viotti, (Dordrecht: Kluwer), 199.
- [91] Fuensalida, J. J., Rosa, F., and Fuentes, F. J. 1988, *Astr. Ap.*, **191**, L13.
- [92] Fujimoto, M. Y. 1982, *Ap. J.*, **257**, 767.

- [93] Gallagher, J. S., Holm, A. V., Anderson, C. M., and Webbink, R. F. 1979, *Ap. J.*, **229**, 994.
- [94] Gaposchkin, S. 1945, *Ann. Harvard. Obs.*, **115**, No. 2, 11.
- [95] Garcia, M. R. 1986, *Astron. J.*, **91**, 1400.
- [96] Garcia, M. R., and Kenyon, S. J. 1988, in *IAU Colloquium 103: The Symbiotic Phenomenon*, ed. J. Mikolajewska, M. Friedjung, S. Kenyon, and R. Viotti, (Dordrecht: Kluwer), 127.
- [97] Ghigo, F. D., and Cohen, N. L. 1981, *Ap. J.*, **245**, 988.
- [98] Giuliani, J. L. 1982, *Ap. J.*, **256**, 624.
- [99] Girard, T., and Willson, L. A. 1987, *Astr. Ap.*, **183**, 247.
- [100] Glass, I. S., and Webster, B. L. 1973, *M.N.R.A.S.*, **165**, 77.
- [101] Glass, I. S., Catchpole, R. M., Feast, M. W., Whitelock, P. A., and Reid, I. N. 1987, in *Late Stages of Stellar Evolution*, ed. S. Kwok, and S. R. Pottasch, (Dordrecht: Reidel), 33.
- [102] Grant, Gordon, and Aller, L. H. 1954, *Astron. J.*, **59**, 321.
- [103] Gregory, P. C., Kwok, S., and Seaquist, E. R. 1977, *Ap. J.*, **211**, 429.
- [104] Gregory, P. C., and Seaquist, E. R. 1974, *Nature*, **247**, 532.
- [105] Gutiérrez-Moreno, A., Moreno, H., and Cortés, G. 1986, *Astr. Ap.*, **166**, 143.
- [106] Gutiérrez-Moreno, A., Moreno, H., and Cortés, G. 1987, *Rev. Mexicana Astron. Astrof.*, **14**, 344.
- [107] Hack, W. J., and Paresce, R. 1993, *P. A.S.P.*, **105**, 1273.
- [108] Hack, M., Rusconi, L., Sedmak, G., Aydin, C., Engin, S., and Yilmaz, N. 1986, *Astr. Ap.*, **159**, 117.
- [109] Hall, P. J., Wark, R. M., and Wright, A. E. 1987, *Proc. ASA*, **7**, 50.
- [110] Harrison, T. E., and Gehrz, R. D. 1988, *Astron. J.*, **96**, 1001.
- [111] Harvey, P. M. 1974, *Ap. J.*, **188**, 95.
- [112] Harvey, P. M., and Wilking, B. A. 1982, *P. A.S.P.*, **94**, 285.

- [113] Hayes, M. A., and Nussbaumer, H. 1986, *Astr. Ap.*, **161**, 287.
- [114] Heck, A. and Manfroid, J. 1985, *Astr. Ap.*, **142**, 341.
- [115] Henize, K. G. 1967, *Ap. J. Sup.*, **14**, 125.
- [116] Henize, K. G. 1976, *Ap. J. Sup.*, **30**, 491.
- [117] Henize, K. G., and Carlson, E. D. 1980, *P. A.S.P.*, **92**, 479.
- [118] Hjellming, R. M. 1981, in *Proceedings of the North American Workshop on Symbiotic Stars*, ed. R. E. Stencel, (Boulder: JILA), 15.
- [119] Hjellming, R. M. 1985, in *Radio Stars*, ed. R. M. Hjellming, D. M. Gibson, (Dordrecht: Reidel), 97.
- [120] Hjellming, R. M. 1988, in *Galactic and Extragalactic Radio Astronomy*, ed. G. L. Verschuur, and K. I. Kellerman, (New York: Springer-Verlag), 381.
- [121] Hoffmeister, C., Richter, G., and Wenzel 1985, *Variable Stars*, trans. S. Dunlop, (Berlin: Springer-Verlag).
- [122] Hogg, F. S. 1934, *P. A.S.P.*, **8**, 34.
- [123] Hopkins, J. 1980, *Glossary of Astronomy and Astrophysics*, (Chicago: University of Chicago Press).
- [124] Hutchings, J. B., Cowley, A. P., and Redman, R. O. 1975, *Ap. J.*, **201**, 404.
- [125] Hutchings, J. B. and Redman, R. O. 1972, *P. A.S.P.*, **84**, 240.
- [126] Iben, I., Jr. 1982, *Ap. J.*, **259**, 244.
- [127] Icke, V. 1988, *Astr. Ap.*, **202**, 177.
- [128] Ipatov, A. P., Taranova, O. G., and Yudin, B. F. 1985, *Astr. Ap.*, **142**, 85.
- [129] Ivison, R. J., Bode, M. F., Roberts, J. A., Meaburn, J., Davis, R. J., Nelson, R. F., and Spencer, R. E. 1991, *M.N.R.A.S.*, **249**, 374.
- [130] Ivison, R. J., Seaquist, E. R., Schwarz, Hughes, and Bode, M. F. 1995, *M.N.R.A.S.*, submitted.
- [131] Johnson, J., and Jones, T. 1991, *Astron. J.*, **101**, 1733.
- [132] Kafatos, M. 1981, in *Proceedings of the North American Workshop on Symbiotic Stars*, edited by R. E. Stencel (JILA, Boulder), p. 9.

- [133] Kafatos, M., and Michalitsianos, A., G. 1984, *Scientific American*, July Issue, 84.
- [134] Kahn, F. D. 1983, in *Planetary Nebulae*, ed. D. R. Flower, (Dordrecht: Reidel), 305.
- [135] Kahn, F. D. and West, K. A. 1985, *M.N.R.A.S.*, **212**, 837.
- [136] Kallrath, J. 1991, *Astr. Ap.*, **247**, 434.
- [137] Kenny, H. T. 1989, MSc Thesis, University of Calgary.
- [138] Kenny, H. T., Taylor, A. R., Davis, R. J., Pavelin, P. E., Bode, M. F., and Bang, M. 1993, in *Sub-arcsecond Radio Astronomy*, ed. R. J. Davis, and R. S. Booth, (Cambridge: Cambridge University Press), 18.
- [139] Kenny, H. T., Taylor, A. R., and Seaquist, E. R. 1991, *Ap. J.*, **366**, 549.
- [140] Kenyon, S. J. 1985, in *Cataclysmic Variables and Low-Mass X-ray Binaries*, ed D. Q. Lamb, and J. Patterson, (Dordrecht: Reidel), 417.
- [141] Kenyon, S. J. 1986, *The Symbiotic Stars*, (Cambridge: Cambridge University Press).
- [142] Kenyon, S. J. 1988a, in *IAU Colloquium 103: The Symbiotic Phenomenon*, ed. J. Mikolajewska, M. Friedjung, S. Kenyon, and R. Viotti, (Dordrecht: Kluwer), 11.
- [143] Kenyon, S. J. 1988b, in *IAU Colloquium 103: The Symbiotic Phenomenon*, ed. J. Mikolajewska, M. Friedjung, S. Kenyon, and R. Viotti, (Dordrecht: Kluwer), 161.
- [144] Kenyon, S. J. 1988c, *Astron. J.*, **96**, 337.
- [145] Kenyon, S. J., and Bateson, F. M. 1984, *P. A.S.P.*, **96**, 321.
- [146] Kenyon, S. J., and Cahn, J. H. 1979, University of Illinois preprint, IAP 79-40.
- [147] Kenyon, S. J., and Fernández-Castro 1987, *Astron. J.*, **93**, 938.
- [148] Kenyon, S. J., Fernández-Castro, T., and Stencel, R. E. 1986, *Astron. J.*, **92**, 1118.
- [149] Kenyon, S. J., Fernández-Castro, T., and Stencel, R. E. 1988, *Astron. J.*, **95**, 6.

- [150] Kenyon, S. J., and Gallagher, J. S. 1983, *Astron. J.*, **88**, 666.
- [151] Kenyon, S. J. and Garcia, M. R. 1989, *Astron. J.*, **97**, 194.
- [152] Kenyon, S. J., and Truran, J. W. 1983, *Ap. J.*, **273**, 280.
- [153] Kenyon, S. J., and Webbink, R. F. 1984, *Ap. J.*, **279**, 252.
- [154] Kenyon, S. J., Michalitsianos, A. G., Lutz, J. H., Kafatos, M. 1985, *P. A.S.P.*, **97**, 268.
- [155] Kenyon, S. J., Oliverson, N. A., Mikolajewska, J., Mikolajewski, M., Stencel, R. E., Garcia, M. R., Anderson, C. M. 1991, *Astron. J.*, **101**, 637.
- [156] Keyes, C. D. 1982, in IAU Colloquium 70, *The Nature of Symbiotic Stars*, ed. M. Friedjung and R. Viotti (Dordrecht:Reidel), p. 201.
- [157] Keyes, C. D., and Plavec, M. J. 1980a, in *IAU Symposium 88, Close Binary Stars: Observations and Interpretations*, ed. M. J. Plavec, D. M. Popper, R. K. Ulrich, (Dordrecht: Reidel), 535.
- [158] Keyes, C. D., and Plavec, M. J. 1980b, in *The Universe at Ultraviolet Wavelengths*, ed. R. D. Chapman, NASA CP-2171, 443.
- [159] Kindl, C., Marxer, N., and Nussbaumer, H. 1982, *Astr. Ap.*, **116**, 265.
- [160] Kwok, S. 1977, *Ap. J.*, **214**, 437.
- [161] Kwok, S. 1981a, in *Proceedings of the North American Workshop on Symbiotic Stars*, ed. R. E. Stencel, (Boulder: JILA), 24.
- [162] Kwok, S. 1981b, in IAU Colloquium 59, *Effects of Mass Loss on Stellar Evolution*, ed. C. Choisi, and R. Stalio, (Dordrecht: Reidel), 499.
- [163] Kwok, S. 1982, in IAU Colloquium 70, *The Nature of Symbiotic Stars*, ed. M. Friedjung & R. Viotti, (Dordrecht: Riedel), 209.
- [164] Kwok, S. 1982b, in IAU Colloquium 70, *The Nature of Symbiotic Stars*, ed. M. Friedjung & R. Viotti, (Dordrecht: Riedel), 17.
- [165] Kwok S. 1983a, in *Planetary Nebulae*, ed. D. R. Flower, (Dordrecht: Reidel), 187.
- [166] Kwok S. 1983b, *M.N.R.A.S.*, **202**, 1149.

- [167] Kwok, S. 1987a, in *Late Stages of Stellar Evolution*, ed. S. Kwok, R. Pottasch, (Dordrecht: Reidel), 321.
- [168] Kwok, S. 1987b, in *IAU Symposium 131: Planetary Nebulae*, ed. S. Torres-Peimbert, (Dordrecht: Riedel), 401.
- [169] Kwok, S. 1988, in *IAU Colloquium 103: The Symbiotic Phenomenon*, ed. J. Mikolajewska, M. Friedjung, S. Kenyon, and R. Viotti, (Dordrecht: Kluwer), 129.
- [170] Kwok, S. 1993, *Ann. Rev. Astr. Ap.*, **31**, 63.
- [171] Kwok, S. 1994, *P. A.S.P.*, **106**, 344.
- [172] Kwok, S., Bignell, R. C., and Purton, C. R. 1984, *Ap. J.*, **279**, 188.
- [173] Kwok, S., and Leahy, D. A. 1984, *Ap. J.*, **283**, 675.
- [174] Kwok, S., and Purton 1978, *Ap. J. (Letters)*, **219**, L125.
- [175] Kwok, S., and Purton 1979, *Ap. J.*, **229**, 187.
- [176] Kwok, S., Purton, C. R., and Fitzgerald, M. P. 1978, *Ap. J.*, **219**, L125.
- [177] Kwok, S., Purton, C. R., and Keenan, D. W. 1981, *Ap. J.*, **250**, 232.
- [178] Lang, K. 1991, *Astrophysical Data: Planets and Stars*, (New York, Springer-Verlag).
- [179] Li, P. S. 1993, Masters Thesis, University of Calgary.
- [180] Livio, M. 1988, in *IAU Colloquium 103: The Symbiotic Phenomenon*, ed. J. Mikolajewska, M. Friedjung, S. Kenyon, and R. Viotti, (Dordrecht: Kluwer), 149.
- [181] Livio, M., Truran, J. W., Webbink, R. F. 1986, *Ap. J.*, **308**, 736.
- [182] Lorenzetti, D., Saraceno, P., and Strafella, F. 1985, *Ap. J.*, **298**, 350.
- [183] Luthardt, R. 1984, *Inf. Bull. Var. Stars*, No. 1189.
- [184] Luthardt, R. 1988, in *IAU Colloquium 103: The Symbiotic Phenomenon*, ed. J. Mikolajewska, M. Friedjung, S. Kenyon, and R. Viotti, (Dordrecht: Kluwer), 259.
- [185] Mamano, A., and Ciatti, F. 1975, *Astr. Ap.*, **39**, 405.

- [186] Marciel, W. J. 1984, *Astr. Ap.Suppl.*, **55**, 253.
- [187] Mattei, J. A. 1984, *Circ. Bureau Central Telegrammes*, 3932.
- [188] Mayall, M. W. 1937, *Ann. Harv. Coll. Obs.*, **105**, 491.
- [189] McGregor, P. J., Hyland, A. R., and Hillier, D. J. 1988, *Ap. J.*, **324**, 1071.
- [190] Meinunger, T. 1981, *Inf. Bull. Var. Stars*, No. 2016.
- [191] Mellema, G. 1993, PhD Thesis, Rijksuniversiteit te Leiden.
- [192] Merrill, P. W. 1951a, *Ap. J.*, **113**, 605.
- [193] Merrill, P. W. 1951b, *Ap. J.*, **114**, 338.
- [194] Merrill, P. W. 1959a, *Sky and Telescope*, July, 490.
- [195] Merrill, P. W. 1959b, *Ap. J.*, **44**, 44.
- [196] Michalitsianos, A. G., Kafatos, M., Fahey, R. P., Viotti, R., Cassatella, A., and Altamore, A. 1988, *Ap. J.*, **331**, 477.
- [197] Michel, F. C., 1991, *Theory of Neutron Star Magnetospheres*, (University of Chicago Press: Chicago).
- [198] Mikolajewska, J. 1988, in *IAU Colloquium 103: The Symbiotic Phenomenon*, ed. J. Mikolajewska, M. Friedjung, S. Kenyon, and R. Viotti, (Dordrecht: Kluwer), 303.
- [199] Mikolajewska J. 1992, in *Variable Star Research*, ed. Percy, Mattei, and Sterken, (New York: Cambridge University Press), 267.
- [200] Mikolajewska, J., and Kenyon 1992, *M.N.R.A.S.*, **256**, 177.
- [201] Mikolajewska, J., Kenyon, S. J., and Mikolajewski, M. 1989, *Astron. J.*, **98**, 1427.
- [202] Milne, D. K. 1979, *Astr. Ap.Suppl.*, **36**, 227.
- [203] Milne, D. K., and Aller, L. H. 1975, *Astr. Ap.*, **38**, 183.
- [204] Modisette, J. J. and Kondo, Y. 1980, *Ap. J.*, **240**, 180.
- [205] Mueller, B. E. A., and Nussbaumer, H. 1985, *Astr. Ap.*, **145**, 144.
- [206] Munari, L. 1988, *Astr. Ap.*, **200**, L13.

- [207] Munari, L. 1989, *Astr. Ap.*, **208**, 63.
- [208] Munari, U., and Whitelock, P. A. 1989, *M.N.R.A.S.*, **237**, 45.
- [209] Mürset, U., Nussbaumer, H. M., Schmid, H. M., and Vogel, M. 1991, *Astr. Ap.*, **248**, 458.
- [210] Muratorio, G, and Friedjung, M. 1982, in IAU Colloquium 70, *The Nature of Symbiotic Stars*, ed. M. Friedjung and R. Viotti (Dordrecht:Reidel), p. 161.
- [211] Nassau, J. J., and Cameron, D. M. 1954, *Ap. J.*, **119**, 75.
- [212] Netzer, N., and Knapp, G. R. 1987, *Ap. J.*, **323**, 734.
- [213] Newell, R. T. and Hjellming, R. M. 1981, in *Proceedings of the North American Workshop on Symbiotic Stars*, ed. R. E. Stencel (Boulder: JILA), 16.
- [214] Norris, R. P., Allen, D. A., Haynes, R. F., and Wright, A. E. 1984, *Proc. Astr. Soc. Aust.*, **5**, 562.
- [215] Nussbaumer, H. 1982, in IAU Colloquium 70, *The Nature of Symbiotic Stars*, ed. M. Friedjung & R. Viotti, (Dordrecht: Riedel), 85.
- [216] Nussbaumer, H. 1988, in *IAU Colloquium 103: The Symbiotic Phenomenon*, ed. J. Mikolajewska, M. Friedjung, S. Kenyon, and R. Viotti, (Dordrecht: Kluwer), 107.
- [217] Nussbaumer, H., and Schild, H. 1981, *Astr. Ap.*, **101**, 118.
- [218] Nussbaumer, H., and Schmid, H. M. 1988, *Astr. Ap.*, **192**, L10.
- [219] Nussbaumer, H., and Schmutz, W. 1983, *Astr. Ap.*, **126**, 59.
- [220] Nussbaumer, H., and Stencel, R. E. 1987, in *Exploring the Universe with the IUE Satellite*, ed. Y. Kondo, (Dordrecht: Reidel), 203.
- [221] Nussbaumer, H., and Vogel, M. 1987, *Astr. Ap.*, **182**, 51.
- [222] Nussbaumer, H., and Vogel, M. 1990, *Astr. Ap.*, **236**, 117.
- [223] Nussbaumer, H., Schild, H., Schmid, H. M., Vogel, M. 1988, *Astr. Ap.*, **198**, 179.
- [224] Oliverson, N. A., and Anderson, C. M. 1983, *Ap. J.*, **268**, 250.

- [225] Oliverson, N. A., Evans, N. R., and Anderson, C. M. 1988, *A Decade of UV Astronomy with IUE, Proc. Celebratory Symposium, ESA SP-281, Vol 2*, Jun 1988, 183.
- [226] Pacynski, B., and Rudak B. 1980, *Astr. Ap.*, **82**, 349.
- [227] Pacynski, B., and Zytkow A. N. 1978, *Ap. J.*, **222**, 604.
- [228] Penston, M. V., and Allen, D. A. 1985, *M.N.R.A.S.*, **212**, 939.
- [229] Penston, M. V. *et al.* 1983, *M.N.R.A.S.*, **202**, 833.
- [230] Piirola, V 1983, in IAU Colloquium 72, *Cataclysmic Variables and Related Objects*, p. 211.
- [231] Pilyugin, L. S., and Khromov, G. S. 1979, *Sov. Astron.*, **23**, 425.
- [232] Plavec, M. J. 1982, in IAU Colloquium 70, *The Nature of Symbiotic Stars*, ed. M. Friedjung & R. Viotti (Dordrecht: Riedel), 231.
- [233] Ponz, D., Cassatella, R., and Viotti, R. 1982, in *IAU Colloquium 70, The Nature of Symbiotic Stars*, ed. M. Friedjung, and R. Viotti, (Dordrecht: Reidel) 217.
- [234] Preite-Martinez, A., Acker, A., Kopper, J., and Stenholm, B. 1989, *Astron. Astrophys. Supp. Ser.*, **81**, 309.
- [235] Puetter, R. C., Russel, R. W., Soifer, B. T. and Willner, S. P. 1978, *Ap. J.*, **223**, L93.
- [236] Purton, C. R., and Feldman, P. A. 1978, in *IAU Symposium 76, Planetary Nebulae: Observations and Theory*, ed. Y. Terzian, (Dordrecht:Reidel), 324.
- [237] Purton, C. R., Feldman, P. A., Marsh, K. A., Allen, D. A., and Wright, A. E. 1982, *M.N.R.A.S.*, **198**, 321.
- [238] Robert, C., Drissen, L. and Moffat, A. F. J. 1989, in *IAU Colloquium 113: Physics of Luminous Blue Variables*, 299.
- [239] Roche, P. F., Allen, D. A., and Aitken, D. K. 1983, *M.N.R.A.S.*, **204**, 1009.
- [240] Rosino, L. 1987, in *RS Ophiuchi (1985) and the Recurrent Nova Phenomenon*, ed. M. F. Bode, (VNU Science Press: Utrecht) 1.
- [241] Rossi, C., Altamore, A., Ferrari-Toniolo, M., Persi, P., and Viotti, R. 1988, *Astr. Ap.*, **206**, 279.

- [242] Rudy, R. J., Cohen, R. D., Rossano, G. S., and Puetter, R. C. 1990, *Ap. J.*, **362**, 346.
- [243] Sahade, J., Brandi, E., and Fontenla, J. M. 1984, *Astr. Ap.Suppl.*, **56**, 17.
- [244] SAO Catalogue (Smithsonian Astrophysical Observatory Star Catalogue) 1966, Smithsonian Institution, Washington, D.C..
- [245] Schaifers, K. 1961, *Berlin Sternw. Mitt. Verand. Sterne.* No. 506-507.
- [246] Schild, H. 1989, *M.N.R.A.S.*, **240**, 63.
- [247] Schmide, H. M., and Schild, H. 1990, *M.N.R.A.S.*, **246**, 84.
- [248] Schulte-Ladbeck, R. E. 1988, *Astr. Ap.*, **189**, 97.
- [249] Schulte-Ladbeck, R. E., Aspin, C., Magalhães, A. M., and Schwarz, H. E. 1990, *Astr. Ap.Sup.*, **86**, 227.
- [250] Seal, P. 1990, *Ap. Space Sci.*, **174**, 321.
- [251] Seaquist, E. R. 1977, *Ap. J.*, **211**, 547.
- [252] Seaquist, E. R. 1988, in *IAU Colloquium 103: The Symbiotic Phenomenon*, ed. J. Mikolajewska, F. Friedjung, S. Kenyon, and Viotti, R., (Dordrecht: Kluwer), 69.
- [253] Seaquist, E. R., and Gregory, P. C. 1973, *Nature Phys. Sci.*, **245**, 85.
- [254] Seaquist, E. R., and Taylor, A. R., and Button S. 1984, *Ap. J.*, **284**, 202.
- [255] Seaquist, E. R., and Taylor, A. R. 1987, *Ap. J.*, **312**, 813.
- [256] Seaquist, E. R., and Taylor, A. R. 1990, *Ap. J.*, **349**, 313.
- [257] Seaquist, E. R., and Taylor, A. R. 1992, *Ap. J.*, **387**, 624.
- [258] Shapiro, S. L, and Teukolsky, S. A. 1983, *Black Holes, White Dwarfs, and Neutron Stars*, (New York: Wiley).
- [259] Skopal, A., Mikolajewski, M., and Tomov, T. 1987, *Ap. Space Sci.*, **131**, 747.
- [260] Skopal, A., Chochol, D., Vittone, A., and Mammano, A. 1988, in *IAU Colloquium 103, The Symbiotic Phenomenon*, ed. J. Mikolajewska, F. Friedjung, S. Kenyon, and Viotti, R., (Dordrecht: Kluwer), 289.

- [261] Shu, F. H. 1992, *The Physics of Astrophysics, Volume II, Gas Dynamics*, (University Science Books: California), 102.
- [262] Sion, E. M., and Starrfield, S. G. 1986, **303**, 130.
- [263] Slovak, M. H. 1978, *Astr. Ap. Letters*, **70**, 75.
- [264] Slovak, M. H. 1980, *Bull. AAS*, **12**, 868.
- [265] Slovak, M. H., and Lambert, D. L. 1988, in IAU Colloquium 103, *The Symbiotic Phenomenon*, ed. J. Mikolajewska, F. Friedjung, S. Kenyon, and Viotti, R., (Kluwer:Dordrecht), p.265.
- [266] Solf, J. 1983, *Ap. J.*, **266**, L113.
- [267] Solf, J. 1984, *Astr. Ap.*, **139**, 296.
- [268] Spitzer, L. 1978, *Physical Processes in the Interstellar Medium*, (New York: Wiley).
- [269] Stäuffer, J. R. 1984, *Ap. J.*, **280**, 695.
- [270] Stenholm, B., and Acker, A. 1987, *Astron. Astrophys. Suppl. Ser.*, **68**, 51.
- [271] Stephenson, C. B., and Sanduleak, N. 1971, *Pub. Warner Swasey Obs.*, **1**, No. 1.
- [272] Stevens, I. R. 1993, private communication.
- [273] Stevens, I. R., Blondin, J. M., and Pollock, A. M. T. 1992, *Ap. J.*, **386**, 265.
- [274] Stoker, N., and Livio, M. 1989, *Ap. J.*, **339**, 268.
- [275] Stover, R. J. and Sivertsen, S. 1977, *Ap. J. (Letters)*, **214**, L33.
- [276] Strafella, F. 1981, *Ap. J.*, **243**, 583.
- [277] Swings, J. P., and Struve, O. 1940, *Ap. J.*, **91**, 546.
- [278] Taranova, O. G., and Yudin, B. F. 1980, *Soviet Astronomy Letters*, **6**, 273.
- [279] Taranova, O. G., and Yudin, B. F. 1981, *Soviet Astr.*, **25**, 710.
- [280] Taranova, O. G., and Yudin, B. F. 1983, *Astr. Ap.*, **117**, 209.
- [281] Taranova, O. G. and Yudin, B. F. 1986, *Astr. Tsirk*, **1454**, 7.

- [282] Taylor, A. R. 1988, in *IAU Colloquium 103: The Symbiotic Phenomenon*, ed. J. Mikolajewska, M. Friedjung, S. Kenyon, and R. Viotti, (Dordrecht: Kluwer), 77.
- [283] Taylor, A. R., and Gregory, P. C. 1984, *Ap. J.*, **283**, 273.
- [284] Taylor, A. R., and Seaquist, E. R. 1984, *Ap. J.*, **286**, 263.
- [285] Taylor, A. R., and Seaquist, E. R., Mattei J. A. 1986, *Nature*, **319**, 38.
- [286] Taylor, A. R., Seaquist, E. R., and Kenyon, S. J. 1988a, in *IAU Colloquium 103: The Symbiotic Phenomenon*, ed. J. Mikolajewska, M. Friedjung, S. Kenyon, and R. Viotti, (Dordrecht: Kluwer), 231.
- [287] Taylor, A. R., Hjellming, R. M., Seaquist, E. R., and Gehrz, R. D. 1988b, *Nature*, **335**, 235.
- [288] Taylor, A. R., Bode, M. F., Davis, R. J., and Porcas, R. W. 1988c, in *IAU Colloquium 103: The Symbiotic Phenomenon*, ed. J. Mikolajewska, M. Friedjung, S. Kenyon, and R. Viotti, (Dordrecht: Kluwer), 335.
- [289] Taylor, A. R., Davis, R. J., Porcas, R. W., and Bode, M. F. 1989a, *M.N.R.A.S.*, **237**, 81.
- [290] Taylor, A. R., Gussie, G. T., and Goss, W. M. 1989b, *Ap. J.*, **340**, 932.
- [291] Tcheng, M-L, and Bloch, M. 1946, *Vistas in Astronomy*, **2**, 1412.
- [292] Thackeray, A. D. 1977, *M.N.R.A.S.*, **83**, 1.
- [293] Thronson, H. and Harvey, P. M. 1981, *Ap. J.*, **248**, 584.
- [294] Torbett, M. V., and Campbell, B. 1989, *Ap. J.*, **340**, L73.
- [295] Tylanda, R. 1977, *Acta Astron.*, **27**, 3.
- [296] Tylanda, R. Acker, A., Gleizes, F., and Stenholm, B. 1989, *Astron. Astrophys. Supp. Ser.*, **77**, 39.
- [297] Viotti, R. 1988, in *IAU Colloquium 103: The Symbiotic Phenomenon*, ed. J. Mikolajewska, M. Friedjung, S. Kenyon, and R. Viotti, (Dordrecht: Kluwer), 269.
- [298] Viotti, R., Griangrande, A., Riccardi, O., and Cassatella, A. 1982, in *IAU Colloquium 70: The Nature of Symbiotic Stars*, ed. M. Friedjung and R. Viotti, (Dordrecht: Reidel), 125.

- [299] Volk K., and Kwok, S. 1987, *Astron. J.*, **315**, 654.
- [300] Wallerstein, G. 1978, *P. A.S.P.*, **90**, 36.
- [301] Wallerstein, G. 1981b, *P. A.S.P.*, **93**, 577.
- [302] Wallerstein, G. 1988, *Astr. Ap.*, **197**, 161.
- [303] Wallerstein, G., Willson, L. A., Salzwert, J., and Brugel, E 1984, *Astr. Ap.*, **133**, 137.
- [304] Wallerstein, G., Schachter, J., Garnavich, P. and Oke, J. B. 1991, *P. A.S.P.*, **103**, 185.
- [305] Webbink, R. F., Livio, M., Truran, J. W., and Orio, M. 1987, *Ap. J.*, **314**, 653.
- [306] Webster, L. B. 1966, *P. A.S.P.*, **68**, 136.
- [307] Webster, L. B. 1969, *M.N.R.A.S.*, **143**, 79.
- [308] Welty, D. E. 1983, *P. A.S.P.*, **95**, 217.
- [309] Whitelock, P. A., 1985, in *First IRAS Conference, Light on Dark Matter*, ed. F. P. Isreal (Dordrecht: Reidel), 323.
- [310] Whitelock, P. A. 1987, *P. A.S.P.*, **99**, 573.
- [311] Whitelock, P. A. 1988, in *IAU Colloquium 103: The Symbiotic Phenomenon*, ed. J. Mikolajewska, M. Friedjung, S. Kenyon, and R. Viotti, (Dordrecht: Kluwer), 47.
- [312] Whitelock, P. A., Catchpole, R. M., and Feast, M. W. 1982, in *IAU Colloquium 70: The Nature of Symbiotic Stars*, ed. M. Friedjung and R. Viotti (Dordrecht: Reidel), 215.
- [313] Whitelock, P. A., Pottasch, S. R., and Feast, M. W. 1987, in *Late Stages of Stellar Evolution*, ed. S. Kwok, and S. R. Pottasch, (Dordrecht: Reidel), 269.
- [314] Whitelock, P. A., Feast, M. W., Roberts, G., Carter, B. S., and Catchpole, R. M. 1983, *M.N.R.A.S.*, **205**, 1207.
- [315] Wilkinson, P. N. 1989, in *Very Long Baseline Interferometry*, ed. M. Felli, and R. E. Spencer, (Dordrecht: Kluwer), 183.

- [316] Wilkinson, P. N., and Woodall, P. 1991, in *Radio Interferometry: Theory, Techniques and Applications, IAU Coll 131, ASP Conference Series, Vol 19*, ed. T. J. Cornwell, and R. A. Perley.
- [317] Willson, L. A. 1981a, *Astroph. Space Sci. Libr.*, **89**, 353.
- [318] Willson, L. A. 1981b, in *Proceeding of the North American Workshop on Symbiotic Stars*, ed. R. E. Stencel, (Boulder: JILA), 23.
- [319] Willson, L. A. 1987, in *Late Stages of Stellar Evolution*, ed. S. Kwok, and S. R. Pottasch, (Dordrecht: Reidel), 253.
- [320] Willson, L. A., Wallerstein, G., Brugel, E. W., and Stencel, R. E. 1984, *Astr. Ap.*, **133**, 154.
- [321] Wright, A. E., and Allen, D. A. 1978, *M.N.R.A.S.*, **184**, 893.
- [322] Wright, A. E., and Barlow, M. F. 1975, *M.N.R.A.S.*, **170**, 41.
- [323] Yamashita, Y., Maehara, H., and Norimoto, Y. 1978, *P. A.S.P.*, **30**, 219.
- [324] Yudin, B. F. 1982, *Soviet Astr.*, **26**, 187.
- [325] Yudin, B. F. 1985, *Astr. Ap.*, **110**, 277.
- [326] Yudin, B. F. 1988, in *IAU Colloquium 103: The Symbiotic Phenomenon*, ed. J. Mikolajewska, M. Friedjung, S. Kenyon, and R. Viotti, (Dordrecht: Kluwer), 261.
- [327] Zilstra, A., te Lintel Hekkert, P., Pottasch, S. R., Caswell, J. L., Ratag, A., and Habing, H. J. 1989, *Astr. Ap.*, **217**, 157.

Appendix A

CWb Boundary Governing Equations

The governing equations for the CWb model are as follows:

$$\begin{aligned}
 r_1' &= -r_1 \tan \zeta; \\
 v' &= \frac{r_1}{4\pi q v \cos \zeta} [-\cos(\phi - \zeta)(\sin(\phi - \zeta) - v)/r_2^2; \\
 &\quad + m \cos \zeta (-w \sin \zeta - v)/r_1^2]; \\
 \zeta' &= \frac{r_1}{4\pi q v^2 \cos \zeta} \left[\frac{(\cos^2(\phi - \zeta) + b)}{r_2^2} - \frac{m(w^2 \cos^2 \zeta + b)}{w r_1^2} \right] - 1; \\
 q &= [1 + \cos(\phi + \theta) + m(1 - \cos \theta)]/4\pi r_1 v \sin \theta; \\
 r_2^2 &= 1 + r_1^2 - 2r_1 \cos \theta; \text{ and} \\
 \phi &= \arccos[(r_1^2 + r_2^2 - 1)/2r_1 r_2], \tag{A.1}
 \end{aligned}$$

where primes (') denote derivatives with respect to θ , and the following dimensionless quantities have been defined:

$$\begin{aligned}
 r_1 &\equiv \frac{R_1}{a}; & r_2 &\equiv \frac{R_2}{a}; \\
 m &\equiv \frac{\dot{M}_1}{M_2}; & w &\equiv \frac{v_1}{v_2}; \\
 v &\equiv \frac{v_{||}}{v_2}; & q &\equiv \frac{\sigma v_2 a}{M_2}; \\
 b &\equiv \frac{kT_w}{\mu_a m_H v_2^2}; \text{ and} & \eta &\equiv \sqrt{\frac{w(1+b)}{m(w^2+b)}}. \tag{A.2}
 \end{aligned}$$

The boundary conditions for $\theta = 0$ are given by:

$$\begin{aligned}
r_1|_{\theta=0} &= [\eta + 1]^{-1}; \\
v|_{\theta=0} &= 0; \\
\zeta|_{\theta=0} &= 0; \\
q|_{\theta=0} &= \frac{(\eta^{-2} + m)(1 + \eta)}{8\pi v'|_{\theta=0}}; \\
r'_1|_{\theta=0} &= 0; \\
v'|_{\theta=0} &= \frac{2}{3} \left(\frac{1}{\eta^{-2} + m} \right) \left[\frac{\eta + 1}{\eta^3} + \zeta'|_{\theta=0}(\eta^{-2} - mw) \right]; \text{ and}
\end{aligned}$$

$$\begin{aligned}
(\zeta'|_{\theta=0})^2 4(1 - mw\eta^2) + \zeta'|_{\theta=0}[11 + 3b - mw\eta^2 + (10 + 3b)\eta^{-1}] \\
+ (1 + \eta^{-1})[4 + (6 + 3b)\eta^{-1}] = 0.
\end{aligned}$$

The physical parameters in the model include: a the binary separation; \dot{M}_1, \dot{M}_2 , v_1 and v_2 , the mass loss rates and velocities from stars 1 and 2 respectively; R_1 and R_2 , the distances from stars 1 and 2 respectively; T_w , the temperature of the undisturbed winds; σ and v_{\parallel} , the surface density and velocity along the interaction shell respectively; and μ_a , the mean atomic weight of nebular particles including electrons. Constants used in the equations include Boltzmann's constant, k , and the mass of a hydrogen atom, m_H . The angles θ, ϕ are defined in Figure 2.10.

Appendix B

Model Imaging

In order to produce a model image, it is necessary to solve the equation of radiative transfer for lines of sight through the model nebula. The solution for the intensity, I_ν , at frequency ν along a line of sight with optical depth τ , through an isothermal plasma of temperature T , is given by

$$I_\nu = B_\nu(T)(1 - e^{-\tau}). \quad (\text{B.1})$$

The Planck function, $B_\nu(T)$, may be approximated in the radio domain by the Rayleigh-Jeans law,

$$B_\nu = \frac{2kT\nu^2}{c^2}, \quad (\text{B.2})$$

where k is Boltzmann's constant and c is the speed of light. Optical depths are related to densities and path lengths through the model nebula via the opacity function, κ_ν :

$$\begin{aligned} \tau &\equiv \int \kappa_\nu ds, \\ \kappa_\nu &= a_\nu n_e^2, \\ a_\nu &= 0.21T^{-1.35}\nu^{-2.1}. \end{aligned} \quad (\text{B.3})$$

Here frequency is measured in [Hz], electron density (n_e) is measured in [cm^{-3}], and integration is performed along the line of sight. It has been assumed that the electron density is equal to the ion density.

The integration to obtain τ is in general non-trivial. Analytic solutions exist however for two special cases of interest. The first case is that of a nebula with a homogeneous density distribution. In this case $\tau_\nu = \kappa_\nu s$ where s is the path length through the nebula, and κ_ν will remain constant along the path. An analytic solution also exists for the case in which matter is distributed according to a wind-like density law: *i.e.* $n_e = A/r^2$ where A is a constant and r is the distance from some central source of mass loss.

Figure B.1 illustrates the parameters relevant to the calculation of optical depth for a line of sight through an arbitrarily shaped nebula supporting a wind-like density distribution. These parameters include: b , the impact parameter of the line of sight to the center of mass loss; x , the distance in the direction of the observer of points within the nebula; X_{near} and X_{far} , which are the x coordinates of the points of intersection of the line sight with the near and far nebular boundaries respectively; $\theta \equiv \tan^{-1}(x/b)$; $\theta_{\text{near}} = \tan^{-1}(X_{\text{near}}/b)$; and $\theta_{\text{far}} = \tan^{-1}(X_{\text{far}}/b)$. The optical depth is given by:

$$\begin{aligned}\tau &= \frac{a_\nu A^2}{b^3} Q, \\ Q &\equiv \frac{1}{2}(\theta + \sin\theta \cos\theta) \Big|_{\theta_{\text{far}}}^{\theta_{\text{near}}}, \\ \theta &\equiv \tan^{-1} \frac{x}{b}.\end{aligned}\tag{B.4}$$

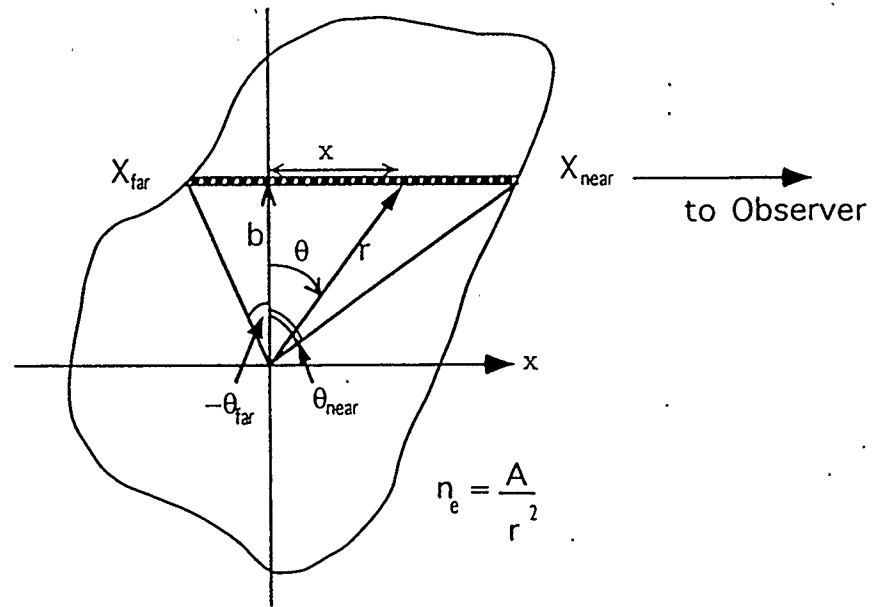


Figure B.1: Geometry for Optical Depth Determination: $1/r^2$ Density
 Illustrated in this figure is a radio emitting region of arbitrary shape, interior to which a wind-like density distribution exists, *i.e.* $n_e = A/r^2$ where A is a constant and r is the distance from the center of mass loss. Various parameters are defined for the determination of optical depth along an arbitrary line of sight (Equation B.4).

Appendix C

Apparent Density: Compressed Nebulae

Consider a spherical nebular shell of uniform density, n , radius R , and thickness Δ , such that $\Delta \ll R$. Suppose now that the shell is compressed so that the thickness is reduced to Δ' . The volume of the shell is therefore reduced from $V \approx 4\pi R^2 \Delta$ to $V' \approx 4\pi R^2 \Delta'$, and this reduction may be expressed by a “filling factor” $\epsilon \equiv V'/V \approx \Delta'/\Delta$. Since the mass of the shell has not changed, the compressed electron density is given by $n' = n/\epsilon$. The free-free optical depth, after compression, may be expressed in terms of the original configuration parameters as:

$$\begin{aligned}\tau &\propto n'^2 \Delta' \\ &\propto \frac{n^2}{\epsilon} \Delta\end{aligned}\tag{C.1}$$

Suppose now that the shell is observed and assumed to occupy its original volume. An apparent electron density, n_a , may be inferred from the observed optical depth according to the relationship: $\tau \propto n_a^2 \Delta$. Equating this optical depth to that in Equation C.1,

$$n_a = \frac{n}{\sqrt{\epsilon}}.\tag{C.2}$$

Similarly, suppose that the original density is given by an inverse square law, $n = A/R^2$, and the nebular material is subsequently compressed into concentric

shells so as to occupy some fraction ϵ of the original volume. The density constant inferred under the assumption of complete filling is given by:

$$A_a = \frac{A}{\sqrt{\epsilon}}. \quad (\text{C.3})$$

Appendix D

Alternative Designations of Program Stars

HM SGE	PK 053-03 2	SVS 2183	IRAS 19396+1637
V1016 Cyg	EM* AS 373	GCRV 70112	CSI+39-19553
	PK 075+05 1	MHA 328-116	JP11 5437
	JP11 5438	IRAS 19553+3941	
AG Peg	HD 207757	AG+12 2570	GEN# +1.00207757
	AGKR 19529	BD+11 4673	PLX 5279
	SKY# 41636	GCRV 13724	EM* MWC 379
	JP11 3412	SAO 107436	YZ 12 8693
	TD1 28516	DC 7622	IRAS 21486+1223
	SBC 879		
Z And	HD 221650	AG+48 2087	GEN# +1.00221650
	PLX 5697	BD+48 4093	IRAS 23312+4832
	GCRV 14773	JP11 3636	EM* MWC 416
	SAO 53146	SV* HV 193	AN 41.1901
BI CRU	HE 3-782	IRAS 12206-6221	
HE 2-106	PK 312-02 1	WRAY 16-148	ESO 97-14
	V835 Cen	NSV 6587	IRAS 14103-6311
HD 149427	PK 331-05 1	PN StWr 2-43	PN PC 11
	HE 2-172	He 3-1223	WRAY 16-228
	ESO 179-11	CD-55 6825	IRAS 16336-5536
RR Tel	AN 166.1908	HE 3-1811	GCRV 6924 E
	SKY# 37701	CSI-55-20003	IRAS 20003-5552
	SV* HV 3181		